Equilibria of a Gyrostat with a Discrete Damper

Ralph A. Sandfry

Dissertation submitted to the Faculty of the
Virginia Polytechnic Institute and State University
in partial fulfillment of the requirements for the degree of

Doctor of Philosophy
in
Aerospace Engineering

Dr. Christopher D. Hall, Chair
Dr. Eugene M. Cliff
Dr. Scott L. Hendricks
Dr. L. Glenn Kraige
Dr. Frederick H. Lutze

July 9, 2001
Blacksburg, Virginia

Keywords: gyrostat, damping, bifurcation

Equilibria of a Gyrostat with a Discrete Damper

Ralph A. Sandfry

(ABSTRACT)

We investigate the relative equilibria of a gyrostat with a spring-mass-dashpot damper to gain new insights into the dynamics of spin-stabilized satellites. The equations of motion are developed using a Newton-Euler approach, resulting in equations in terms of system momenta and damper variables. Linear and nonlinear stability methods produce stability conditions for simple spins about the nominal principal axes. We use analytical and numerical methods to explore system equilibria, including the bifurcations that occur for varying system parameters for varying rotor momentum and damper parameters. The equations and bifurcations for zero rotor absolute angular momentum are identical to those for a rigid body with an identical damper. For the more general case of non-zero rotor momentum, the bifurcations are complex structures that are perturbations of the zero rotor momentum case. We examine the effects of spring stiffness, damper position, and inertia properties on the global equilibria. Stable equilibria exist for many different spin axes, including some that do not lie in the nominally principal planes. Some bifurcations identify regions where a jump phenomenon is possible. We use Liapunov-Schmidt reduction to determine an analytic relationship between parameters to determine if the jump phenomenon occurs. Bifurcations of the nominal gyrostat spin are characterized in parameter space using two-parameter continuation and the Liapunov-Schmidt reduction technique. We quantify the effects of rotor or damper alignment errors by adding small displacements to the alignment vectors, resulting in perturbations of the bifurcations for the standard model. We apply the global bifurcation results to several practical applications. We relate the general set of all possible equilibria to specific equilibria for dual-spin satellites with typical parameters. For systems with tuned dampers, where the natural frequency of the spring-mass-damper matches the gyrostat precession frequency, we show numerically and analytically that the existence of certain equilibria are related to the damper tuning condition. Finally, the global equilibria and bifurcations for varying rotor momentum provide a unique perspective on the dynamics of simple rotor spin-up maneuvers.

Dedication

To Marilyn, Kate, and Matthew,

You've sustained me though the tough times and blessed me with your love and support. Every day you remind me of what is truly important.

Acknowledgments

It hardly seems possible that this long journey is at an end. Many people played a role in making this possible. I first thank my advisor, Dr. Chris Hall. He is an outstanding educator who combines academic excellence with a special ability to communicate with students. He has given me insight, encouragement, and more than my fair share of his vast patience and energies.

I also thank Professors Eugene M. Cliff, Scott L. Hendricks, L. Glenn Kraige, and Frederick H. Lutze for their support and valuable discussions about my research, dynamics and even things totally unrelated to school.

This work was made possible by the financial support of the Air Force through the Air Force Institute of Technology Civilian Institution program. I especially thank Colonel Michael DeLorenzo, the Department Head of the Department of Astronautics, US Air Force Academy. The confidence and support of this warrior-scholar are greatly appreciated.

Of course, I an indebted in countless ways to my parents, Jim and Nancy Sandfry, as well as my whole family. Their love and guidance made so much possible.

Most important to me has been the love and support of my wife, Marilyn, and our children, Kate and Matthew. Thanks for your sacrifices, encouragement, and strength.

Contents

List of Figures

List of Tables

Chapter 1

Introduction

The gyrostat, consisting of a rigid body and a spinning rotor, is an important model for studying the attitude dynamics of spin-stabilized satellites. The gyroscopic effects of the rotor can stabilize the spin vector for otherwise unstable configurations. Energy dissipation plays a pivotal role in the stability of spin-stabilized satellites. Most research has focused on the directional stability of the nominal spin axis, when the spin axis is aligned with the rotor spin axis. However, multiple equilibria exist, including different types of stable equilibria. The number and stability of these steady spins are significantly affected by system parameters, including the rotor momentum, damper parameters, and inertia properties. This dissertation produces a new, more complete perspective of the possible relative equilibria of this important model, and determines how the equilibria depend on system parameters.

1.1 Objective and Approach

This dissertation investigates the dynamics of a spinning, torque-free, satellite by studying a specific satellite model with energy dissipation. We seek a more complete understanding of the dynamics of a spinning rigid body with a single, axial rotor and energy dissipation provided by a spring-mass-dashpot damper. Specifically, we apply numerical and analytical methods to investigate the possible stationary spins and how the number and stability of these equilibria are affected by changing certain key system parameters.

The model we study is shown in Fig. 1.1, consisting of a rigid body, $\mathcal{B}$, containing a rigid axisymmetric rotor, $\mathcal{R}$, and a mass particle $\mathcal{P}$, which is constrained to move along a line $\mathbf{n}$ fixed in $\mathcal{B}$. A rigid body with damper is denoted $\mathcal{B}+\mathcal{P}$ while the gyrostat with damper is $\mathcal{B}+\mathcal{R}+\mathcal{P}$. The body frame axes $\mathbf{b}_i$ are system principal axes when $\mathcal{P}$ is in its undeformed position. The vector $\mathbf{n}$ is parallel to $\mathbf{b}_1$, which is the nominal spin axis for the spacecraft. The particle is connected to a linear spring and a linear dashpot damper. The rotor spin axis is in the $\mathbf{a}$ direction, parallel to the $\mathbf{b}_1$ axis and in the same principal plane as $\mathcal{P}$. All vectors and tensors are expressed with respect to

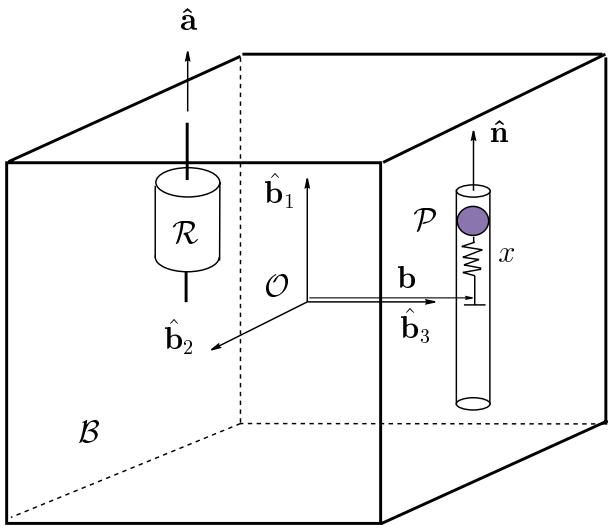

Figure 1.1: Single-rotor axial gyrostat with aligned discrete damper and axisymmetric rotor.

the body frame. This configuration is a reasonable model for a spacecraft with a momentum wheel and a "ball-in-tube" type damper. Depending on the location and size of the rotor relative to the rigid body, this could also model a dual-spin satellite with damping on the platform. The damper properties could also be adjusted to model a flexible appendage attached to the rigid body.

We develop the equations of motion using a Newton-Euler approach. After non-dimensionalizing the equations, we first study the stability of simple spins about principal axes. Routh-Hurwitz stability criteria are used in the linear stability analysis, generating stability conditions for the nominal spin axis. A non-linear, Liapunov-based approach is necessary to establish stability boundaries explicitly for all three simple spins.

We use numerical continuation techniques, primarily using the software package AUTO,[22] to create branches of equilibria in state-parameter space. These equilibria are presented on the momentum sphere as well as in bifurcation diagrams. We consider the effects of damper parameters, rotor momentum, and inertia properties on the global equilibria and their stability. Using two-parameter continuation and Liapunov-Schmidt reduction, key changes in the equilibria are determined both analytically and numerically and presented in parameter space. We also determine numerically the effects of rotor or damper alignment errors by adding small perturbations to the model. Numerical continuation then is applied to the perturbed model.

1.2 Background

Energy dissipation plays a critical role in the asymptotic stability of spacecraft steady spins. In 1958 the United States launched Explorer I, and satellite engineers learned that the effect of energy dissipation cannot be ignored in the stability analysis of spinning satellites.[46] Designers of Explorer I applied the classic rigid body spin stability results–a spinning rigid body is stable for spins about either a major or minor axis. Explorer I was designed to spin about its minor axis, but after about 90 minutes it was in a flat spin about its major axis. Like all real systems, Explorer I was not a rigid body, but instead had several means of dissipating energy including flexible antenna. Following the Explorer I experience, engineers showed analytically that with energy dissipation, or damping, an otherwise rigid spinning body is only stable when spinning about the major axis.

The "major axis rule" for rigid bodies is rather limiting for satellite designers. A relatively flat, disk-shaped satellite required for stability does not efficiently use the space in a typical launch vehicle fairing. However, engineers recognized fairly early that the addition of a spinning rotor within the satellite could contain enough angular momentum to stabilize a satellite's spin axis, even for minor or intermediate axes.[46] This led to the development of dual-spin satellites, with a relatively fast-spinning rotor and a slowly spinning platform. TACSAT I in 1969 was the first demonstration of this concept. The large rotor spun about the system's minor axis while keeping the communication payload's antenna pointed at the Earth. Prior to launch, extensive analysis and simulation of a gyrostat with damping was completed to ensure the stability of TACSAT I. Its on-orbit success validated the conclusion that the dual-spin concept could spin-stabilize a satellite even about a minor axis.

Much of the original stability analysis for spinning bodies and gyrostats with damping was done with approximate methods, generally referred to as energy-sink methods. The stability conclusions from these methods are useful, but they often produce necessary but not sufficient stability criteria. For precise stability criteria, the actual damping mechanism must be included in the system model. Of course, this higher precision comes with the price of dealing with the additional degrees of freedom needed to model the damper.

Almost all the work to date on this problem has centered on the stability of the nominal spin. This spin axis is usually aligned with the rotor spin axis. However, many other equilibria are possible for this system. Operational problems and environmental effects always pose the risk of perturbing a satellite, perhaps severely, from its intended attitude. When perturbed, a torque-free gyrostat with damping should eventually reach a stable, although possibly different, equilibrium state. An understanding of all possible equilibrium states and their stability is an important step to addressing these operational issues. The current work will investigate the system equilibria more globally than previous efforts and create a more complete understanding of the system dynamics.

Understanding the dynamics of a specific satellite configuration is certainly useful, but of perhaps greater interest is how these dynamics change when varying certain system parameters. Changing the damper parameters, such as spring stiffness or damper location, can have significant effects on the number of equilibria and their stability. Certain parameter values can possibly destabilize

otherwise stable configurations. Also, the effect of varying the rotor momentum is of considerable interest. Unlike damper parameters, rotor momentum may be easily varied even on-orbit. The set of stable equilibria for increasing rotor momentum determines a possible path in state-space for rotor spin-up, for sufficiently small rotor torques.

The effects of energy dissipation on rigid bodies and gyrostats are fundamental to the dynamics of spinning satellites. Identifying the global steady motions of these models and how varying parameters affect their equilibria are key to fully understanding spin-stabilized satellite dynamics.

1.3 Summary of Contributions

This dissertation provides the first thorough description of the possible equilibria for a gyrostat with a discrete damper. Whereas earlier works concentrated on the stability of the nominal spin, this work establishes an extensive catalog of equilibria and their dependence on certain system parameters. Many possible stable equilibria are identified other than the nominal spin, including many previously undocumented steady spins corresponding to unique possible trap states.

Analytical stability analysis reveals explicit stability conditions for several important simple spins. The previously known stability conditions for the nominal spin are put in a new context as bifurcation points of equilibria for changing system parameters.

Some of the equilibria that bifurcate from the nominal-spin state are represented in a useful, concise manner in parameter space. Liapunov-Schmidt reduction allows the key nominal-spin bifurcation point to be characterized analytically, which provides explicit conditions for predicting the onset of a jump phenomenon. This technique produces a valuable design criteria for selecting damper parameters to avoid the jump phenomenon.

An analysis of rotor or damper alignment errors identifies the effects on the global equilibria. In general, these errors break certain symmetries and perturb previously symmetric equilibrium structures. Specific types of errors break specific pitchfork bifurcations and create new asymmetric branches of equilibria. The perturbed equilibria indicate that perturbing the rotor or damper axes out of a principal plane can impart a coning motion to the intended nominal spin.

Finally, the vast class of possible equilibria, for a wide range of system parameters, is put in the context of realistic dual-spin satellite parameters. Typical parameter values for current dual-spin satellites produce relatively simple global equilibria. The global perspective of stable equilibria, for varying rotor momentum, produces new insights into rotor spin-up dynamics. For typical parameters, the spin-up dynamics are reasonably benign, but for off-design conditions the spin-axis may take an unusual path in state space. In all cases, the stable, global equilibria for varying rotor momentum can approximately predict the system state trajectories during rotor spin-up.

1.4 Overview

In Ch. 2, we summarize previous research related to stability of spinning satellites. We include results for both rigid bodies as well as satellites with rotors.

Chapter 3 develops the equations of motion using a Newton-Euler approach. The equations are reduced using several simplifying assumptions, resulting in five first-order equations in terms of system angular momentum and damper variables. However, the system is truly fourth-order due to the first integral due to conserved angular momentum. A spherical-coordinate transformation is proposed that reduces the equations to a system of four variables.

The stability conditions for the nominal spin axis are derived in Ch. 4. We also determine the stability conditions for flat spins about the other two principal axes. Linear and nonlinear stability methods produce explicit stability boundaries.

In Ch. 5, numerical continuation produces bifurcation diagrams for varying damper and rotor parameters. The effects of different inertia properties are also explored. We generate complete sets of bifurcation results for each case considered. Selected results are in Ch. 5 whereas the complete results are in the Appendices.

We present important bifurcations of equilibria in parameter space in Ch. 6. Two-parameter continuation produces branches of singular, turning points. Key transitions in types of equilibria are explicitly determined using Liapunov-Schmidt reduction.

Chapter 7 considers the effects of alignment errors of the rotor or damper. Perturbations to the alignment vectors are added to the system model. Numerical continuation produces the bifurcation diagrams for the resulting equilibria.

Finally, Chapters 8 and 9 provide correlation of these results to real systems, followed by conclusions and recommendations for further work.

Chapter 2

Literature Review

In this chapter we summarize the significant works related to satellite spin dynamics and stability. We first review the results for spinning bodies with energy dissipation. Two methods of analyzing energy dissipation are considered: a non-specific energy-sink and a discrete damper. We then discuss the developments for dual-spin satellites with damping. Finally, we review works that consider equilibria other than the nominal spin.

2.1 Spin-Stabilization With Energy Dissipation

The instability of Explorer I made engineers immediately aware of the effects of energy dissipation on satellite spin stability. The Explorer I instability was actually anticipated by Bracewell and Garriott,[11] who recognized that with energy dissipation, an otherwise rigid body in torque-free motion is destined to spin about an axis of maximum inertia. Dr. Ronald Bracewell was a radio astronomer at Stanford and had determined, using Sputnik's radio signals, that the Soviet satellite was spinning about an axis of symmetry. Using ideas from his understanding of rotational dynamics of galaxies, he concluded that Sputnik must be spinning about its major axis. The key aspect of this condition is that it minimizes kinetic energy for a particular angular momentum value. Bracewell attempted to contact the Explorer I designers to make sure they were aware of this effect, but the security surrounding the project prevented any contact. Bracewell published his ideas with Owen Garriott in September 1958, too late to help Explorer I. According to Likins,[46] an RCA engineer named Vernon Landon preceded Bracewell by deducing the same major-axis spin criteria in early 1957. Landon's laboratory notes showed that he recognized that energy dissipation violates the assumptions behind the classic rigid-body results of Euler and Poinsot, resulting in an unstable minor-axis spin. Unfortunately, Landon did not successfully publish until later. These conclusions were supported by Haseltine[32] who also used energy arguments to deduce the instability of a minor-axis spin for a rigid body with energy dissipation.

2.1.1 Energy-Sink Methods

Satellite designers did not have rigorous methods of analyzing the stability of generic satellite models, so analysts developed a class of approximate methods, known as energy-sink methods. Bracewell derived his original conclusions from an energy-sink method.[11] Many other authors also used these methods to gain insight into the required stability conditions for rigid bodies and gyrostats with energy dissipation.[4, 9, 10, 12, 32, 36, 42, 45, 47, 52, 66] Fundamental to these methods is the *energy-sink hypothesis* which states that the kinetic energy of any real body is slowly dissipated into heat energy. Also included in the hypothesis is the assumption that the dissipating motion is sufficiently small so that the spacecraft has an essentially constant inertia ellipsoid. These methods often involve using solutions to related problems without damping to help approximate the solutions for systems with damping. In specific cases (such as axisymmetric or asymmetric rigid bodies) solutions exist for torque-free rigid bodies where energy is conserved. From the energy-sink hypothesis, the rigid-body solutions are reasonable approximations to the solutions of the full equations with energy dissipation. Energy-sink methods often substitute these rigid-body solutions into the complete equations with energy dissipation. The equations representing the internal damping degrees of freedom can then be used to generate stability criteria or approximate energy dissipation rates. While not rigorous, the stability conditions for these "quasi-rigid" bodies provide useful results for satellite designers.

2.1.2 Specific Damping Devices

Whereas energy-sink methods provide useful general stability criteria, caution must be used in applying these results. In his spacecraft attitude dynamics text, Hughes[34] compared the stability results of an energy-sink method to the results for a specific damper model, both applied to a rigid body. He uses an energy-sink analysis to confirm the major-axis rule for quasi-rigid bodies. He also developed the equations of motion for a rigid body with a spring-mass-damper. The stability analysis of this specific model concludes that the major-axis spin may be de-stabilized by two causes: 1) a sufficiently soft spring or 2) placing the damper too far from the spin axis. The stability conclusions for a rigid body with a spring-mass-damper were originally derived using a linearized analysis in 1976 by Sarychev and Sazonov.[58] Chinnery[16] derived the same conditions using a Liapunov analysis. The additional degrees of freedom of including the damper mechanism in the model make analysis more cumbersome and the results less general, but the results are more precise. The energy-sink methods provide useful general stability trends, but exact stability criteria require analysis of specific damper mechanisms.

Researchers have studied the performance of different damper devices and configurations with rigid bodies. Two major types of damping mechanisms that were modeled and analyzed include spring-mass-dashpot dampers and viscous-ring nutation dampers. Schneider and Likins[60] studied the effectiveness of spring-mass-dashpot dampers in passively damping the coning motion of spinning rigid bodies. They studied dampers mounted parallel and normal to the desired satellite spin axis. The damper mounted parallel to the spin axis, sometimes called an axial damper in the

literature, is excited by the precession, or coning motion of the symmetry axis about the inertially fixed angular momentum vector, and was therefore referred to as a precession damper. The damper aligned normal to the spin axis, often referred to as a circumferential damper, is excited by nutation, or the nodding oscillation of the spin axis about its conical path, and was called a nutation damper. Despite the more precise definitions of Schnieder and Likins, the term "nutation damper" has been used throughout the literature for any device which damps coning motion. For stable, spinning, asymmetric bodies either a precession or nutation damper attenuates both precession and nutation. Schneider and Likins used an energy-sink method and numerical simulation to support the conclusion that for any physically feasible spacecraft the precession damper dissipates more energy per unit mass than the nutation damper for small coning angles. For larger coning angles and certain rigid body asymmetries, nutation dampers have superior average energy dissipation rates. In 1980 Cochran and Thompson[21] re-examined the same problem as Schneider and Likins. Using a different method for approximating the elliptic functions in the energy-sink method, they validated the superiority of precession dampers for small coning angles. Also, they achieved better agreement with numerical simulation than Schneider and Likins for larger coning angles, where nutation dampers had larger average dissipation rates.

Rings partially filled with viscous fluid have been used on satellites as nutation dampers. Carrier and Miles were the first to examine a partially filled viscous ring damper.[12,51] They approached the problem from a fluid mechanics standpoint and found that for small nutation angles the fluid spreads out around the outer part of the ring. But for larger angles, gaps begin to appear in the fluid and somewhere between 0.5°-1° the fluid behaves as a rigid slug. Cartwright, Massingill, and Trueblood treated the fluid as a rigid slug in their analysis of a spinning rigid body with a ring damper.[13] For spins about a body axis of symmetry, they identified two distinct motions which they named the nutation-synchronous and spin-synchronous modes. For larger nutation angles the slug moves within the ring roughly synchronous with the satellite precession. As damping continues, nutation angle decreases until the spin-synchronous mode begins. This mode is roughly synchronous with the satellite spin-rate and continues damping the nutation angle, although in an oscillatory manner. Alfriend reexamined this problem and generated an approximate solution for the nutation angle time history for both modes.[2]

In 1996, Chang, Liu, and Alfriend[15] studied the dynamics and stability of an inertially symmetric, spinning, rigid body with a viscous-ring damper mounted normal to the spin axis. They found three distinct equilibria: one corresponds to spins about the axis of symmetry and previously analyzed,[2,13] and two correspond to spins about a transverse axis, with and without precession. In examining the stability of these equilibria, the analysis was complicated by a persistent zero eigenvalue in the linearized equations. Therefore, linear stability analysis is inconclusive. They used the non-linear equations directly by using center manifold theory to isolate the stable subspace and determine stability of the flow in the center manifold. The equations for stability conditions and the decay time constant for these equilibria were generated explicitly.

Although much of the research has focused on partially-filled ring dampers, completely-filled ring dampers also dissipate energy and damp nutation. Bhuta and Koval investigated a completely-filled viscous-ring damper with a spinning rigid-body.[10] The damping rate was not as high as for

partially-filled ring dampers, but a completely-filled ring does not appreciably change the inertia properties of the spacecraft.

Researchers have studied other damping device possibilities. Alper[4] and Bhuta and Koval[9] studied damping of asymmetric rigid bodies with two degree of freedom pendulum dampers. Other devices considered include eddy current spherical magnetically anchored dampers,[40] viscous spherical nutation dampers,[43,68] and elastomer dampers.[14]

Whatever the means of energy dissipation, an otherwise rigid body with damping is stable only in spins about a major axis. While this was satisfactory for many early satellites, the required oblate shape was a design obstacle for satellite designers. Launch vehicle payload fairings constrained the growing size of new communication satellites. A useful method of gyroscopically stabilizing satellites with a spinning rotor led to the development of dual-spin satellites, which allows stable minor-axis spins.

2.2 Dual-Spin Satellites

The idea of designing satellites with a spinning section and a despun, or slowly spinning, section originated from the desire to use spin-stabilization on an earth-pointing satellite. Often the high spin-rate section is referred to as the rotor while the slowly spinning section is called the platform. This concept, later named "dual-spin," was successfully demonstrated in 1962 by Ball Brothers with the orbit of their OSO I satellite.[46] However, OSO I spins about a principal axis of maximum inertia. According to Flatley,[24] Huston[35] was the first to publish, in 1963, the dual-spin principle for gyroscopic stabilization in the open literature. However, since OSO I was launched in 1962 the concept obviously had earlier origins. Huston's analysis did not include the effects of energy dissipation.

The gyrostat model, consisting of a rigid-body satellite and a single rigid, axisymmetric, rotor constrained to rotate about its symmetry axis, was studied extensively to understand the dynamics of satellites with rotors. Development of the gyrostat equations of motion and stability analysis of their equilibria is included in the spacecraft attitude dynamics text by Hughes.[34] Ignoring damping, the equations of motion for gyrostats have two well-known integrable cases. One case is for a constant-speed rotor, often called a *Kelvin gyrostat.* The other is for a torque-free rotor, referred to as an *apparent gyrostat.* These solutions form the basis of a perturbation method used by Hall to study spinup dynamics for gyrostats.[29]

The energy dissipation lessons of Explorer I had been learned perhaps too well, and in the early 1960's little consideration was given to possible stable minor-axis spin concepts. However, Vernon Landon was aware that storing enough angular momentum in a rotor could overcome the minor-axis spin instability, but his attempt to publish in 1962 was rejected.[46] In 1964, along with Brian Stewart, he published a paper showing stability criteria for two co-axial axisymmetric bodies with energy dissipation on one of the bodies.[42] The model was rather restrictive, but the energy-sink

approximation yielded an important result: the system could be stable in a minor-axis spin with energy dissipation on the platform. Landon's analysis did not allow for energy dissipation on both the platform and rotor simultaneously. Landon noted that with a motor, a torque could be applied to the rotor to keep the relative angular rate constant. He identified the motor as an energy source or sink which must be accounted for in the analysis.

Independent of Landon and Stewart, Tony Iorillo at Hughes also discovered that with energy dissipation on the platform, a dual-spin satellite could be stable in spin about the minor axis.[36] Iorillo also used an energy-sink analysis to study a dual-spin configuration, but he included energy dissipation on both the platform and rotor. He concluded that the spin axis can be stable provided the energy dissipation of the platform was large enough relative to that of the rotor. Iorillo's work led to the development of TACSAT I, the first on-orbit demonstration in 1969 of Hughes' "Gyrostat" satellite concept, what we usually refer to as a dual-spin satellite.

The term "dual-spin" originated with Peter Likins in his 1967 paper on the stability of a gyrostat with damping.[45] Likins' work supported the Hughes' stability concept by performing two separate analyses. First, he examined the full equations of a specific dual-spin satellite with a spring-mass-dashpot damper on one of the bodies. The model he used consisted of an asymmetric platform and an axisymmetric rotor. The damper was mounted on a principal axis and parallel to the satellite spin axis. By applying Routh-Hurwitz stability criteria to the linearized equations of motion, he found that damping on the platform can stabilize the attitude of a minor-axis spin. However, he realized that any real system has some energy dissipation on both the platform and rotor. To address this issue, Likins next performed an energy-sink analysis on a quasi-rigid gyrostat: a rigid asymmetric body with rigid axisymmetric rotor with energy dissipation throughout. Although not as rigorous as the previous study, the resulting stability conditions were similar to Iorillo's results. For the special case of a despun platform, he found that damping on the platform is stabilizing, but damping on the rotor is destabilizing if the rotor spin moment of inertia is less than the average of the two platform transverse moments of inertia. This stability condition was later modified by Spencer, who developed a more generalized condition in terms of time-varying quantities.[64]

In 1967 the U.S. Air Force sponsored a dual-spin satellite symposium.[1] Several of the previously described works were presented. Also included were papers concerning:

- results of numerical simulations studies on stability of dual spin systems
- interactions between pointing control system and nutation motion of dual-spin spacecraft
- theory and design of nutation dampers
- attitude control systems
- specific spacecraft configurations

Although the general stability results for dual-spin satellites had been established, more work went into examining energy dissipation on both the platform and rotor. Again, for precise sta-

bility conclusions, specific damper mechanisms must be included in the model. For spring-mass-dampers on both bodies, the resulting partially-linearized equations of motion contain periodic coefficients. Mingori used Floquet theory to study the stability of such a model.[52] Several other researchers used various perturbation methods to approximate the dynamics and generate stability conditions.[6,24,49,58,67]

Often the energy dissipation mechanism can not be easily modeled, particularly on the rotor, so an energy-sink approach is used. Energy-sink methods are also used as a less complex approach to obtaining stability information, although they may not be as precise. Many dual-spin satellites are designed to maintain a constant rotor speed, using a motor and wheel-speed controller. Some researchers questioned whether this energy addition invalidated energy-sink methods for these applications.

2.2.1 Energy Sink Methods For Dual-Spin Satellites

A question over the applicability of energy-sink methods to systems with driven rotors was raised by Kane and Levinson.[39] They pointed out that systems such as those with constant-speed rotors require a motor torque which adds energy to the system. These and other problems with energy addition seem to violate the energy-sink hypothesis in that total energy is not decreasing. Nevertheless, many researchers have applied energy-sink methods to just such problems.[19,36,45,47,52,64] However, several researchers have shown that when properly used, energy-sink methods produce accurate results even for driven rotors.

Cochran and Shu examined an axisymmetric dual-spin satellite with energy addition due to a constant-speed rotor and energy dissipation provided by a spring-mass-dashpot damper.[20] They applied the generalized method of averaging, assuming a small damper mass, as well as an energy-sink method. By accounting for the contribution of the rotor torque to rotational kinetic energy, the energy-sink method produced an average time rate of change of nutation angle which agreed well with the generalized method of averaging and numerical simulation.

Ross also showed that energy-sink methods were applicable even in problems with a driven rotor.[56] He showed that if the work done by the rotor torque is properly taken into account, as originally prescribed by Landon and Stewart,[42] the energy-sink methods still yield consistent results. He suggested that since total energy could be added or removed by a motor, perhaps a better term was "energy-state approximation" rather than an energy-sink. Ross also showed that the system "core energy," as defined by Hubert,[33] was the more meaningful energy term to consider in energy-sink analysis. Hubert defined core energy as the potential energy and rotational kinetic energy of a fictitious body, with the inertia properties of the entire gyrostat, that has the angular velocity of the platform. Ross ignored any flexibility contributions and therefore dealt with just the kinetic energy. Hubert contended that core energy was the correct energy-sink parameter in that it was always decreasing, even for driven rotors. Ross showed that this was not always true, as in the case of sufficiently rapid rotor despin. However, the derived relationship between core energy and energy dissipation can assist in damper design. Ross later developed a stability condition in terms

of core energy for the case when the platform and rotor are quasi-rigid.[57] He also showed that the original Landon-Iorillo stability criterion produce accurate results even for cases with driven rotors.

Energy-sink methods are still applicable to dual-spin satellites, even for systems with driven rotors. Like with rigid (or quasi-rigid) bodies, more accurate stability boundaries are possible if the damping mechanism is included in the gyrostat model.

2.2.2 Specific Damping Devices for Dual-Spin Satellites

As with damped spin-stabilized satellites, energy-sink methods provide useful stability guidelines, but precise stability information requires analysis of specific damping devices.

Some of the same damping devices and configurations used for spinning (single-spin) satellites also were proposed for dual-spin satellites. In addition to the spring-mass-dampers previously discussed, other damper models were also examined for dual-spin satellites. Bainum, Feuchsel and Mackison studied dual-spin satellite stability with a pendulum-type spring-damper with torsional stiffness and damping.[7] The pendulum was mounted on the platform and moved in a plane normal to the nominal spin axis. The rotor had constant speed and its axis was parallel to the satellite spin axis. The resulting equations of motion were linearized about the nominal spin condition and Routh-Hurwitz criteria were applied to obtain the stability conditions. They examined variations in damper parameters and their effects on the damping time constant. Numerical studies showed considerable degradation in nutational damping performance for dynamic mass unbalance of the main body.

Other damping devices proposed for dual-spin satellites included a four-mass nutation damper with torsional damping and restoring force.[61] Symmetrically configured about the mass center, the damper motion did not vary the inertia properties. Alfriend and Hubert examined a dual-spin satellite with a partially-filled ring damper on the rotor and a spring-mass-damper on the platform.[3] They used approximate equations of motion to develop time constants and stability conditions.

Specific results were obtained for particular damper mechanisms and configurations. Most of this work focused on stability of the nominal spin for satellites with linear damper forces. However, some researchers considered other aspects of dual-spin satellite dynamics.

2.2.3 Other Developments

Research of the damped dual-spin satellite model has branched into several other areas. Although many researchers have used a linear spring-mass-dashpot damper model, with linear spring force and damping, several researchers studied the effects of non-linear damper forces. Likins, Mingori, and Tseng[47,53] found that with a non-linear spring force or non-linear damping, a dual-spin satellite can produce stable limit cycles, precessing about the nominal spin axis. This behavior was impor-

tant in explaining the occasional coning motion of TACSAT I. Johnson studied the dynamics of n-body axisymmetric spinning bodies with a damper on each.[38] The resulting periodic-coefficient differential equations were solved by an asymptotic expansion method, followed by a stability analysis. For the specific case of triple-spin satellites, he used a numerical method based on Floquet theory to validate the derived analytical stability results.

Several researchers found chaos in certain dual-spin satellite problems.[27,50,55] Chaos is possible for problems with energy addition to the system in the form of driven rotors or damping devices. Meehan and Asokanthen reported chaotic motions are possible for a dual-spin satellite with an axial damper, excited by sinusoidal rotor torques.[50] These varying torques could be generated by control system problems, or during spin-up of an unbalanced rotor, or due to rotor motor voltage fluctuations. Gray, Kammer, Dobson and Miller used Melnikov's method to analytically predict the onset of chaos in a dual-spin satellite model for a minor-axis spin to major-axis spin maneuver.[27] The damper motion was a prescribed sinusoidal motion, making transitional chaos possible during the maneuver.

Most researchers studied the dynamics and stability of a specific equilibrium state for dual-spin satellites: the nominal spin. In the next section we review the results that consider other possible equilibrium states.

2.3 Multiple Equilibria

Most initial research focused on evaluating stability of the nominal spin equilibrium condition for either a single or dual-spin satellite. This is the most practical equilibrium condition, but some researchers also began studying the other possible equilibria.

Several researchers investigated multiple equilibria in rigid bodies with discrete dampers. Bifurcation theory was used by several researchers to characterize the global dynamics and how system parameters affect equilibria. Levi[44] studied a rigid body with fixed mass-center and a spring-mass damper, constrained to move along the major axis. He identified multiple equilibria including some not aligned with an original (undeformed damper) principal axis. Bifurcations for varying spring stiffness were identified, including pitchfork bifurcations for the two undeformed principal-axis spins normal to the damper axis.

Chinnery and Hall[17] identified multiple equilibria for a spinning, rigid body with damper mounted parallel to a principal axis and the undeformed mass on another principal axis. Equilibria for which angular momentum lies in this principal plane were identified for varying damper location using numerical continuation. Multiple equilibria were found for a given spring stiffness and damper location. Jump phenomena were observed as multiple stable equilibria may exist. They found a persistent pitchfork bifurcation for spins about the body axis parallel to the damper, the nominal axis. The pitchfork changes from a subcritical pitchfork for a softer spring to a supercritical pitchfork for a stiffer spring. They used Liapunov-Schmidt reduction to analytically determine the

critical spring stiffness for the transition from subcritical to supercritical pitchforks.

Multiple equilibria have also been examined for dual-spin satellites with damping. Cloutier[18,19] studied a dual-spin model with two axisymmetric rigid bodies and a spring-mass-dashpot nutation damper mounted on one of the bodies, normal to the nominal spin axis. The resulting stability criteria for the nominal spin are similar to previous results for other dual-spin models, but he also considered the resulting motion when stability criteria were violated. Of the two derived stability criteria, the first pertained to inertia properties and spin rates and the second was affected by, in addition to inertia properties and spin rates, damper location and spring stiffness. If the first stability criterion is violated, the nominal spin is unstable and the satellite eventually spins about a transverse axis. If the second stability criterion is violated, the satellite tends toward a steady spin about a canted axis, not an axis of symmetry. This new spin axis is in the plane formed by the original nominal spin axis and the direction of damper motion.

Fang used miminization of kinetic energy to produce conditions for two possible stable equilibria for prolate dual-spin satellites with damping.[23] One state corresponded to a pure minor-axis spin, with the angular momentum vector aligned with the system minor axis. The second equilibrium state had the angular momentum vector inclined relative to the satellite minor axis, which resulted in precession of the intended spin axis around the angular momentum vector.

Bifurcation phenomena have also been found by Liu and Rimrott[48] in the study of an asymmetrical gyrostat with external or internal energy dissipation. Several damping mechanisms were considered, including a gyrostat containing viscous fluid. For each class of energy dissipation, the number and type of equilibrium motions vary with mass geometry and the rotor speed. Stability regions in parameter space were identified and characterized by a stable or unstable node, a saddle, or a stable or unstable focus.

Hall[30] studied the motion of a torque-free, rigid gyrostat with a spring-mass-dashpot damper. He considered the case of a single-rotor gyrostat with rotor axis parallel to an undeformed system principal axis. The damper was configured as in Ref. 17, with damper axis parallel to the rotor axis. He used a linear analysis to derive stability criteria for the nominal spin. Bifurcations for multiple equilibria were presented in the slow state space of the rotor momenta and the unperturbed system Hamiltonian.

Much work has been done in understanding the dynamics and stability of rigid bodies and gyrostats, including the effects of energy dissipation. Researchers have applied bifurcation theory to rigid bodies with damping, but much can be learned from applying these ideas and associated methods to a gyrostat with damping.

2.4 Summary

We reviewed much of the work related to the dynamics of spinning spacecraft with energy dissipation. For rigid bodies, energy dissipation leads to the major-axis rule: a rigid body with energy dis-

sipation is only directionally stable in spins about a major axis. For a gyrostat, energy dissipation on the platform tends to be stabilizing whereas damping on the rotor tends to be de-stabilizing. For stability analysis, many researchers used energy-sink methods to produce useful results. Adding the damping mechanism explicitly to the model makes analysis more difficult, but the stability conclusions are more precise. Many different types of damping devices have been considered; perhaps the most common is the spring-mass damper with linear spring force and linear damping. Some researchers studied multiple equilibria of spinning rigid bodies and gyrostats using both analytical and numerical methods. Now familiar with the related work, we proceed to develop the equations of motion for a gyrostat with a spring-mass damper.

Chapter 3

Equations of Motion

In this chapter we develop the equations of motion for a rigid body with a single rigid axisymmetric rotor and a single spring-mass-dashpot damper. A Newton-Euler approach is used to develop equations for the linear and angular momentum of the system. Much of the notation and methodology used in this chapter are adapted from the spacecraft dynamics text by Hughes.[34] We begin by developing the momentum and motion equations for the rigid body and then add the contributions of the rotor and damper. Although the results for the rigid body are well known, we use this first case to precisely define the terms and methods used in producing the complete system equations. For this development we use a specific vector notation. General vectors, independent of a specific reference frame, are denoted as bold with an over-arrow. Vector quantities in a specific reference frame are expressed as bold letters. Lowercase letters represent vector quantities, whereas uppercase letters denote dyadic or matrix quantities.

3.1 Rigid Body Equations

We consider a rigid body, $\mathcal{B}$, as shown in Fig. 3.1. The body frame, $\mathcal{F}_b$, is centered at point $\mathcal{O}$ which is not presumed to be the mass center. A typical mass element, dm, is located within the rigid body by the vector $\vec{\mathbf{r}}$. Therefore, the position and velocity of dm relative to the inertial frame, $\mathcal{F}_i$, are

$$\begin{aligned} \vec{\mathbf{r}}_i &= \vec{\mathbf{r}}_o + \vec{\mathbf{r}} \\ \vec{\mathbf{v}} &= \dot{\vec{\mathbf{r}}}_i \end{aligned}$$

For an arbitrary body-fixed reference frame, $\mathcal{F}_b$, centered at point $\mathcal{O}$ and with an angular velocity $\vec{\boldsymbol{\omega}}$ with respect to $\mathcal{F}_i$, the inertial velocity of dm is

$$\vec{\mathbf{v}} = \dot{\vec{\mathbf{r}}}_o + \vec{\boldsymbol{\omega}} \times \vec{\mathbf{r}}$$

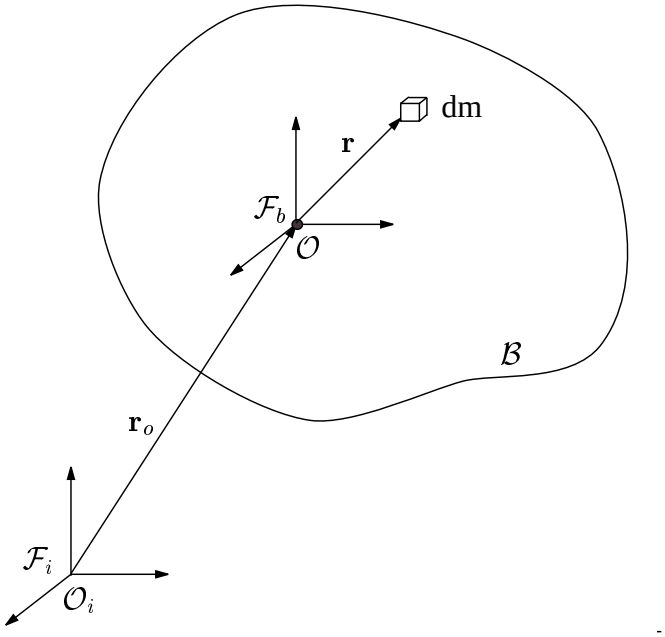

Figure 3.1: Rigid body

Integrating over the body, the linear momentum is

$$\vec{\mathbf{p}} = \int_{\mathcal{B}} \vec{\mathbf{v}}\, dm = \int_{\mathcal{B}} (\vec{\mathbf{v}}_o + \vec{\boldsymbol{\omega}} \times \vec{\mathbf{r}})\, dm$$

where $\vec{\mathbf{v}}_o = \dot{\vec{\mathbf{r}}}_o$. Since $\vec{\mathbf{v}}_o$ and $\vec{\boldsymbol{\omega}}$ do not vary within $\mathcal{B}$, they can be taken outside the integral:

$$\begin{aligned} \vec{\mathbf{p}} &= \vec{\mathbf{v}}_o \int_{\mathcal{B}} dm + \vec{\boldsymbol{\omega}} \times \int_{\mathcal{B}} \vec{\mathbf{r}}\, dm \\ \vec{\mathbf{p}} &= m\vec{\mathbf{v}}_o + \vec{\boldsymbol{\omega}} \times \vec{\mathbf{c}} \end{aligned} \tag{3.1}$$

where $\vec{\mathbf{c}} = \int_{\mathcal{B}} \vec{\mathbf{r}}\, dm$ is the first mass moment of $\mathcal{B}$ about point $\mathcal{O}$.

We define the absolute angular momentum of the rigid body, about point $\mathcal{O}$, as

$$\vec{\mathbf{h}}_b^o = \int_{\mathcal{B}} \vec{\mathbf{r}} \times \vec{\mathbf{v}}\, dm$$

The notation used for $\vec{\mathbf{h}}$ in this section includes a subscript, identifying the object, and a superscript, defining the point from which $\vec{\mathbf{r}}$ is measured. The superscript is dropped in following sections to simplify the notation. Expanding the velocity term and the resulting vector product,

$$\begin{aligned} \vec{\mathbf{h}}_b^o &= \int_{\mathcal{B}} \left[\vec{\mathbf{r}} \times (\dot{\vec{\mathbf{r}}}_o + \vec{\boldsymbol{\omega}} \times \vec{\mathbf{r}})\right]\, dm \\ &= \int_{\mathcal{B}} \left[\vec{\mathbf{r}} \times \vec{\mathbf{v}}_o + (\vec{\mathbf{r}} \cdot \vec{\mathbf{r}})\vec{\boldsymbol{\omega}} - (\vec{\mathbf{r}} \cdot \vec{\boldsymbol{\omega}})\vec{\mathbf{r}}\right]\, dm \\ &= \int_{\mathcal{B}} \vec{\mathbf{r}}\, dm \times \vec{\mathbf{v}}_o + \int_{\mathcal{B}} \left[(\vec{\mathbf{r}} \cdot \vec{\mathbf{r}})\vec{\boldsymbol{\omega}} - (\vec{\mathbf{r}} \cdot \vec{\boldsymbol{\omega}})\vec{\mathbf{r}}\right]\, dm \end{aligned}$$

The first term is the first mass moment cross the inertial velocity of point $\mathcal{O}$. The second term is simplified using the unit dyadic,[34] $\vec{\mathbf{1}}$, with property $\vec{\mathbf{1}} \cdot \vec{\boldsymbol{\omega}} = \vec{\boldsymbol{\omega}}$ and becomes

$$\begin{aligned} \int_{\mathcal{B}} \left[(\vec{\mathbf{r}} \cdot \vec{\mathbf{r}}) \vec{\boldsymbol{\omega}} - (\vec{\mathbf{r}} \cdot \vec{\boldsymbol{\omega}}) \vec{\mathbf{r}} \right] \, dm &= \int_{\mathcal{B}} \left(r^2 \vec{\mathbf{1}} \cdot \vec{\boldsymbol{\omega}} - \vec{\mathbf{r}} \vec{\mathbf{r}} \cdot \vec{\boldsymbol{\omega}} \right) \, dm \\ &= \int_{\mathcal{B}} \left(r^2 \vec{\mathbf{1}} - \vec{\mathbf{r}} \vec{\mathbf{r}} \right) \, dm \cdot \vec{\boldsymbol{\omega}} \end{aligned}$$

Defining

$$\vec{\mathbf{J}} = \int_{\mathcal{B}} \left(r^2 \vec{\mathbf{1}} - \vec{\mathbf{r}} \vec{\mathbf{r}} \right) \, dm$$

as the second moment of inertia about point $\mathcal{O}$, the absolute angular momentum of the rigid body about point $\mathcal{O}$ is

$$\vec{\mathbf{h}}_b^o = \vec{\mathbf{c}} \times \vec{\mathbf{v}}_o + \vec{\mathbf{J}} \cdot \vec{\boldsymbol{\omega}} \tag{3.2}$$

If point $\mathcal{O}$ is the mass center, then the equation simplifies to

$$\vec{\mathbf{h}}_b^c = \vec{\mathbf{J}} \cdot \vec{\boldsymbol{\omega}}$$

where the superscript c denotes the mass center.

Once the equations for the system momenta are developed, we use Newton's Second Law and Euler's equation to express the kinetic equations. Using Newton's Second Law, the rate of change of linear momentum in inertial space is simply the applied force:

$$\dot{\vec{\mathbf{p}}} = \vec{\mathbf{f}} \tag{3.3}$$

Applying Euler's equation for a rigid body is complicated by taking angular momentum about point $\mathcal{O}$, which may not be an inertial point or the mass center. Using Euler's equation, the total angular momentum about an inertial point, $\mathcal{O}_i$, is

$$\vec{\mathbf{h}}_b^i = \int_{\mathcal{B}} \vec{\mathbf{r}}_i \times \vec{\mathbf{v}} \, dm$$

and

$$\dot{\vec{\mathbf{h}}}_b^i = \vec{\mathbf{g}}_i$$

where $\vec{\mathbf{g}}_i$ is the external torque on the body. Since $\mathcal{O}$ is a non-inertial point, we use the previous definition of angular momentum about point $\mathcal{O}$:

$$\begin{aligned} \vec{\mathbf{h}}_b^o &= \int_{\mathcal{B}} \vec{\mathbf{r}} \times \vec{\mathbf{v}} \, dm \\ &= \int_{\mathcal{B}} (\vec{\mathbf{r}}_i - \vec{\mathbf{r}}_o) \times \vec{\mathbf{v}} \, dm \\ &= \vec{\mathbf{h}}_b^i - \vec{\mathbf{r}}_o \times \vec{\mathbf{p}} \end{aligned}$$

Differentiating and substituting,

$$\begin{aligned}
\dot{\vec{\mathbf{h}}}_b^o &= \dot{\vec{\mathbf{h}}}_b^i - \frac{d}{dt}(\vec{\mathbf{r}}_o \times \vec{\mathbf{p}}) \\
\dot{\vec{\mathbf{h}}}_b^o &= \vec{\mathbf{g}}_i - \vec{\mathbf{v}}_o \times \vec{\mathbf{p}} - \vec{\mathbf{r}}_o \times \dot{\vec{\mathbf{p}}} \\
\dot{\vec{\mathbf{h}}}_b^o &= -\vec{\mathbf{v}}_o \times \vec{\mathbf{p}} + \vec{\mathbf{g}}_i - \vec{\mathbf{r}}_o \times \vec{\mathbf{f}}
\end{aligned}$$

The external torque about point $\mathcal{O}$ is related to the torque about the origin of $\mathcal{F}_i$:

$$\vec{\mathbf{g}}_i = \vec{\mathbf{g}}_o + \vec{\mathbf{r}}_o \times \vec{\mathbf{f}}$$

Therefore,

$$\dot{\vec{\mathbf{h}}}_b^o = -\vec{\mathbf{v}}_o \times \vec{\mathbf{p}} + \vec{\mathbf{g}}_o \tag{3.4}$$

To express the motion equations in scalar form, vector equations 3.1– 3.4 are expressed in a specific coordinate system. We use a different notation, using the skew-symmetric matrix form of the vector cross product, denoted as a superscript cross. We choose a body-fixed frame, resulting in the following scalar equations

$$\begin{aligned}
\mathbf{p} &= m\mathbf{v}_o + \boldsymbol{\omega}^\times \mathbf{c} && (3.5)\\
\mathbf{h}_b^o &= \mathbf{c}^\times \mathbf{v}_o + \mathbf{J}\boldsymbol{\omega} && (3.6)\\
\dot{\mathbf{p}} &= -\boldsymbol{\omega}^\times \mathbf{p} + \mathbf{f} && (3.7)\\
\dot{\mathbf{h}}_b^o &= -\boldsymbol{\omega}^\times \mathbf{h} - \mathbf{v}_o^\times \mathbf{p} + \mathbf{g}_o && (3.8)
\end{aligned}$$

These rigid body equations of motion are only the first step. Equations for the momentum and kinetics for the damper and rotor are still needed. These are developed in the next section and combined to produce equations of motion for the complete system.

3.2 System Equations

The development of the rigid-body equations demonstrated the Newton-Euler approach to generating equations of motion. A similar approach is used to produce equations for the damper and rotor. A general version of the system, with arbitrary $\hat{\mathbf{n}}$ and $\hat{\mathbf{a}}$, is seen in Fig. 3.2.

The system consists of a rigid body $\mathcal{B}$, containing a rigid axisymmetric rotor, $\mathcal{R}$, and a spring-mass-dashpot damper with mass particle $\mathcal{P}$, which is constrained to move along a line defined by the unit vector $\hat{\mathbf{n}}$, fixed in $\mathcal{B}$. The rest of the damper is considered massless. The rotor spins about its axis of symmetry, defined by the unit vector, $\hat{\mathbf{a}}$. The body frame, $\mathcal{F}_b$, is fixed in $\mathcal{B}$ and has origin $\mathcal{O}$. We maintain the generality of these vectors and the body frame throughout this section. In Chs. 4– 6 we will study a specific orientation of these elements, with the rotor and damper aligned with the $\hat{\mathbf{b}}_1$ axis, but a more general approach will allow for study of perturbations to the nominal

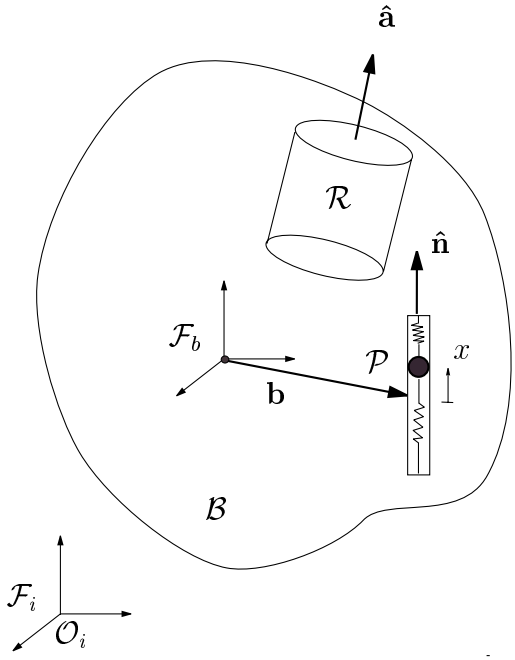

Figure 3.2: Single-rotor axial gyrostat with discrete damper

configuration, included in Ch. 7. Note that unit vectors are represented as bold letters with a hat (e.g. $\hat{\mathbf{a}}$) while vectors of variable length are merely bold. The particle is connected to a linear spring and a linear dashpot damper. All vectors and tensors are expressed with respect to the body frame.

3.2.1 Linear Momentum

The linear momentum of $\mathcal{B}$ was developed previously, and the linear momentum relations for the damper particle and rotor are similarly generated. To aid in this development several new vectors are defined. The location of the damper particle, which is treated as a point mass, is denoted $\mathbf{r}_d = \mathbf{b} + x\hat{\mathbf{n}}$. The rotor location is not restricted within $\mathcal{B}$, and $\mathbf{r}_w$ locates the rotor mass center. Using these definitions, it is straightforward to represent the damper mass and rotor linear momentum as

$$\begin{aligned} \mathbf{p}_d &= m_d(\mathbf{v}_o + \boldsymbol{\omega}^{\times}\mathbf{r}_d + \dot{x}\hat{\mathbf{n}}) \\ \mathbf{p}_w &= m_w(\mathbf{v}_o + \boldsymbol{\omega}^{\times}\mathbf{r}_w) \end{aligned}$$

where m_d is the mass of the damper particle, and m_w is the rotor mass. The total system mass is the sum of the three parts: $m = m_b + m_d + m_w$.

The total system linear momentum is the sum of the three parts,

$$\begin{aligned}\mathbf{p} &= \mathbf{p}_b + \mathbf{p}_d + \mathbf{p}_w \\ &= m\mathbf{v}_o + \boldsymbol{\omega}^\times(\mathbf{c}_b + m_d\mathbf{r}_d + m_w\mathbf{r}_w) + m_d\dot{x}\hat{\mathbf{n}}\end{aligned}$$

where $\mathbf{c}_b$ is the previously defined first mass moment for the rigid body about point $\mathcal{O}$. For an arbitrary $\mathcal{F}_b$, the system first mass moment about point $\mathcal{O}$ is

$$\mathbf{c} = \mathbf{c}_b + m_d\mathbf{r}_d + m_w\mathbf{r}_w$$

and the system linear momentum may be written as

$$\mathbf{p} = m\mathbf{v}_o + \boldsymbol{\omega}^\times\mathbf{c} + m_d\,\dot{x}\hat{\mathbf{n}} \tag{3.9}$$

Of special interest is the component of $\mathbf{p}_d$ along $\hat{\mathbf{n}}$, which is denoted p_n:

$$\begin{aligned}p_n &= \hat{\mathbf{n}}\cdot\mathbf{p}_d \\ &= m_d\hat{\mathbf{n}}^{\mathrm{T}}(\mathbf{v}_o - \mathbf{b}^\times\boldsymbol{\omega} - x\hat{\mathbf{n}}^\times\boldsymbol{\omega} + \dot{x}\hat{\mathbf{n}})\end{aligned}$$

which after simplifying becomes

$$p_n = m_d(\hat{\mathbf{n}}^{\mathrm{T}}\mathbf{v}_o - \hat{\mathbf{n}}^{\mathrm{T}}\mathbf{b}^\times\boldsymbol{\omega} + \dot{x}) \tag{3.10}$$

Having derived expressions for the linear momentum, we now focus on the angular momentum.

3.2.2 Angular Momentum about Point $\mathcal{O}$

The angular momentum of the system about point $\mathcal{O}$ is developed by summing the contributions from the three system components. From the earlier development, the rigid-body contribution is written as

$$\mathbf{h}_b = \mathbf{c}_b \times \mathbf{v}_o + \mathbf{J}_b\boldsymbol{\omega}$$

The angular momentum of the damper particle about point $\mathcal{O}$ is

$$\begin{aligned}\mathbf{h}_d &= \mathbf{r}_d^\times\mathbf{p}_d \\ &= m_d\,\mathbf{r}_d^\times(\mathbf{v}_o + \boldsymbol{\omega}^\times\mathbf{r}_d + \dot{x}\hat{\mathbf{n}}) \\ &= m_d\,\mathbf{r}_d^\times\mathbf{v}_o + m_d(r_d^2\mathbf{1} - \mathbf{r}_d\mathbf{r}_d^{\mathrm{T}})\boldsymbol{\omega} + m_d\,\dot{x}\mathbf{r}_d^\times\hat{\mathbf{n}}\end{aligned}$$

Defining $\mathbf{J}_d = m_d(r_d^2\mathbf{1} - \mathbf{r}_d\mathbf{r}_d^{\mathrm{T}})$ and $\mathbf{c}_d = m_d\mathbf{r}_d$ and using $\mathbf{r}_d = \mathbf{b} + x\hat{\mathbf{n}}$, the damper angular momentum simplifies to

$$\mathbf{h}_d = \mathbf{c}_d^\times\mathbf{v}_o + \mathbf{J}_d\boldsymbol{\omega} + m_d\,\dot{x}\mathbf{b}^\times\hat{\mathbf{n}} \tag{3.11}$$

The rotor angular momentum about point $\mathcal{O}$ includes contributions from the motion of the rotor about $\mathcal{O}$ as well as the angular momentum of the rotor about its own rotation axis. Simply stated, the angular momentum of the rotor about point $\mathcal{O}$ is

$$\mathbf{h}_w = \int_{\mathcal{R}} \mathbf{r}^{\times} \mathbf{v} \, dm \tag{3.12}$$

where $\mathbf{r}$ represents the position of each differential mass element of the rotor relative to point $\mathcal{O}$ and $\mathbf{v}$ represents the corresponding inertial velocity. To relate this to the previous angular momentum expressions, several new parameters are defined. Whereas $\boldsymbol{\omega}$ is the absolute angular velocity of $\mathcal{B}$, relative to the inertial frame, $\boldsymbol{\omega}_w$ is defined as the absolute angular velocity of $\mathcal{R}$ relative to the inertial frame. These two velocities are related by the relative angular velocity of the rotor, relative to the body, defined as $\boldsymbol{\omega}_s = \boldsymbol{\omega}_w - \boldsymbol{\omega}$. Figure 3.3 shows how the location of each rotor differential mass element is defined as

$$\mathbf{r} = \mathbf{r}_o + \mathbf{r}_w + \boldsymbol{\rho}$$

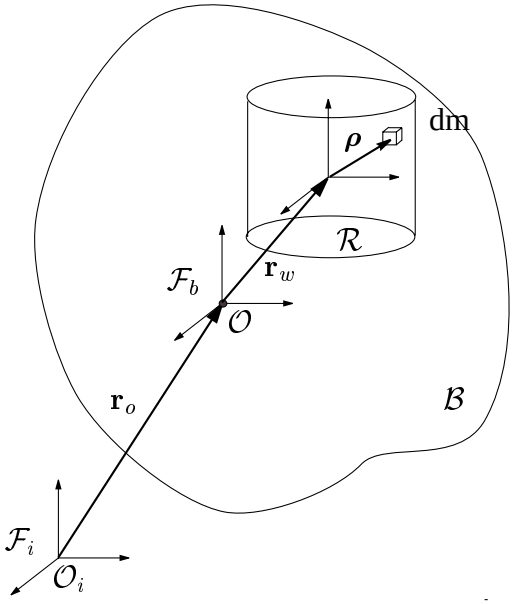

Figure 3.3: Rigid body with axisymmetric rotor

Expanding Eq. 3.12 and proceeding as in the rigid body development,

$$\begin{aligned}
\mathbf{h}_w &= \int_{\mathcal{R}} (\mathbf{r}_w + \boldsymbol{\rho})^{\times} (\mathbf{v}_o + \boldsymbol{\omega}^{\times} \mathbf{r}_w + \boldsymbol{\omega}_w^{\times} \boldsymbol{\rho}) \, dm \\
&= \left(\int_{\mathcal{R}} \mathbf{r}_w \, dm \right)^{\times} \mathbf{v}_o + \int_{\mathcal{R}} \mathbf{r}_w^{\times} (\boldsymbol{\omega}^{\times} \mathbf{r}_w) \, dm + \int_{\mathcal{R}} \mathbf{r}_w^{\times} (\boldsymbol{\omega}_w^{\times} \boldsymbol{\rho}) \, dm \\
&\quad + \int_{\mathcal{R}} \boldsymbol{\rho}^{\times} \mathbf{v}_o \, dm + \int_{\mathcal{R}} \boldsymbol{\rho}^{\times} (\boldsymbol{\omega}^{\times} \mathbf{r}_w) \, dm + \int_{\mathcal{R}} \boldsymbol{\rho}^{\times} (\boldsymbol{\omega}_w^{\times} \boldsymbol{\rho}) \, dm
\end{aligned}$$

The first term, $\mathbf{c}_w = \int_{\mathcal{R}} \mathbf{r}_w \, dm$, is recognized as the first mass moment of the rotor about point $\mathcal{O}$. Also, the vectors $\mathbf{r}_o$, $\mathbf{r}_w$, $\boldsymbol{\omega}$, $\boldsymbol{\omega}_w$, and $\mathbf{v}_o$ do not vary within the rotor and may be taken outside the integral:

$$\begin{aligned}\mathbf{h}_w &= \mathbf{c}_w^{\times}\mathbf{v}_o + (r_w^2\mathbf{1} - \mathbf{r}_w\mathbf{r}_w^{\mathrm{T}})\boldsymbol{\omega}\, m_w + \mathbf{r}_w^{\times}\boldsymbol{\omega}_w^{\times}\left(\int_{\mathcal{R}} \boldsymbol{\rho}\, dm\right) \\ &\quad + \left(\int_{\mathcal{R}} \boldsymbol{\rho}\, dm\right)^{\times}\mathbf{v}_o + \left(\int_{\mathcal{R}} \boldsymbol{\rho}\, dm\right)^{\times}(\boldsymbol{\omega}^{\times}\mathbf{r}_w) + \int_{\mathcal{R}}(\rho^2\mathbf{1} - \boldsymbol{\rho}\boldsymbol{\rho}^{\mathrm{T}})\, dm\, \boldsymbol{\omega}_w\end{aligned}$$

Since $\boldsymbol{\rho}$ is measured from the rotor mass center, integrating $\boldsymbol{\rho}\, dm$ over the entire rotor is zero, resulting in

$$\mathbf{h}_w = \mathbf{c}_w^{\times}\mathbf{v}_o + m_w(r_w^2\mathbf{1} - \mathbf{r}_w\mathbf{r}_w{}^{\mathrm{T}})\boldsymbol{\omega} + \mathbf{I}_w\boldsymbol{\omega}_w$$

where

$$\mathbf{I}_w = \int_{\mathcal{R}}(\rho^2\mathbf{1} - \boldsymbol{\rho}\boldsymbol{\rho}^{\mathrm{T}})\, dm$$

is the inertia tensor of the rotor about its mass center. Note that $\mathbf{I}$ is used when the inertia tensor is taken about the mass center, instead of $\mathbf{J}$ for inertia tensors about a point other than the mass center. Since $\boldsymbol{\omega}_s = \hat{\mathbf{a}}\omega_s$, we can write $\mathbf{h}_w$ as

$$\mathbf{h}_w = \mathbf{c}_w^{\times}\mathbf{v}_o + \mathbf{J}_w\boldsymbol{\omega} + \mathbf{I}_w\boldsymbol{\omega}_s$$

where

$$\mathbf{J}_w = m_w(r_w^2\mathbf{1} - \mathbf{r}_w\mathbf{r}_w^{\mathrm{T}}) + \mathbf{I}_w$$

is the inertia tensor of the rotor about point $\mathcal{O}$.

The inertia tensor of the rotor can be expressed as

$$\mathbf{I}_w = I_t\mathbf{1} + (I_s - I_t)\hat{\mathbf{a}}\hat{\mathbf{a}}^{\mathrm{T}} \tag{3.13}$$

where I_s and I_t are the axial and transverse moments of inertia of the axisymmetric rotor.[34] Using this relation,

$$\begin{aligned}\mathbf{I}_w\boldsymbol{\omega}_s &= I_t\boldsymbol{\omega}_s + (I_s - I_t)\hat{\mathbf{a}}\hat{\mathbf{a}}^{\mathrm{T}}\boldsymbol{\omega}_s \\ &= I_t\omega_s\hat{\mathbf{a}} + (I_s - I_t)\omega_s\hat{\mathbf{a}} \\ &= I_s\omega_s\hat{\mathbf{a}}\end{aligned}$$

Therefore, the total angular momentum about $\mathcal{O}$ is the sum of the three components, $\mathbf{h} = \mathbf{h}_b + \mathbf{h}_d + \mathbf{h}_w$, which becomes

$$\mathbf{h} = \mathbf{J}\boldsymbol{\omega} + \mathbf{c}^{\times}\mathbf{v}_o + m_d\dot{x}\mathbf{b}^{\times}\hat{\mathbf{n}} + \mathbf{h}_s \tag{3.14}$$

where

$$\mathbf{J} = \mathbf{J}_b + \mathbf{J}_d + \mathbf{J}_w \tag{3.15}$$

$$\mathbf{c} = \mathbf{c}_b + \mathbf{c}_d + \mathbf{c}_w \tag{3.16}$$

$$\mathbf{h}_s = I_s\omega_s\hat{\mathbf{a}} \tag{3.17}$$

Of particular interest is the absolute angular momentum of the rotor about its spin axis, the axis of symmetry. Denoted h_a, an expression for this component of rotor angular momentum is developed from the definition of angular momentum of the rotor about its mass center:

$$\mathbf{h}_{w_c} = \int_{\mathcal{R}} \boldsymbol{\rho}^{\times} \mathbf{v} \, dm$$

By a subset of the previous development,

$$\mathbf{h}_{w_c} = \mathbf{I}_w \boldsymbol{\omega}_w = \mathbf{I}_w(\boldsymbol{\omega}_s + \boldsymbol{\omega}) = I_s \omega_s \hat{\mathbf{a}} + \mathbf{I}_w \boldsymbol{\omega}$$

Therefore, the component of this angular momentum in the $\hat{\mathbf{a}}$ direction is

$$\begin{aligned} h_a &= \mathbf{h}_{w_c}^{\mathrm{T}} \hat{\mathbf{a}} \\ &= I_s \omega_s \hat{\mathbf{a}}^{\mathrm{T}} \hat{\mathbf{a}} + \boldsymbol{\omega}^{\mathrm{T}} \mathbf{I}_w \hat{\mathbf{a}} \\ &= I_s \omega_s + \boldsymbol{\omega}^{\mathrm{T}} \mathbf{I}_w \hat{\mathbf{a}} \end{aligned}$$

By expanding $\mathbf{I}_w$ in terms of I_s and I_t as before, the absolute angular momentum of the rotor about its spin axis becomes

$$h_a = I_s \omega_s + I_s \hat{\mathbf{a}}^{\mathrm{T}} \boldsymbol{\omega} \tag{3.18}$$

Notice that the absolute angular momentum of the rotor includes the relative angular momentum, $h_s = I_s \omega_s$ as well as a contribution from the system angular velocity, $\boldsymbol{\omega}$.

3.2.3 Motion Equations

We first define the various forces and torques that act on the system components. On $\mathcal{B}$ the external force and moment are $\vec{\mathbf{f}}$ and $\vec{\mathbf{g}}$, and $\mathcal{P}$ exerts a force $-\vec{\mathbf{f}}_{bd}$ on $\mathcal{B}$. By Newton's third law, $\mathcal{B}$ exerts an equal and opposite force $\vec{\mathbf{f}}_{bd}$ on $\mathcal{P}$. The damper force on $\mathcal{B}$ creates a torque on the rigid body, $\vec{\mathbf{g}}_{bd} = -\vec{\mathbf{r}}_d^{\times} \vec{\mathbf{f}}_{bd}$. Let the force and torque acting on $\mathcal{R}$ due to $\mathcal{B}$ be $\vec{\mathbf{f}}_{bw}$ and $\vec{\mathbf{g}}_{bw}$. Again, an equal and opposite force and torque act on $\mathcal{B}$ due to $\mathcal{R}$.

Applying Newton's second law to the system components we obtain,

$$\begin{aligned} \dot{\vec{\mathbf{p}}}_b &= \vec{\mathbf{f}} - \vec{\mathbf{f}}_{bd} - \vec{\mathbf{f}}_{bw} \\ \dot{\vec{\mathbf{p}}}_d &= \vec{\mathbf{f}}_{bd} \\ \dot{\vec{\mathbf{p}}}_w &= \vec{\mathbf{f}}_{bw} \end{aligned}$$

where the damper force is a function of the damping and spring coefficients as well as a constraint force, $\vec{\mathbf{f}}_{bd} = -\hat{\mathbf{n}}(c_d \dot{x} + k_d x) + \vec{\mathbf{f}}_{con}$. The net linear momentum rate for the system is

$$\sum \dot{\vec{\mathbf{p}}}_i = \dot{\vec{\mathbf{p}}} = \vec{\mathbf{f}}$$

In the body-fixed, rotating reference frame, this becomes

$$\dot{\mathbf{p}} = -\boldsymbol{\omega}^{\times} \mathbf{p} + \mathbf{f} \tag{3.19}$$

Applying Euler's moment equation to the system components, as in developing Eq. 3.4, results in

$$\begin{aligned}\dot{\vec{\mathbf{h}}}_b + \vec{\mathbf{v}}_o^{\times}\vec{\mathbf{p}}_b &= \vec{\mathbf{g}} - \vec{\mathbf{g}}_{bd} - \vec{\mathbf{g}}_{bw} \\ \dot{\vec{\mathbf{h}}}_d + \vec{\mathbf{v}}_o^{\times}\vec{\mathbf{p}}_d &= \vec{\mathbf{g}}_{bd} \\ \dot{\vec{\mathbf{h}}}_w + \vec{\mathbf{v}}_o^{\times}\vec{\mathbf{p}}_w &= \vec{\mathbf{g}}_{bw}\end{aligned}$$

We sum the component equations to determine the net angular momentum rate for the system:

$$\sum \dot{\vec{\mathbf{h}}} + \mathbf{v}_o^{\times} \sum \mathbf{p} = \dot{\vec{\mathbf{h}}} + \vec{\mathbf{v}}_o^{\times}\vec{\mathbf{p}} = \vec{\mathbf{g}}$$

In the body-fixed, rotating reference frame, this becomes

$$\dot{\mathbf{h}} = -\boldsymbol{\omega}^{\times}\mathbf{h} - \vec{\mathbf{v}}_o^{\times}\vec{\mathbf{p}} + \mathbf{g} \tag{3.20}$$

The equation of motion for the damper momentum component, p_n, is found from differentiating its definition:

$$\begin{aligned}\dot{p}_n &= \frac{d}{dt}\left(\hat{\mathbf{n}} \cdot \mathbf{p}_d\right) \\ &= \dot{\hat{\mathbf{n}}} \cdot \mathbf{p}_d + \hat{\mathbf{n}} \cdot \dot{\mathbf{p}}_d \\ &= m_d \left(\boldsymbol{\omega}^{\times}\hat{\mathbf{n}}\right)^{\mathrm{T}} \left(\mathbf{v}_o - \mathbf{b}^{\times}\boldsymbol{\omega} - x\hat{\mathbf{n}}^{\times}\boldsymbol{\omega} + \dot{x}\hat{\mathbf{n}}\right) - c_d\dot{x} - k_d x + \hat{\mathbf{n}}^{\mathrm{T}}\mathbf{f}_{con}\end{aligned}$$

We do not restrict the motion of the damper, and assume $\mathbf{f}_{con}$ is normal to the damper motion direction, $\hat{\mathbf{n}} \cdot \mathbf{f}_{con} = 0$, resulting in

$$\dot{p}_n = m_d \boldsymbol{\omega}^{\mathrm{T}}\hat{\mathbf{n}}^{\times} \left(\mathbf{v}_o - \mathbf{b}^{\times}\boldsymbol{\omega} - x\hat{\mathbf{n}}^{\times}\boldsymbol{\omega} + \dot{x}\hat{\mathbf{n}}\right) - c_d\dot{x} - k_d x \tag{3.21}$$

The final equation of motion describes the motion of the rotor about its spin axis. Proceeding from the definition of h_a, in a similar fashion to the p_n development, leads to

$$\begin{aligned}\dot{h}_a &= \frac{d}{dt}\left(\hat{\mathbf{a}} \cdot \mathbf{h}_w\right) \\ &= \left(\boldsymbol{\omega}^{\times}\hat{\mathbf{a}}\right) \cdot \mathbf{h}_w + \hat{\mathbf{a}} \cdot \dot{\mathbf{h}}_w \\ &= \boldsymbol{\omega}^{\mathrm{T}}(\hat{\mathbf{a}}^{\times}\mathbf{I}_w\boldsymbol{\omega}_w) + \hat{\mathbf{a}}^{\mathrm{T}}\mathbf{g}_{bw}\end{aligned}$$

The torque about the rotor spin axis is defined as $g_a = \hat{\mathbf{a}} \cdot \mathbf{g}_{bw}$, where this torque could conceivably be the combination of rotor motor or bearing friction torques. Using this definition and Eq. 3.13,

$$\begin{aligned}\dot{h}_a &= I_t \boldsymbol{\omega}^{\mathrm{T}}\hat{\mathbf{a}}^{\times}(\boldsymbol{\omega} + \boldsymbol{\omega}_s) + g_a \\ &= I_t(-\boldsymbol{\omega}^{\mathrm{T}}\boldsymbol{\omega}^{\times}\hat{\mathbf{a}} + \boldsymbol{\omega}^{\mathrm{T}}\hat{\mathbf{a}}^{\times}\hat{\mathbf{a}}\omega_s) + g_a\end{aligned}$$

Since for any two vectors $\mathbf{u}$ and $\mathbf{v}$, $\mathbf{u} \cdot (\mathbf{u} \times \mathbf{v}) = (\mathbf{u} \times \mathbf{u}) \cdot \mathbf{v} = 0$, the final equation of motion simplifies to

$$\dot{h}_a = g_a \tag{3.22}$$

This result completes the motion equation development. However, we also need the expressions for total system energy. We derive the energy equations in the following section.

3.2.4 Total Energy

We derive the system kinetic and potential energies using previous definitions. The total mechanical energy is defined here as the sum of the kinetic and potential energies. The potential energy is merely the potential energy of the spring

$$U = \frac{1}{2} k_d x^2 \tag{3.23}$$

The kinetic energy of a particle is defined as

$$T = \frac{1}{2} m \vec{\mathbf{v}} \cdot \vec{\mathbf{v}} \tag{3.24}$$

We define kinetic energy of a rigid body as

$$T = \frac{1}{2} \int \vec{\mathbf{v}} \cdot \vec{\mathbf{v}} \, dm \tag{3.25}$$

The kinetic energy of the system is therefore expressed as

$$\begin{aligned} T &= \frac{1}{2} \int_{\mathcal{B}} \left(\mathbf{v}_o + \boldsymbol{\omega}^{\times} \mathbf{r} \right) \cdot \left(\mathbf{v}_o + \boldsymbol{\omega}^{\times} \mathbf{r} \right) \, dm \\ &\quad + \frac{1}{2} \int_{\mathcal{R}} \left(\mathbf{v}_{cw} + \boldsymbol{\omega}_w{}^{\times} \boldsymbol{\rho} \right) \cdot \left(\mathbf{v}_{cw} + \boldsymbol{\omega}_w{}^{\times} \boldsymbol{\rho} \right) \, dm \\ &\quad + \frac{1}{2} m_d \left(\mathbf{v}_o + \boldsymbol{\omega}^{\times} \mathbf{r}_d + \dot{x} \hat{\mathbf{n}} \right) \cdot \left(\mathbf{v}_o + \boldsymbol{\omega}^{\times} \mathbf{r}_d + \dot{x} \hat{\mathbf{n}} \right) \end{aligned} \tag{3.26}$$

where the velocity of the rotor mass center is

$$\mathbf{v}_{cw} = \mathbf{v}_o + \boldsymbol{\omega}^{\times} \mathbf{r}_w$$

Using previous definitions, the kinetic energy of the system becomes

$$T = \frac{1}{2} m \mathbf{v}_o{}^{\mathrm{T}} \mathbf{v}_o + \frac{1}{2} \boldsymbol{\omega}^{\mathrm{T}} \mathbf{J} \boldsymbol{\omega} + \frac{1}{2} I_s \omega_s^2 + \frac{1}{2} m_d \dot{x}^2 - \mathbf{v}_o \mathbf{c}^{\times} \boldsymbol{\omega} + I_s \omega_s \hat{\mathbf{a}}^{\mathrm{T}} \boldsymbol{\omega} + m_d \dot{x} \mathbf{v}_o{}^{\mathrm{T}} \hat{\mathbf{n}} - m_d \dot{x} \hat{\mathbf{n}}^{\mathrm{T}} \mathbf{b}^{\times} \boldsymbol{\omega} \tag{3.27}$$

We express the kinetic energy of this system more elegantly in terms of velocities and a system matrix, as developed by Hughes in Ref. 34. The kinetic energy is

$$T = \frac{1}{2} \boldsymbol{\upsilon}^{\mathrm{T}} \mathcal{M} \boldsymbol{\upsilon} \tag{3.28}$$

where

$$\boldsymbol{\upsilon} = \begin{bmatrix} \mathbf{v}_o \\ \boldsymbol{\omega} \\ \dot{x} \\ \omega_s \end{bmatrix} \tag{3.29}$$

and

$$\mathcal{M} = \begin{bmatrix} m_d\,\mathbf{1} & -\mathbf{c}^{\times} & m_d\,\hat{\mathbf{n}} & \mathbf{0} \\ \mathbf{c}^{\times} & \mathbf{J} & m_d\,\mathbf{b}^{\times}\hat{\mathbf{n}} & I_s\hat{\mathbf{a}} \\ m_d\,\hat{\mathbf{n}}^{\mathbf{T}} & -m_d\,\hat{\mathbf{n}}^{\mathbf{T}}\mathbf{b}^{\times} & m_d & 0 \\ \mathbf{0}^{\mathbf{T}} & I_s\hat{\mathbf{a}}^{\mathbf{T}} & 0 & I_s \end{bmatrix} \tag{3.30}$$

The system matrix $\mathcal{M}$ is symmetric and positive-definite. The system momenta are also expressible using the system matrix,

$$\boldsymbol{\varrho} = \mathcal{M}\boldsymbol{\upsilon} \tag{3.31}$$

where

$$\boldsymbol{\varrho} = \begin{bmatrix} \mathbf{p} \\ \mathbf{h} \\ p_n \\ h_a \end{bmatrix} \tag{3.32}$$

These relations are used to form an energy-based Liapunov function in Ch. 4. Also, total energy is used to verify simulation results. The damper dissipates energy at the rate of $\dot{V} = -c_d\dot{x}^2$. The equations of motion are numerically integrated to simulate the system dynamics. As part of the simulation, total energy is determined from Eqs. 3.28 and 3.23. Independently, the energy state history is determined by numerically integrating the energy state, using $\dot{V}$. We ensure the two energy histories are the same, helping verify the simulation results.

This discussion concludes the development of the system energy equations. Next, we summarize the equations of motion.

3.2.5 Summary of Equations of Motion

The system momenta, expressed in $\mathcal{F}_b$, are

$$\mathbf{p} = m\mathbf{v}_o - \mathbf{c}^{\times}\boldsymbol{\omega} + m_d y\hat{\mathbf{n}} \tag{3.33}$$

$$\mathbf{h} = \mathbf{J}\boldsymbol{\omega} + \mathbf{c}^{\times}\mathbf{v}_o + m_d y\mathbf{b}^{\times}\hat{\mathbf{n}} + \mathbf{h}_s \tag{3.34}$$

$$p_n = m_d\left(\hat{\mathbf{n}}^{\mathrm{T}}\mathbf{v}_o - \hat{\mathbf{n}}^{\mathrm{T}}\mathbf{b}^{\times}\boldsymbol{\omega} + y\right) \tag{3.35}$$

$$h_a = I_s\hat{\mathbf{a}}^{\mathrm{T}}\boldsymbol{\omega} + I_s\omega_s \tag{3.36}$$

where

$$\begin{aligned} y &= \dot{x} \\ m &= m_b + m_d + m_w \\ \mathbf{c} &= \mathbf{c}_b + \mathbf{c}_d + \mathbf{c}_w \\ \mathbf{J} &= \mathbf{J}_b + \mathbf{J}_d + \mathbf{J}_w \end{aligned}$$

The motion equations, also expressed in $\mathcal{F}_b$, are

$$\dot{\mathbf{p}} = -\boldsymbol{\omega}^{\times}\mathbf{p} + \mathbf{f} \tag{3.37}$$

$$\dot{\mathbf{h}} = -\boldsymbol{\omega}^{\times}\mathbf{h} - \mathbf{v}_o^{\times}\mathbf{p} + \mathbf{g} \tag{3.38}$$

$$\dot{p}_n = m_d\boldsymbol{\omega}^{\mathrm{T}}\hat{\mathbf{n}}^{\times}\left[\mathbf{v}_o - (\mathbf{b} + x\hat{\mathbf{n}})^{\times}\boldsymbol{\omega}\right] - c_d y - k_d x \tag{3.39}$$

$$\dot{h}_a = g_a \tag{3.40}$$

$$\dot{x} = y \tag{3.41}$$

These equations are valid for any body frame, and position or orientation of the rotor and damper. We next make specific choices for $\mathcal{F}_b$, $\hat{\mathbf{a}}$, and $\hat{\mathbf{n}}$ to represent a typical satellite configuration

3.3 Nominal System Configuration

We select a nominal configuration of these elements which models a satellite with a single rotor aligned with the intended spin axis. The alignment of the rotor and nominal spin axes is often called an axial gyrostat. This configuration allows the rotor momentum to have the maximum effect in influencing the dynamics of the typical spacecraft spin. Also, the spring-mass-dashpot damper is aligned parallel to this nominal spin axis, effectively acting as an axial damper. This configuration dissipates more energy per unit mass, for smaller coning angles, than dampers aligned perpendicular to the spacecraft spin axis.[60]

The nominal system configuration is shown in Fig. 3.4. We choose the body frame, $\mathcal{F}_b$, such that its origin is the system mass center and the body frame axes $\vec{\mathbf{b}}_i$ are system principal axes when $\mathcal{P}$ is in its rest position $(x = 0)$. This configuration results in considerable simplification of the equations and their resulting equilibria. The vector $\hat{\mathbf{n}}$ is parallel to $\hat{\mathbf{b}}_1$, which is the nominal spin axis for the spacecraft. The particle is connected to a linear spring and a linear dashpot damper. The rotor spin axis is in the $\hat{\mathbf{a}}$ direction, parallel to the $\hat{\mathbf{b}}_1$ axis.

By selecting the body frame origin as the system mass center, the first mass moment of the system simplifies to $\mathbf{c} = m_d x\hat{\mathbf{n}}$. Also, the defined body axes allow a simpler description of the system second mass moment of inertia matrix, $\mathbf{J}$. Because the origin is nominally a mass center, we denote the system inertia matrix as $\mathbf{I}$ rather than $\mathbf{J}$. For $x = 0$, the system inertia matrix is diagonal and defined as $\mathbf{I}_o$. For non-zero damper displacement, the inertia tensor is described in terms of $\mathbf{I}_o$ as

$$\mathbf{I} = \mathbf{I}_o + m_d\left(r_d^2\mathbf{1} - \mathbf{r}_d\mathbf{r}_d^{\mathrm{T}}\right) - m_d\left(b^2\mathbf{1} - \mathbf{b}\mathbf{b}^{\mathrm{T}}\right) \tag{3.42}$$

which becomes after substitution for r_d

$$\mathbf{I} = \mathbf{I}_o + m_d\left[\left(2x\mathbf{b}^{\mathrm{T}}\hat{\mathbf{n}} + x^2\right)\mathbf{1} - x\left(\mathbf{b}\hat{\mathbf{n}}^{\mathrm{T}} + \hat{\mathbf{n}}\mathbf{b}^{\mathrm{T}}\right) - x^2\hat{\mathbf{n}}\hat{\mathbf{n}}^{\mathrm{T}}\right] \tag{3.43}$$

The resulting momentum equations for the nominal system configuration are

$$\mathbf{p} = m\mathbf{v}_o - m_d x\hat{\mathbf{n}}^{\times}\boldsymbol{\omega} + m_d y\hat{\mathbf{n}} \tag{3.44}$$

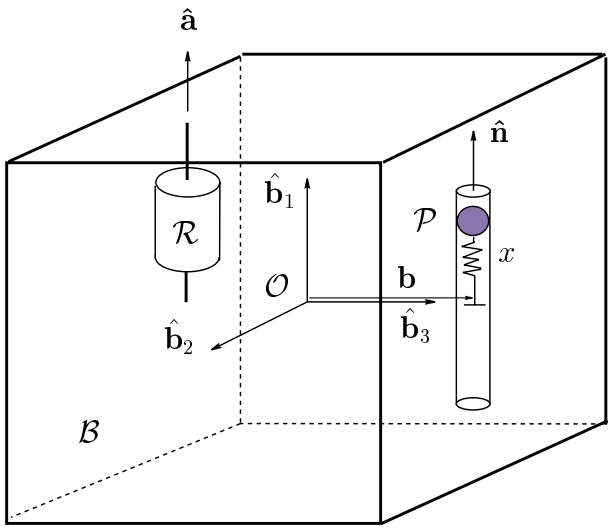

Figure 3.4: Single-rotor axial gyrostat with aligned discrete damper

$$\mathbf{h} = m_d x \hat{\mathbf{n}}^{\times} \mathbf{v}_o + \mathbf{I}\boldsymbol{\omega} + m_d y \mathbf{b}^{\times} \hat{\mathbf{n}} + \mathbf{h}_s \tag{3.45}$$

$$p_n = m_d \left(\hat{\mathbf{n}}^{\mathrm{T}} \mathbf{v}_o - \hat{\mathbf{n}}^{\mathrm{T}} \mathbf{b}^{\times} \boldsymbol{\omega} + y \right) \tag{3.46}$$

$$h_a = I_s \hat{\mathbf{a}}^{\mathrm{T}} \boldsymbol{\omega} + I_s \omega_s \tag{3.47}$$

The last two momentum equations are unchanged as are the motion equations.

We study the equilibria of the nominal configuration in Chs. 4– 6. In Ch. 7, we consider the effects of rotor or damper alignment errors by perturbing the direction of the $\hat{\mathbf{a}}$ and $\hat{\mathbf{n}}$ vectors.

3.4 Dimensionless Equations

An important step in analyzing mathematical models of physical systems is to non-dimensionalize the variables and parameters of the problem. The relative magnitude of different system elements can then be fairly judged without the bias of dimensional units. Before converting the equations to dimensionless quantities, they are first restated with the dimensionality clearly indicated by adding a * superscript to each element. This distinguishes the dimensional quantities from the dimensionless ones, which appear without the * superscript. The dimensional momentum equations are therefore

$$\mathbf{p}^* = m^* \mathbf{v}^*{}_o - m_d^* x^* \hat{\mathbf{n}}^{\times} \boldsymbol{\omega}^* + m_p^* y^* \hat{\mathbf{n}} \tag{3.48}$$

$$\mathbf{h}^* = m_d^* x^* \hat{\mathbf{n}}^{\times} \mathbf{v}_o^* + \mathbf{I}^* \boldsymbol{\omega}^* + m_d^* y^* \mathbf{b}^{*\times} \hat{\mathbf{n}} + \mathbf{h}_s^* \tag{3.49}$$

$$p_n^* = m_d^* \left(\hat{\mathbf{n}}^{\mathrm{T}} \mathbf{v}_o^* - \hat{\mathbf{n}}^{\mathrm{T}} \mathbf{b}^{*\times} \boldsymbol{\omega}^* + y^* \right) \tag{3.50}$$

$$h_a^* = I_s^* \hat{\mathbf{a}}^{\mathrm{T}} \boldsymbol{\omega}^* + I_s^* \omega_s^* \tag{3.51}$$

The motion equations are

$$\dot{\mathbf{p}}^* = -\boldsymbol{\omega}^{*\times} \mathbf{p}^* + \mathbf{f}^* \tag{3.52}$$

$$\dot{\mathbf{h}}^* = -\boldsymbol{\omega}^{*\times} \mathbf{h}^* - \mathbf{v}_o^{*\times} \mathbf{p}^* + \mathbf{g}^* \tag{3.53}$$

$$\dot{p}_n^* = m_d^* \boldsymbol{\omega}^{*\mathrm{T}} \hat{\mathbf{n}}^{\times} \left[\mathbf{v}_o^* - (\mathbf{b} + x^* \hat{\mathbf{n}})^{\times} \boldsymbol{\omega}^* \right] - c_d^* y^* - k_d^* x^* \tag{3.54}$$

$$\dot{h}_a^* = g_a^* \tag{3.55}$$

$$\dot{x}^* = y^* \tag{3.56}$$

The full equations are made dimensionless by defining characteristic length, mass, and time units. These quantities are used to non-dimensionalize the variables and parameters of the problem. Many possible characteristic quantities are possible, a few of which are included in Table 3.1. Whereas all possible choices lead to dimensionless equations, certain quantities lead to equations with desirable or undesirable qualities. We desire satellites with the same dimensional inertia properties to have the same non-dimensional inertia properties. If we select damper parameters as characteristic quantities, then the same satellite with two different dampers would have different non-dimensional inertia properties. We want to avoid this difference so we choose characteristic values without damper parameters.

Table 3.1: Examples of characteristic length, mass, and time

Characteristic	Examples
Length	b^*, I_i^*/m^*b^*, $\sqrt{\mathrm{tr}\,\mathbf{I}_o^*/m^*}$
Mass	m^*, m_d^*, I_i^*/b^{*2}
Time	$\sqrt{m_d^*/k_d^*}$, ω^{*-1}, $b^*/\mathbf{v}_o^*$

We select the following characteristic quantities,

$$\begin{aligned} \text{Length} &= \sqrt{\frac{\mathrm{tr}\,\mathbf{I}_0{}^*}{m^*}} \\ \text{Mass} &= m^* \\ \text{Time} &= \frac{\mathrm{tr}\,\mathbf{I}_0{}^*}{h^*} \end{aligned}$$

These definitions produce equations with two notable features: the trace of the dimensionless inertia matrix is always one, $\mathrm{tr}\,\mathbf{I}_0 = 1$, and the dimensionless angular momentum vector also has unit length, $\mathbf{h}^{\mathrm{T}}\mathbf{h} = 1$. This latter feature is only true if $\mathbf{g} = \mathbf{0}$. Also, these definitions require

$h^* \neq 0$, so for a zero momentum system different characteristic quantities are necessary to non-dimensionalize the equations.

The following relationships are used to make the full equations dimensionless.

$$\begin{array}{cc}
\mathbf{p}^* = \left(h^*\sqrt{m^*/\mathrm{tr}\,\mathbf{I}_0{}^*}\right)\mathbf{p} & \mathbf{h}^* = h^*\mathbf{h} \\
p_n^* = \left(h^*\sqrt{m^*/\mathrm{tr}\,\mathbf{I}_0{}^*}\right)p_n & \mathbf{v}_o^* = \left(h^*/\sqrt{m^*\mathrm{tr}\,\mathbf{I}_0{}^*}\right)\mathbf{v}_o \\
\boldsymbol{\omega}^* = \left(h^*/\mathrm{tr}\,\mathbf{I}_0{}^*\right)\boldsymbol{\omega} & y^* = \left(h^*/\sqrt{m^*\mathrm{tr}\,\mathbf{I}_0{}^*}\right)y \\
x^* = \left(\sqrt{\mathrm{tr}\,\mathbf{I}_0{}^*/m^*}\right)x & \boldsymbol{\omega}_s^* = \left(h^*/\mathrm{tr}\,\mathbf{I}_0{}^*\right)\boldsymbol{\omega}_s \\
t^* = \left(\mathrm{tr}\,\mathbf{I}_0{}^*/h^*\right)t & \mathbf{h}_a^* = h^*\mathbf{h}_a \\
\mathbf{b}^* = \left(\sqrt{\mathrm{tr}\,\mathbf{I}_0{}^*/m^*}\right)\mathbf{b} & m_d^* = \varepsilon m^* \\
\mathbf{I}^* = \mathrm{tr}\,\mathbf{I}_0{}^*\mathbf{I} & \mathbf{I}_s^* = \mathrm{tr}\,\mathbf{I}_0{}^*\mathbf{I}_s \\
c_d^* = \left(m^*h^*/\mathrm{tr}\,\mathbf{I}_0{}^*\right)c_d & k^* = \left(m^*h^{*2}/\mathrm{tr}\,\mathbf{I}_0{}^{*2}\right)k \\
\dot{\mathbf{p}}^* = \left(h^{*2}\sqrt{m^*/\mathrm{tr}\,\mathbf{I}_0{}^{*3}}\right)\dot{\mathbf{p}} & \dot{\mathbf{h}}^* = \left(h^{*2}/\mathrm{tr}\,\mathbf{I}_0{}^*\right)\dot{\mathbf{h}}
\end{array} \tag{3.57}$$

The resulting dimensionless state variables are $\mathbf{h}$, p_n, and x. We do no limit the motion of the damper. As previously stated, $\mathrm{tr}\,\mathbf{I}_0 = 1$ and $h = 1$, however h_a is unbounded. We only consider systems with positive damping, so $c_d > 0$. The natural symmetry of the model produces identical results for $\pm b$, so we restrict the analysis to $b \geq 0$. The maximum value of b is related to I_2 and ε, as discussed in App. A. Also, the other damper parameters must be positive, so $k > 0$ and $\varepsilon > 0$.

Substituting for the dimensional quantities results in the following dimensionless equations of motion

$$\dot{\mathbf{p}} = -\boldsymbol{\omega}^\times\mathbf{p} + \mathbf{f} \tag{3.58}$$
$$\dot{\mathbf{h}} = -\boldsymbol{\omega}^\times\mathbf{h} - \mathbf{v}_o^\times\mathbf{p} + \mathbf{g} \tag{3.59}$$
$$\dot{h}_a = g_a \tag{3.60}$$
$$\dot{p}_n = \varepsilon\boldsymbol{\omega}^T\hat{\mathbf{n}}^\times[\mathbf{v}_o - (\mathbf{b} + x\hat{\mathbf{n}})^\times\boldsymbol{\omega}] - c_d y - kx \tag{3.61}$$
$$\dot{x} = y \tag{3.62}$$

with dimensionless system momenta

$$\mathbf{p} = \mathbf{v}_o - \varepsilon x\hat{\mathbf{n}}^\times\boldsymbol{\omega} + \varepsilon y\hat{\mathbf{n}} \tag{3.63}$$
$$\mathbf{h} = \mathbf{I}\boldsymbol{\omega} + \varepsilon x\hat{\mathbf{n}}^\times\mathbf{v}_o + \varepsilon y\mathbf{b}^\times\hat{\mathbf{n}} + I_s\omega_s\hat{\mathbf{a}} \tag{3.64}$$
$$h_a = I_s(\mathbf{a}^T\boldsymbol{\omega} + \omega_s) \tag{3.65}$$
$$p_n = \varepsilon(\hat{\mathbf{n}}^T\mathbf{v}_o - \hat{\mathbf{n}}^T\mathbf{b}^\times\boldsymbol{\omega} + y) \tag{3.66}$$

The dimensionless moment of inertia matrix is

$$\mathbf{I} = \mathbf{I}_o + \varepsilon\left[\left(2x\mathbf{b}^T\hat{\mathbf{n}} + x^2\right)\mathbf{1} - x(\mathbf{b}\hat{\mathbf{n}}^T + \hat{\mathbf{n}}\mathbf{b}^T) - x^2\hat{\mathbf{n}}\hat{\mathbf{n}}^T\right] \tag{3.67}$$

Once non-dimensionalized, we reduce the system equations by several simplifying assumptions.

3.5 Reduced Equations of Motion

We make several assumptions, consistent with the intention of studying the free motion of the damped gyrostat, which simplify the equations of motion. We assume $\mathbf{f} = \mathbf{g} = \mathbf{0}$ and $g_a = 0$. Thus, $\mathbf{p}$, $\mathbf{h}$, and h_a are all constant. Rotor momentum, h_a, is treated as a system parameter rather than a variable. One final simplifying choice is made by selecting the constant system linear momentum to be zero, $\mathbf{p} = \mathbf{0}$. By making this choice, we can solve for the velocity:

$$\mathbf{v}_o = \varepsilon x \hat{\mathbf{n}}^{\times} \boldsymbol{\omega} - \varepsilon y \hat{\mathbf{n}}$$

Substituting for $\mathbf{v}_o$ in the expression for angular momentum, we can solve for the angular velocity

$$\boldsymbol{\omega} = \mathbf{K}^{-1}\mathbf{m}$$

by defining $\varepsilon' = 1 - \varepsilon$, and

$$\begin{aligned} \mathbf{K} &= \mathbf{I}_o - I_s \hat{\mathbf{a}}\hat{\mathbf{a}}^{\mathrm{T}} + \varepsilon \left[2x\mathbf{b}^{\mathrm{T}}\hat{\mathbf{n}}\mathbf{1} - x(\mathbf{b}\hat{\mathbf{n}}^{\mathrm{T}} + \hat{\mathbf{n}}\mathbf{b}^{\mathrm{T}}) - \varepsilon' x^2 \hat{\mathbf{n}}^{\times}\hat{\mathbf{n}}^{\times} \right] \\ \mathbf{m} &= \mathbf{h} - h_a \hat{\mathbf{a}} - \varepsilon y \mathbf{b}^{\times}\hat{\mathbf{n}} \end{aligned}$$

Given the stated assumptions and eliminating the velocities from the equations of motion reduces the system to five scalar equations in $\mathbf{h}$, p_n, and x:

$$\dot{\mathbf{h}} = \mathbf{h}^{\times}\mathbf{K}^{-1}\mathbf{m} \tag{3.68}$$

$$\dot{p}_n = -\varepsilon \mathbf{m}^{\mathrm{T}}\mathbf{K}^{-1}\hat{\mathbf{n}}^{\times}\left[(\mathbf{b} + \varepsilon' x \hat{\mathbf{n}})^{\times}\mathbf{K}^{-1}\mathbf{m} \right] - c_d y - kx \tag{3.69}$$

$$\dot{x} = y \tag{3.70}$$

where

$$\varepsilon y = \frac{p_n + \varepsilon \hat{\mathbf{n}}^{\mathrm{T}}\mathbf{b}^{\times}\mathbf{K}^{-1}(\mathbf{h} - h_a\hat{\mathbf{a}})}{\varepsilon' + \varepsilon \hat{\mathbf{n}}^{\mathrm{T}}\mathbf{b}^{\times}\mathbf{K}^{-1}\mathbf{b}^{\times}\hat{\mathbf{n}}} \tag{3.71}$$

The system state variables are:

h_1	angular momentum in $\hat{\mathbf{b}}_1$ direction
h_2	angular momentum in $\hat{\mathbf{b}}_2$ direction
h_3	angular momentum in $\hat{\mathbf{b}}_3$ direction
p_n	linear momentum component of $\mathcal{P}$ in $\hat{\mathbf{n}}$ direction
x	damper displacement

and the dimensionless system parameters are:

I_1	moment of inertia about $\hat{\mathbf{b}}_1$-axis
I_2	moment of inertia about $\hat{\mathbf{b}}_2$-axis

I_3	moment of inertia about $\hat{\mathbf{b}}_3$-axis
I_s	rotor axial moment of inertia about $\hat{\mathbf{a}}$
$\mathbf{b}$	damper position vector
b	magnitude of $\mathbf{b}$, damper location distance
ε	damper particle mass
k	damper spring stiffness
c_d	damping coefficient

The reduced, dimensionless equations are used in the numerical and analytical studies in this dissertation.

3.6 Comments on Equations of Motion

The equations of motion have several properties which are important to later developments. Some of these properties are a product of the Newton-Euler development and the choices made for the system states. Although the equations describing the motion of the system are expressible in different forms, such as generalized coordinates, the advantage of the Newton-Euler approach is found in the relatively simple form of the equations. Nevertheless, the form of these equations do present certain challenges to analysis, mostly due to the presence of a conserved quantity.

3.6.1 Conserved Angular Momentum

If the system is free of external torques, system angular momentum is conserved. In general terms of the state vector, $\mathbf{z}$, a conserved quantity takes the form,

$$C(\mathbf{z}) = 0$$

which for conserved angular momentum becomes

$$\mathbf{h}^{\mathrm{T}}\mathbf{h} - 1 = 0 \tag{3.72}$$

or

$$h_1^2 + h_2^2 + h_3^2 - 1 = 0 \tag{3.73}$$

This constraint between the states has the effect of a persistent zero eigenvalue in the system Jacobian matrix (defined in Sec. 4.1.3). A singular Jacobian affects how we can achieve the objective of characterizing the possible system equilibria. Also, the conserved quantity complicates the stability analysis of relative system equilibria.

Solving Eq. 3.73 for one of the angular momentum components, such as $h_1 = \sqrt{1 - h_2^2 - h_3^2}$, and substituting into the system equations effectively reduces the order of the equations by one.

However, the resulting Jacobian has elements with the term $\sqrt{1-h_2^2-h_3^2}$ in the denominator. These elements of the Jacobian matrix are singular when $h_1 = 0$, which is a significant portion of the state space. We use numerical techniques in later chapters which require a continuous, full-rank Jacobian. Therefore, direct substitution for one of the momentum coordinates is not a practical method of reducing the system.

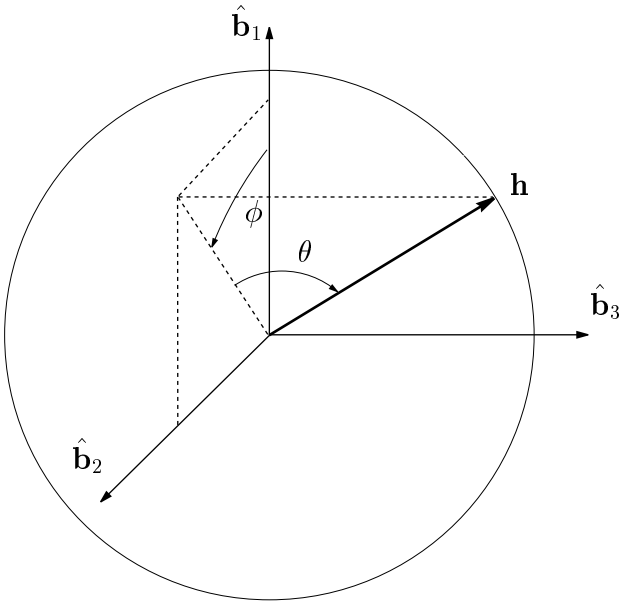

Figure 3.5: Spherical coordinate definition for angular momentum

Instead of using the conserved quantity to eliminate one of the states, we change variables to spherical coordinates and achieve the same reduction in order with fewer numerical problems. The conserved magnitude of the angular momentum vector, denoted as h, forces all possible states to lie on a momentum sphere of radius h. As such, the three state variables representing the angular momentum vector, (h_1, h_2, h_3), can be expressed in spherical coordinates, (h, θ, ϕ). Different definitions are possible for the two angles, but one such definition is shown in Fig. 3.5, where

$$h_1 = h\cos\theta\cos\phi \tag{3.74}$$

$$h_2 = h\cos\theta\sin\phi \tag{3.75}$$

$$h_3 = h\sin\theta \tag{3.76}$$

By converting the state from (h_1, h_2, h_3, p_n, x) to $(h, \theta, \phi, p_n, x)$, we effectively reduce the system to four first-order equations. This is possible because, in terms of these variables, the conserved quantity itself becomes a state, and $\dot{h} = 0$ by definition. We convert Eqs. 3.69–3.70 to the new variables by simply substituting for $\mathbf{h}$. To convert Eq. 3.68 to the new variables requires use of a

transformation matrix derived from the spherical coordinate definitions. For the above definitions, the matrix is

$$\begin{bmatrix} \dot{h} \\ \dot{\theta} \\ \dot{\phi} \end{bmatrix} = \frac{1}{h} \begin{bmatrix} h\cos\theta\cos\phi & h\cos\theta\sin\phi & h\sin\theta \\ -\sin\theta\cos\phi & -\sin\theta\sin\phi & \cos\theta \\ -\sin\phi/\cos\theta & \cos\phi/\cos\theta & 0 \end{bmatrix} \begin{bmatrix} \dot{h}_1 \\ \dot{h}_2 \\ \dot{h}_3 \end{bmatrix} \tag{3.77}$$

Obviously, this transformation is singular when $\cos\theta = 0$, corresponding to a pure spin about the $\hat{\mathbf{b}}_3$ axis. Similar to kinematic expressions for Euler angle rates, no one set of spherical coordinate angles is non-singular for the entire state space. However, by choosing the transformation wisely, the singularity can be placed in an unimportant region of state space. Being aware of the singularity, we can use an alternate transformation if numerical problems occur when working in regions of state space near the original transformation's singularity.

3.6.2 Symmetry of Equilibria

The natural symmetry of the axial gyrostat with aligned damper produces symmetry in the equilibrium solutions of Eqs. 3.68–3.70. The equations are invariant for several transformations. Three possible transformations correspond to rotating the body frame through π about one of the body axes. Rotating the body frame through π about $\hat{\mathbf{b}}_3$ produces symmetry within the $\hat{\mathbf{b}}_1$–$\hat{\mathbf{b}}_3$ and $\hat{\mathbf{b}}_2$–$\hat{\mathbf{b}}_3$ planes. Equations 3.68–3.70 are invariant under the transformation

$$(h_1, h_2, h_3, p_n, x, h_a) \mapsto (-h_1, -h_2, h_3, -p_n, -x, -h_a) \tag{3.78}$$

Two other transformations exist for rotations about $\hat{\mathbf{b}}_1$ and $\hat{\mathbf{b}}_2$, but they require $\mathbf{b} \mapsto -\mathbf{b}$. The two transformations are

$$(h_1, h_2, h_3, p_n, x, b) \mapsto (h_1, -h_2, -h_3, p_n, x, -b) \tag{3.79}$$

for the $\hat{\mathbf{b}}_1$ rotation, and

$$(h_1, h_2, h_3, p_n, x, h_a, b) \mapsto (-h_1, h_2, -h_3, -p_n, -x, -h_a, -b) \tag{3.80}$$

for a $\hat{\mathbf{b}}_2$ rotation. We acknowledge the symmetry associated with $\pm\mathbf{b}$, but we are more interested in symmetries for a specific damper location. Two transformations related to the $\hat{\mathbf{b}}_1$ and $\hat{\mathbf{b}}_2$ rotations exist. These transformations have opposite signs for the damper variables compared to the pure rotation transformations in Eqs. 3.79–3.80. For a fixed $\mathbf{b}$, the transformation

$$(h_1, h_2, h_3, p_n, x, h_a) \mapsto (h_1, -h_2, -h_3, -p_n, -x, h_a) \tag{3.81}$$

is associated with symmetry within the $\hat{\mathbf{b}}_1$–$\hat{\mathbf{b}}_2$ and $\hat{\mathbf{b}}_1$–$\hat{\mathbf{b}}_3$ planes. The transformation

$$(h_1, h_2, h_3, p_n, x, h_a) \mapsto (-h_1, h_2, -h_3, p_n, x, -h_a) \tag{3.82}$$

is associated with symmetry within the $\hat{\mathbf{b}}_1$–$\hat{\mathbf{b}}_2$ and $\hat{\mathbf{b}}_2$–$\hat{\mathbf{b}}_3$ planes.

The symmetries of equilibria are evident in the numerical results in Ch. 5. The natural symmetry of the model is perturbed in Ch. 7 by adding rotor or damper alignment errors. These errors also break the symmetry of equilibria.

3.6.3 Equivalence with Rigid Body and Damper Model

A related problem to the gyrostat with discrete damper (identified as $\mathcal{B}+\mathcal{R}+\mathcal{P}$) is the rigid body with discrete damper (identified as $\mathcal{B}+\mathcal{P}$). Chinnery and Hall[17] developed equations of motion for such a model, configured as the previously defined nominal configuration but without the rotor. The equations for the $\mathcal{B}+\mathcal{R}+\mathcal{P}$ case can be reduced to those for the $\mathcal{B}+\mathcal{P}$ case by the transformation

$$(h_a, I_1') \mapsto (0, I_1) \tag{3.83}$$

where $I_1' = I_1 - I_s$. Therefore, results obtained for $h_a = 0$ are applicable to the $\mathcal{B}+\mathcal{P}$ case and compared to previous results by Chinnery and Hall.

The equivalence defined by Eq. 3.83 does not imply the rotor is fixed. It does imply that the dynamics of the $\mathcal{B}+\mathcal{R}+\mathcal{P}$ system are the same as the $\mathcal{B}+\mathcal{P}$ system, but for a different inertia matrix. For $h_a = 0$, the rotor velocity relative to the rigid body is

$$\omega_s = -\hat{\mathbf{a}}^{\mathrm{T}}\boldsymbol{\omega} \tag{3.84}$$

The rotor will rotate in an opposite sense relative to the contribution of $\boldsymbol{\omega}$ in order to maintain the *absolute* angular momentum of zero, in the absence of any rotor torques. A fixed rotor would be characterized by $h_s = 0$, and equations reduce to those for the $\mathcal{B}+\mathcal{P}$ model.

3.6.4 Absolute vs. Relative Rotor Angular Momentum

We derived the equations of motion in terms of the absolute angular momentum, h_a, but we could alternatively express the equations in terms of the relative rotor momentum:

$$h_s = h_a - I_s\hat{\mathbf{a}}^{\mathrm{T}}\boldsymbol{\omega} \tag{3.85}$$

The advantage of using h_a lies in the motion equations:

$$\dot{h}_a = g_a \tag{3.86}$$

The axial rotor torque, g_a, is the obvious control variable for any control scheme using rotor momentum to control or maneuver the system. The equivalent motion equation in terms of h_s is

$$\dot{h}_s = g_a - I_s\hat{\mathbf{a}}^{\mathrm{T}}\dot{\boldsymbol{\omega}} \tag{3.87}$$

where $\dot{\boldsymbol{\omega}}$ is a complicated expression found by differentiating Eq. 3.64 or manipulating Eq. 3.59. Also, we can easily determine the relative momentum state at any point using Eq. 3.85. Therefore, the motion equations are more simply expressed in terms of h_a rather than h_s.

3.7 Summary

We derived the equations of motion for a gyrostat with a spring-mass damper. The equations of motion were developed with a Newton-Euler approach, leading to equations in terms of system momenta and damper variables. We made the equations dimensionless, and after several simplifying assumptions, were left with five first-order differential equations. Conserved angular momentum requires further reduction, to fourth-order equations, to eliminate a persistent zero eigenvalue in the system Jacobian. A change of variables to spherical coordinates is proposed to take advantage of the conserved quantity and reduce the equations. With these results, we next consider the stability conditions for simple spins.

Chapter 4

Stability of Simple Spins

In this chapter we examine the stability of specific relative equilibria which correspond to steady spins about the body frame axes. The spin about the $\hat{\mathbf{b}}_1$ axis, previously named the nominal spin, is of particular practical interest as it corresponds to the most likely intended spin of a dual-spin satellite. The stability conditions for a dual-spin satellite with a spring-mass damper were studied by Likins[45] in 1967, and reformulated by Hall.[30] Both used a linear stability analysis to establish stability conditions, but just for the nominal spin. We also use a linear analysis, but a nonlinear, Liapunov analysis is then used to independently verify these results. The other two pure spins, about the $\hat{\mathbf{b}}_2$ and $\hat{\mathbf{b}}_3$ axes, are possible only for zero rotor momentum, $h_a = 0$, since the rotor is perpendicular to these axes. These latter two equilibria are important for the $\mathcal{B} + \mathcal{P}$ case, or for a gyrostat spinning about a transverse axis, prior to initial rotor spin-up. We use both linear and nonlinear stability analyses to derive stability conditions for these two equilibria.

We begin by defining key stability ideas and outlining methods to be used in generating stability conditions. These methods are then used to determine stability conditions for the simple spins.

4.1 Stability Definitions and Methods

Intuitively, stability implies that trajectories near a desired operating point are well behaved in a certain region. There are different precise definitions of stability, with sometimes subtle but important distinctions. The objective of this section is to define some key stability concepts and theorems that will be applied to determine stability conditions for certain relative equilibria. First, a definition of equilibrium is presented, along with the related concept of relative equilibrium. Then, stability definitions and theorems are presented for both linear and nonlinear stability analysis. Many texts offer an extensive discussion of stability concepts and theory, including Ref. 63, which is used for many of the formal definitions and theorems in this section.

4.1.1 Equilibrium

We consider a nonlinear, autonomous system:

$$\dot{\mathbf{z}} = \mathbf{f}(\mathbf{z}) \tag{4.1}$$

State vectors which satisfy $\mathbf{0} = \mathbf{f}(\mathbf{z})$ are defined as *equilibrium* points. Equilibria can be found by solving the resulting nonlinear algebraic equations. In some cases, solving these equations may be difficult analytically, leaving a numerical solution as the only practical alternative. Also, with nonlinear systems it may not be possible to know how many equilibria exist. More formally,

Definition 4.1 *A state $\mathbf{z}_e$ is an equilibrium point of the system if once $\mathbf{z}(t)$ is equal to $\mathbf{z}_e$, it remains equal to $\mathbf{z}_e$ for all future time*

If Eq. 4.1 describes the motion of a system expressed in a moving or rotating reference frame, then an equilibrium for this system is defined as a *relative equilibrium*.

4.1.2 Stability Definitions

State variables may be transformed such that a specific equilibrium state is translated to the origin. As such, we focus on the stability of the equilibrium state, $\mathbf{z} = \mathbf{0}$. Stability of the origin is formally stated, in the Liapunov sense as follows:

Definition 4.2 *The equilibrium state $\mathbf{z} = \mathbf{0}$ is said to be stable if, for any $R > 0$, there exists $r > 0$, such that if $\|\mathbf{z}(0)\| < r$, then $\|\mathbf{z}(t)\| < R$ for all $t \geq 0$. Otherwise, the equilibrium point is unstable.*

This definition means that the system trajectory will remain arbitrarily close to the origin by starting sufficiently near the origin. Whereas the trajectory is bounded in an arbitrarily small region about the origin, it may not converge to the origin. This more desirable quality is captured in the definition for asymptotic stability.

Definition 4.3 *An equilibrium point $\mathbf{0}$ is asymptotically stable if it is stable, and in addition there exists some $r > 0$ such that $\|\mathbf{z}(0)\| < r$ implies that $\mathbf{z}(t) \to \mathbf{0}$ as $t \to \infty$.*

The region in state space, $\|\mathbf{z}\| < r$ is referred to as the *domain of attraction* of the equilibrium point. Locally, an equilibrium point may be asymptotically stable, but if a trajectory begins sufficiently far away from the point it may be outside the domain of attraction and be unstable. This local stability feature is unique to nonlinear systems. Linear time-invariant systems are either globally asymptotically stable, unstable, or marginally stable, as defined in the following section.

4.1.3 Linearization and Local Stability

A Taylor series expansion of Eq. 4.1 about $\mathbf{z}_e$ yields

$$\delta\dot{\mathbf{z}} = \mathbf{A}(\mathbf{z}_e)\delta\mathbf{z} + \mathcal{O}\left(\delta\mathbf{z}^2\right) \tag{4.2}$$

where $\delta\mathbf{z} = \mathbf{z} - \mathbf{z}_e$ is the perturbed state vector and the system Jacobian matrix is

$$\mathbf{A}(\mathbf{z}_e) = \left[\frac{\partial\mathbf{f}(\mathbf{z})}{\partial\mathbf{z}}\right]_{\mathbf{z}=\mathbf{z}_e}$$

Neglecting all terms higher than first order in Eq. 4.2 gives the linearized system of equations

$$\delta\dot{\mathbf{z}} = \mathbf{A}(\mathbf{z}_e)\delta\mathbf{z} \tag{4.3}$$

The stability of the linear system is determined by the eigenvalues of $\mathbf{A}$. If all eigenvalues of $\mathbf{A}$ are in the open set of the left-half complex plane, then the origin is *asymptotically stable*. If at least one eigenvalue of $\mathbf{A}$ is in the open right-half complex plane, then the origin is *unstable*. If *none* of the eigenvalues are in the right-half complex plane, but at least one is on the imaginary axis, then the linear system is *marginally stable*. It should be noted that if there are repeated complex pairs of eigenvalues on the imaginary axis then the system is unstable. Applying these concepts to the linearization of a nonlinear system provides valuable local stability information about the reference equilibrium point.

The linearization of a system to locally evaluate the stability of an equilibrium point is often referred to as Liapunov's linearization or Liapunov's first method. The following states the well-known relationship between the stability of the linearized system and the original nonlinear system.

Theorem 4.1 (Liapunov's linearization method) *For the nonlinear, autonomous system, Eq. 4.1, linearized about a reference equilibrium state, the following stability conclusions are made:*

- *If the linearized system is asymptotically stable, then the reference equilibrium point is asymptotically stable for the original nonlinear system*
- *If the linearized system is unstable, then the reference equilibrium point is unstable for the nonlinear system*
- *If the linearized system is marginally stable, then no conclusion can be made from the linear approximation regarding the stability of the nonlinear system*

A proof of this theorem is in many nonlinear dynamics texts, including Khalil,[41] but the rationale behind these concepts is relatively simple. If the linearized system is strictly stable or unstable, and since near the equilibrium point the linearized system closely approximates the original system,

the nonlinear system is likewise stable or unstable. However, if the linearized system is marginally stable, then the effects of the neglected higher-order (nonlinear) terms may become critical in whether the system is stable or unstable. In this latter case, the linearized analysis is inconclusive. Simple nonlinear systems may be globally asymptotically stable even though their linearized systems are marginally stable. To determine the stability in these cases, a nonlinear stability analysis is required.

4.1.4 Nonlinear Stability

Liapunov's direct method, sometimes called his second method, is the most common nonlinear method of establishing stability. The method is based on observation of physical systems and energy. If the total energy of a dynamical system is continuously dissipated, then the system motion eventually damps out to an equilibrium state. The equilibrium point is a minimum energy state, although it may only be a local minimum. The Liapunov direct method involves a similar but more general approach. An "energy-like" scalar function is used, along with its time derivative, to determine stability of an equilibrium state.

We are concerned with the stability of a particular solution to a set of differential equations. It is often convenient to work with perturbed coordinates, $\delta\mathbf{z}$. In these coordinates, the reference solution is always $\delta\mathbf{z} = \mathbf{0}$, so we consistently consider the stability of the origin. The basic definitions and theorems in this section are expressed in terms of stability of the origin.

Definition 4.4 *A scalar function, $V(\mathbf{z})$, is a Liapunov function if and only if it is continuously differentiable and is locally positive definite, that is*

$$V(\mathbf{0}) = 0 \quad \text{and} \quad V(\mathbf{z}) > 0 \quad \text{for} \quad \mathbf{z} \neq \mathbf{0}$$

within a region $\|\mathbf{z}\| < R$, and its time derivative along any state trajectory is negative semi-definite,

$$\dot{V}(\mathbf{z}) \leq 0$$

If V is positive definite

Liapunov functions are related to the stability of dynamical systems, and this relationship is established in Liapunov's direct method.

Theorem 4.2 (Liapunov theorem for local stability) *If in a region $\|\mathbf{z}\| < R$, there exists a scalar function V of the state $\mathbf{z}$, with continuous first order derivatives such that*

- *$V(\mathbf{z})$ is positive definite within $\|\mathbf{z}\| < R$*
- *$\dot{V}(\mathbf{z})$ is negative definite within $\|\mathbf{z}\| < R$*

then the equilibrium at the origin is locally asymptotically stable.

It is important to recognize that Liapunov's direct method provides only sufficient, not necessary stability conditions. Failure to satisfy conditions for stability does not provide any stability information. It only means stability cannot be established with this particular Liapunov function.

The requirement for $\dot{V}$ to be negative definite seems to preclude application to many physical problems, particularly those using total energy as Liapunov function. Since energy dissipation can be zero, and therefore is semi-definite, Liapunov's method seems to not apply. However, it is still possible to draw stability conclusions with the help of invariant set theorems attributed to LaSalle.[41] If we can establish that no system trajectory can stay forever at points where $\dot{V} = 0$, except at the origin, then the origin is globally asymptotically stable. To state LaSalle's theorem, we need to use the concept of an invariant set.

Definition 4.5 *A set **G** is an invariant set for a dynamic system if every system trajectory which starts from a point in **G** remains in **G** for all future time.*

LaSalle's theorem can then be stated as

Theorem 4.3 *: Consider an autonomous system, Eq. 4.1, with continuous* $\mathbf{f}$ *and scalar function* $V(\mathbf{z})$ *with continuous partial first derivatives. Assume that*

- $\dot{V}(\mathbf{z}) \leq 0$ *over the whole state space*
- $V(\mathbf{z}) \to \infty$ *as* $\|\mathbf{z}\| \to \infty$

*Let **R** be the set of all points where* $\dot{V}(\mathbf{z}) = 0$*, and **M** be the largest invariant set in **R**. Then all solutions globally asymptotically converge to **M** as* $t \to \infty$*.*

The term "largest" invariant set is understood to include the *union* of all invariant sets, whether they be equilibrium points or perhaps limit cycles. Therefore, for multiple equilibria, the invariant set of equilibria are collectively globally asymptotically stable.

4.2 Stability Analysis for the Nominal, $\hat{\mathrm{b}}_1$-Axis Spin

The stability concepts of the preceding sections can be applied to the steady-spin equilibria for the $\mathcal{B} + \mathcal{R} + \mathcal{P}$ model. First, a linear stability analysis is considered. Once the system of equations are linearized about a specific equilibrium state, the task of evaluating the stability of the linearized system matrix, $\mathbf{A}$, remains. As previously stated, this involves determining the eigenvalues of $\mathbf{A}$ and using the sign of the real parts to assess stability. For a specific system configuration it is a

simple matter to determine the eigenvalues. Of greater interest is determining what conditions on the system parameters are required to ensure stability of the equilibrium state. As previous works have established the major-axis rule for a spinning rigid body with energy dissipation, we can use linear and nonlinear stability concepts to generate similar stability conditions for the damped gyrostat.

Routh-Hurwitz stability criteria (Ref. 34, Appendix A) are used to determine whether eigenvalues of $\mathbf{A}$ are in the left half-plane. Instead of calculating the eigenvalues directly, the stability is determined by proxy, working instead with the coefficients of the characteristic polynomial

$$P_n(\mu) = \det(\mu \mathbf{1} - \mathbf{A})$$

which can be expanded as

$$P_n(\mu) = \mu^n + a_1 \mu^{n-1} + \cdots + a_{n-1}\mu + a_n$$

The characteristic equation, $P_n(\mu) = 0$, has the eigenvalues of $\mathbf{A}$ as its roots. It may be difficult to determine the eigenvalues themselves from the coefficients a_i, but the Routh-Hurwitz method provides criteria for the coefficients that ensure all the eigenvalues are in the open left half-plane.

For the nominal spin about the $\hat{\mathbf{b}}_1$ axis, the relative equilibrium state for Eqs. 3.68-3.70 is the state $(\mathbf{h}, p_n, x) = (\pm 1, 0, 0, 0, 0)$. Linearizing the reduced, non-dimensional equations of motion about this reference condition (for $h_1 = +1$) yields the following Jacobian matrix,

$$\mathbf{A}(\mathbf{z}_e) = \begin{bmatrix} 0 & 0 & 0 & 0 & 0 \\ 0 & 0 & \frac{\varepsilon}{\varepsilon' I_2 - b^2\varepsilon} + \frac{h_a - 1}{I_1 - I_s} & \frac{bc}{\varepsilon' I_2 - b^2\varepsilon} & \frac{-b}{\varepsilon' I_2 - b^2\varepsilon} \\ 0 & \frac{I_1 - I_s + I_3(h_a - 1)}{-I_3(I_1 - I_s)} & 0 & \frac{b\varepsilon(h_a - 1)}{I_3(I_1 - I_s)} & 0 \\ 0 & 0 & \frac{-b}{\varepsilon' I_2 - b^2\varepsilon} & \frac{-cI_2}{\varepsilon(\varepsilon' I_2 - b^2\varepsilon)} & \frac{I_2}{\varepsilon(\varepsilon' I_2 - b^2\varepsilon)} \\ 0 & \frac{b\varepsilon(h_a - 1)}{I_3(I_1 - I_s)} & 0 & \frac{-b^2\varepsilon^2(h_a - 1)^2}{I_3(I_1 - I_s)^2} - k_d & 0 \end{bmatrix}$$

Immediately, the influence of the conserved angular momentum is apparent. The system state is constrained to lie on surfaces of constant angular momentum magnitude. The Jacobian is singular, with a zero eigenvalue associated with conserved angular momentum. The null space of the Jacobian is the eigenvector associated with the zero eigenvalue. This null space is the direction in state space of the conserved angular momentum gradient. If the states h_2, h_3, p_n, and x all asymptotically approach zero, then h_1 must approach ± 1 asymptotically, at least locally, to maintain the conserved angular momentum. Therefore, we can reasonably exclude the row and column associated with the zero eigenvalue and examine stability conditions for the resulting (4×4) Jacobian. We will use other methods to confirm the stability conditions and validate the stability of the center manifold.

Applying Routh-Hurwitz stability criteria to the reduced matrix results in four quantities, all of which must be positive to ensure the eigenvalues are all in the left half-plane. These four quantities

are

$$\begin{aligned}
\frac{cI_2}{\varepsilon(\varepsilon' I_2 - b^2\varepsilon)} &> 0 \\
\frac{c\,(I_1 + (-1+h_a)\,I_2 - I_s)\,(I_1 + (-1+h_a)\,I_3 - I_s)}{\varepsilon\,(\varepsilon' I_2 - b^2\varepsilon)\,I_3\,(I_1 - I_s)^2} &> 0 \\
\frac{(I_1 + (-1+h_a)\,I_2 - I_s)\left(b^2\,\varepsilon^2\,(-1+h_a)^3 + (I_1 - I_s)^2\,(I_1 + (-1+h_a)\,I_3 - I_s)\,k_d\right)}{\varepsilon\,\varepsilon' I_2 - b^2\varepsilon\,I_3\,(I_1 - I_s)^4} &> 0 \\
\frac{b^2\,c^2\,(I_1 + (-1+h_a)\,I_2 - I_s)\,(-I_1 + I_2 - h_a\,I_2 + I_3 - h_a\,I_3 + I_s)^2}{\varepsilon\,\varepsilon' I_2 - b^2\varepsilon^3\,{I_3}^2\,(I_1 - I_s)^3} &> 0
\end{aligned}$$

Defining several new parameters: $I_1' = I_1 - I_s$, $I_2' \triangleq \varepsilon' I_2 - b^2\varepsilon$, and $\lambda = h_a - 1$. The stability criteria become

$$\frac{cI_2}{\varepsilon I_2'} > 0 \tag{4.4}$$

$$\frac{c\,(I_1' + \lambda I_2)\,(I_1' + \lambda I_3)}{\varepsilon I_1'^2 I_2' I_3} > 0 \tag{4.5}$$

$$\frac{(I_1' + \lambda I_2)\,(I_1'^3 k + I_1'^2 I_3 \lambda k + b^2\varepsilon^2\lambda^3)}{\varepsilon I_1'^4 I_2' I_3} > 0 \tag{4.6}$$

$$\frac{b^2\varepsilon^2\,(I_1' + \lambda I_2)\,(I_1' + (I_2 + I_3)\,\lambda)^2}{\varepsilon I_1'^3 I_2'^3 I_3^2} > 0 \tag{4.7}$$

From Eq. 4.4, we see that if I_2' is positive then this condition is always satisfied. Appendix A demonstrates that in fact I_2' is always positive, and we can use this result to conclude that the denominators of the remaining three stability conditions are all positive. Therefore, stability of the linearized system depends on the sign of the remaining three numerators.

From Eq. 4.7 we require that

$$I_1' + \lambda I_2 > 0$$

Applying this requirement to Eq. 4.5, it is clear that

$$I_1' > -\lambda I_2 \quad \text{and} \quad I_1' > -\lambda I_3$$

Finally, applying these results to Eq. 4.6 produces the final condition for stability:

$$I_1'^3 k + I_1'^2 I_3 \lambda k + b^2\varepsilon^2\lambda^3 > 0$$

In summary, the conditions for stability of the nominal $\hat{\mathbf{b}}_1$ axis spin can be expressed as

$$I_1' > -\lambda \max(I_2, I_3) \tag{4.8}$$

$$k > \frac{-b^2\varepsilon^2\lambda^3}{I_1'^2\,(I_1' + \lambda I_3)} \tag{4.9}$$

In examining these stability conditions, it is clear from Eq. 4.8 that a version of the major-axis rule influences the stability of a $\hat{\mathbf{b}}_1$ axis spin. For the rigid-body equivalent of this system, with $h_a = 0$ and therefore $\lambda = -1$, I_1' must be the largest moment of inertia rather than the system I_1 principal moment of inertia. Also, from Eq. 4.9 we see that there is a minimum spring stiffness for stability. Alternatively, for a given spring stiffness there exists a maximum damper location distance, b, above which the equilibrium is unstable. If Eq. 4.8 is satisfied, then Eq. 4.9 effectively divides the k–b parameter space into regions of stable and unstable nominal spins, shown in Fig. 4.1.

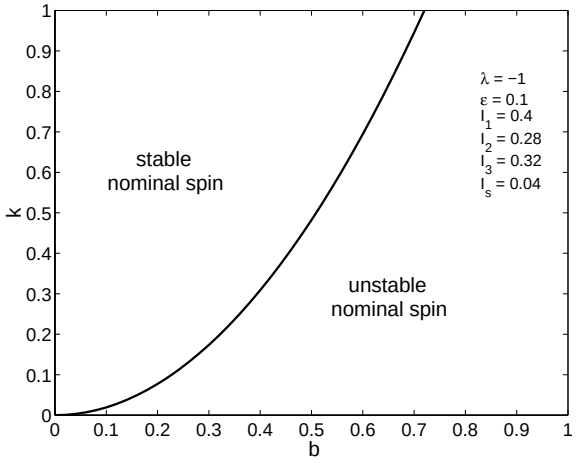

Figure 4.1: Nominal spin stability boundaries in k–b parameter space

Returning to the issue of the zero eigenvalue, it is possible to use the spherical coordinate version of the equations of motion, introduced in Chapter 3, to validate the decision to exclude the zero eigenvalue in the previous stability analysis. By converting to spherical coordinates, as defined by Eqs. 3.74–3.77, we can linearize about a $\hat{\mathbf{b}}_1$ axis spin condition defined by $(h, \theta, \phi, p_n, x) = (1, 0, 0, 0, 0)$. The $\dot{h}$ equation is identically zero, leaving four first-order equations. The resulting Jacobian, evaluated at the reference condition, is

$$\mathbf{A} = \begin{bmatrix} 0 & \frac{-\left(I_1' + \lambda I_3\right)}{I_1' I_3} & \frac{b\varepsilon\lambda}{I_1' I_3} & 0 \\ \frac{\varepsilon' I_1' + \lambda I_2'}{I_1' I_2'} & 0 & \frac{bc}{I_2'} & \frac{-b}{I_2'} \\ \frac{-b}{I_2'} & 0 & \frac{-cI_2}{\varepsilon I_2'} & \frac{I_2}{\varepsilon I_2'} \\ 0 & \frac{b\varepsilon\lambda}{I_1' I_3} & -k - \frac{(b\varepsilon\lambda)^2}{I'^2{}_1 I_3} & 0 \end{bmatrix} \tag{4.10}$$

Applying Routh-Hurwitz criteria as before leads to four quantities which must all be positive for the reference equilibrium to be stable

$$\frac{cI_2}{\varepsilon I_2'} > 0 \tag{4.11}$$

$$\frac{c\left(I_1' + \lambda I_2\right)\left(I_1' + \lambda I_3\right)}{\varepsilon I_1'^2 I_2' I_3} > 0 \tag{4.12}$$

$$\frac{(I_1' + \lambda I_2)\left(I_1'^3 k + I_1'^2 I_3 \lambda k + b^2\varepsilon^2\lambda^3\right)}{\varepsilon I_1'^4 I_2' I_3} > 0 \tag{4.13}$$

$$\frac{b^2\varepsilon^2\,(I_1' + \lambda I_2)\left(I_1' + (I_2 + I_3)\,\lambda\right)^2}{\varepsilon I_1'^3 I_2'^3 I_3^2} > 0 \tag{4.14}$$

These are the same as Eqs. 4.4– 4.7, and produce the same conditions for stability. Therefore, we validated the decision to exclude the zero eigenvalue in the original linear stability analysis by a separate linear analysis for a formulation which excludes the zero eigenvalue. For the stability analysis of the remaining $\hat{\mathbf{b}}_2$- and $\hat{\mathbf{b}}_3$-axis spins we use the less cumbersome original equations, Eqs. 3.68–3.70, and exclude the zero eigenvalue.

A nonlinear Liapunov stability analysis, using the system energy as the Liapunov function, is also performed. Details of this approach are presented in a later section, but the nonlinear stability analysis produces the same stability conditions as the linear analysis.

4.3 Stability Analysis for the $\hat{\mathbf{b}}_3$-Axis Spin

We next consider the stability of the pure spin about the $\hat{\mathbf{b}}_3$ axis. For both this condition and the $\hat{\mathbf{b}}_2$-axis spin, the equilibrium only exists if the rotor has zero absolute angular momentum, $h_a = 0$. As such, these two conditions also correspond to equilibria for the $\mathcal{B} + \mathcal{P}$ case. However, these equilibria were not treated in earlier works on this model[17] and are included here for completeness.

Proceeding as with the $\hat{\mathbf{b}}_1$-axis spin, the system is linearized about the equilibrium condition associated with $\hat{\mathbf{b}}_3$-axis spin, $(h_1, h_2, h_3, p_n, x) = (0, 0, 1, 0, 0)$, with the additional requirement $h_a = 0$. After eliminating the zero row and column from the Jacobian and applying Routh-Hurwitz criteria, we again have four quantities which must be positive for stability.

$$\frac{cI_2}{\varepsilon I_2'} > 0 \tag{4.15}$$

$$\frac{c(I_3 - I_2)(I_3 - I_1')}{\varepsilon I_1' I_2' I_3^2} > 0 \tag{4.16}$$

$$\frac{(I_3 - I_2)\left[(I_3 - I_1')(kI_3^2 - \varepsilon\varepsilon') - b^2\varepsilon^2\right]}{\varepsilon I_1' I_2' I_3^4} > 0 \tag{4.17}$$

$$\frac{b^2c^2(I_3 - I_2)(I_2 + I_3 - I_1')^2}{\varepsilon {I_1'}^2 {I_2'}^3 {I_3}^3} > 0 \tag{4.18}$$

The resulting conditions for a stable $\hat{\mathbf{b}}_3$ axis spin are

$$I_3 > \max(I_1', I_2) \tag{4.19}$$

$$k > \frac{b^2\varepsilon^2 + \varepsilon\varepsilon'(I_3 - I_1')}{{I_3}^2(I_3 - I_1')} \tag{4.20}$$

These stability conditions are similar to those developed for the $\hat{\mathbf{b}}_1$-axis spin for a rigid body, in Ref. 17. Notice that Eq. 4.19 is similar to a major-axis rule. However there exists the possibility, since $I_1' = I_1 - I_s$, that a stable configuration could have $I_1 > I_3 > I_1'$. For this special case I_3 is not the major axis of the rigid body, but is still a stable equilibrium. Also, Eq. 4.20 illustrates that for stability the spring must again be sufficiently stiff, although for a different minimum value than for a $\hat{\mathbf{b}}_1$-axis spin.

We again perform a nonlinear stability analysis for the $\hat{\mathbf{b}}_3$-axis spin. As in the nominal-spin case, the Liapunov stability analysis produces the same stability conditions. The details of the Liapunov analysis are similar to those presented in the next section for a $\hat{\mathbf{b}}_2$-axis spin, where the linear analysis is inconclusive and the nonlinear analysis is necessary to generate stability conditions.

4.4 Stability Analysis for the $\hat{\mathbf{b}}_2$-Axis Spin

We examine the stability of a $\hat{\mathbf{b}}_2$-axis spin with a linear stability analysis, but we show that this analysis is inconclusive. A nonlinear stability analysis is necessary to generate stability conditions for this equilibrium. Liapunov's direct method is used with a Liapunov function based on system energy.

For the linear analysis, we proceed as before and linearize the system about the equilibrium condition associated with a $\hat{\mathbf{b}}_2$-axis spin. However, in this case the damper variables may not be zero. For a $\hat{\mathbf{b}}_2$-axis spin the angular momentum vector is $\mathbf{h} = (0, \pm 1, 0)$. We choose to examine the $h_2 = 1$ case, but the symmetry of the model implies that the results are not significantly different for either sense of the spin. Substituting $\mathbf{h} = (0, 1, 0)$, and $h_a = 0$, into the equilibrium equations results in $b\dot{f}h = 0$. This decouples the motion of the damper from the rest of the system, for this equilibrium. The remaining damper motion equations constitute a submanifold of the motion whose stability affects the overall stability of this equilibrium. The stability of the submanifold is a function of the system parameters, and is analyzed in terms of the stability of the two-dimensional submanifold. However, a stable submanifold is only a necessary condition; the reference equilibrium point may be unstable independent of the stability of the submanifold. We first consider the stability conditions of the two types of submanifolds using a linear stability analysis. Then, we consider the stability of a full five-state equilibrium point.

4.4.1 Stability of Submanifolds

For the conditions $\mathbf{h} = (0, 1, 0)$, and $h_a = 0$, the equations of motion reduce to

$$\dot{p}_n = -kx + \frac{\varepsilon\varepsilon' x\left(\varepsilon' - bp_n\right)^2}{\left[b^2\varepsilon - \varepsilon'\left(I_2 + \varepsilon\varepsilon' x^2\right)\right]^2} + \frac{c\left[-b\varepsilon + p_n\left(I_2 + \varepsilon\varepsilon' x^2\right)\right]}{\varepsilon\left[b^2\varepsilon - \varepsilon'\left(I_2 + \varepsilon\varepsilon' x^2\right)\right]} \tag{4.21}$$

$$\dot{x} = \frac{-b\varepsilon + p_n\left(I_2 + \varepsilon\varepsilon' x^2\right)}{\varepsilon\left[b^2\varepsilon - \varepsilon'\left(I_2 + \varepsilon\varepsilon' x^2\right)\right]} \tag{4.22}$$

Setting these two equations to zero, we solve for equilibrium values of p_n and x. Two possible types of equilibria exist for a $\hat{\mathbf{b}}_2$-axis spin. The first equilibrium state is

$$(p_n, x)_1 = (b\varepsilon/I_2, 0)$$

and the second, a pair of points, is

$$(p_n, x)_{2,3} = \left(b\sqrt{\frac{\varepsilon k}{\varepsilon'}}, \pm\sqrt{\frac{\sqrt{\varepsilon\varepsilon' k} - I_2 k}{\varepsilon\varepsilon' k}} \right) \tag{4.23}$$

Linearizing the two-dimensional reduced equations about the first equilibrium state and applying Routh-Hurwitz criteria produces the following two expressions; each must be positive for stability:

$$cI_2 > 0 \tag{4.24}$$

$$\varepsilon\varepsilon' - {I_2}^2 k > 0 \tag{4.25}$$

The first expression is always positive, and the second leads to the stability condition

$$k > \frac{\varepsilon\varepsilon'}{{I_2}^2} \tag{4.26}$$

This agrees with our expectation that the equilibrium state with zero damper displacement requires a sufficiently stiff spring for stability. Therefore, as long as Eq. 4.26 is satisfied, the dynamics within the submanifold in (p_n, x) space of the equilibrium state $\mathbf{h} = (0, 1, 0, b\varepsilon/I_2, 0)$ are locally stable.

We evaluate the stability conditions for the second submanifold equilibrium using a similar linear analysis and produce the following expressions for stability,

$$-\varepsilon\varepsilon' + I_2^2 k > 0 \tag{4.27}$$

$$\varepsilon'^3 - k\varepsilon b^4 > 0 \tag{4.28}$$

Using the definition of I_2' from App. A, it can be shown that the first condition implies the second. Therefore, the stability of the second equilibrium, within the submanifold, requires

$$k < \frac{\varepsilon\varepsilon'}{{I_2}^2} \tag{4.29}$$

This critical spring stiffness marks the stability boundary between the two equilibria, within the submanifold. Examining Eq. 4.23, we see that if the submanifold stability condition, Eq. 4.29, is not met, the equilibrium state does not exist. Therefore, Eq. 4.29 defines an existence condition for the $\hat{\mathbf{b}}_2$-axis spin with $x \neq 0$. We revisit this existence condition in Ch. 8. Stability of the submanifold is a necessary condition for stability of the full-state equilibrium point, considered in the following section.

4.4.2 Linear Stability Analysis

We now focus on the stability of the full-state equilibrium condition for a $\hat{\mathbf{b}}_2$-axis spin. We concentrate on the first equilibrium point, with zero damper displacement. This state is certainly of greater practical interest as most applications desire a zero-damper displacement equilibrium. A similar nonlinear stability analysis is considered for the second pair of equilibria, but their complexity prevents simple analytical stability boundaries.

We linearize the system equations about the reference $\hat{\mathbf{b}}_2$-axis spin condition:

$$(\mathbf{h}, p_n, x) = (0, 1, 0, b\varepsilon/I_2)$$

Eliminating the zero eigenvalue associated with the conserved angular momentum, Routh-Hurwitz criteria are applied. Proceeding as for the $\hat{\mathbf{b}}_1$ and $\hat{\mathbf{b}}_3$-axis spin cases, we generate the following four quantities which must be positive for stability. But in this case, one of these is identically zero, and we can not satisfy the Routh-Hurwitz criteria and demonstrate asymptotic stability.

$$\frac{cI_2}{\varepsilon I_2'} > 0 \tag{4.30}$$

$$\frac{c(I_2 - I_1')(I_2 - I_3)}{\varepsilon I_1' I_2 I_2' I_3} > 0 \tag{4.31}$$

$$\frac{(I_2 - I_1')(I_2 - I_3)(kI_2^2 - \varepsilon\varepsilon')}{\varepsilon I_1' I_2^3 I_2' I_3} > 0 \tag{4.32}$$

$$0 = 0 \tag{4.33}$$

Another popular method of implementing Routh-Hurwitz criteria is to build a Routh Table, described in many linear systems texts including Ref.54. In this form, the zero in Eq. 4.33 leads to a zero row in the Routh Table. According to Nise, this situation occurs when there is an even polynomial that is a factor of the original polynomial.[54] This even polynomial has only even powers of μ, and only has roots that are symmetric about the origin. The system is either unstable, with roots of the even polynomial symmetric about the imaginary axis, or marginally stable, with the roots on the imaginary axis. Therefore, the linear analysis can only prove instability in this case. However, we use nonlinear stability theory in the next section to establish asymptotic stability conditions.

Despite the shortcomings of the linear analysis, it does provide some information. From Eq. 4.31 we learn that I_2 must be greater than or less than both I_1' and I_3. Equation 4.32 defines a stability condition for spring stiffness,

$$k > \frac{\varepsilon\varepsilon'}{I_2^2} \tag{4.34}$$

that is the requirement for stability within the submanifold. Intuitively, we expect another condition which requires I_2 to be a maximum, not minimum moment of inertia.

The reason for the failure of the Routh-Hurwitz method is that this equilibrium condition has two purely imaginary eigenvalues, making the linear analysis inconclusive. Therefore, a nonlinear, Liapunov stability analysis is necessary to fully characterize the stability conditions for this equilibrium condition.

4.4.3 Liapunov Stability Analysis

To demonstrate asymptotic stability with Liapunov's direct method, we must choose an appropriate Liapunov function. A likely candidate is the system total mechanical energy, which is the sum of potential and kinetic energies, or $V = T + U$. As described in Ch. 3, the potential energy of the system is

$$U = \frac{1}{2}kx^2 \tag{4.35}$$

and the kinetic energy is expressed as

$$T = \frac{1}{2}\,\boldsymbol{v}^{\mathrm{T}}\mathcal{M}\boldsymbol{v} \tag{4.36}$$

where

$$\boldsymbol{v} = \begin{bmatrix} \mathbf{v}_o \\ \boldsymbol{\omega} \\ y \\ \omega_s \end{bmatrix} \tag{4.37}$$

and

$$\mathcal{M} = \begin{bmatrix} \mathbf{1} & -\varepsilon x\hat{\mathbf{n}}^{\times} & \varepsilon\hat{\mathbf{n}} & \mathbf{0} \\ \varepsilon x\hat{\mathbf{n}}^{\times} & \mathbf{I} & \varepsilon\mathbf{b}^{\times}\hat{\mathbf{n}} & I_s\hat{\mathbf{a}} \\ \varepsilon\hat{\mathbf{n}}^{\mathbf{T}} & -\varepsilon\hat{\mathbf{n}}^{\mathbf{T}}\mathbf{b}^{\times} & \varepsilon & 0 \\ \mathbf{0}^{\mathbf{T}} & I_s\hat{\mathbf{a}}^{\mathbf{T}} & 0 & I_s \end{bmatrix} \tag{4.38}$$

To consider the stability locally, near a specific equilibrium state, we translate the state to perturbed coordinates referenced to the equilibrium state:

$$\boldsymbol{\xi} = \mathbf{z} - \mathbf{z}_{\mathbf{e}} \tag{4.39}$$

We effectively translate the equilibrium state to the origin and apply the Liapunov stability theorem. For simplicity, the notation for individual states remains unchanged, although they have been displaced by the equilibrium values.

Substituting for $\boldsymbol{\omega}$, ω_s, and $\mathbf{v}_o$ as in Ch. 3 produces an expression for total energy in terms of the state variables $(\mathbf{h}, p_n, x)$. For this to be a valid Liapunov function, it must be a positive definite function and $\dot{V} < 0$. There are issues with both of these requirements. First, the energy dissipation rate is simply the energy dissipated in the damper,

$$\dot{V} = -c_d\dot{x}^2 \tag{4.40}$$

Therefore, $\dot{V}$ is only semi-definite, but as with many systems using an energy-based Liapunov function, LaSalle's Theorem provides a means to overcome this shortcoming and demonstrate asymptotic stability. In this case, the set of equilibria is the smallest invariant set such that $\dot{V} = 0$. Trajectories can not satisfy $\dot{V} = 0$ other than at equilibrium points. So Theorem 4.3 is applied and

the conditions for asymptotic stability of the equilibrium points become merely those for V to be positive definite.

The total energy is positive semi-definite. For each equilibrium state, an infinite set of points such that V is a local minimum exist, but these minimum energy states correspond to different values of the conserved quantity, h. For a specific value of angular momentum, there exists a unique, finite set of equilibria which may be correspond to positive definite Liapunov functions in a constrained sense.

With the conserved quantity, the equilibria become constrained extremum of the Liapunov function. To derive useful stability criteria we use a constrained-minimum method described by Beck in Ref. 8. The conserved quantity affects the selection of the Liapunov function itself as well as the necessary and sufficient conditions for the Liapunov function to be a minimum. For a specific value of h, only certain values of $\boldsymbol{\xi}$ are feasible, all satisfying the constraint $C(\boldsymbol{\xi}) = \mathbf{h}^{\mathrm{T}}\mathbf{h} - 1 = 0$. Therefore, the candidate Liapunov function is augmented to include a conserved quantity term,

$$V = \frac{1}{2}\boldsymbol{v}^{\mathrm{T}}\mathcal{M}\boldsymbol{v} + \frac{1}{2}kx^2 + \Lambda(\mathbf{h}^{\mathrm{T}}\mathbf{h} - 1) \tag{4.41}$$

where Λ is a Lagrange multiplier. The form of this equation is similar to the variational Lagrangian function used in nonlinearly constrained optimization theory.[25] The function is described as variational to distinguish it from the Lagrangian function commonly used in mechanics. The variational-Lagrangian Liapunov function satisfies the positive definite requirement. Also, we must examine more closely the requirements for the Liapunov function to be a positive definite function. To understand why, it is useful to consider the Taylor series expansion for a quadratic Liapunov function about an equilibrium point,

$$V(0 + \delta\boldsymbol{\xi}) = V(0) + \left[\frac{\partial V}{\partial \boldsymbol{\xi}}\right]^{\mathrm{T}} \delta\boldsymbol{\xi} + \delta\boldsymbol{\xi}^{\mathrm{T}} \left[\frac{\partial^2 V}{\partial \boldsymbol{\xi}^2}\right] \delta\boldsymbol{\xi} \tag{4.42}$$

For V to be a positive definite function, V must be a minimum at the origin. We introduce the definitions for the gradient and Hessian of the Liapunov function,

$$\mathbf{g} = \left[\frac{\partial V}{\partial \boldsymbol{\xi}}\right]_{\boldsymbol{\xi}=\mathbf{0}}$$

and

$$\mathbf{H} = \left[\frac{\partial^2 V}{\partial \boldsymbol{\xi}^2}\right]_{\boldsymbol{\xi}=\mathbf{0}}$$

However, not all possible $\delta\boldsymbol{\xi}$ in state space are feasible. Rather, perturbations from the equilibrium are constrained such that locally $\delta\boldsymbol{\xi}$ must be tangent to the conserved quantity surface, and therefore perpendicular to $\nabla C(\boldsymbol{\xi})$, that is

$$\delta\boldsymbol{\xi}^{\mathrm{T}}\nabla C = 0$$

We define $\mathbf{P}$ as an orthogonal projection matrix, projecting $\delta\boldsymbol{\xi}$ onto the perpendicular subspace of ∇C. We find this projection by first defining $\mathbf{K} \triangleq \nabla C(\boldsymbol{\xi})$ and letting $\mathbf{Q}(\boldsymbol{\xi})$ be the rank-one projection onto $\mathbf{K}$. The rank-one projection operator is (see Ref. 65, Ch. 3),

$$\mathbf{Q}(\boldsymbol{\xi}) = \frac{\mathbf{K}\mathbf{K}^{\mathrm{T}}}{\mathbf{K}^{\mathrm{T}}\mathbf{K}} \tag{4.43}$$

Then the desired projection matrix is

$$\mathbf{P} = \mathbf{1} - \mathbf{Q} \tag{4.44}$$

We define $\mathbf{Z}$ as a matrix whose columns form a basis for the subspace orthogonal to ∇C, which is the same as the range space of $\mathbf{P}$. Possible state perturbations are in the range space of $\mathbf{Z}$. The arbitrary perturbation, $\delta\boldsymbol{\xi}$ is replaced using the relationship $\delta\boldsymbol{\xi} = \mathbf{Z}\delta\boldsymbol{\zeta}$, where $\delta\boldsymbol{\zeta}$ is an arbitrary vector with dimension equal to the rank of $\mathbf{Z}$. The first-order necessary condition for an extremum involves the *projected gradient*,

$$\mathbf{g}(\boldsymbol{\Lambda})^{\mathrm{T}}\mathbf{Z} = \mathbf{0} \tag{4.45}$$

We solve Eq. 4.45 to determine the Lagrange multiplier, Λ, in terms of the system parameters for each equilibrium state.

The second-order sufficient condition for V to be a minimum is

$$\delta\boldsymbol{\zeta}^{\mathrm{T}}\mathbf{Z}^{\mathrm{T}}\mathbf{H}\mathbf{Z}\delta\boldsymbol{\zeta} > 0$$

and therefore the *projected Hessian* must be positive definite:

$$\mathbf{Z}^{\mathrm{T}}\mathbf{H}\mathbf{Z} > 0 \tag{4.46}$$

Using the projected Hessian of the variational-Lagrangian Liapunov function, we can show Liapunov stability of the $\hat{\mathbf{b}}_2$-axis spin.

Application of Liapunov Stability to $\hat{\mathbf{b}}_2$-Axis Spin We use the Liapunov function of Eq. 4.41 to determine the stability of the $\hat{\mathbf{b}}_2$-axis spin with $x = 0$. To determine the projected gradient and Hessian, we first calculate the projection matrix from the gradient of the conserved quantity. The perturbed coordinates, near the state $\mathbf{z}_e = (0, 1, 0, b\varepsilon/I_2, 0)$, are $\boldsymbol{\xi} = (h_1, 1-h_2, h_3, b\varepsilon/I_2 - p_n, x)$. The projection matrix is calculated from Eqs. 4.43– 4.44, where h is the magnitude of the angular momentum vector. From the range space of $\mathbf{P}$, we calculate the matrix

$$\mathbf{Z} = \frac{1}{h}\begin{bmatrix} (1-h_2)^2 + h_3^2 & -h_1h_3 & 0 & 0 \\ -h_1(1-h_2) & -(1-h_2)h_3 & 0 & 0 \\ -h_1h_3 & h_1^2 + (1-h_2)^2 & 0 & 0 \\ 0 & 0 & h & 0 \\ 0 & 0 & 0 & h \end{bmatrix} \tag{4.47}$$

The first-order necessary condition, at this equilibrium point, is

$$g(\Lambda)^{\mathrm{T}} = \mathbf{0}$$

and yields the Lagrange multiplier,

$$\Lambda = -1/(2I_2)$$

Since the conditions of LaSalle's Theorem are met, the conditions for asymptotic stability of the equilibria then become the conditions for the projected Hessian to be positive definite. For the $\hat{\mathbf{b}}_2$-axis spin, with zero damper displacement, the projected Hessian becomes

$$\begin{bmatrix} (I_2 - I_1')/I_1' I_2 & 0 & 0 & 0 \\ 0 & (I_2 - I_3)/I_2 I_3 & 0 & 0 \\ 0 & 0 & I_2 I_2'/\varepsilon {I_2'}^2 & 0 \\ 0 & 0 & 0 & (k I_2^2 - \varepsilon\varepsilon')/I_2^2 \end{bmatrix} \tag{4.48}$$

This diagonal matrix is positive definite if all the diagonal entries are positive. The stability conditions are therefore

$$I_2 > \max(I_1', I_3) \tag{4.49}$$

$$k > \frac{\varepsilon\varepsilon'}{I_2^2} \tag{4.50}$$

The nonlinear stability analysis provides the condition missing from the linear analysis, that I_2 must be a maximum moment of inertia.

Repeating this analysis for both the $\hat{\mathbf{b}}_1$ and $\hat{\mathbf{b}}_3$-axis spins leads to the same stability conditions as the linear analysis.

4.5 Summary

The stability analysis of the three simple spins demonstrate the advantages of including the damper mechanism in the system model. For zero rotor momentum, the results demonstrate that the major-axis rule for stable spins is a necessary condition, as forecast by previous energy-sink results. But there is another condition necessary for stability, consisting of some requirement on the damper parameters. A spring-mass-dashpot damper, while still providing damping, may in fact destabilize the equilibrium point. One way of stating this parameter limitation is to note that for each equilibrium condition there is a minimum spring stiffness, below which the equilibrium is unstable. For non-zero rotor momentum ($\hat{\mathbf{b}}_1$-axis spin only), the rotor momentum modifies the major-axis rule by providing a means to gyroscopically stabilize the equilibrium.

We succeeded in analyzing these simple spins analytically, but other possible equilibria are more complex. It is unlikely that simple analytic expressions are even possible for these other equilibria. However, we can start from the simple spin solutions and use numerical continuation to generate branches of equilibria.

Chapter 5

Bifurcations of Equilibria

This chapter includes results for some of the fundamental issues of this investigation: how do varying system parameters affect the system equilibria? These qualitative changes, or bifurcations, affect the number and type of equilibrium solutions. The primary tool used in answering these questions is numerical continuation, sometimes called Euler-Newton continuation. We first define terms and explain some of the concepts related to bifurcations and numerical continuation. The persistent zero eigenvalue in the system Jacobian, caused by the conserved angular momentum, precludes using numerical continuation on the full, fifth-order system of equations. As a result of this problem, the complete bifurcation analysis has two phases. First, we use third-order equations corresponding to equilibria in the $\hat{\mathbf{b}}_1$-$\hat{\mathbf{b}}_3$ plane, constrained by the conserved quantity. These equations generate bifurcation diagrams in state-parameter space for a subset of all possible equilibria. Later, the fourth-order equations in spherical coordinates, described in Ch. 3, are used to apply numerical continuation to the full state-parameter space. The continuation software AUTO[22] is used to perform the numerical continuation results of this chapter. We use damper location and rotor momentum as bifurcation parameters to examine the effects of damper parameters, rotor momentum, and inertia properties on system equilibria.

5.1 Numerical Continuation Concepts

A bifurcation indicates a qualitative change in the system dynamics as one or more control parameters are varied. Bifurcations are often classified as continuous or discontinuous, depending on whether states of the system behave continuously or discontinuously as the control, or bifurcation, parameter is changed. Furthermore, a bifurcation that requires at least m different bifurcation parameters to occur is called a *codimension-m bifurcation.*

The goal is to numerically generate bifurcation branches, or paths of equilibrium points in state-parameter space, given an initial equilibrium state and bifurcation parameter. Continuation proceeds from the initial point in a predictor-corrector fashion, generating branches of equilibria while

also checking for bifurcation points. Specific tasks include predicting the next point, correcting the estimated point, controlling step size, detecting bifurcation or turning points, determining branch stability, and switching to new branches at bifurcation points. There are several techniques for each of these tasks, each with certain advantages and disadvantages. Seydel provides a complete description of these techniques in his excellent text.[62] We take a closer look at the method to better understand how numerical continuation is used to characterize the damped gyrostat equilibria.

We consider the system of nonlinear equations

$$\dot{\mathbf{z}} = \mathbf{f}(\mathbf{z}, \alpha) \tag{5.1}$$

representing the equations of motion in terms of the n-dimensional state vector, $\mathbf{z}$, and the bifurcation parameter, α. The equilibrium state is found by solving the nonlinear algebraic equations

$$\mathbf{0} = \mathbf{f}(\mathbf{z}, \alpha) \tag{5.2}$$

for a given α. Equilibrium states, or fixed points, are defined as *hyperbolic* if all the Jacobian's eigenvalues have non-zero real parts. Consider the collection of equilibrium points in state-parameter space when the bifurcation parameter is slowly varied. Suppose that as this parameter is varied, a fixed point becomes non-hyperbolic, also called degenerate. If the branches of equilibria in state-parameter space are qualitatively different after this point, the location is called a bifurcation point. The degeneracy of bifurcation points is detected by a singularity, or zero eigenvalue, in the system Jacobian matrix. However, not all singularities indicate the start of new branches.

Given an initial equilibrium state, the path in $\mathbf{z}$-α space of nearby equilibria is uniquely determined, for a full rank system, via the implicit function theorem.[62] A tangent predictor for a neighboring point on this bifurcation branch may be found by differentiating both sides of Eq. 5.2, yielding a Newton step

$$\mathbf{0} = d\mathbf{f} = \mathbf{A}d\mathbf{z} + \mathbf{f}_\alpha d\alpha \tag{5.3}$$

and therefore

$$\frac{d\mathbf{z}}{d\alpha} = -\mathbf{A}^{-1}\mathbf{f}_\alpha \tag{5.4}$$

where $\mathbf{A}$ is the Jacobian and $\mathbf{f}_\alpha$ is the vector of partial derivatives with respect to α. Examining Eq. 5.4, it is clear that for continuation to work as planned the Jacobian must be invertible. Normally, a singular Jacobian indicates either a turning point or bifurcation point. A turning point occurs when the branch experiences a locally infinite slope, where an element of the Jacobian becomes singular. If $\mathbf{f}_\alpha$ does *not* lie in the range space of $\mathbf{A}$, then a change of variable allows continuation around the turning point and the branch may continue. However, if $\mathbf{f}_\alpha$ *does* lie in the range space of $\mathbf{A}$, the singularity can not be eliminated and multiple solutions exist at this bifurcation point, indicating the start of new branches.

Seydel[62] provides the following formal definitions for bifurcation and turning points of a continuous, autonomous system:

Definition 5.1 $(\mathbf{z}_o, \alpha_o)$ *is a* ***simple stationary bifurcation point*** *if the following four conditions hold:*

1. $\mathbf{f}(\mathbf{z}_o, \alpha_o) = \mathbf{0}$
2. *rank* $\mathbf{A}(\mathbf{z}_o, \alpha_o) = n - 1$
3. $\mathbf{f}_\alpha(\mathbf{z}_o, \alpha_o) \in range\ \mathbf{A}(\mathbf{z}_o, \alpha_o)$
4. *exactly two branches of stationary solutions intersect with two distinct tangents*

A simple bifurcation refers to one with a single zero eigenvalue, and therefore a Jacobian rank of $n - 1$. The formal definition for a turning point is:

Definition 5.2 $(\mathbf{z}_o, \alpha_o)$ *is a* ***turning point*** *of stationary solutions if the following four conditions hold:*

1. $\mathbf{f}(\mathbf{z}_o, \alpha_o) = \mathbf{0}$
2. *rank* $\mathbf{A}(\mathbf{z}_o, \alpha_o) = n - 1$
3. *rank* $[\mathbf{A}(\mathbf{z}_o, \alpha_o) \mid \mathbf{f}_\alpha(\mathbf{z}_o, \alpha_o)] = n$
4. *there is a parameterization* $\mathbf{z}(\sigma)$, $\alpha(\sigma)$ *with* $\mathbf{z}(\sigma_o) = \mathbf{z}_o$, $\alpha(\sigma_o) = \alpha_o$ *and* $d^2\alpha(\sigma_o)/d\sigma^2 \neq 0$

Condition 3 results from $\mathbf{f}_\alpha(\mathbf{z}_o, \alpha_o)$ and $\mathbf{A}(\mathbf{z}_o, \alpha_o)$ spanning n-space. Condition 4 formalizes the idea that an alternate local parameterization exists which allows continuation around turning points.

The continuation software AUTO[22] uses an arclength parameterization rather than a bifurcation parameter-based approach for continuation. The equations are parameterized by arc length, s, including the bifurcation parameter itself, $\alpha = \alpha(s)$. The primary advantage of this approach is that it avoids singularities at turning points.

Figure 5.1 illustrates an example bifurcation diagram. Point A is a bifurcation point; specifically it is a pitchfork bifurcation. Points B and C are turning points. Bifurcation diagrams illustrate the change of some scalar measure of the state $\mathbf{z}$ as a function of the bifurcation parameter. For systems with larger dimensional states, there are many different possible scalar measures. The simplest and often most enlightening scalar measure is to use one of the state variables, although this creates n different diagrams. Functions of the states, such as the total energy or system Hamiltonian could be used as scalar measures for bifurcation diagrams.[29,30] The challenge is to select the proper scalar measure which best illustrates the bifurcation phenomena and the resulting branches of equilibria.

A bifurcation, such as a pitchfork bifurcation, may occur for a system of algebraic equations, but any model is subject to small errors or perturbations. To examine the effect of these model perturbations we consider the following scalar example. A scalar equation exhibiting a pitchfork bifurcation is

$$0 = y^3 + \alpha y \tag{5.5}$$

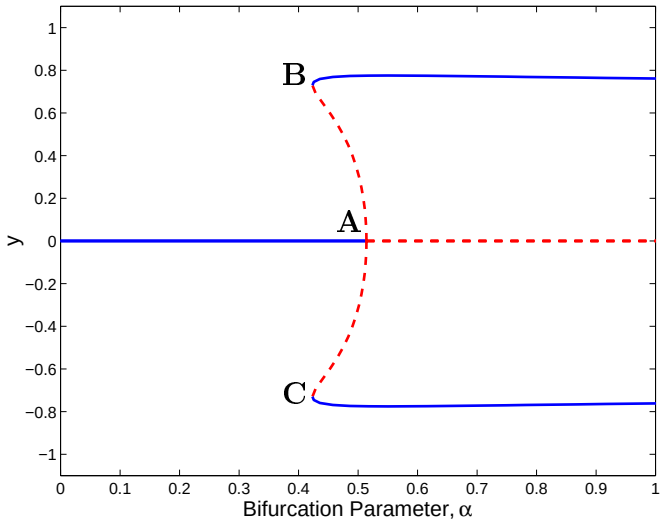

Figure 5.1: Example bifurcation diagram

We perturb the equation by adding a single perturbation parameter, φ:

$$0 = y^3 + \alpha y + \varphi \tag{5.6}$$

Applying numerical continuation to Eq. 5.6 yields significantly different results for $\varphi = 0$ and $\varphi \neq 0$, illustrated in Fig. 5.2. In Fig. 5.2(a), the pitchfork is unperturbed. In the perturbed case, the bifurcation is destroyed, producing two branches of equilibria: one with a turning point and a separate continuous branch. This *unfolding* of the pitchfork bifurcation is illustrated in Fig. 5.2(b). Refs. 62 and 28 include more detailed examinations of bifurcation theory and unfolding.

Since our system model is based on simplifying assumptions, relaxing these assumptions may introduce perturbations that break, or unfold, bifurcations of equilibira. We examine several possible perturbations in Ch. 7. Unfolding is also used to interpret the equilibria of several special cases, such as $b = 0$ and $h_a = 0$. The equilibria for $b \neq 0$ and $h_a \neq 0$ are perturbations of the special cases, and we examine the unfolding of certain bifurcations later in this chapter.

5.2 Characterizing Global Bifurcations of Equilibria

In this section we examine in detail the bifurcations which occur for system equilibria as a bifurcation parameter is varied. Bifurcations for the different system states are considered as well as the equilibria characterized by the angular momentum vector.

We apply numerical continuation to the full-system equations. These equations are reduced to 4th order by converting angular momentum to spherical coordinates. As the damper location, b, and spring stiffness, k, are normally fixed parameters for a given spacecraft, the most meaningful

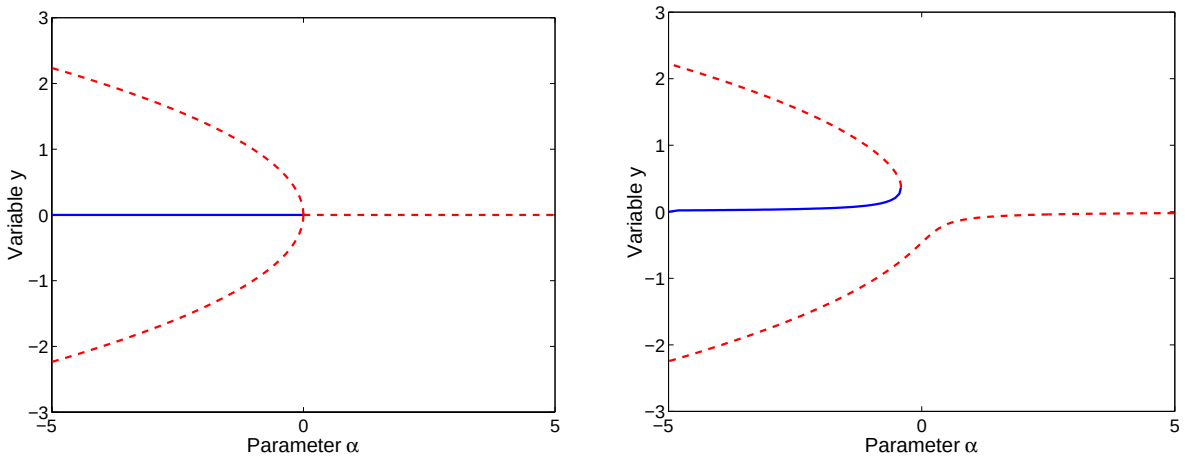

(a) Pitchfork bifurcation

(b) Perturbed pitchfork

Figure 5.2: Unfolding of a pitchfork bifurcation. The symmetric pitchfork is destroyed by a small perturbation, resulting in two separate branches.

bifurcation parameter is the rotor momentum, h_a. We select h_a as the initial bifurcation parameter, but in the next section we also use damper position as the bifurcation parameter.

The existence of different types of equilibria is illustrated by the numerical continuation results. For relatively simple cases like the simple spins of Ch. 4 we have analytical solutions for the equilibrium points and stability conditions. For the more complex equilibria, found numerically by continuation, the stability of equilibrium branches is determined numerically.

5.2.1 Equilibria on the Momentum Sphere

For zero external torques, the magnitude of $\mathbf{h}$ is constant. All possible $\mathbf{h}$ lie on a sphere in the three-dimensional space of momentum components, (h_1, h_2, h_3). This momentum sphere has radius $h = |\mathbf{h}|$. For the non-dimensionalization described in Ch. 3, $h = 1$. The momentum sphere is useful for describing different states of a torque-free system. System dynamics can be represented as trajectories of h on the momentum sphere. Individual equilibrium states are single points on the momentum sphere, but a set of equilibria for varying system parameters may appear on the sphere as lines, or branches, of equilibria.

We use numerical continuation with the parameters of Table 5.1 to produce multiple branches of equilibria for varying h_a, illustrated in terms of h_1, h_2, and h_3 in Fig. 5.3. Each point on these branches represents an equilibrium state in terms of the angular momentum components. These components define the direction of the angular momentum vector for different equilibria. It is useful to note that for equilibrium, Eq. 3.68 requires that the angular momentum vector and the angular velocity vector be aligned. Therefore, the location of equilibria on the momentum sphere also

Table 5.1: System parameters for first example of gyrostat equilibria

Inertia Properties	Damper Parameters
$I_1 = 0.40$	$k = 0.40$
$I_2 = 0.28$	$b = 0.33$
$I_3 = 0.32$	$\varepsilon = 0.10$
$I_s = 0.04$	$c = 0.10$

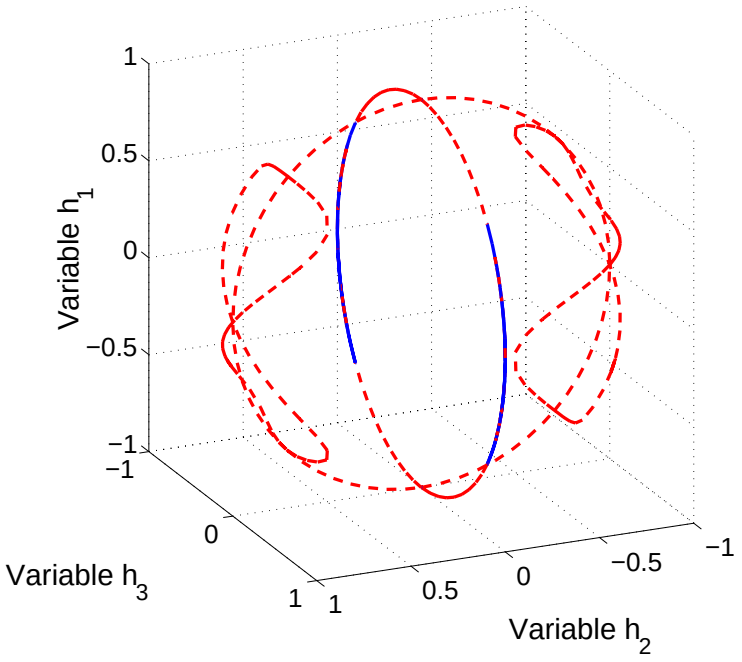

Figure 5.3: Equilibria in h_1-h_2-h_3 space

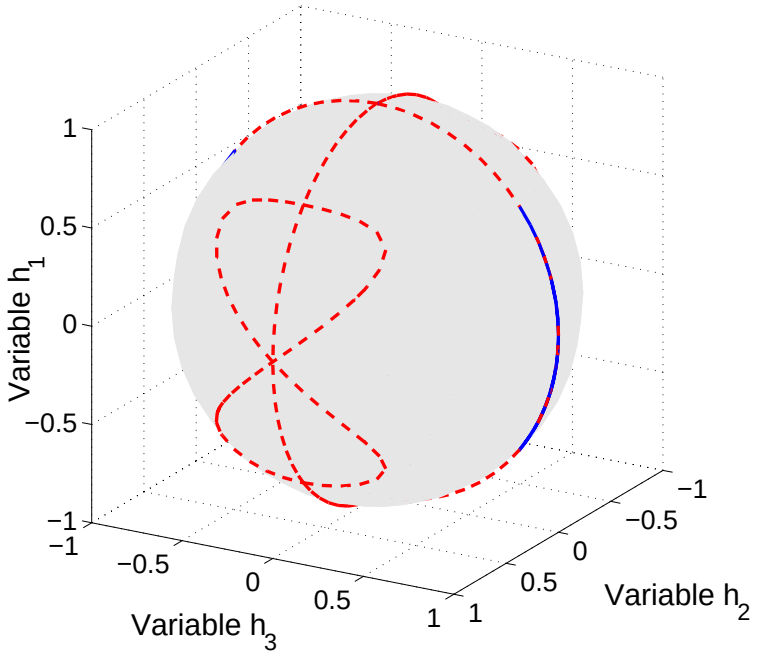

Figure 5.4: Equilibria on the momentum sphere

indicates the direction of the steady spin. From the natural symmetry of the model about the $\hat{\mathbf{b}}_1$-$\hat{\mathbf{b}}_2$ plane, this perspective is enhanced by showing these equilibria on the momentum sphere, shown in Fig. 5.4, where the center of the sphere is at the origin of the body-fixed coordinate system. Although the momentum sphere graphically provides a useful global perspective of the possible equilibria, this view does not show how h_a varies along the equilibrium branches. The momentum sphere representation is not a true bifurcation diagram in that we lose the correlation with the bifurcation parameter. Another shortcoming of this perspective is that the behavior of the damper particle is not discernible. To provide the most complete information, the momentum sphere view of the equilibria is supplemented with a series of 2-dimensional bifurcation diagrams, each using an individual state as the scalar measure. Before these bifurcations diagrams are presented, we first examine the different types of equilibria apparent from Fig. 5.4.

5.2.2 Types of Equilibria

There are several different types of equilibria which occur for varying h_a. The different types are defined below and identified on Fig. 5.5. We use a simple model of the nominal configuration to illustrate these equilibria. The model is shown in Fig. 5.6, defining the body axes, rotor spin axis, damper motion direction, damper displacement and damper location. Six different types of equilibrium states are defined using this system model; each type is illustrated in Figs. 5.7– 5.14.

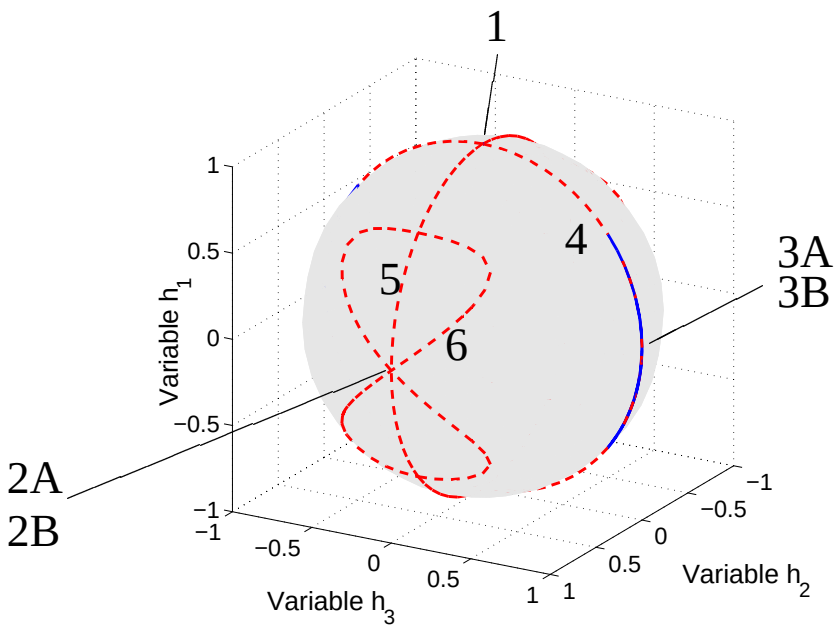

Figure 5.5: Identifying types of equilibria on the momentum sphere

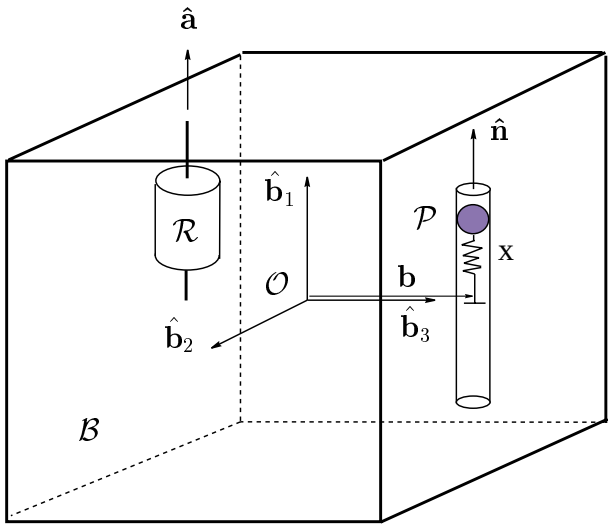

Figure 5.6: Defining axes and parameters of gyrostat with damper

Equilibrium Type 1

Nominal, $\hat{\mathbf{b}}_1$-Axis Spin

$\mathbf{h} = [1, 0, 0]$

$p_n = 0$

$x = 0$

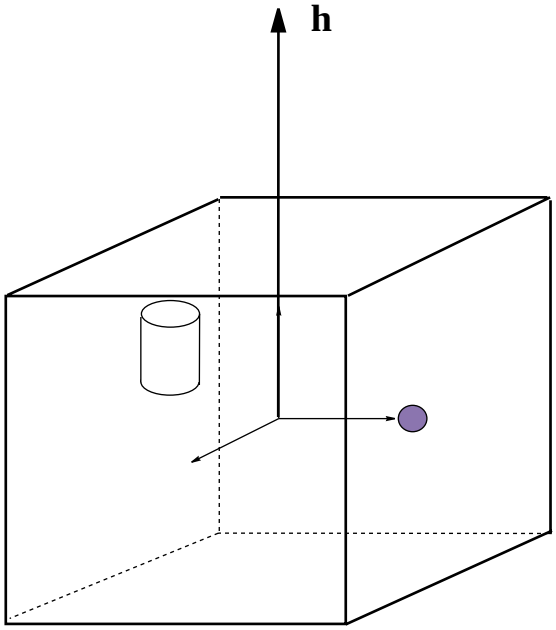

Figure 5.7: Equilibrium Type 1

Equilibrium Type 2A

$\hat{\mathbf{b}}_2$-Axis Spin

$\mathbf{h} = [0, 1, 0]$

$p_n \neq 0$

$x = 0$

$h_a = 0$

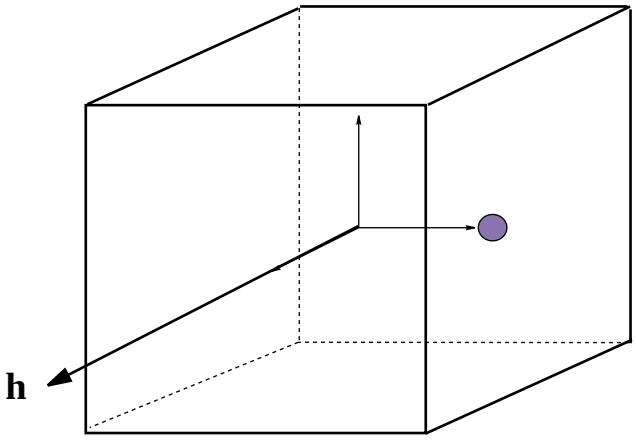

Figure 5.8: Equilibrium Type 2A

Equilibrium Type 2B

$\hat{\mathbf{b}}_2$-Axis Spin

$\mathbf{h} = [0, 1, 0]$

$p_n \neq 0$

$x \neq 0$

$h_a = 0$

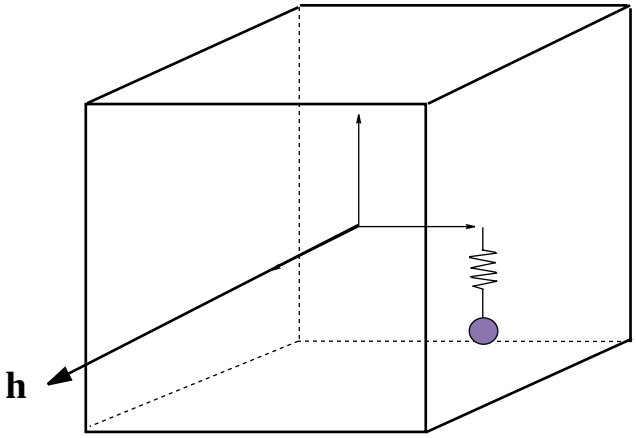

Figure 5.9: Equilibrium Type 2B

Equilibrium Type 3A

$\hat{\mathbf{b}}_3$-Axis Spin

$\mathbf{h} = [0, 0, 1]$

$p_n = 0$

$x = 0$

$h_a = 0$

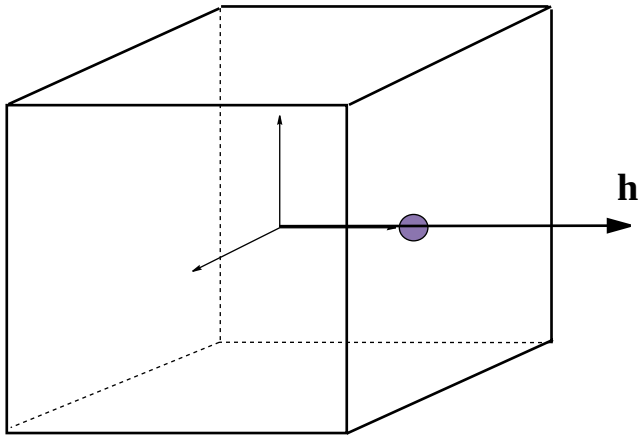

Figure 5.10: Equilibrium Type 3A

Equilibrium Type 3B

$\hat{\mathbf{b}}_3$-Axis Spin

$\mathbf{h} = [0, 0, 1]$

$p_n = 0$

$x \neq 0$

$h_a \neq 0$

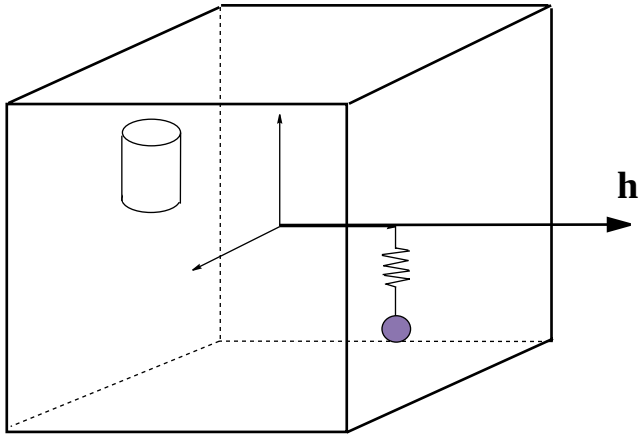

Figure 5.11: Equilibrium Type 3B

Equilibrium Type 4

Spin Axis in $\hat{\mathbf{b}}_1$-$\hat{\mathbf{b}}_3$ Plane

$\mathbf{h} = [h_1, 0, h_3]$

$p_n = 0$

$x \neq 0$

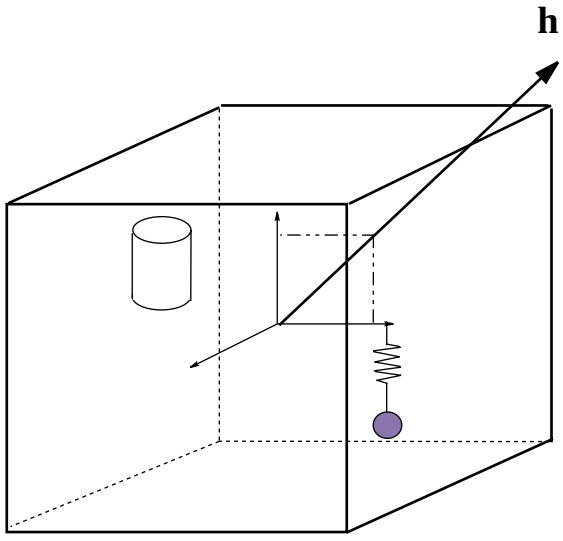

Figure 5.12: Equilibrium Type 4

Equilibrium Type 5

Spin Axis $\hat{\mathbf{b}}_1$-$\hat{\mathbf{b}}_2$ Plane

$\mathbf{h} = [h_1, h_2, 0]$

$p_n \neq 0$

$x = 0$

$h_a \neq 0$

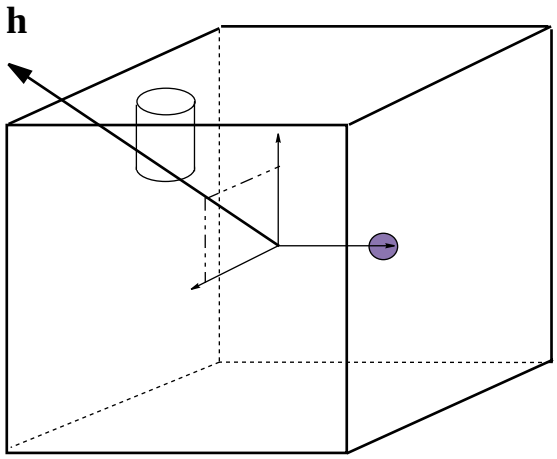

Figure 5.13: Equilibrium Type 5

Equilibrium Type 6

Off-Axis Spin

$\mathbf{h} = [h_1, h_2, h_3]$

$p_n \neq 0$

$x \neq 0$

$h_a \neq 0$

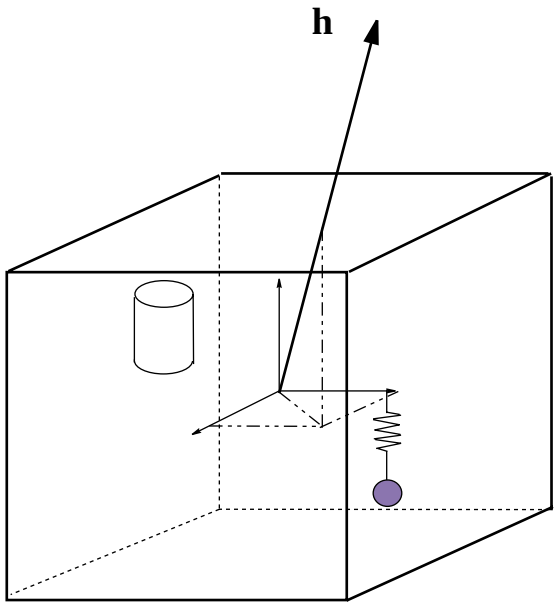

Figure 5.14: Equilibrium Type 6

The first three types of equilibria (Figs. 5.7–5.11) are the simple spins about the three body axes. Analytical equilibrium solutions and stability conditions were presented in Ch. 4. Nominal spin equilibria, Type 1, have $x = 0$, but may include $h_a \neq 0$. Spins about the $\hat{\mathbf{b}}_2$-axis are Type 2A and Type 2B, which require $h_a = 0$. For Type 2A, the damper is not displaced, but $x \neq 0$ for Type 2B. The Type 3A equilibrium has $x = h_a = 0$. Type 3B equilibria require $x \neq 0$ and $h_a \neq 0$.

The remaining branches of equilibria fall into one of three general types. Equilibrium Types 4-6 (Figs. 5.12–5.14) are not isolated states, but rather a collection of similar equilibria. Type 4 is the closed set of all equilibria with $\mathbf{h}$ in the $\hat{\mathbf{b}}_1$–$\hat{\mathbf{b}}_3$ plane, not including the simple spins. This type of equilibria is characterized by a non-zero damper displacement, $x \neq 0$, but $p_n = 0$. Examples of Type 4 equilibria exist for both $h_a = 0$, and $h_a \neq 0$. Equilibrium Type 5 is the closed set of all equilibria in the $\hat{\mathbf{b}}_1$–$\hat{\mathbf{b}}_2$ plane, not including the simple spins, and for which $x = 0$ and $p_n \neq 0$. Equilibrium Type 5 requires the rotor to gyroscopically stabilize the spin, so that for these branches $h_a \neq 0$. The final type of equilibrium, Type 6, is the closed set of equilibria with $\mathbf{h}$ not in either the $\hat{\mathbf{b}}_1$–$\hat{\mathbf{b}}_2$ or $\hat{\mathbf{b}}_1$–$\hat{\mathbf{b}}_3$ planes, not including Type 2B. These Type 6 equilibria are characterized in general by non-zero components for $\mathbf{z} = (h_1, h_2, h_3, p_n, x)$. Both the damper and rotor are required to stabilize these off-axis equilibria.

Most of the different equilibrium types are identifiable on the momentum sphere, but to completely distinguish them requires examination of the state-parameter bifurcation diagrams. Once their existence is established, the stability of these equilibria is considered.

5.2.3 Bifurcation Diagrams: A First Example

By numerically generating different equilibria for different values of h_a, we produce bifurcation diagrams that illustrate where multiple equilibria exist. Linear stability analysis is most often used to determine the stability of the branches between turning points and/or bifurcation points. In some cases, pure imaginary eigenvalue pairs exist. To determine stability in these cases, we use a numerical version of the Liapunov analysis from Ch. 4. Unless otherwise noted, solid lines are branches of stable equilibria and dashed lines are branches of unstable equilibria. For this first look at bifurcations for this problem, we present bifurcation diagrams for each of the five states. In subsequent discussions, pertinent diagrams are presented in the main text while complete sets of diagrams are included in the appendices.

Using the data in Table 5.1, we produce h_a bifurcation diagrams, shown in Figs. 5.15–5.19. This parameter set describes a system with the nominal spin axis as the major axis. From the stability conditions derived in Ch. 4, Type 2 and 3 equilibria are unstable. Type 1, the nominal spin, may be stable or unstable depending on the value of h_a.

We first produce the h_1-h_a bifurcation diagram, shown in Fig. 5.15. The Type 1 branches are easily identified. Two bifurcation points exist: one branches into Type 5 equilibria and the second, defined by Eq. 4.9, clearly marks the beginning of a new branch as well as a stability change for the Type 1 equilibria. As seen in Fig. 5.4, all the Type 5 and Type 6 equilibria are unstable. For the

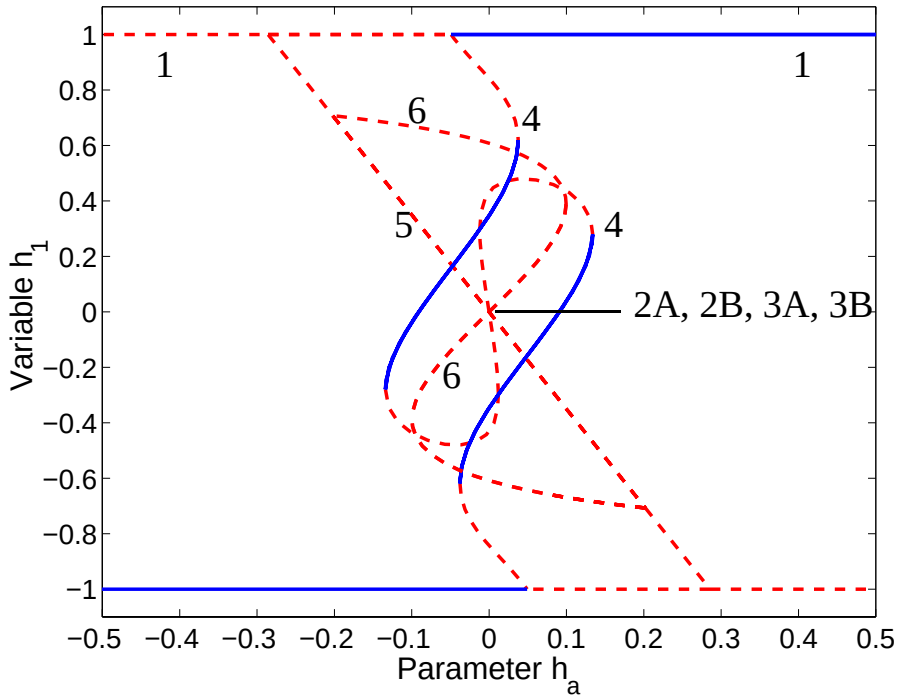

Figure 5.15: Bifurcation diagram: h_1 *vs.* h_a for $b = 0.33$, $k = 0.4$

first time, we see more detail for the equilibria in the $\hat{\mathbf{b}}_1$–$\hat{\mathbf{b}}_3$ plane. These Type 4 equilibria have both stable and unstable branches. This behavior will be more closely examined in Sec. 5.3. Since the rotor is aligned in the $\hat{\mathbf{b}}_1$ direction, varying h_a has significant effects on the possible equilibria. The natural symmetry of the problem creates symmetry throughout the bifurcation diagrams.

We next generate the h_2-h_a bifurcation diagram, shown in Figure 5.16. This perspective clearly displays the equilibria branching out of the $\hat{\mathbf{b}}_1$–$\hat{\mathbf{b}}_3$ plane. These Type 5 and Type 6 equilibria are all unstable for this combination of inertia properties and damper parameters. The $h_2 = 0$ axis is marked with a dash-dot line, indicating a mixture of stable and unstable equilibria from different equilibrium types. This situation occurs often, where there are many stability transitions taking place on a single, usually zero, axis. In these cases, a dash-dot line is used to signal a mixed stability situation. The precise stability changes are always more easily distinguished in alternate state-parameter bifurcation diagrams. This diagram also displays the inherent symmetry of the problem with respect to the $\hat{\mathbf{b}}_1$–$\hat{\mathbf{b}}_3$ plane. The branches of Type 5 and 6 equilibria exist in symmetric pairs.

The bifurcation diagram illustrating h_3 for varying h_a, Fig. 5.17, clearly shows the bifurcation points where new branches of equilibria emanate from the $\hat{\mathbf{b}}_1$–$\hat{\mathbf{b}}_2$ plane. Type 5 equilibria are co-located with Types 1 and 2 equilibria along the $h_3 = 0$ axis, obscuring in this view the bifurcation point marking the beginning of the Type 5 branches. The pitchfork bifurcations marking the start of

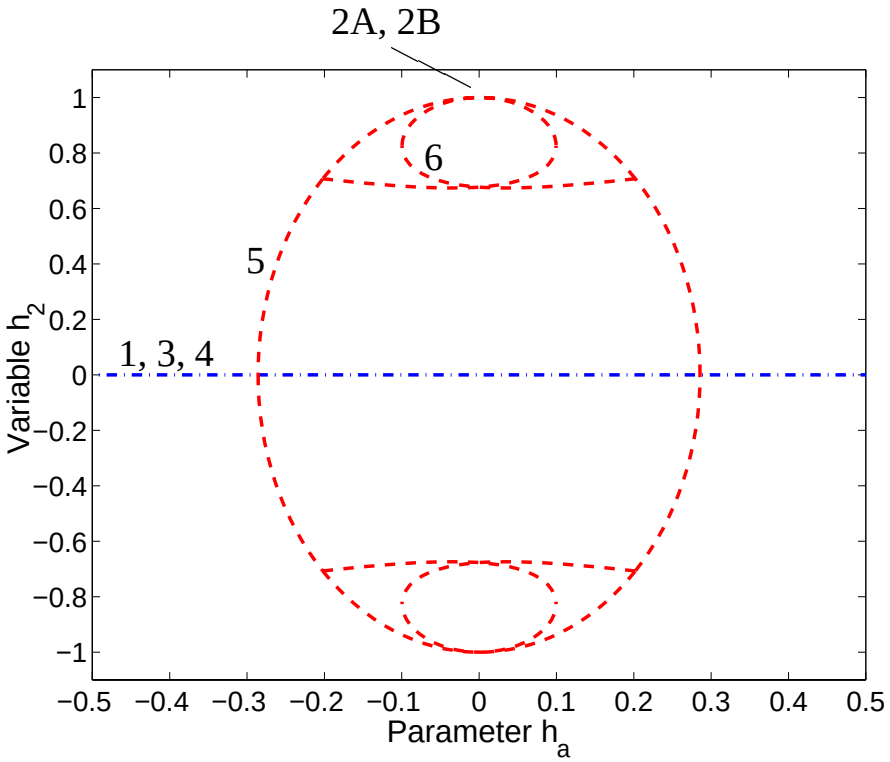

Figure 5.16: Bifurcation diagram: h_2 *vs.* h_a for $b = 0.33$, $k = 0.4$

Type 6 and Type 4 equilibrium branches are evident, creating in each case two separate branches. Referring back to Fig. 5.4, the Type 6 equilibria exist in two separate "figure eight" branches which in Fig. 5.17 appear intertwined. The Type 4 branches are distinguished by their h_3 sign. As with Fig. 5.15, the Type 4 equilibria in the $\hat{\mathbf{b}}_1$–$\hat{\mathbf{b}}_3$ plane show a mixture of branches and stability to be examined more closely in Sec. 5.3.

The bifurcation diagram for p_n, shown in Fig. 5.18, is similar to the h_2 diagram. Two sets of bifurcation points exist: where Type 5 branches originate from the $\hat{\mathbf{b}}_1$–$\hat{\mathbf{b}}_3$ plane and where Type 6 branches emanate from the Type 5 equilibria.

Figure 5.19 looks complex, but this x-h_a bifurcation diagram consists of primarily Type 4 and Type 6 equilibrium branches. These, along with Type 2B, are the only equilibria with non-zero damper displacement. Some of the same bifurcation points as seen in previous diagrams are evident. Symmetric pairs of equilibrium branches exist as in earlier diagrams. The simple $\hat{\mathbf{b}}_2$-axis spins are distinguished, one with zero damper displacement and one with the maximum damper displacement. On the momentum sphere these two points appear the same, but Figs. 5.18–5.19 clearly show these two equilibria differ in the damper variables. As predicted by the stability conditions in Ch. 4, both Type 2A and 2B equilibria are unstable for $I_2 < I_1$.

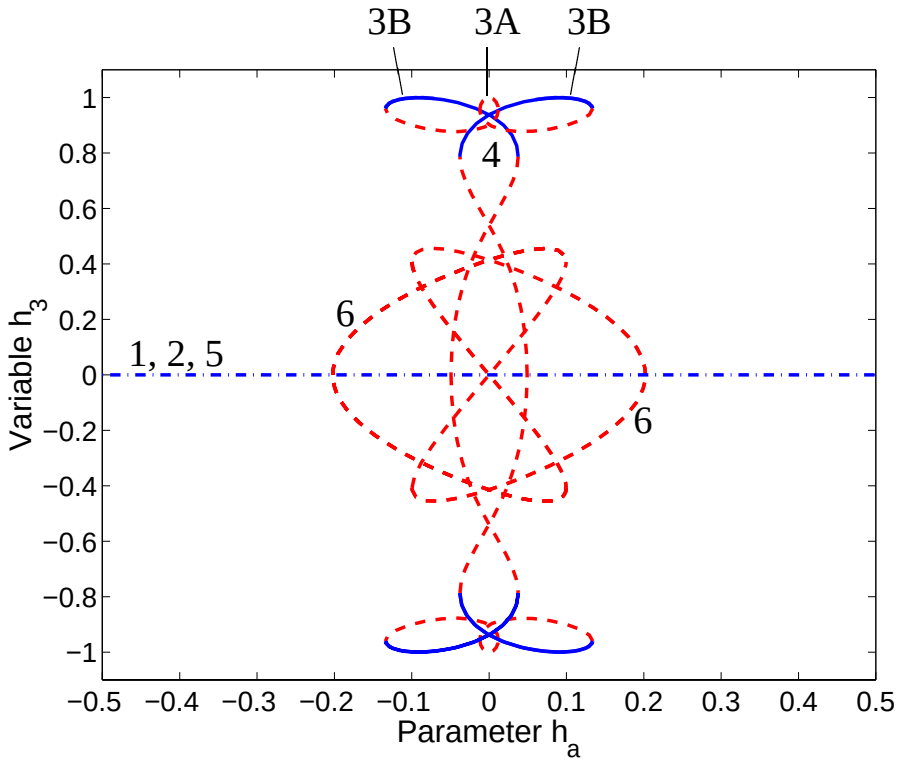

Figure 5.17: Bifurcation diagram: h_3 *vs.* h_a for $b = 0.33$, $k = 0.4$

5.2.4 Summary of Equilibria

We considered a major-axis gyrostat, as defined in Table 5.1, and found that distinct types of equilibria exist, but only a few are stable. The stable equilibria may be useful, like the nominal spin, or perhaps detrimental, as potential trap states. The nominal spin equilibrium (Type 1) is stable given sufficient rotor momentum. Some branches of Type 4 equilibria are also stable. Obviously, the effects of the damper parameters and system inertia properties must be examined. In the following section, the equilibria in the $\hat{\mathbf{b}}_1$–$\hat{\mathbf{b}}_3$ plane are considered more closely. The effects of the damper parameters and rotor momentum on the various equilibria are evaluated numerically. Subsequent sections consider the effects of damper parameters and inertia properties on equilibria in the full state space.

5.3 Bifurcations in the $\hat{\mathbf{b}}_1$ – $\hat{\mathbf{b}}_3$ Plane

We focus on the equilibria in the $\hat{\mathbf{b}}_1$– $\hat{\mathbf{b}}_3$ plane for the major-axis gyrostat defined by Table 5.1. The previous section demonstrates how numerical continuation is used to produce branches of equilibria. The method is dependent on detecting a singular Jacobian to identify singular points: turning points and bifurcation points. However, for a system with a conserved quantity, there

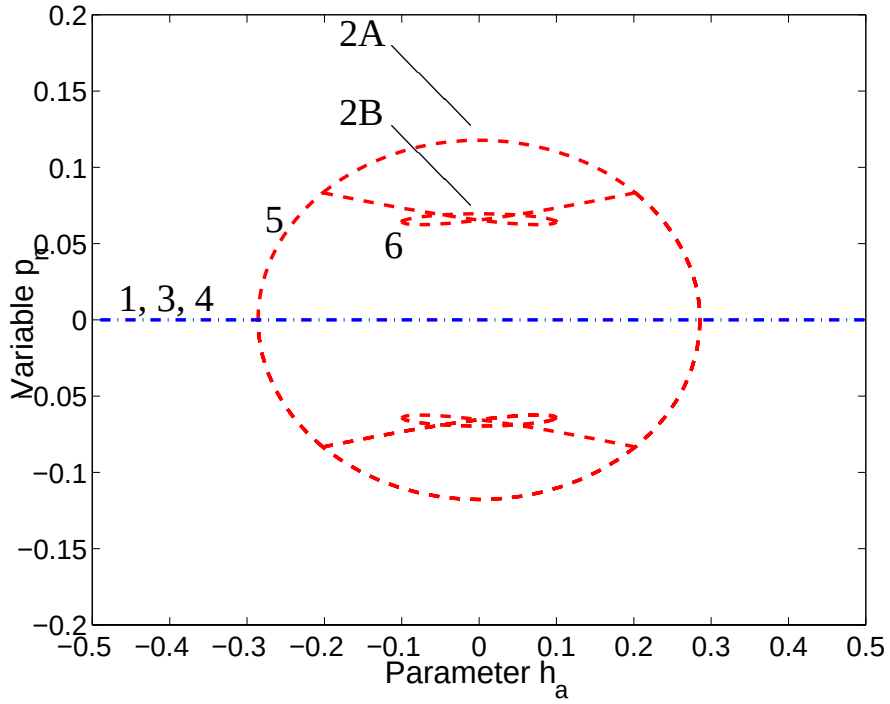

Figure 5.18: Bifurcation diagram: p_n *vs.* h_a for $b = 0.33$, $k = 0.4$

exists a zero eigenvalue at all points. Reducing the system to four first-order differential equations is possible using the spherical coordinate form of the equations described in Ch. 3. However, there is a singularity in the matrix that transforms the $\dot{\mathbf{h}}$ equations to $(\dot{h}, \dot{\theta}, \dot{\phi})$. We choose the spherical angles to control where the singularity occurs, and can effectively explore equilibria in the full state space. However, for the purpose of investigating the $\hat{\mathbf{b}}_1$– $\hat{\mathbf{b}}_3$ plane, an alternate reduction is used that allows numerical continuation in a three-dimensional state. As a result, a two-phase approach is used in examining the complete bifurcation topology. In the first phase, we focus on the equilibria in the $\hat{\mathbf{b}}_1$–$\hat{\mathbf{b}}_3$ plane. Subsequently, bifurcations in the remaining portion of state space are examined using the spherical coordinate equations.

Since the angular momentum must lie in the $\hat{\mathbf{b}}_1$– $\hat{\mathbf{b}}_3$ plane, this limits the possible equilibria to Types 1, 3 and 4. Chinnery and Hall reduced the equations for the similar $\mathcal{B} + \mathcal{P}$ problem by noting that $h_2 = 0$ requires $p_n = 0$ at equilibrium.[17] These conditions are also true for the $\mathcal{B} + \mathcal{R} + \mathcal{P}$ model. Substituting these conditions into the full equations reduces the system to two equations with three variables. The first integral due to conservation of angular momentum, $\mathbf{h}^{\mathrm{T}}\mathbf{h} = 1$, is added to the system of equations. This results in three equations in the reduced state space, h_1, h_3 and x, for which the Jacobian is only singular at turning points or bifurcation points:

$$-b\varepsilon x(h_1\lambda - h_3^2) + h_3\lambda(I_3 + \varepsilon\varepsilon' x^2) - h_1 h_3 I_1' = 0 \tag{5.7}$$

$$\varepsilon[h_3 I_1' + b\varepsilon x\lambda] \cdot [h_3 x(\varepsilon' I_1' - b^2\varepsilon) - I_3 b\lambda] - D^2 kx = 0 \tag{5.8}$$

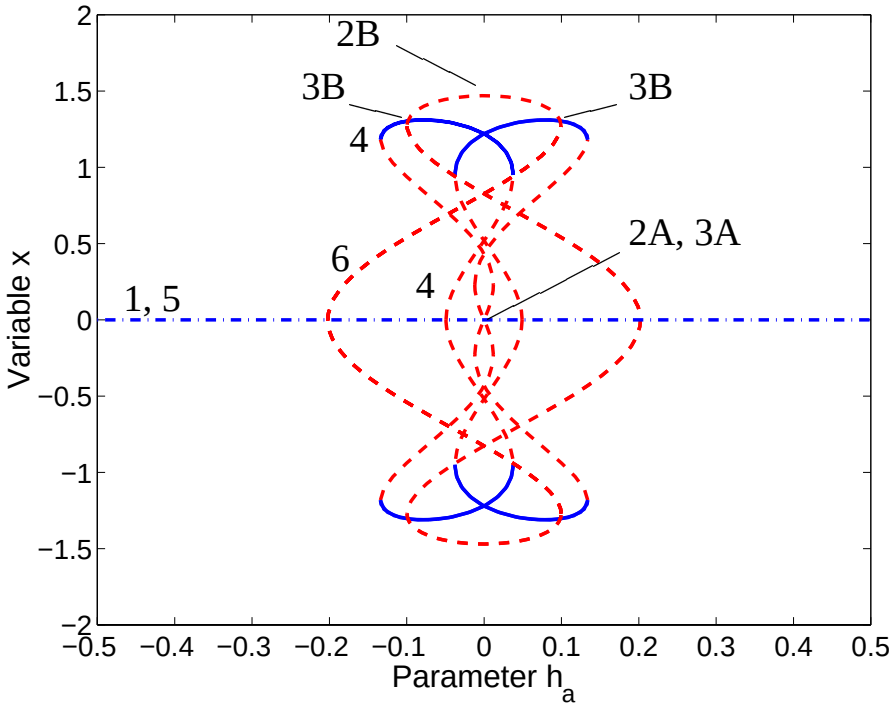

Figure 5.19: Bifurcation diagram: x *vs.* h_a for $b = 0.33$, $k = 0.4$

$$1 - h_1^2 - h_3^2 = 0 \tag{5.9}$$

where

$$\begin{aligned} D &= I_1'(I_3 + \varepsilon\varepsilon' x^2) - (b\varepsilon x)^2 \\ I_1' &= I_1 - I_s \\ \lambda &= h_a - 1 \end{aligned}$$

Applying numerical continuation to these equations we find branches of equilibria in the $\hat{\mathbf{b}}_1$– $\hat{\mathbf{b}}_3$ plane while varying system parameters. We first examine the bifurcations which occur for $h_a = 0$. As discussed in Ch. 3, the resulting equations are identical to those for the $\mathcal{B} + \mathcal{P}$ case.[17] Subsequently, we examine bifurcations for the complete $\mathcal{B} + \mathcal{R} + \mathcal{P}$ model.

5.3.1 Damper Location Bifurcations, Zero Rotor Momentum

For $h_a = 0$ the equations of motion are identical to those developed in Ref. 17 for $\mathcal{B} + \mathcal{P}$ with a similarly configured damper (see Sec. 3.6). Choosing b as the bifurcation parameter, AUTO is used with the 3rd-order equations to generate bifurcation diagrams for $h_a = 0$ and $k = 0.4$, as shown in Figures 5.20, 5.21 and 5.22. The $h_3 = 0$ and $h_1 = \pm 1$ branches correspond to Type 1 equilibria.

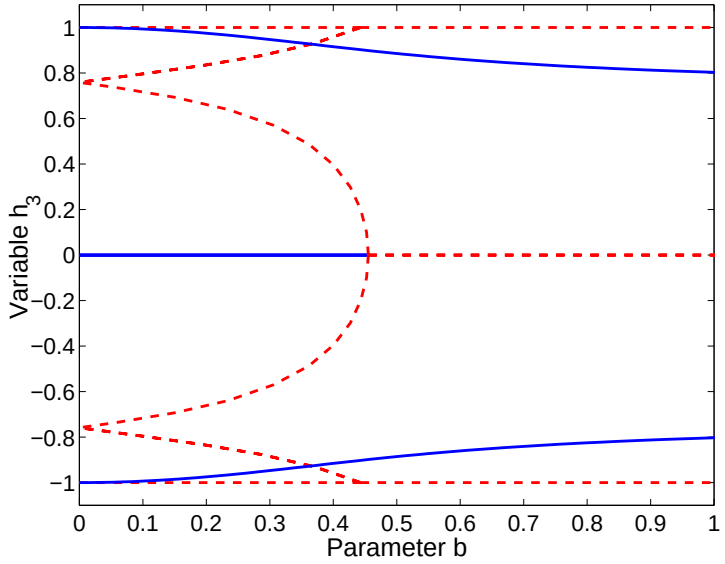

Figure 5.20: Bifurcation diagram: h_3 *vs.* b for $k = 0.4$, $h_a = 0$. A subcritical pitchfork bifurcation occurs, bifurcating Type 1 equilibria into Type 1 and Type 4 branches.

Similarly, the $h_1 = 0$ and $h_3 = \pm 1$ lines indicate Type 3A equilibria for different b values.

The stability of the Type 1 branches is defined by Eq. 4.9 which determines where an eigenvalue of the Jacobian crosses the imaginary axis. A zero eigenvalue of the Jacobian may also indicate a bifurcation point. For this spin about $\hat{\mathbf{b}}_1$, the stability changes at the bifurcation point. A stability change is the most common case, but other bifurcation points may exist without a stability change across the point. The subcritical pitchfork bifurcation in Fig. 5.21 is an example of the latter case. For any value of b, the spin about the $\hat{\mathbf{b}}_3$ (intermediate) axis is unstable. For both of these bifurcation points, the new branches are Type 4. Of considerable interest is the separate, stable branch of Type 4 equilibria. This branch corresponds to the stable Type 4 branches seen in h_a bifurcations. The bifurcation diagram for $h_a = 0$ and $k = 0.4$ is captured in three dimensions in Fig. 5.23. Figure 5.23 in the h_1–h_3 plane is simply a circle of radius $h = 1$. Conservation of angular momentum requires that all equilibrium solutions for $h_2 = 0$ lie on the h_1–h_3 unit circle. Figures 5.20, 5.21, and 5.23 seem to indicate possible new transcritical bifurcation points where pitchfork branches stemming from the $h_3 = \pm 1$ axis cross. In fact, when compared to Fig. 5.22 it is clear that these branches have different values of damper displacement, x, and therefore do not actually intersect in the full state space.

For different values of spring stiffness, k, the resulting bifurcation diagrams may include subcritical or supercritical pitchfork bifurcations. Figure 5.20, for $k = 0.4$, includes a subcritical pitchfork bifurcation. For larger values of spring stiffness the pitchfork becomes supercritical, as shown in Fig. 5.26 for $k = 0.7$. The transition to supercritical pitchforks is accompanied by a stability change for the Type 4 equilibrium branches emanating from the bifurcation point. Reference 17

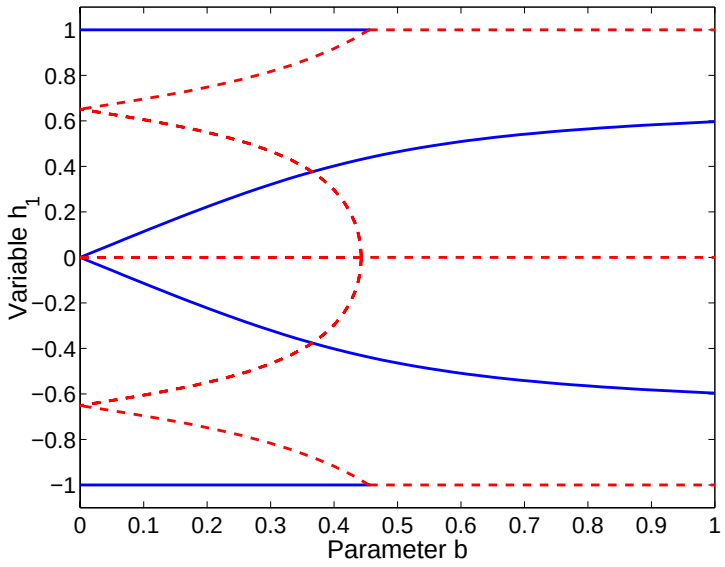

Figure 5.21: Bifurcation diagram: h_1 *vs.* b for $k = 0.4$, $h_a = 0$. A subcritical pitchfork bifurcation occurs, bifurcating Type 3A equilibria into Type 3A and Type 4. The Type 1 - 4 bifurcation points are visible along the $h_1 = \pm 1$ lines.

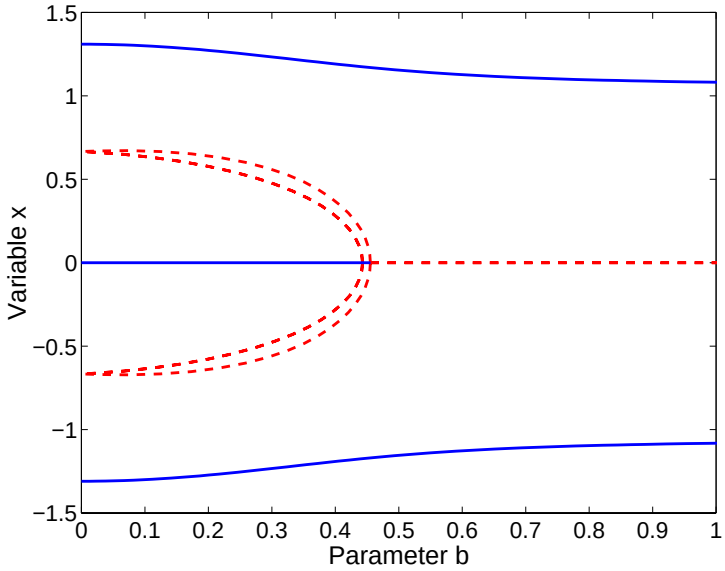

Figure 5.22: Bifurcation diagram: x *vs.* b for $k = 0.4$, $h_a = 0$. Both the Type 3A - 4 and Type 1 - 4 pitchfork bifurcation points are on the $x = 0$ axis.

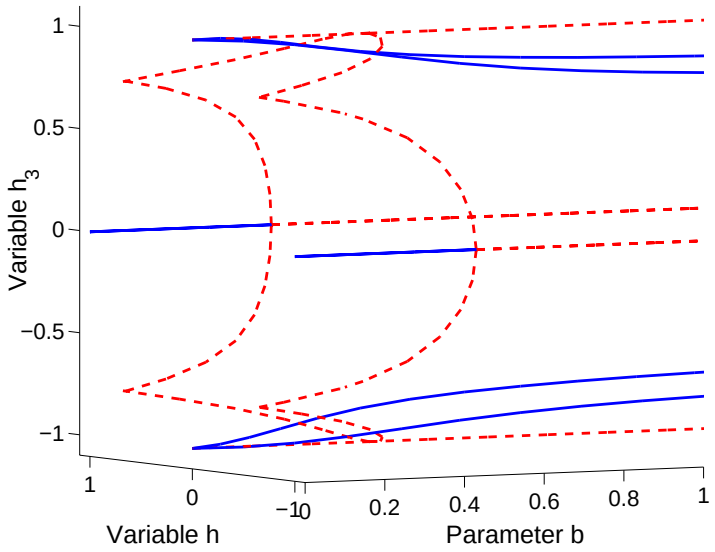

Figure 5.23: Bifurcation diagram in three dimensions: $k = 0.4$ and $h_a = 0$. The pitchfork bifurcations occur in sets of two points each.

did not include the pitchfork bifurcation which occurs for spins about the $\mathbf{b}_3$ axis. Figure 5.21 shows this pitchfork in the h_1–b plane.

A transcritical bifurcation also appears for a critical value of $k_{cr} = 0.50075$. This transcritical bifurcation is shown in Fig. 5.24. For larger values of spring stiffness, as shown in Fig. 5.25 for $k = 0.51$, the pitchfork has unstable Type 4 branches, but have turning points that produce stable Type 4 branches. If the system were to operate in parameter space on the stable nominal spin branch, but near the bifurcation point, a small increase in b causes the system to jump to the nearest stable equilibrium point. This discontinuity in stable equilibria is called a *jump phenomena*. In this case, the change to the stable Type 4 state would be a large jump. A more smooth transition occurs if the system has a higher spring stiffness, resulting in a supercritical pitchfork as in Fig. 5.26. Clearly, we want to have a sufficiently stiff spring to avoid the jump phenomenon.

For $h_a = 0$, simple spins about $\hat{\mathbf{b}}_3$ have zero damper displacement and, for this set of parameters, $\hat{\mathbf{b}}_3$ is not the major axis, so they are always unstable. The other stability condition for this equilibrium, Eq. 4.20, defines the critical point where an eigenvalue passes through the imaginary axis. This defines the relationship for the bifurcation point:

$$b = \sqrt{(I_3 - I_1')(kI_3^2 - \varepsilon\varepsilon')/\varepsilon^2} \tag{5.10}$$

This analytical expression locates the subcritical pitchfork bifurcation point. However, this point only exists for $h_a = 0$. Non-zero rotor momentum breaks the natural symmetry in the problem and the associated bifurcation structures.

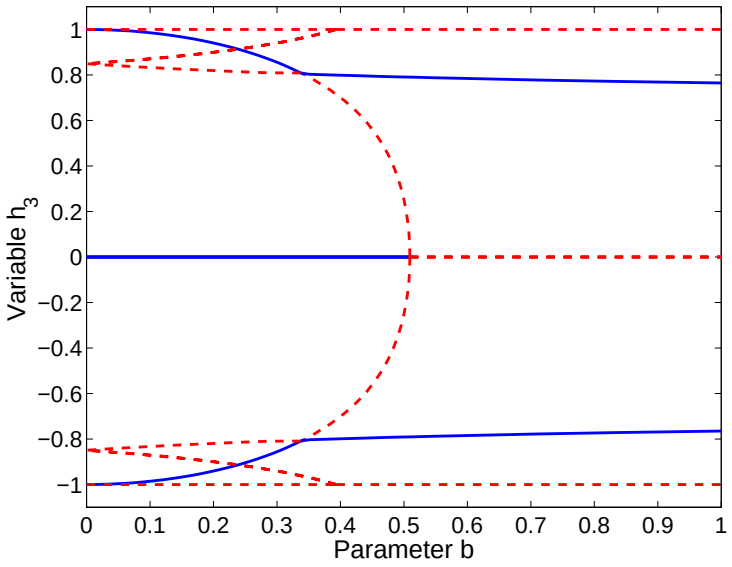

Figure 5.24: Bifurcation diagram: h_3 *vs.* b for $k = 0.50075$, $h_a = 0$. A transcritical bifurcation occurs for Type 4 equilibria.

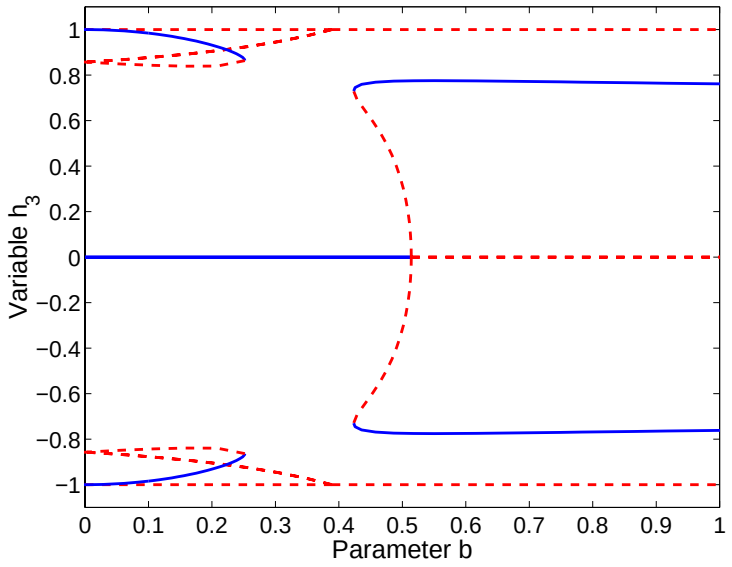

Figure 5.25: Bifurcation diagram: h_3 *vs.* b for $k = 0.51$, $h_a = 0$. For k greater than the transcritical value, there are separate branches of equilibria with turning points. The Type 1-4 pitchfork remains subcritical.

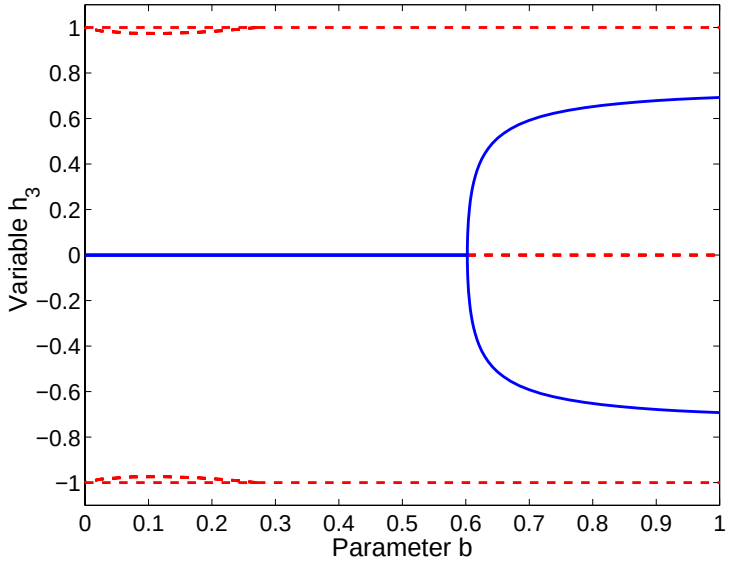

Figure 5.26: Bifurcation diagram: h_3 *vs.* b for $k = 0.7$, $h_a = 0$. For sufficiently large k, the separate Type 4 branch does not exist. The Type 1-4 pitchfork bifurcation is supercritical, with stable Type 4 branches.

The symmetry of the bifurcation results thus far is a product of the natural symmetry of the problem, discussed in Sec. 3.6. Symmetry in the $\hat{\mathbf{b}}_1$–$\hat{\mathbf{b}}_3$ plane is defined by the transformations in Eqs. 3.78 and 3.81. The only value of h_a that provides the symmetry of both Eqs. 3.78 and 3.81 is $h_a = 0$. For the $h_a = 0$ case, the equilibrium branches are the same for $\pm h_1$ and $\pm h_3$, although the damper displacement, x, also changes sign. By allowing the rotor momentum to vary, this symmetry is broken as are some of the bifurcation branch structures.

5.3.2 Rotor Momentum Bifurcations

We examine bifurcation diagrams with rotor momentum, h_a, as the bifurcation parameter. Unlike b or k, the rotor momentum is easily changed by applying a rotor torque. This inherent variability makes h_a an especially important parameter to study. The variable system parameters considered thus far include b, k, and h_a. To examine the possible bifurcations, we hold two parameters constant while the third takes the role of bifurcation parameter.

Effects of Varying Spring Stiffness on Rotor Momentum Bifurcations

Holding the damper location constant, we use numerical continuation to generate branches of equilibria for varying h_a and different values of spring stiffness, k. Figures 5.27– 5.28 show the

bifurcations for $k = 0.4$ and $b = 0.33$. This value for b coincides with the transcritical bifurcation. The equilibria branches remain symmetric in $\pm h_a$ with respect to h_3, as expected from physical ar-

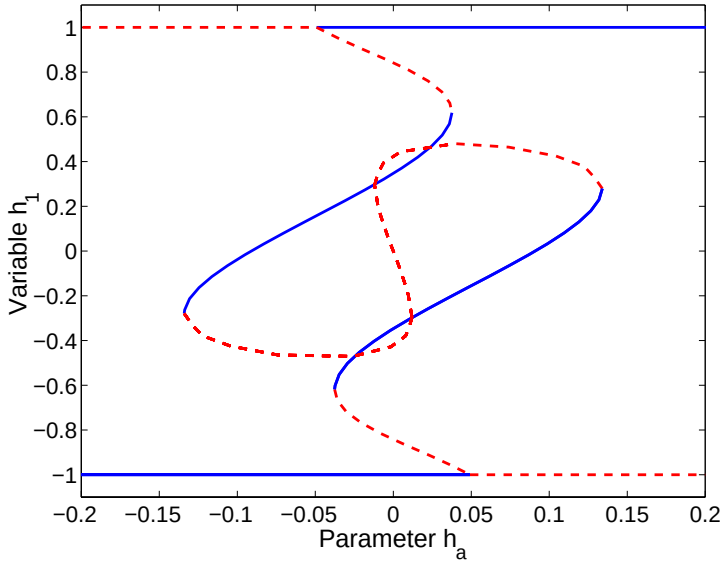

Figure 5.27: Bifurcation diagram: h_1 *vs.* h_a for $k = 0.4$, $b = 0.33$. A bifurcation point occurs on each nominal-spin equilibrium branch, $h_1 = \pm 1$. The remaining branches are Type 4.

guments as well as the symmetric transformations of Sec. 3.6. However, the number and character of equilibrium solutions change for different ranges of $\pm h_a$, as shown in Table 5.2.

Table 5.2: Number of equilibria for $k = 0.4$, $b = 0.33$

h_a	Equilibria	Stable Equilibria
0	16	6
± 0.025	12	4
± 0.04	10	3
± 0.1	6	3
± 0.15	2	1

The $h_3 = 0$ axis of Type 1 equilibria in Fig. 5.28 is stable for a region between the two bifurcation points, shown as a solid line. Recall that this axis corresponds to $h_1 = \pm 1$. For regions of $|h_a|$ greater than the magnitude of the bifurcation values, the axis is denoted by the dash-dot line. This line type indicates one stable and one unstable branch, more easily seen in Fig. 5.27. We use the dash-dot line to indicate mixed stability throughout this dissertation.

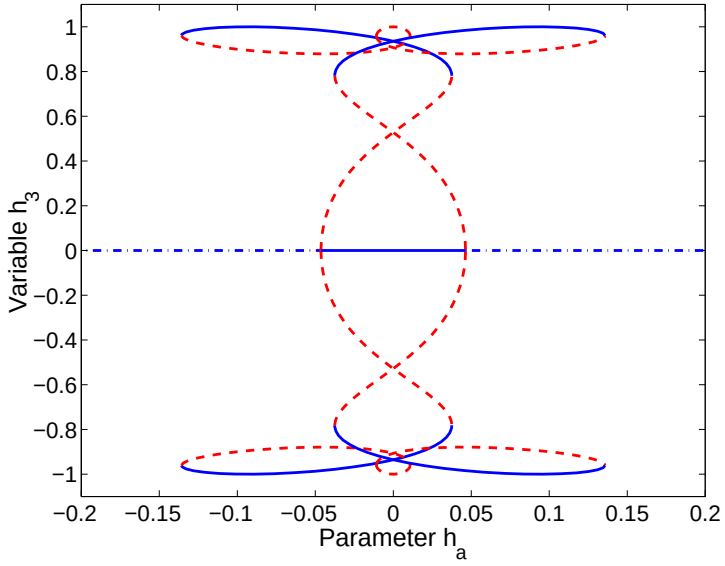

Figure 5.28: Bifurcation diagram: h_3 *vs.* h_a for $k = 0.4$, $b = 0.33$. Pitchfork bifurcations occur on the nominal spin-axis ($h_3 = 0$), creating Type 4 branches. The Type 4 equilibria are symmetric for $\pm ha$.

Changing the spring stiffness as with the h_3–b bifurcation diagrams, we find changes to the h_3–h_a diagrams. Figure 5.29 shows how the symmetric pitchfork bifurcations move further from the origin as k is increased. Also, two sets of limit points move in opposite directions and touch at $h_a = 0$. This corresponds to the transcritical bifurcation of Fig. 5.24. The number and character of equilibrium solutions for different ranges of h_a is shown in Table 5.3.

Table 5.3: Number of equilibria for $k = 0.50075$, $b = 0.33$

h_a	Equilibria	Stable Equilibria
0	10^*	4^*
± 0.004	12	4
± 0.03	10	3
± 0.08	6	3
± 0.15	2	1

*Includes two transcritical bifurcation points

Increasing the spring stiffness to $k = 0.7$ results in the bifurcation diagram shown in Fig. 5.30. The pitchfork bifurcation points move further from the origin. For systems with greater spring stiffness, more momentum may be stored in the rotor while retaining the stability of the nominal

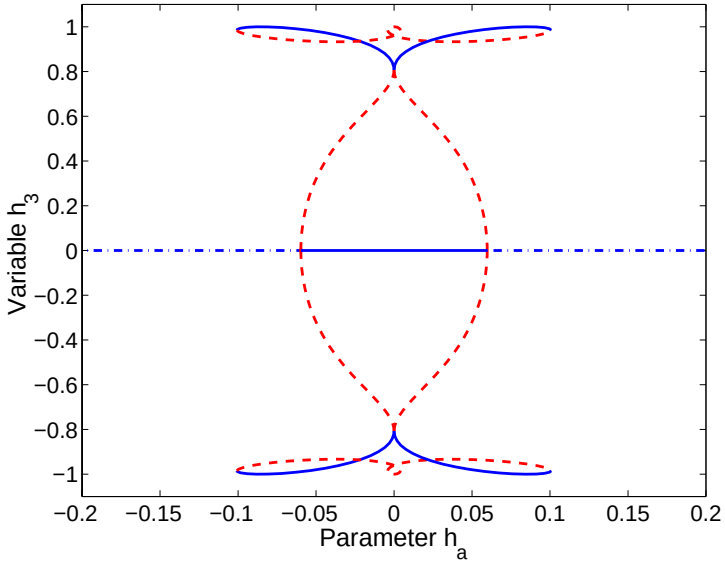

Figure 5.29: Bifurcation diagram: h_3 *vs.* h_a for $k = 0.50075$, $b = 0.33$. For this k, two Type 4 limits points coalesce into the transcritical bifurcation of Fig. 5.24.

spin (about $\mathbf{b}_1$). This plot is for a specific damper location, in this case $b = 0.33$. For this damper location, fewer equilibrium solutions are present for the larger spring stiffness (Table 5.4). As the spring stiffness is further increased, the nominal spin becomes the only stable spin for any value of h_a, shown in Table 5.5 . This steady spin is stable for an even larger range of h_a (Fig. 5.31).

Table 5.4: Number of equilibria for $k = 0.7$, $b = 0.33$

h_a	Equilibria	Stable Equilibria
0	4	1
± 0.05	8	3
± 0.065	4	1
± 0.1	2	1

The bifurcation diagrams for all these cases, including those for h_1 and x, are included in Appendix B.

Effects of Varying Damper Location on Rotor Momentum Bifurcations

For a constant spring stiffness, the bifurcations for varying rotor momentum are produced for different values of damper location, b. Unlike spring stiffness, the damper location of zero is phys-

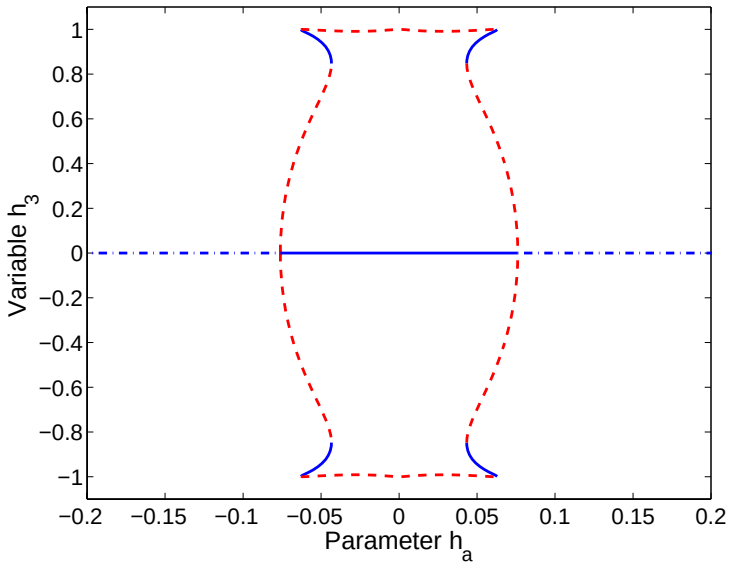

Figure 5.30: Bifurcation diagram: h_3 *vs.* h_a for $k = 0.7$, $b = 0.33$. Fewer stable Type 4 equilibria exist for this value of k.

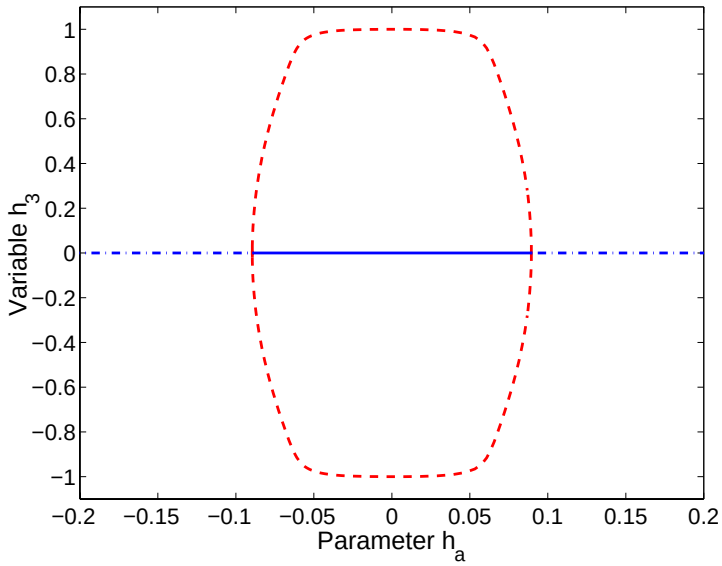

Figure 5.31: Bifurcation diagram: h_3 *vs.* h_a for $k = 1$, $b = 0.33$. The Type 4 branches do not have any turning points and are entirely unstable.

Table 5.5: Number of equilibria for $k = 1$, $b = 0.33$

h_a	Equilibria	Stable Equilibria
0	4	1
± 0.1	2	1

ically meaningful. Figure 5.32 is a bifurcation diagram for the $b = 0$, $k = 0.4$ case. The Jacobian for these equilibria includes, in addition to the zero eigenvalue associated with the conserved quantity, a pair of eigenvalues on the imaginary axis. Therefore, the Liapunov function of Ch. 4 is used to numerically determine the stability of the branches.

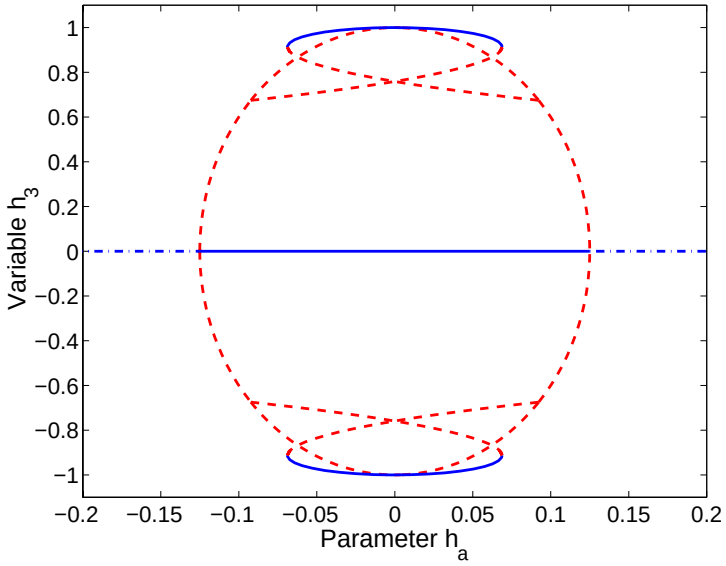

Figure 5.32: Bifurcation diagram: h_3 *vs.* h_a for $b = 0$, $k = 0.4$. In addition to the pitchfork bifurcations along the nominal-spin branch, there are bifurcations on the Type 4 branches. At $h_3 = \pm 1$ are the Type 3A and Type 3B equilibrium states. This is a special, organizing case that is perturbed by $b \neq 0$.

Allowing b to increase slightly, as in Fig. 5.33, perturbs the $b = 0$ bifurcation into new equilibrium branch structures. This is an example of the unfolding of a bifurcation structure by adding a new parameter. In this case, a non-zero b is the perturbation parameter which unfolds the $b = 0$ bifurcation. These bifurcations are actually codimension-2, requiring the original parameter h_a and the second parameter b. In this sense, all bifurcation diagrams for $h_a \neq 0$ and $b \neq 0$ are codimension-2. The bifurcation structure evolves as b increases, although the number of branches remains basically the same. Figures 5.34 and 5.28 show the changing h_3–h_a bifurcations. The pair of nominal spin pitchfork bifurcations, for $h_a = \pm 1$, occur for smaller rotor momentum magnitude

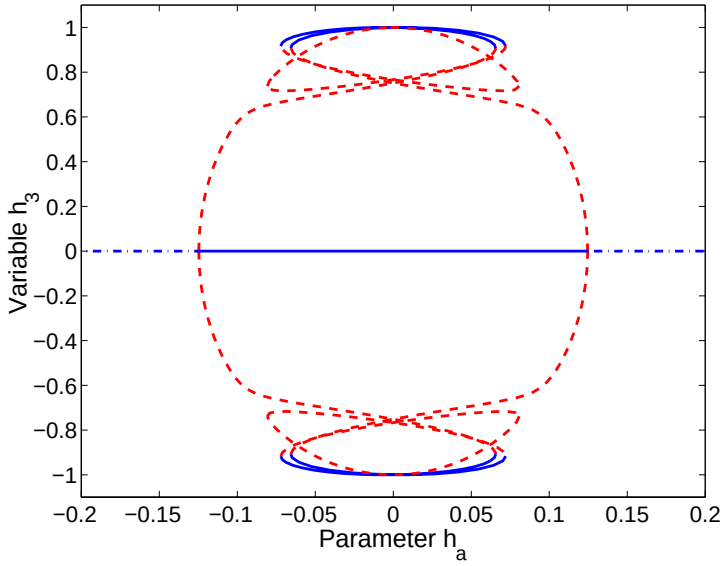

Figure 5.33: Bifurcation diagram: h_3 *vs.* h_a for $b = 0.02$, $k = 0.4$. A small b value perturbs the $b = 0$ bifurcations along the Type 4 branches into separate branches.

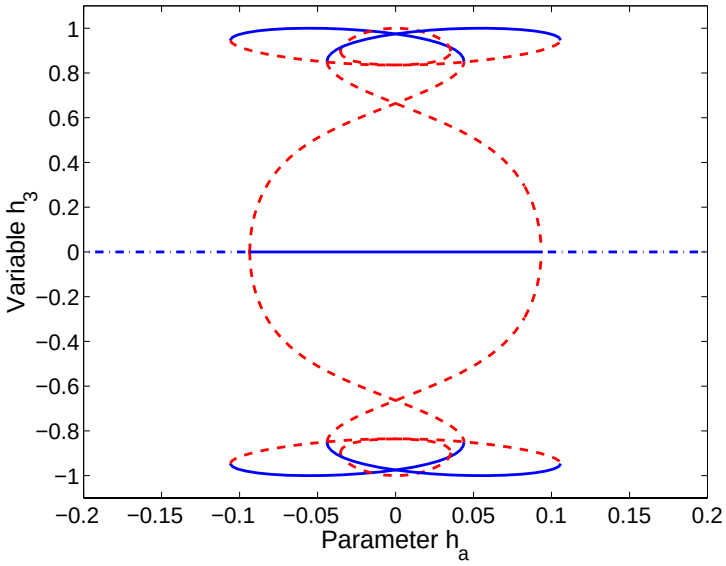

Figure 5.34: Bifurcation diagram: h_3 *vs.* h_a for $b = 0.2$, $k = 0.4$. For larger k, the stable Type 3B spins occur for larger $|h_a|$.

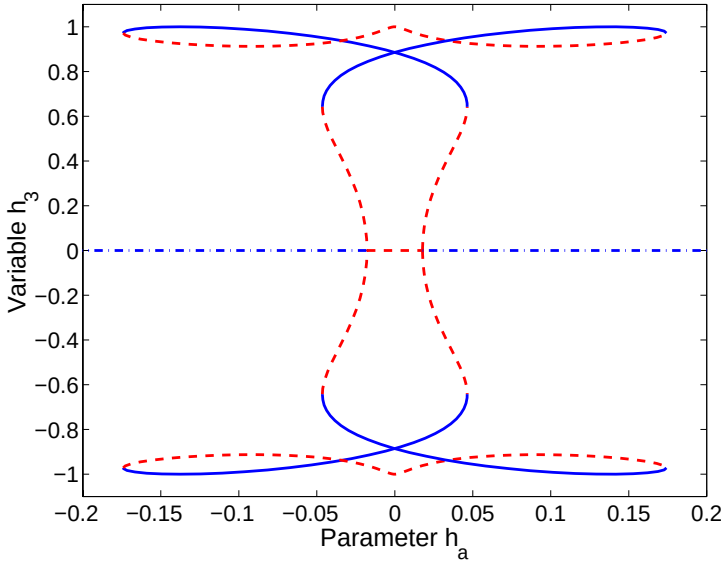

Figure 5.35: Bifurcation diagram: h_3 *vs.* h_a for $b = 0.5$, $k = 0.4$. For sufficiently large b, the stability changes due to Eq. 4.9, and the nominal spin is unstable for small h_a.

as b increases. As b passes the stability threshold defined in Eq. 4.9, the Type 1 equilibrium branches change their stability, as seen in Fig. 5.35.

The bifurcation diagrams for all these cases, including those for h_1 and x, are included in App. B.

5.3.3 Damper Location Bifurcations, Non-Zero Rotor Momentum

For $h_a \neq 0$, the h_1 symmetry is broken and the bifurcation diagram structures that are symmetric about the h_3–b plane for $h_a = 0$ are also broken. Figure 5.36 shows how a small perturbation from $h_a = 0$ breaks the pitchfork bifurcation of Fig. 5.21 into two separate branches, including a saddle node. This is another example of a bifurcation unfolding, with h_a acting as the perturbation parameter in this case. These are codimension-2 bifurcations, with b and h_a being the two parameters necessary for the existence of these bifurcations. While non-zero rotor momentum breaks the symmetry of the h_1–b bifurcations, it does not unfold the pitchforks seen in the h_3–b bifurcations. However, the Type 1 bifurcation points for $h_1 = \pm 1$ are affected.

The two subcritical pitchfork bifurcations for positive and negative $\mathbf{b}_3$ spins (Type 3A), which for $h_a = 0$ are identical and symmetric about the h_3–b plane, diverge for non-zero wheel momentum. For $h_a = 0.01$, Fig. 5.37 clearly illustrates this effect. The number of equilibrium branches which cross the $b = 1$ line agree with Table 5.2: 4 stable and 8 unstable equilibrium points.

As h_a increases further, the nature of the bifurcation diagram continues to change. Figures 5.36–5.39 show how the pitchfork bifurcation for positive $\mathbf{b}_1$ spins (the pitchfork to the right) transitions

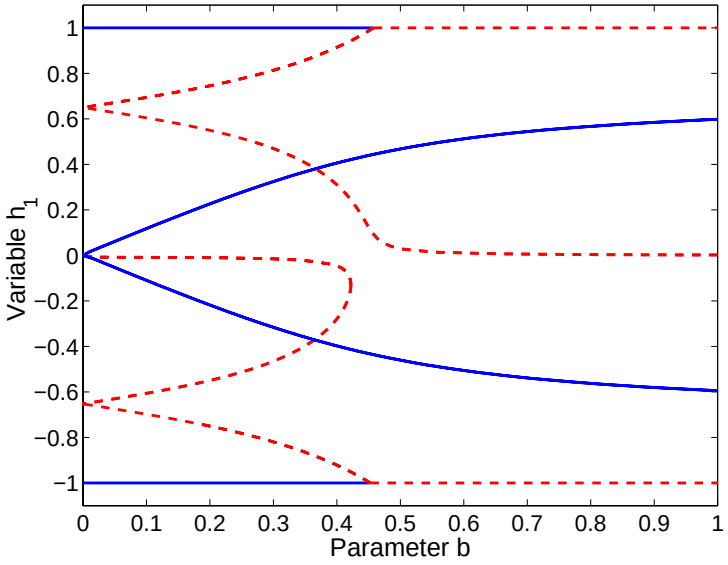

Figure 5.36: Bifurcation diagram: h_1 *vs.* b for $k = 0.4$, $h_a = 0.001$. Small h_a perturbs the Type 3A - 4 pitchfork bifurcations into two separate branches.

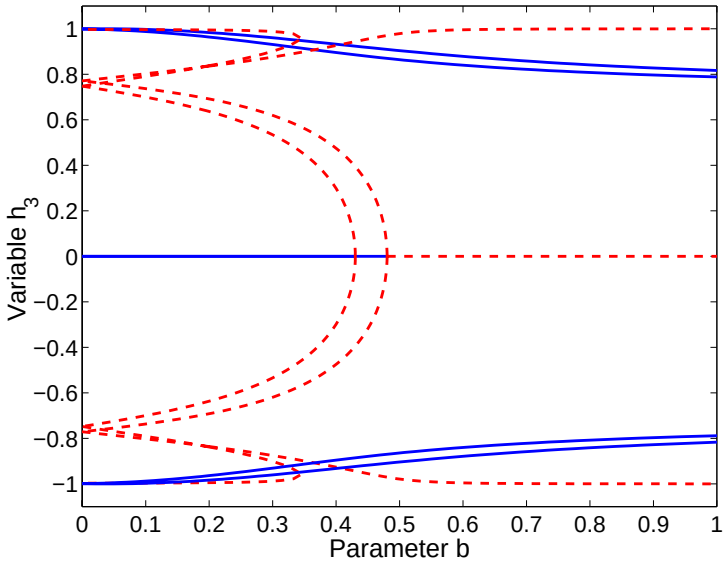

Figure 5.37: Bifurcation diagram: h_3 *vs.* b for $k = 0.4$, $h_a = 0.01$. For a larger h_a perturbation, the effects of unfolding the Type 3A - 4 pitchfork bifurcation are more evident. The Type 1 - 4 pitchforks are not broken by $h_a \neq 0$, but occur for different values of b.

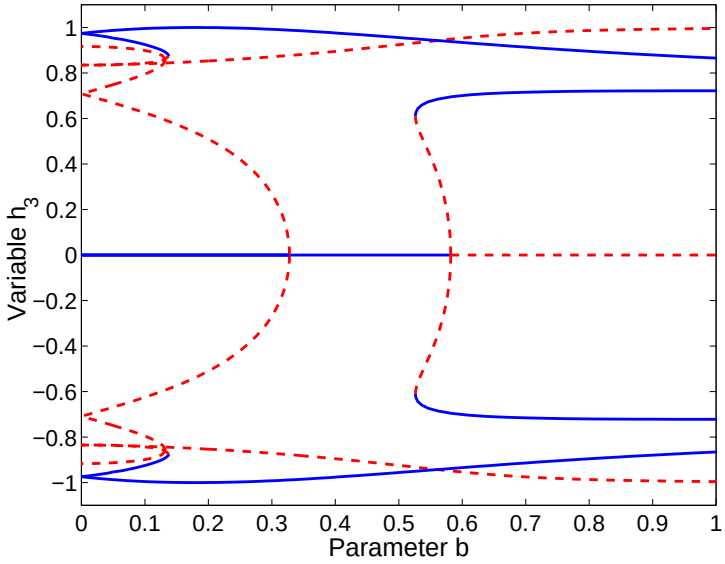

Figure 5.38: Bifurcation diagram: h_3 *vs.* b for $k = 0.4$, $h_a = 0.05$. For larger values of h_a, the branches with $h_1 > 0$ transition through the transcritical bifurcation point. The $h_1 < 0$ branches behave differently, as the Type 1 - 4 bifurcation occurs for lower b.

from a subcritical to a supercritical pitchfork as the bifurcation value of b increases. The pitchfork to the left, for negative $\mathbf{b}_1$ spins, remains subcritical but the bifurcation value of b decreases. As h_a continues to increase, this latter pitchfork eventually disappears for $h_a = h_1 = 1$. At this point all the system momentum is stored in the wheel and the platform is stationary in inertial space.

For each combination of system parameters discussed in this section, complete sets of bifurcation diagrams are included in App. B.

5.4 Effects of Spring Stiffness and Damper Location on Global Equilibria

In Sec. 5.3, we studied the equilibria and bifurcations that occur in the $\hat{\mathbf{b}}_1$–$\hat{\mathbf{b}}_3$ plane. In this and following sections, the focus returns to the global equilibria. In examining the $\hat{\mathbf{b}}_1$–$\hat{\mathbf{b}}_3$ equilibria, bifurcation parameter b is especially useful in examining bifurcations of the nominal spin. The resulting bifurcation diagrams also provide a basis to compare results with previous works for a similar $\mathcal{B} + \mathcal{P}$ model. For this section, h_a is used exclusively as the bifurcation parameter. The effects of spring stiffness and damper location are examined through different sets of h_a bifurcation diagrams for discrete changes in k and b.

The momentum sphere is a useful representation of the global equilibria for the $\mathcal{B} + \mathcal{R} + \mathcal{P}$ system.

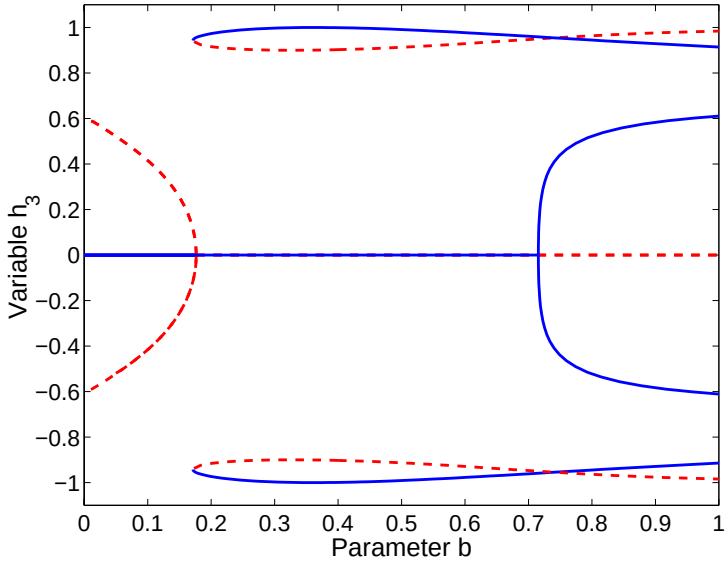

Figure 5.39: Bifurcation diagram: h_3 *vs.* b for $k = 0.4$, $h_a = 0.1$. The pitchfork for $h_1 = +1$ is supercritical, whereas the pitchfork for $h_1 = -1$ remains subcritical.

As previously described, an equilibrium point on the sphere indicates the direction of the steady spin angular momentum and angular velocity vectors. To completely describe the equilibria, additional bifurcation diagrams are included which show the equilibria for varying h_a. Bifurcations of branches out of the $\hat{\mathbf{b}}_1$–$\hat{\mathbf{b}}_3$ plane exist, generating equilibria of Types 2, 5 and 6. Figure 5.4 and Figs. 5.15–5.19 show an example of the global equilibria. Changing spring stiffness or damper location can substantially alter the nature of these equilibria.

Table 5.6 defines the system parameters used throughout this section, corresponding to a major-axis, nominal-spin configuration. The possible combinations of k and b are infinite, but to explore

Table 5.6: System parameters for gyrostat equilibria, varying k and b

Inertia Properties	Damper Parameters
$I_1 = 0.40$	$\varepsilon = 0.10$
$I_2 = 0.28$	$c = 0.10$
$I_3 = 0.32$	
$I_s = 0.04$	

the parameter space we hold one parameter constant and vary the second. The combinations of these parameters investigated are represented in Fig. 5.40. Complete bifurcation diagrams for the momentum sphere and the state variables versus rotor momentum are included in Appendices C–D.

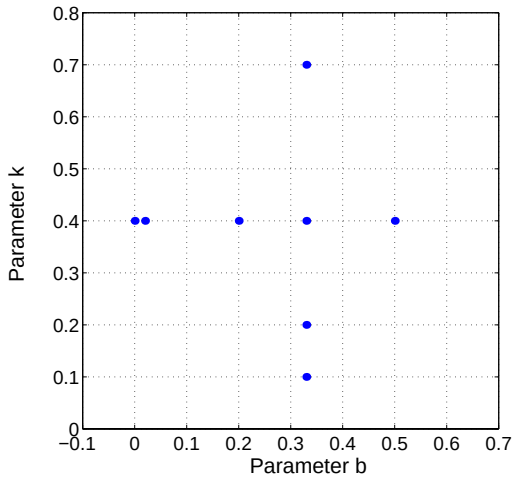

Figure 5.40: Selected points in k–b parameter space

5.4.1 Effects of Changing Spring Stiffness, k

The global equilibria for different values of k are calculated and presented on the momentum sphere in Fig. 5.41. A broader range of k is needed than in Sec. 5.3 to capture the significant changes to the equilibria. In addition to the effects discussed in Sec. 5.3, changing spring stiffness also affects the Type 6 equilibria branches. Figure 5.41(a) shows that there are two distinct versions of Type 6 branches. One version bifurcates from Type 4 and Type 5 branches, seen in Figure 5.41(a) as rings of equilibria about the $\hat{\mathbf{b}}_1$-axis. The second version of Type 6 equilibria bifurcates from Type 4 equilibria. On the momentum sphere, the Type B state appears to be a bifurcation point with Type 5 equilibria, but this Type 2B equilibrium has a non-zero damper displacement and does not coincide in state space with Type 5 equilibria. All of the Type 2, 5, and 6 equilibria are unstable for this combination of system parameters.

As k increases, a transcritical bifurcation is passed and the two distinct Type 6 branches merge into one, as shown in Fig. 5.41(b). The equilibria remain unstable on either side of the turning point. Further increases in k result in slight modification of the Type 6 branches, creating a slimmer "figure-8" branch on the momentum sphere.

To understand how changing spring stiffness affects the bifurcations relative to h_a, we look more closely at the bifurcation diagrams for h_3 *vs.* h_a, as shown in Fig. 5.42. In Figs. 5.42(a)–5.42(b) we see the new Type 6 branches of equilibria. In Fig. 5.42(a) the Type 6 equilibria bifurcate from both the Type 4 and Type 5 branches. The Type 1 and 5 branches are located along the $h_3 = 0$ axis, creating a mixture of stable and unstable equilibria indicated by the dash-dot line. Figure 5.42(b) illustrates the passing of the transcritical bifurcation; the Type 6 branches bifurcate only from the Type 5 branches.

In general, increasing the spring stiffness affects the bifurcation points of Type 6 equilibrium

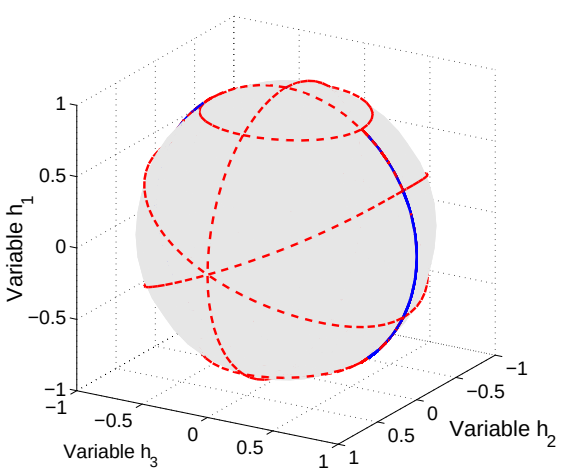

(a) $b = 0.33$, $k = 0.1$

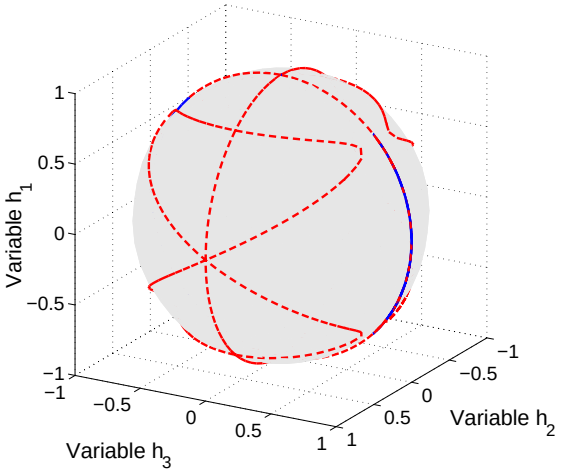

(b) $b = 0.33$, $k = 0.2$

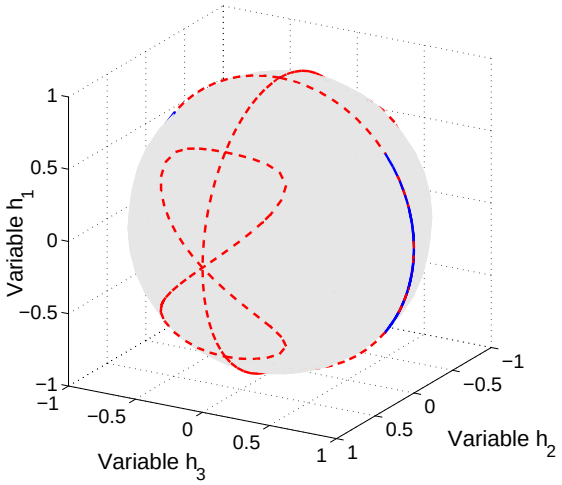

(c) $b = 0.33$, $k = 0.4$

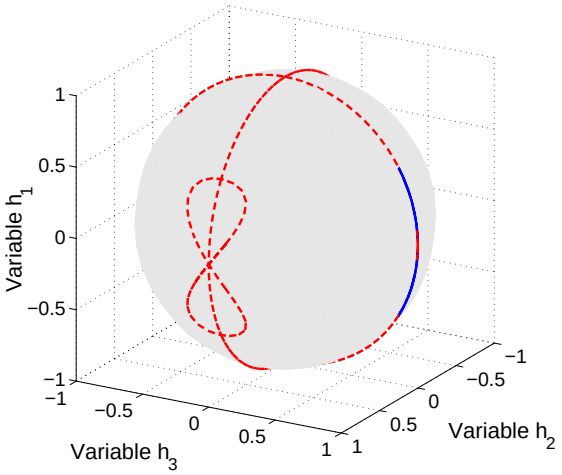

(d) $b = 0.33$, $k = 0.7$

Figure 5.41: Equilibria of oblate gyrostats on the momentum sphere for different k. The Type 6 equilibria transition from separate branches ($k = 0.1$), through bifurcation point that combines the Type 6 branches into a single branch with a turning point ($k = 0.2$). The $k = 0.4$ case has been discussed in Sec. 5.2. As k increases, the Type 6 branches approach the $\hat{\mathbf{b}}_1$–$\hat{\mathbf{b}}_2$ plane.

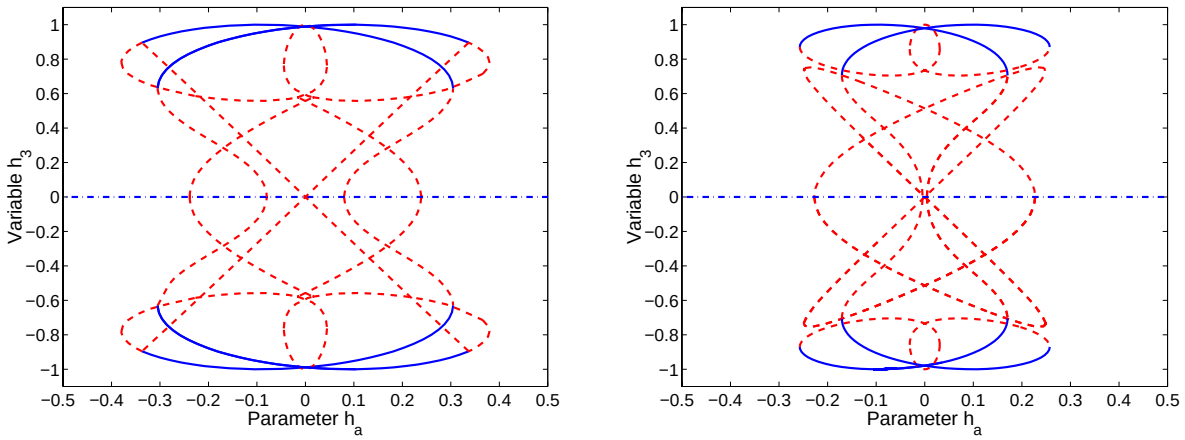

(a) $b = 0.33$, $k = 0.1$ (b) $b = 0.33$, $k = 0.2$

Figure 5.42: Bifurcation diagrams for h_3 *vs.* h_a and different k. For $k = 0.1$ Type 6 branches bifurcate from Type 4 branches, whereas for $k = 0.2$ the Type 6 equilibria are separate branches with a turning point.

branches. However, for $I_1 > I_3 > I_2$, the only stable equilibria lie in the $\hat{\mathbf{b}}_1$–$\hat{\mathbf{b}}_3$ plane. These include the nominal spin (Type 1) and canted-axis (Type 4) equilibria.

5.4.2 Effects of Changing Damper Location, b

The global equilibria for different values of b are calculated and presented on the momentum sphere in Figs. 5.43–5.45.

In general, increasing the damper position parameter, b, produces the same qualitative effects on the equilibria structure as decreasing the spring stiffness, k.

As in Sec. 5.3, we examine the $b = 0$ case. As $b \to 0$, the Type 6 equilibria collapse to the $\hat{\mathbf{b}}_1$–$\hat{\mathbf{b}}_2$ plane, and $h_3 \to 0$. For this case, Type 6 equilibria ($x \neq 0$) are distinct from Type 5 equilibria ($x = 0$). Placing the damper at the origin produces linearly marginal equilibria for most of the equilibria in the $\hat{\mathbf{b}}_1$–$\hat{\mathbf{b}}_2$ plane. To establish the stability of these branches, the Liapunov function of Ch. 4 is used to numerically determine the stability of these branches.

The unfolding of the $b = 0$ set of equilibria is evident in the bifurcation diagrams for $b = 0.02$. Figure 5.43(a) shows the Type 6 equilibria perturbed from the $\hat{\mathbf{b}}_1$–$\hat{\mathbf{b}}_2$ plane. Another useful perspective is shown in Figs. 5.44(a)– 5.45(b).

For the h_1–h_a and h_3–h_a bifurcation diagrams, the Type 4 and Type 6 equilibria share some of the same h_1 and h_3 values for $b = 0$ (Figs. 5.44(a) and 5.45(a)), but for $b = 0.02$ the perturbation is evident as these branches diverge (Figs. 5.44(b) and 5.45(b)).

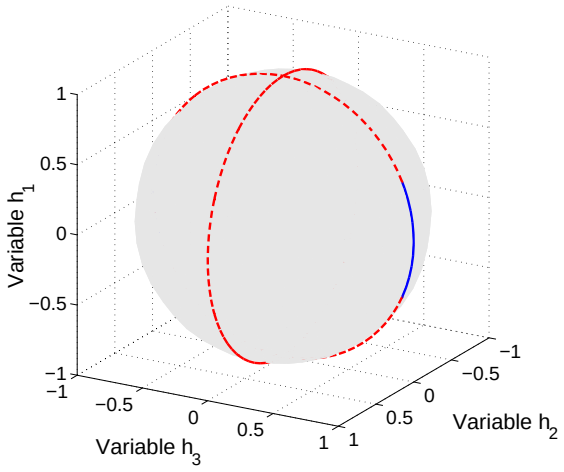

(a) $b = 0$, $k = 0.4$

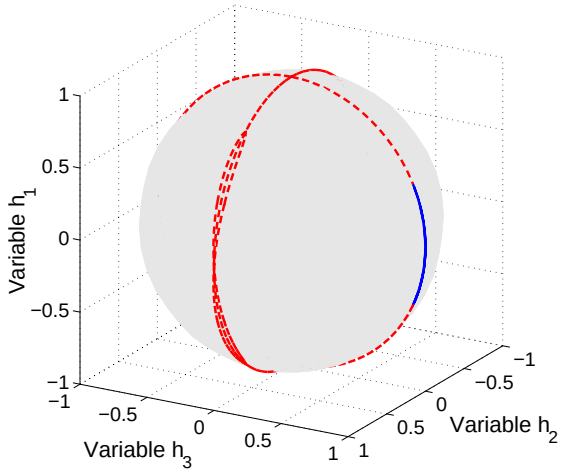

(b) $b = 0.02$, $k = 0.4$

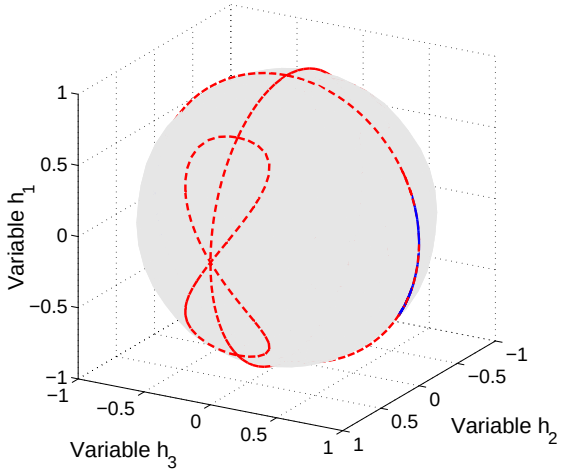

(c) $b = 0.2$, $k = 0.4$

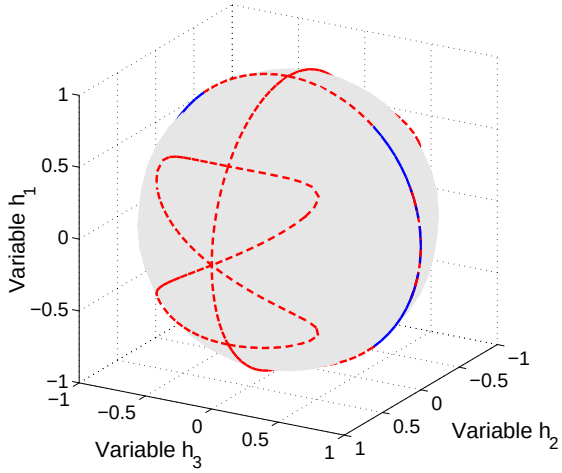

(d) $b = 0.5$, $k = 0.4$

Figure 5.43: Equilibria of oblate gyrostats on the momentum sphere for different b. For $b = 0$, the Type 6 equilibria lie in the $\hat{\mathbf{b}}_1$–$\hat{\mathbf{b}}_2$ plane. Small b perturbs the Type 6 branches off the $\hat{\mathbf{b}}_1$–$\hat{\mathbf{b}}_2$ plane. The Type 6 branches evolve further in the h_3 direction for increasing b.

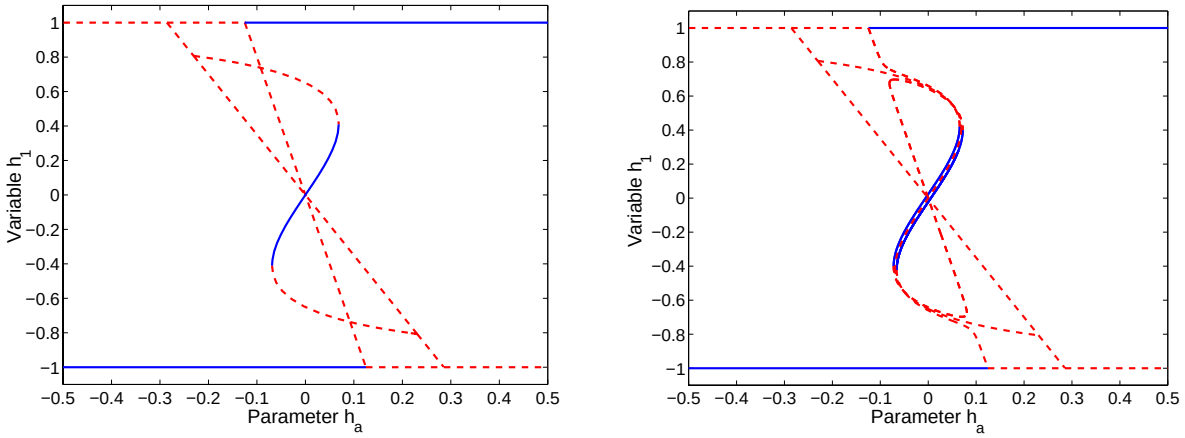

(a) $b = 0$, $k = 0.4$ (b) $b = 0.02$, $k = 0.4$

Figure 5.44: Bifurcation diagrams for h_1 *vs.* h_a and different k. For $b = 0$, the Type 4 and Type 6 equilibria are co-located in the h_1–h_a diagram. Small b breaks the Type 4 branch bifurcation point and perturbs the pair of Type 4 branches from each other, distinguishing them from the Type 6 branch.

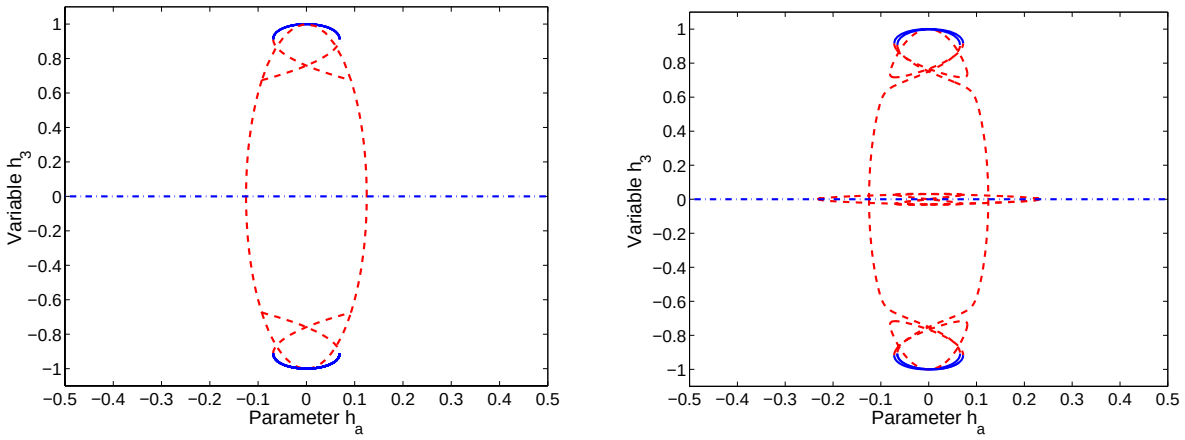

(a) $b = 0$, $k = 0.4$ (b) $b = 0.02$, $k = 0.4$

Figure 5.45: Bifurcation diagrams for h_3 *vs.* h_a and different k.. For $b = 0$, the Type 4 and Type 6 equilibria are co-located in the h_3–h_a diagram. Small b breaks the Type 4 branch bifurcation point and perturbs the pair of Type 4 branches from each other, distinguishing them from the Type 6 branch.

5.5 Effects of Alternate Inertia Properties

The inertia properties of a rigid body or gyrostat are key parameters affecting equilibria and stability. In Ch. 4, some analytical results were derived related to inertia properties for the stability of simple spins. For more complex equilibria, we use numerical analysis to evaluate stability. In this section, the model's inertia values are permuted in relative magnitude and used with numerical continuation to investigate the effects on equilibria and stability.

We define a gyrostat designed to spin about a major axis as an *oblate* gyrostat (I_1 is the maximum moment of inertia). Similarly, a gyrostat designed to spin about a minor axis is denoted a *prolate* gyrostat (I_1 is the minimum moment of inertia).

5.5.1 Oblate Gyrostat

All the previous results correspond to an oblate gyrostat, with $I_1 > I_1' > I_3 > I_2$, and are not repeated. However, we consider the oblate gyrostat with $I_1 > I_1' > I_2 > I_3$. Numerical continuation is applied to the model with system parameters defined in Table 5.7.

Table 5.7: System parameters for oblate gyrostat equilibria, $I_2 > I_3$

Inertia Properties	Damper Parameters
$I_1 = 0.40$	$k = 0.40$
$I_2 = 0.32$	$b = 0.33$
$I_3 = 0.28$	$\varepsilon = 0.10$
$I_s = 0.04$	$c = 0.10$

Figure 5.46 illustrates several key points, whereas complete results are included in App. E. For $I_2 > I_3$, several stability changes occur. All Type 3 and Type 4 equilibria are unstable. Previously unstable Type 6 equilibria are stable. Figure 5.46(b) shows the turning point marking the stability change in the Type 6 branches. The Type 2B spin is stable, but for a lower k value the Type 2A spin may be stable if the stability conditions of Eqs. 4.49– 4.50 are met.

5.5.2 Prolate Gyrostat

A gyrostat designed to spin about an axis of least inertia is an important configuration in satellite design. As discussed in Ch. 2, the gyroscopic stabilization provided by a rotor makes prolate dual-spin satellites possible, even with energy dissipation. One limitation of the model considered here is the presence of energy dissipation only on the rigid body. For a large, dual-spin satellite, the effects of energy dissipation on the rotor itself are important. Previous works[36,45,52] have shown

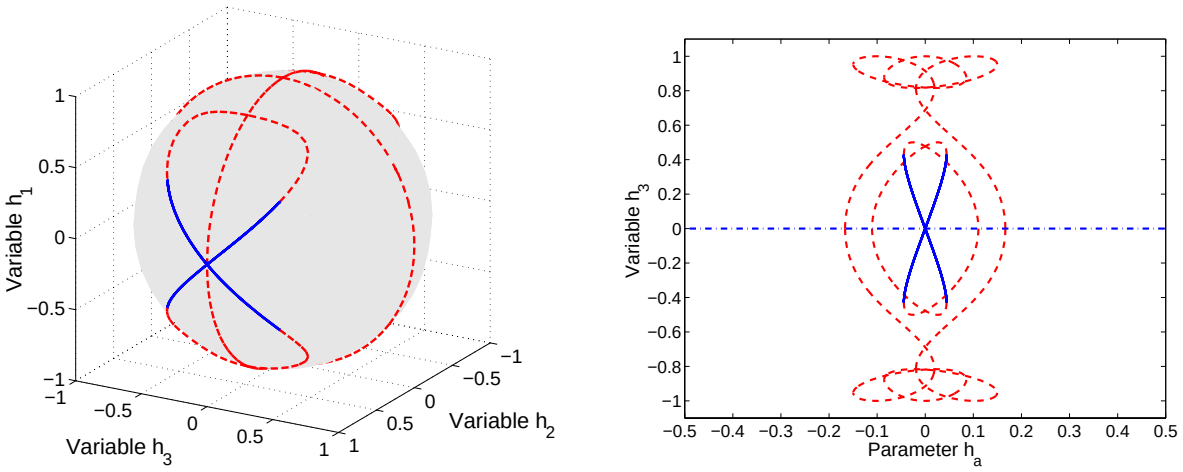

(a) Momentum sphere

(b) h_3 *vs.* h_a

Figure 5.46: Equilibria of oblate gyrostat, $I_1 = 0.28$, $I_2 = 0.4$, and $I_3 = 0.32$

that a prolate gyrostat, with damping throughout, can be stable if the damping on the rigid body is large enough relative to the damping on the rotor. Therefore, the results of this section are a reasonable approximation of the equilibria possible for a similar gyrostat with sufficiently small rotor damping.

We use a range of inertia values to examine the spectrum of possible prolate gyrostats. Keeping I_1 constant, the I_2 and I_3 values are varied as in Table 5.8. Figures 5.47–5.48 show the sequence of momentum spheres for the different inertia combinations. Complete sets of bifurcation diagrams are included in App. E.

Table 5.8: Range of inertia properties for a prolate gyrostat

I_1	I_2	I_3
0.28	0.32	0.40
0.28	0.35	0.37
0.28	0.356	0.364
0.28	0.3559	0.361
0.28	0.36	0.36
0.28	0.37	0.35
0.28	0.37155	0.34845
0.28	0.372	0.348
0.28	0.40	0.32

The evolution of the equilibrium branches is similar to the effects of changing damper position

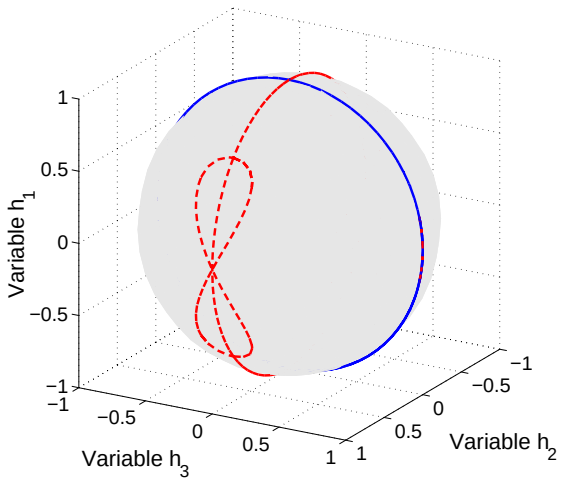

(a) $\mathbf{I} = \text{diag}(0.280, 0.320, 0.400)$

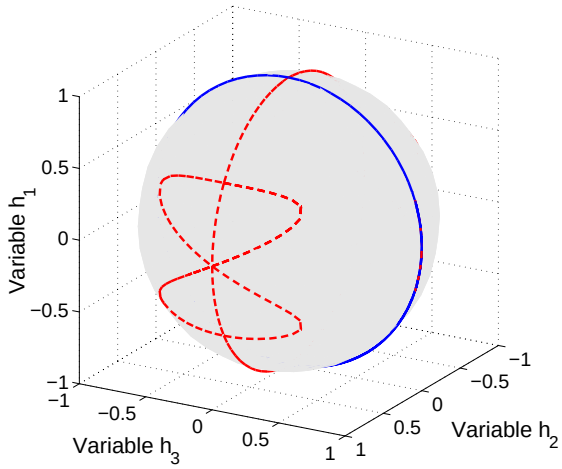

(b) $\mathbf{I} = \text{diag}(0.280, 0.350, 0.370)$

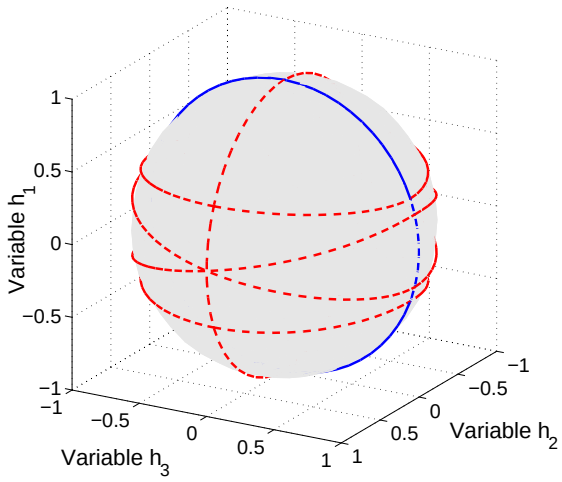

(c) $\mathbf{I} = \text{diag}(0.280, 0.356, 0.364)$

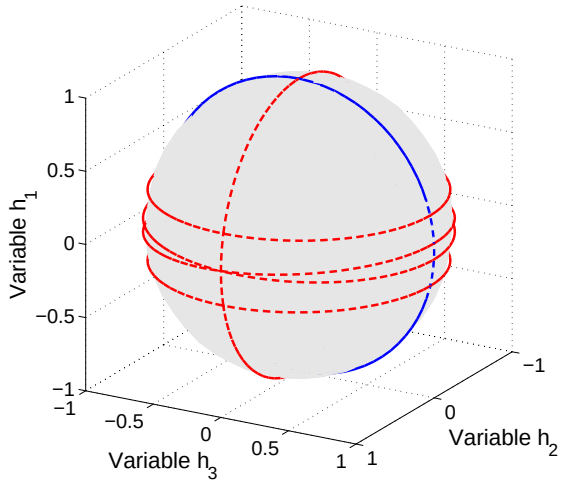

(d) $\mathbf{I} = \text{diag}(0.280, 0.359, 0.361)$

Figure 5.47: Equilibria of prolate gyrostats, $I_2 < I_3$. The Type 5 equilibria are all unstable. The Type 4 equilibria are generally stable, but there are some unstable branches causing mixed stability regions near the $\hat{\mathbf{b}}_3$ axis. Type 6 equilibria are unstable. As I_2 increases, the Type 6 equilibria changes are similar to increasing b or decreasing k. As $I_2 \to I_3$, the Type 6 branches approach the $\hat{\mathbf{b}}_2$–$\hat{\mathbf{b}}_3$ plane.

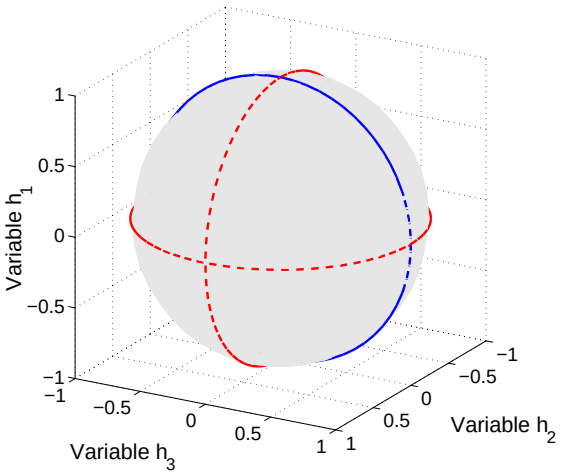

(a) $\mathbf{I} = \text{diag}(0.280, 0.360, 0.360)$, axisymmetric

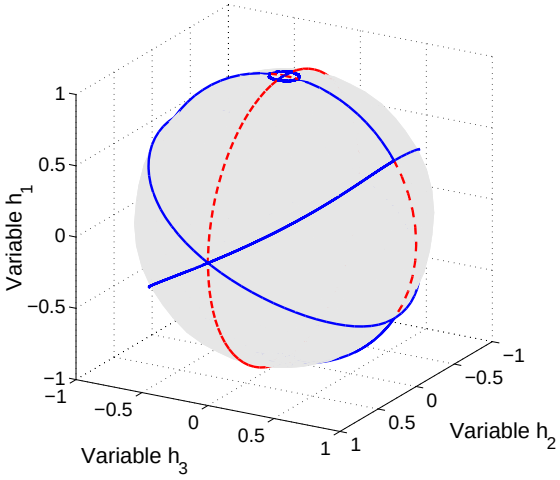

(b) $\mathbf{I} = \text{diag}(0.280, 0.370, 0.350)$

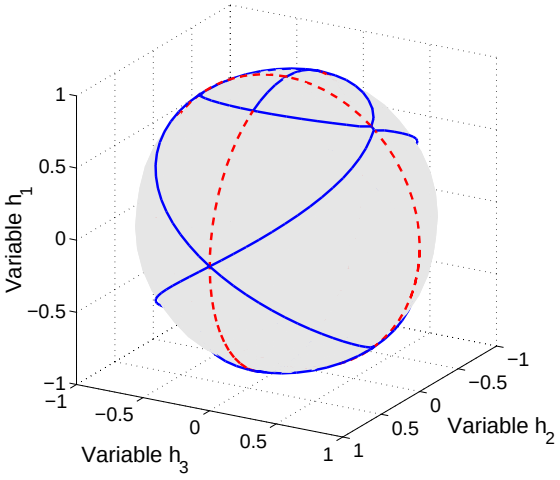

(c) $\mathbf{I} = \text{diag}(0.28000, 0.37155, 0.34845)$

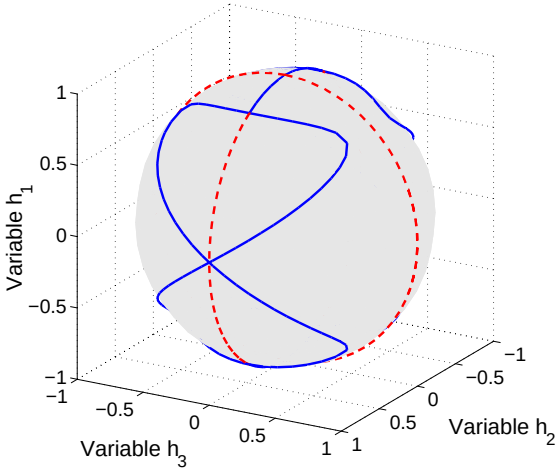

(d) $\mathbf{I} = \text{diag}(0.280, 0.372, 0.348)$

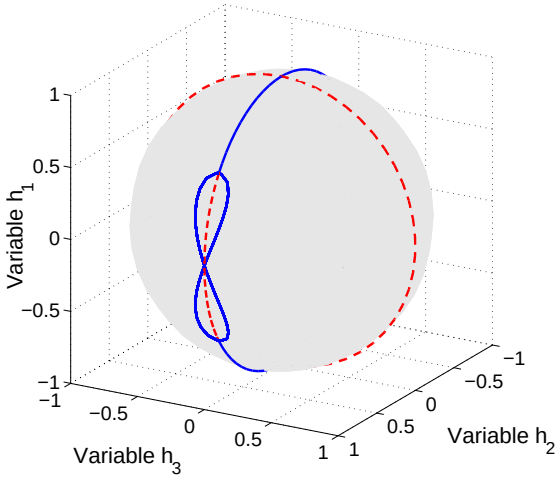

(e) $\mathbf{I} = \text{diag}(0.280, 0.400, 0.320)$

Figure 5.48: Equilibria of prolate gyrostts, axisymmetric and $I_2 > I_3$

or spring stiffness. The most significant qualitative changes occur for the Type 6 equilibria. For $I_2 < I_3$, as shown in Fig. 5.47, increasing I_2 changes the Type 6 equilibria in roughly the same manner as increasing b or decreasing k. As $I_2 \to I_3$, the unstable Type 6 branches approach the $\hat{\mathbf{b}}_2$–$\hat{\mathbf{b}}_3$ plane.

The axisymmetric gyrostat, defined as $I_2 = I_3$, has equilibria only in the pseudo-principal planes (the body-axis planes are principal only for $x = 0$). Figure 5.48(a) shows that for the axisymmetric gyrostat the Type 4 equilibria are stable, but Types 5 and 6 are unstable.

For $I_2 > I_3$, as shown in Fig. 5.48, the Type 6 branches are stable. However, the stability threshold does not coincide with $I_2 = I_3$. The Type 6 equilibria are too complex for the Liapunov analysis of Ch. 4 to produce stability thresholds analytically. Numerically, this stability transition can be examined by considering inertia cases closer to an axisymmetric gyrostat. For the case where $\mathbf{I} = \text{diag}[0.280, 0.362, 0.358]$, the Type 6 branches are unstable. For $\mathbf{I} = \text{diag}[0.280, 0.363, 0.357]$ there is a turning point and stability change in the Type 6 branches, signaling the onset of the stability change while $I_2 > I_3$. For I_2 slightly larger than I_3, the Type 6 branches emerge from the $\hat{\mathbf{b}}_2$–$\hat{\mathbf{b}}_3$ plane in two places: a pair of branches intersecting at the $\hat{\mathbf{b}}_2$ axis and rings of equilibria very near the $\hat{\mathbf{b}}_1$ axis, as shown in Fig. 5.48(b). These stable Type 6 rings of equilibria are very near the intended nominal-axis spin, but they only occur for h_a values less than required to stabilize the nominal spin. Transitioning from Fig. 5.48(b) to Fig. 5.48(c), the separate branches of Type 6 equilibria combine into a continuous branch. For larger values of k, the Type 6 branches become a single branch with a turning point, as shown in Figs. 5.48(d) and 5.48(e).

5.5.3 Intermediate-Axis Gyrostat

The final class of inertia values are the intermediate-axis gyrostats. The two possibilities in this class are for either I_2 or I_3 to be the largest moment of inertia.

For I_2 as the largest moment of inertia, we consider the case, $I_2 > I_1 > I_1' > I_3$. Numerical continuation is applied to the model with the system parameters defined in Table 5.9.

Table 5.9: System parameters for intermediate-axis gyrostat equilibria, $I_2 > I_3$

Inertia Properties	Damper Parameters
$I_1 = 0.32$	$k = 0.40$
$I_2 = 0.42$	$b = 0.33$
$I_3 = 0.26$	$\varepsilon = 0.10$
$I_s = 0.04$	$c = 0.10$

The possible equilibria for this intermediate-axis gyrostat, with $I_2 > I_3$, are similar to those for a prolate gyrostat with $I_2 > I_3$. Figure 5.49 shows that the Type 4 equilibria are all unstable. Type 6 equilibria are all stable, forming a "figure-8" branch on the momentum sphere. The Type 5 branches include stable and unstable equilibria, with the stability changes occurring at the Type 6 branch bifurcation points. The qualitative nature of these branches, as well as their stability, are the same as for $\mathbf{I} = \text{diag}[0.28, 0.40, 0.32]$ and the same damper parameters.

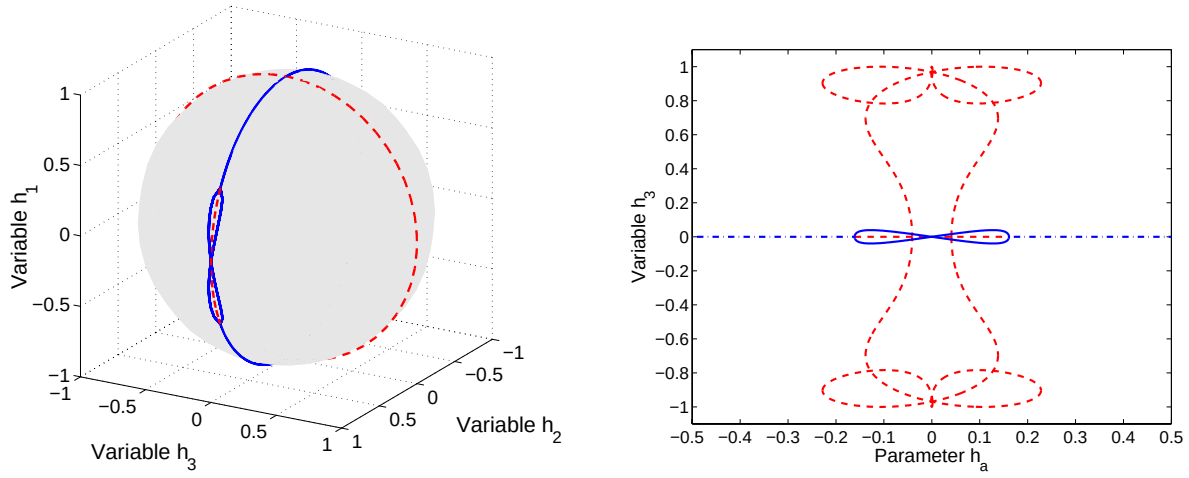

(a) Momentum sphere

(b) h_3 *vs.* h_a

Figure 5.49: Equilibria of intermediate-axis gyrostat, $I_1 = 0.32$, $I_2 = 0.42$, and $I_3 = 0.26$

For I_3 as the largest moment of inertia, numerical continuation is applied to the model with the system parameters defined in Table 5.10, resulting in Fig. 5.50. This intermediate-axis gyrostat

Table 5.10: System parameters for intermediate-axis gyrostat equilibria, $I_3 > I_2$

Inertia Properties	Damper Parameters
$I_1 = 0.32$	$k = 0.40$
$I_2 = 0.26$	$b = 0.33$
$I_3 = 0.42$	$\varepsilon = 0.10$
$I_s = 0.04$	$c = 0.10$

has equilibria similar to a prolate gyrostat with $I_3 > I_2$. Figure 5.50(a) is similar to Fig. 5.47(a), showing that the Type 5 and Type 6 branches are all unstable. Figure 5.50(b) illustrates how most of the Type 4 equilibria are stable. For any value of h_a, there is at least one stable equilibrium in the $\hat{\mathbf{b}}_1$–$\hat{\mathbf{b}}_3$ plane.

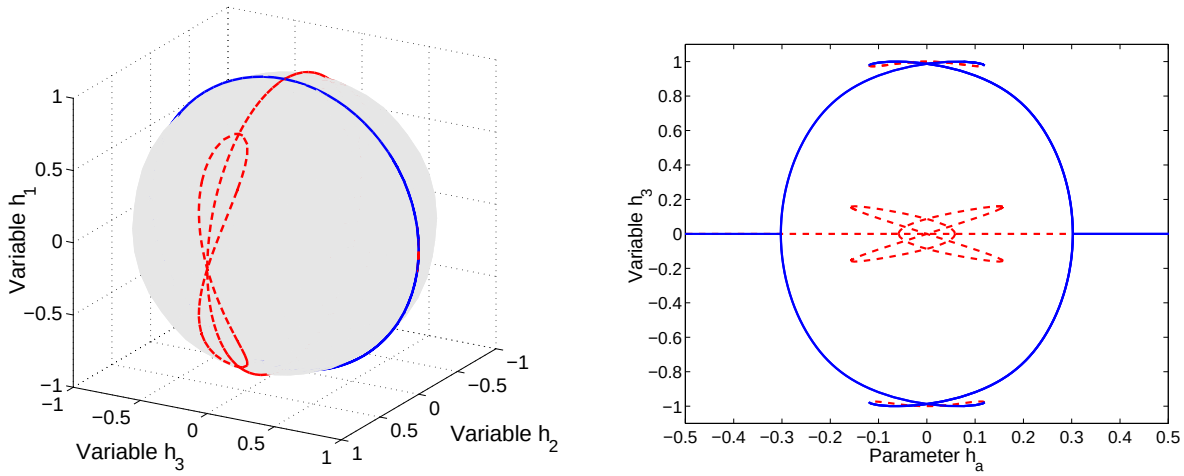

(a) Momentum sphere

(b) h_3 *vs.* h_a

Figure 5.50: Equilibria of intermediate-axis gyrostat, $I_1 = 0.32$, $I_2 = 0.26$, and $I_3 = 0.42$

5.6 Summary

We applied numerical continuation to the equations of motion for a gyrostat with a spring-mass damper. The results were presented in terms of equilibria on the momentum sphere and individual state bifurcation diagrams. Many different equilibria are possible for this relatively simple model. In addition to the simple spins about principal axes, multiple equilibria exist in the three body-axis planes. Some equilibria do not lie in any principal plane of the undeformed system. Changing damper parameters, rotor momentum, and inertia properties all have significant effects on the global equilibria.

Chapter 6

Bifurcations in Parameter Space

The behavior of solutions to the system equilibrium equations depends on the values of a number of system parameters, such as k, b, and h_a. The parameter space, $\boldsymbol{\alpha} = [k, b, h_a]$, of all feasible parameters forms a three-dimensional space. Inertia properties are also system parameters, but we consider the inertia properties fixed in this chapter. The loci in this parameter space of singular points form critical boundaries, called bifurcation curves. In this chapter, key bifurcation points and turning points are determined in parameter space, creating parameter charts of bifurcation curves.

Both numerical and analytical methods are used to determine the bifurcation branches and key points in parameter space. The primary numerical tool is two-parameter continuation, which is an extension of the previously described one-parameter bifurcation methods. Two-parameter continuation generates branches of turning points in two-parameter space. Analytically, we find critical transitions in branching behavior using Liapunov-Schmidt reduction. These methods are discussed briefly in the following section. We focus on the branching behavior of the nominal spin and turning points in the $\hat{\mathbf{b}}_1$–$\hat{\mathbf{b}}_3$ plane, with emphasis on avoiding jump phenomena, as described in Ch. 5.

6.1 Numerical and Analytical Methods

In this section we describe two methods used in characterizing equilibria in parameter space. Two-parameter continuation is a numerical technique, based on the continuation concepts in Ch. 5 for a single bifurcation parameter, that follows a turning point in two-parameter space. Liapunov-Schmidt reduction is a method that reduces a multi-dimensional problem to an equivalent scalar problem. We use this technique to determine analytic solutions, in terms of system parameters, to an important transition of the nominal-spin bifurcation point.

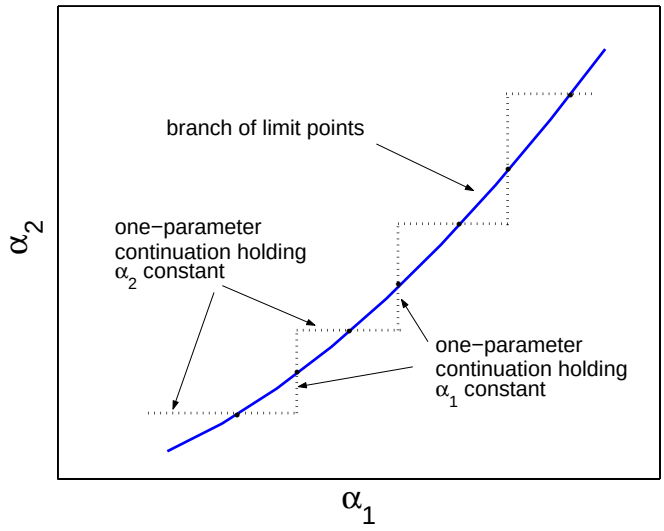

Figure 6.1: Tracing of bifurcation curves

6.1.1 Two-Parameter Continuation

In the most general sense, the system equilibria depend on the values of a vector of system parameters, $\boldsymbol{\nu} = [\alpha_1, \alpha_2, \alpha_3 ... \alpha_n]$. Standard, or single-parameter, numerical continuation requires holding all but one parameter fixed while the bifurcation parameter is varied. Two-parameter continuation generates branches of bifurcation points in a two-dimensional parameter space. The method is an extension of one-parameter continuation, applied in an indirect fashion to trace bifurcation curves.

The process, shown graphically in Fig. 6.1, starts with one-parameter continuation, holding the second parameter fixed. A turning point is identified indirectly and saved as the next starting point. In the next step, the second parameter becomes the bifurcation parameter and the first is held fixed. The actual starting point is near, but not exactly, the turning point so that the next bifurcation point in parameter space is also found indirectly. Continuation proceeds, alternating bifurcation parameters and tracing the path of turning points.

6.1.2 Liapunov-Schmidt Reduction

The following is a brief description of the theory and method of Liapunov-Schmidt reduction. A complete discussion of this technique may be found in Ref. 26.

The basic idea of Liapunov-Schmidt reduction is to reduce a multi-dimensional problem,

$$\mathbf{0} = \mathbf{f}(\mathbf{z}, \alpha) \tag{6.1}$$

with multiple solutions to an equivalent single scalar equation. Under the assumption of a mini-

mally degenerate case, that is, a Jacobian of rank $n-1$ at bifurcation points, the solutions of the full system, Eq. 6.1, may be put in one-to-one correspondence with solutions of a single equation

$$g(u,\alpha) = 0 \tag{6.2}$$

where $g : \mathbb{R} \times \mathbb{R} \to \mathbb{R}$ is a smooth mapping. The scalar function $g(u,\alpha)$ is defined implicitly, but rarely is it possible to explicitly determine a formula for $g(u,\alpha)$. However, expressions for derivatives of $g(u,\alpha)$ are possible.

To derive the reduced equations, we first reformulate the equations through a change in variables such that $\mathbf{f}(\mathbf{0},0) = \mathbf{0}$. Let $\mathbf{A}$ be the $n \times n$ Jacobian matrix evaluated at $(\mathbf{0},0)$. We must choose vector space complements to the null space and range space of the Jacobian, $\mathbf{A}$:

$$\mathbb{R}^n = \mathcal{N}(\mathbf{A}) \oplus \mathbf{M} \tag{6.3}$$
$$\mathbb{R}^n = \mathbf{N} \oplus \mathcal{R}(\mathbf{A}) \tag{6.4}$$

where $\mathcal{N}(\mathbf{A})$ is the null space of $\mathbf{A}$, $\mathcal{R}(\mathbf{A})$ is the range space of $\mathbf{A}$, and $\mathbf{M}$ and $\mathbf{N}$ are the vector space complements to $\mathcal{N}(\mathbf{A})$ and $\mathcal{R}(\mathbf{A})$, respectively. Figure 6.2 illustrates the vector subspaces for $n = 3$. We consider the minimally degenerate case where

$$\operatorname{rank} \mathbf{A} = n - 1$$

Therefore, the dimension of the subspaces are

$$\dim \mathbf{N} = \dim \mathcal{N}(\mathbf{A}) = 1$$

and

$$\dim \mathbf{M} = \dim \mathcal{R}(\mathbf{A}) = n - 1$$

Possible choices for the subspaces are $\mathbf{M} = \mathcal{R}(\mathbf{A}^{\mathrm{T}})$ and $\mathbf{N} = \mathcal{N}(\mathbf{A}^{\mathrm{T}})$, but $\mathbf{M}$ and $\mathbf{N}$ are not required to be orthogonal subspaces to $\mathcal{N}(\mathbf{A})$ and $\mathcal{R}(\mathbf{A})$, respectively. Let $\mathbf{E}$ be the projection matrix which projects $\mathbb{R}^n$ onto $\mathcal{R}(\mathbf{A})$ with $\mathcal{N}(\mathbf{E}) = \mathbf{N}$. The complementary projection $\mathbf{I} - \mathbf{E}$ has a range equal to $\mathbf{N}$ and a null space equal to $\mathcal{R}(\mathbf{A})$.

If $\mathbf{u} \in \mathbb{R}^n$, $\mathbf{u} = \mathbf{0}$ if and only if $\mathbf{E}\mathbf{u} = \mathbf{0}$ and $(\mathbf{I} - \mathbf{E})\mathbf{u} = \mathbf{0}$. The same idea can be applied to the vector field, $\mathbf{f}(\mathbf{z},\alpha) = \mathbf{0}$,

$$\mathbf{E}\,\mathbf{f}(\mathbf{z},\alpha) = \mathbf{0} \tag{6.5}$$
$$(\mathbf{I} - \mathbf{E})\,\mathbf{f}(\mathbf{z},\alpha) = \mathbf{0} \tag{6.6}$$

thereby decomposing Eq. 6.1 into complementary vector subspaces. The fundamental idea behind Liapunov-Schmidt reduction is that Eq. 6.5 may be solved for $n-1$ of the variables. These can then be substituted into Eq. 6.6, yielding a single scalar equation for the remaining unknown.

We split the vector $\mathbf{z}$ into the form $\mathbf{z} = \mathbf{v} + \mathbf{w}$, where $\mathbf{v} \in \mathcal{N}(\mathbf{A})$ and $\mathbf{w} \in \mathbf{M}$. We rewrite Eq. 6.5 as

$$\mathbf{E}\,\mathbf{f}(\mathbf{v} + \mathbf{w},\alpha) = \mathbf{0} \tag{6.7}$$

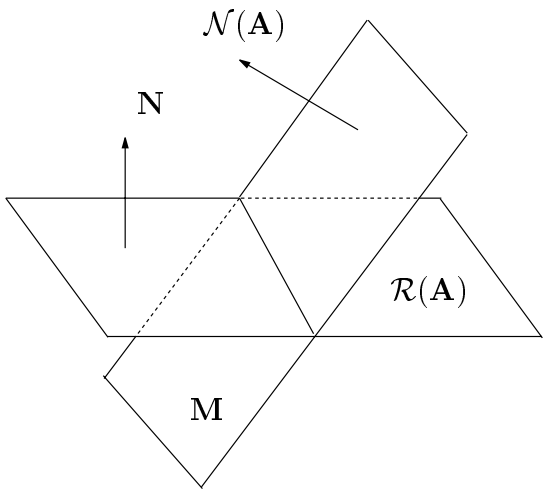

Figure 6.2: Definitions of vector subspaces for $n = 3$

and use the fact that the Jacobian is a linear map, $\mathbf{A} : \mathbf{M} \to \mathcal{R}(\mathbf{A})$ and is invertible on $\mathcal{R}(\mathbf{A})$. This invertibility allows Eq. 6.5 to be uniquely solved at the origin for $\mathbf{w}$, and we write the solution, implicitly, as $\mathbf{w} = \mathbf{w}(\mathbf{v}, \alpha)$. Therefore,

$$\mathbf{E}\,\mathbf{f}(\mathbf{v} + \mathbf{w}(\mathbf{v}, \alpha), \alpha) = \mathbf{0} \tag{6.8}$$

and we can substitute for $\mathbf{w}$ in Eq. 6.6, defining a reduced mapping ϕ,

$$\phi(\mathbf{v}, \alpha) = (\mathbf{I} - \mathbf{E})\,\mathbf{f}(\mathbf{v} + \mathbf{w}(\mathbf{v}, \alpha), \alpha) \tag{6.9}$$

where $\phi : \mathcal{N}(\mathbf{A}) \times \mathbb{R} \to \mathbf{N}$. The zeros of the reduced function, $\phi(\mathbf{v}, \alpha)$, are in one-to-one correspondence with the zeros of $\mathbf{f}(\mathbf{z}, \alpha)$. The reduced function, ϕ maps from the one-dimensional subspace $\mathbf{v}$ to the one-dimensional subspace $\mathbf{N}$. By selecting a basis vector for $\mathbf{v}$, ϕ can be converted to a scalar equation.

Let $\mathbf{v} = u\mathbf{v}_0$, where $u \in \mathbb{R}$ and $\mathbf{v}_0$ is a non-zero vector in $\mathcal{N}(\mathbf{A})$. Also define $\mathbf{v}_0^*$ as a non-zero vector in $\mathcal{N}(\mathbf{A}^{\mathrm{T}})$, and is therefore perpendicular to $\mathcal{R}(\mathbf{A})$. Since $\phi(u\mathbf{v}_0, \alpha) \in \mathbf{N}$ and $\mathbf{N}$ is the complementary subspace to $\mathcal{R}(\mathbf{A})$, we conclude that ϕ is not perpendicular to $\mathbf{v}_0^*$. Therefore, the inner product of $\phi(u\mathbf{v}_0, \alpha)$ and $\mathbf{v}_0^*$ should be zero if and only if $\phi(\mathbf{v}_0, \alpha) = 0$. Defining the inner product for $\mathbf{a}, \mathbf{b} \in \mathbb{R}$ as

$$\langle \mathbf{a}, \mathbf{b} \rangle = \sum a_i b_i \tag{6.10}$$

we define $g : \mathbb{R} \times \mathbb{R} \to \mathbb{R}$ by

$$g(u, \alpha) = \langle \mathbf{v}_0^*, \phi(u\mathbf{v}_0, \alpha) \rangle. \tag{6.11}$$

Partial derivatives of $g(u, \alpha)$ are determined by successive application of the chain rule. Using the notation of Golubitsky and Schaeffer (Ref. 26), the formulas for the higher-order derivatives of g are

$$\begin{aligned}
g_u &= 0 && (6.12)\\
g_{uu} &= \langle \mathbf{v}_0^*, \mathrm{d}^2\mathbf{f}(\mathbf{v}_0, \mathbf{v}_0) \rangle && (6.13)\\
g_{uuu} &= \langle \mathbf{v}_0^*, \mathrm{d}^3\mathbf{f}(\mathbf{v}_0, \mathbf{v}_0, \mathbf{v}_0) - 3\mathrm{d}^2\mathbf{f}(\mathbf{v}_0, \mathbf{A}^{-1}\mathbf{E}\mathrm{d}^2\mathbf{f}(\mathbf{v}_0, \mathbf{v}_0)) \rangle && (6.14)\\
g_\alpha &= \langle \mathbf{v}_0^*, \mathbf{f}_\alpha \rangle && (6.15)\\
g_{\alpha u} &= \langle \mathbf{v}_0^*, \mathrm{d}\mathbf{f}_\alpha \cdot \mathbf{v}_0 - \mathrm{d}^2\mathbf{f}(\mathbf{v}_0, \mathbf{A}^{-1}\mathbf{E}\mathbf{f}_\alpha) \rangle && (6.16)
\end{aligned}$$

where the additional derivatives of $\mathbf{f}(\mathbf{z}, \alpha)$ are denoted $\mathrm{d}^2\mathbf{f}$, $\mathrm{d}^3\mathbf{f}$, $\mathbf{f}_\alpha$, and $\mathrm{d}\mathbf{f}_\alpha$. These additional derivatives are all evaluated at $(\mathbf{0}, 0)$. Note that $\mathrm{d}^2\mathbf{f}$ and $\mathrm{d}^3\mathbf{f}$ are third- and fourth-rank tensors, respectively.

Several arbitrary choices must be made throughout the Liapunov-Schmidt process which affect the form of the results. These choices include selecting suitable subspaces $\mathbf{N}$, $\mathbf{M}$, defined by their basis vectors, as well as selecting $\mathbf{v}_0$ and $\mathbf{v}_0^*$. Although different choices lead to different forms of Eq. 6.2, Theorem 3.2 in Ref. 26 proves that these different forms are equivalent under reasonable hypotheses.

The main problem with computing the partial derivatives of g is evaluating the inverse of $\mathbf{A}$. This inverse matrix, $\mathbf{A}^{-1}$, inverts $\mathbf{A}$ where it is invertible, transforming the column space of $\mathbf{A}$ back to the row space of $\mathbf{A}$. It is similar to the pseudoinverse of a full-rank rectangular matrix in this regard.[65] As with the pseudoinverse, it also transforms the left null space to the zero vector. Using these properties, we develop a method of deriving a suitable $\mathbf{A}^{-1}$.

The Jacobian matrix is a linear transformation which transforms any vector in R^n to the column space of $\mathbf{A}$. Therefore, it also transforms a vector in the row space of $\mathbf{A}$ to the column space of $\mathbf{A}$. For simplicity, we choose to use orthogonal subspaces, selecting $\mathbf{N} = \mathcal{N}(\mathbf{A}^{\mathrm{T}})$ and $\mathbf{M} = \mathcal{R}(\mathbf{A}^{\mathrm{T}})$. We choose basis vectors for the various subspaces,

$$\begin{aligned}
[\mathbf{r}_1\ \mathbf{r}_2\ \ldots \mathbf{r}_{n-1}] &= \mathcal{R}(\mathbf{A}) && (6.17)\\
\mathbf{r}_n &= \mathcal{N}(\mathbf{A}^{\mathrm{T}}) && (6.18)\\
[\mathbf{m}_1\ \mathbf{m}_2\ \ldots \mathbf{m}_{n-1}] &= \mathcal{R}(\mathbf{A}^{\mathrm{T}}) && (6.19)\\
\mathbf{m}_n &= \mathcal{N}(\mathbf{A}) && (6.20)
\end{aligned}$$

In both cases, the sets of vectors $\mathbf{r}$ and $\mathbf{m}$ each span $\mathbb{R}^n$.

The transformation of $\mathbf{m}_i$ to $\mathcal{R}(\mathbf{A})$ produces a vector which may be written as a linear combination

of $[\mathbf{r}_1, \mathbf{r}_2, \ldots \mathbf{r}_{n-1}]$. Using the case $n = 3$ as an example,

$$\mathbf{A}\mathbf{m}_1 = [\mathbf{r}_1\ \mathbf{r}_2\ \mathbf{r}_3] \begin{bmatrix} \alpha_1 \\ \beta_1 \\ 0 \end{bmatrix} \tag{6.21}$$

and

$$\mathbf{A}\mathbf{m}_2 = [\mathbf{r}_1\ \mathbf{r}_2\ \mathbf{r}_3] \begin{bmatrix} \alpha_2 \\ \beta_2 \\ 0 \end{bmatrix} \tag{6.22}$$

which can be put in the form

$$\mathbf{A}\,[\mathbf{m}_1\ \mathbf{m}_2] = [\mathbf{r}_1\ \mathbf{r}_2\ \mathbf{r}_3] \begin{bmatrix} \alpha_1 & \alpha_2 \\ \beta_1 & \beta_2 \\ 0 & 0 \end{bmatrix} \tag{6.23}$$

Equations 6.21– 6.22 are used to solve for the coefficients α_1, α_2, β_1, and β_2.

The desired linear transformation takes vectors in the column space back to the row space.

$$\mathbf{A}^{-1}\,[\mathbf{r}_1\ \mathbf{r}_2\ \mathbf{r}_3] \begin{bmatrix} \alpha_1 & \alpha_2 \\ \beta_1 & \beta_2 \\ 0 & 0 \end{bmatrix} = [\mathbf{m}_1\ \mathbf{m}_2\ ] \tag{6.24}$$

To solve for $\mathbf{A}^{-1}$, we must use the action of $\mathbf{A}^{-1}$ on the left null space,

$$\mathbf{A}^{-1}\mathbf{r}_3 = \mathbf{0} \tag{6.25}$$

that can be combined with Eq. 6.24 as

$$\mathbf{A}^{-1}\,[\mathbf{r}_1\ \mathbf{r}_2\ \mathbf{r}_3] \begin{bmatrix} \alpha_1 & \alpha_2 & 0 \\ \beta_1 & \beta_2 & 0 \\ 0 & 0 & 1 \end{bmatrix} = [\mathbf{m}_1\ \mathbf{m}_2\ \mathbf{0}] \tag{6.26}$$

Equation 6.26 may be solved for $\mathbf{A}^{-1}$ since both matrices on the left side of the equality are invertible.

$$\mathbf{A}^{-1} = [\mathbf{m}_1\ \mathbf{m}_2\ \mathbf{0}] \begin{bmatrix} \alpha_1 & \alpha_2 & 0 \\ \beta_1 & \beta_2 & 0 \\ 0 & 0 & 1 \end{bmatrix}^{-1} [\mathbf{r}_1\ \mathbf{r}_2\ \mathbf{r}_3]^{-1} \tag{6.27}$$

Using this method, the $\mathbf{A}^{-1}$ matrix is derived for the applications in the following sections.

6.2 Parameter Space for $\hat{\mathrm{b}}_1$–$\hat{\mathrm{b}}_3$ Plane ($h_a = 0$)

Of considerable interest are the bifurcations from the nominal-spin equilibrium, including the Type 4 branches in the $\hat{\mathrm{b}}_1$–$\hat{\mathrm{b}}_3$ plane. Chinnery and Hall studied the bifurcations in this plane

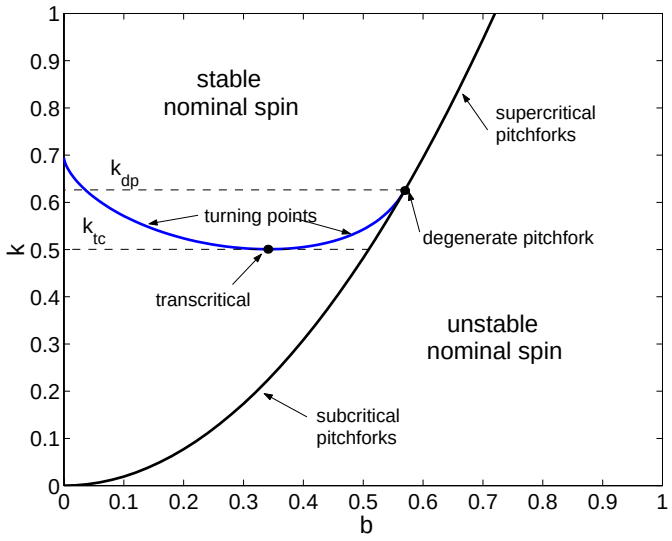

Figure 6.3: Bifurcations in the k–b parameter plane; $h_a = 0$

for the $\mathcal{B} + \mathcal{P}$ case. We first study the equivalent case, for $h_a = 0$, before proceeding to the more general case for $h_a \neq 0$. Focusing on the $h_1 = 1$ spin, the bifurcation point is described in terms of the damper parameters by the stability condition Eq. 4.9. Using this relationship,

$$k = \frac{-b^2 \varepsilon^2 \lambda^3}{I_1'^2 \left(I_1' + \lambda I_3\right)} \tag{6.28}$$

the locus of nominal-spin bifurcation points is established on the k–b parameter plane. However, other turning points exist in the $\hat{\mathbf{b}}_1$–$\hat{\mathbf{b}}_3$ plane which may be characterized in parameter space with two-parameter continuation. The complete picture is shown in Fig. 6.3. We include a series of h_3–b bifurcation diagrams for a range of k, as shown in Fig. 6.4, to illustrate the equilibria corresponding to specific k values in Fig. 6.3. To simplify the bifurcation diagrams, we only include the equilibrium branches associated with the nominal-spin pitchfork (for $h_1 = +1$) and the related turning points. The other system parameters for Figs. 6.3–6.4 are $\mathbf{I} = \text{diag}\,[0.40, 0.28, 0.32]$, $I_s = 0.04$, $c = 0.1$, and $\varepsilon = 0.1$. Unless otherwise noted, we use these same parameters for all the numerical result in this chapter.

The nominal-spin bifurcation line divides the parameter space into stable and unstable nominal-spin equilibria. Superimposed on this space is the line of turning points which emanate from the degenerate pitchfork point. For fixed values of k, there are possibly 0, 1 or 2 pairs of turning points in the pitchfork branches for varying b. The transcritical bifurcation occurs at parameters b_{tc} and k_{tc}. For values of $k < k_{tc}$, there are no turning points on the subcritical pitchfork branch, seen in Fig. 6.4(a). The transcritical point bifurcation in Fig. 6.4(b) is the only singular point on the subcritical pitchfork branch. Increasing spring stiffness slightly, there are two pairs of turning points as seen in Fig. 6.4(c). The threshold between subcritical and supercritical pitchforks is a

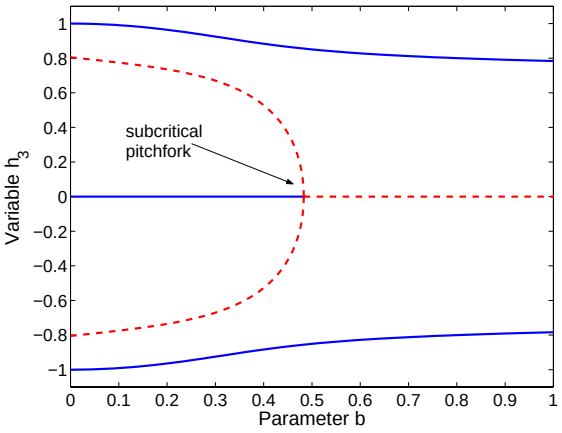

(a) $k = 0.45 < k_{tc}$

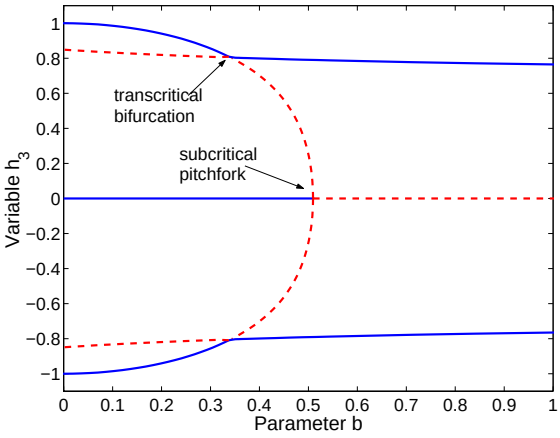

(b) $k = 0.50075 = k_{tc}$

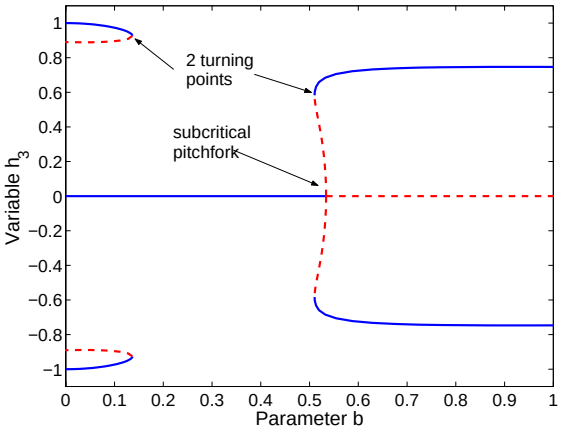

(c) $k = 0.55, k_{tc} < k < k_{dp}$

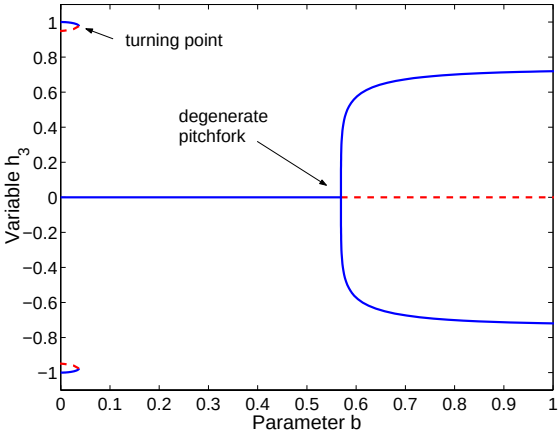

(d) $k = 0.625 = k_{dp}$

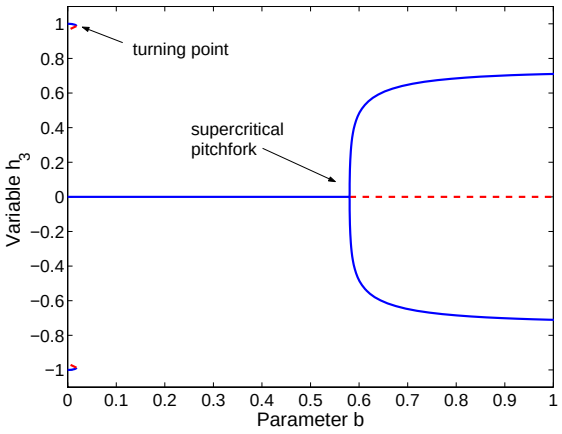

(e) $k = 0.65 > k_{dp}$

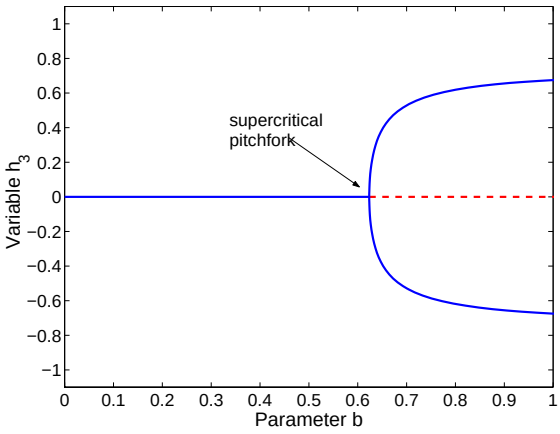

(f) $k = 0.75$

Figure 6.4: Bifurcation diagrams, h_3 *vs.* b, for different k, illustrating selected points in k–b parameter space for $h_a = 0$

degenerate pitchfork, as shown in Fig. 6.4(d), with parameters b_{dp} and k_{dp}. As k slightly exceeds k_{dp}, the pitchfork is supercritical, and there is a single pair of turning points as shown in Fig. 6.4(e). As k increases further, there are zero turning points, as shown in Fig. 6.4(f). These results are qualitatively the same as those found by Chinnery and Hall,[17] with the only differences due to selection of parameters and non-dimensionalization.

The degenerate pitchfork point is especially important to determine. This marks the transition from subcritical to supercritical pitchfork bifurcations. With the associated stability changes of the pitchfork branches, the supercritical bifurcation does not exhibit the jump phenomenon of the subcritical pitchfork (Fig. 6.4(c)). Liapunov-Schmidt reduction is used to analytically determine the k-b relationship for the degenerate pitchfork point.

Some distinguishing feature of the reduced function derivatives must be exploited to make use of the reduction. The qualitative properties of the local bifurcation of the full equations are equivalent to the scalar normal form for a pitchfork bifurcation

$$g(u,\alpha) = u\alpha \pm u^3 = 0 \tag{6.29}$$

with the $\pm$ corresponding to a supercritical or subcritical pitchfork. The reduced, scalar function $g(u,\alpha)$ has a pitchfork bifurcation at $g(0,0)$ when

$$g = g_u = g_{uu} = g_\alpha = 0 \tag{6.30}$$

and

$$g_{\alpha u} > 0$$
$$g_{uuu} \begin{cases} > 0 & \text{subcritical} \\ < 0 & \text{supercritical} \end{cases}$$

with the latter inequality depending on the $\pm$ sign in Eq. 6.29.

We translate the bifurcation point to the origin using the mapping

$$(h_1, h_2, h_3, p_n, x, b) \mapsto (h_1 + 1, h_2, h_3, p_n, x, \alpha + b)$$

so that the bifurcation point $\mathbf{f}(\mathbf{z},\alpha) = \mathbf{f}(\mathbf{0},0) = \mathbf{0}$. In state-parameter space, the Jacobian becomes

$$\mathbf{A} = \begin{bmatrix} I_3 - I_1' & 0 & -b\varepsilon \\ -b\varepsilon I_1' I_3 & 0 & b^2\varepsilon^2 I_1' I_3 / (I_3 - I_1') \\ 0 & -2 & 0 \end{bmatrix} \tag{6.31}$$

As described in Sec. 6.1.2, we select orthogonal subspaces $\mathbf{M}$ and $\mathbf{N}$ and choose basis vectors per Eq. 6.17–6.20. The null space of $\mathbf{A}$ is spanned by the vector

$$\mathbf{n}_A = \left[\frac{b\varepsilon}{I_3 - I_1'},\ 0,\ 1 \right] \tag{6.32}$$

The range space of $\mathbf{A}$ is spanned by the two vectors

$$\mathbf{r}_1 = \left[1,\ \frac{b\varepsilon I_1' I_3}{I_1' - I_3},\ 0\right] \tag{6.33}$$

$$\mathbf{r}_2 = [0,\ 0,\ 1] \tag{6.34}$$

The subspace $\mathbf{N}$ is the left null space of $\mathbf{A}$, spanned by the vector

$$\mathbf{n}_R = \left[\frac{b\varepsilon I_1' I_3}{I_3 - I_1'},\ 1,\ 0\right] \tag{6.35}$$

The subspace $\mathbf{M}$ is the row space of $\mathbf{A}$, spanned by the two vectors

$$\mathbf{m}_1 = [I_3 - I_1',\ 0,\ -b\varepsilon] \tag{6.36}$$

$$\mathbf{m}_2 = [0,\ 1,\ 0] \tag{6.37}$$

The projection matrix onto $\mathcal{R}(\mathbf{A})$ is

$$\mathbf{E} = \frac{1}{D_1}\begin{bmatrix} (I_3 - I_1')^2 & b\varepsilon I_1' I_3 (I_1' - I_3) & 0 \\ b\varepsilon I_1' I_3 (I_1' - I_3) & (b\varepsilon I_1' I_3)^2 & 0 \\ 0 & 0 & D_1 \end{bmatrix} \tag{6.38}$$

where

$$D_1 = (I_3 - I_1')^2 + (b\varepsilon I_1' I_3)^2$$

The non-singular transformation from $\mathcal{R}(\mathbf{A})$ to $\mathbf{M}$ is found using the method described in the previous section,

$$\mathbf{A}^{-1} = \frac{1}{D_2}\begin{bmatrix} (I_3 - I_1')^3 & -b\varepsilon I_1' I_3 (I_1' - I_3)^2 & 0 \\ 0 & 0 & -D_2/2 \\ -b\varepsilon (I_3 - I_1')^2 & b^2\varepsilon^2 I_1' I_3 (I_3 - I_1') & 0 \end{bmatrix} \tag{6.39}$$

where

$$D_2 = \left[(I_3 - I_1')^2 + b^2\varepsilon^2\right]\left[(I_3 - I_1')^2 + (b\varepsilon I_1' I_3)^2\right] \tag{6.40}$$

The partial derivatives of the implicit scalar function, $g(u, b)$ are calculated using Eqs. 6.12– 6.16. After verifying $g = g_u = g_{uu} = g_\alpha = 0$, the following expressions are produced for the remaining partial derivatives

$$g_{\alpha u} = \frac{\varepsilon^2 I_3^2}{I_1' - I_3} \tag{6.41}$$

$$g_{uuu} = \frac{12\varepsilon^3 b^2 I_3^2[\varepsilon' I_1'(I_1' - I_3) + b^2\varepsilon(I_3 - 2I_1')]}{I_1'(2I_1' - I_3)} \tag{6.42}$$

For $I_1' > I_3$, $g_{\alpha u} > 0$ for any value of b, so the critical value is determined from g_{uuu}. The transition from subcritical to supercritical occurs when $g_{uuu} = 0$, therefore the value of b for the degenerate pitchfork is determined by

$$b_{dp}^2 = \frac{\varepsilon' I_1'(I_1' - I_3)}{\varepsilon(2I_1' - I_3)} \tag{6.43}$$

Using Eq. 4.9, the critical spring stiffness is

$$k_{dp} = \frac{\varepsilon'\varepsilon}{I_1'(2I_1' - I_3)} \tag{6.44}$$

This leads to a design guideline for avoiding the jump phenomenon. For $k > k_{dp}$, the pitchfork is supercritical, and there is no jump phenomenon.

For $I_1' < I_3$ and $h_a = 0$, the pitchfork bifurcation does not exist. Not all combination of parameters produce a pitchfork bifurcation. Examining Eq. 4.9, we see that a bifurcation point only exists for $h_a > 1 - I_1'/I3$. For $h_a = 0$, this only occurs for $I_1' > I_3$. Therefore, the $\mathcal{B} + \mathcal{P}$ model only exhibits bifurcations of equilibria for $I_1' > I_3$.

6.3 Parameter Space for $\hat{\mathbf{b}}_1$–$\hat{\mathbf{b}}_3$ Plane ($h_a \neq 0$)

In the previous section, we examined equilibria in the k–b parameter plane for $h_a = 0$. In this section, we consider $h_a \neq 0$. We first describe equilibria with $\mathbf{h}$ in the $\hat{\mathbf{b}}_1$–$\hat{\mathbf{b}}_3$ body-axis plane by using the k–b parameter plane, for a given value of h_a. Then, we fix the value of b and examine equilibria in the k–h_a parameter plane.

6.3.1 Equilibria in the k–b Parameter Plane, for Fixed h_a

We expand the scope of bifurcations in the k–b plane and consider the effects of rotor momentum. With three possible bifurcation parameters, we keep one parameter fixed while performing two-parameter continuation on the remaining two parameters. The natural extension of the previous section is to determine the k–b parameter chart for different h_a values.

Equation. 4.9 and two-parameter continuation generate branches of singular points (pitchfork bifurcation points and turning points) in k–b parameter space for different values of h_a. However, the Liapunov-Schmidt reduction must be modified to analytically determine the degenerate pitchfork bifurcation point.

We translate the bifurcation point to the origin using the mapping

$$(h_1, h_2, h_3, p_n, x, b) \mapsto (h_1 + 1, h_2, h_3, p_n, x, \alpha + b)$$

so that the bifurcation point $\mathbf{f}(\mathbf{z},\alpha)=\mathbf{f}(\mathbf{0},0)=\mathbf{0}$. In state-parameter space, the Jacobian becomes

$$\mathbf{A}=\begin{bmatrix} -I_1'-I_3\lambda & 0 & b\varepsilon\lambda \\ b\varepsilon\lambda I_1' I_3 & 0 & -b^2\varepsilon^2\lambda^2 I_1' I_3/\left(I_1'+I_3\lambda\right) \\ 0 & -2 & 0 \end{bmatrix} \tag{6.45}$$

where $\lambda = h_a - 1$.

We select orthogonal subspaces $\mathbf{M}$ and $\mathbf{N}$ and choose basis vectors per Eqs. 6.17–6.20. The null space of $\mathbf{A}$ is spanned by the vector

$$\mathbf{n}_A=\left[\frac{b\varepsilon\lambda}{I_1'+I_3\lambda},\ 0,\ 1\right] \tag{6.46}$$

The range space of $\mathbf{A}$ is spanned by the two vectors

$$\mathbf{r}_1 = \left[1,\ \frac{-b\varepsilon I_1' I_3\lambda}{I_1'+I_3\lambda},\ 0\right] \tag{6.47}$$

$$\mathbf{r}_2 = [0,\ 0,\ 1] \tag{6.48}$$

The subspace $\mathbf{N}$ is the left null space of $\mathbf{A}$, spanned by the vector

$$\mathbf{n}_R=\left[b\varepsilon\lambda I_1' I_3,\ I_1'+I_3\lambda,\ 0\right]; \tag{6.49}$$

The subspace $\mathbf{M}$ is the row space of $\mathbf{A}$, spanned by the two vectors

$$\mathbf{m}_1 = [-I_1'-I_3\lambda,\ 0,\ b\varepsilon\lambda] \tag{6.50}$$

$$\mathbf{m}_2 = [0,\ 1,\ 0] \tag{6.51}$$

The projection matrix onto $\mathcal{R}(\mathbf{A})$ is

$$\mathbf{E}=\frac{1}{D_3}\begin{bmatrix} \left(I_1'+I_3\lambda\right)^2 & -b\varepsilon\lambda I_1' I_3\left(I_1'+I_3\lambda\right) & 0 \\ -b\varepsilon\lambda I_1' I_3\left(I_1'+I_3\lambda\right) & \left(b\varepsilon\lambda I_1' I_3\right)^2 & 0 \\ 0 & 0 & D_3 \end{bmatrix} \tag{6.52}$$

where

$$D_3=\left(I_1'+I_3\lambda\right)^2+\left(b\varepsilon\lambda I_1' I_3\right)^2$$

The non-singular transformation from $\mathcal{R}(\mathbf{A})$ to $\mathbf{M}$ is found using the method described in the previous section,

$$\mathbf{A}^{-1}=\frac{1}{D_4}\begin{bmatrix} -\left(I_1'+I_3\lambda\right)^3 & b\varepsilon\lambda I_1' I_3\left(I_1'+I_3\lambda\right)^2 & 0 \\ 0 & 0 & -D_4/2 \\ b\varepsilon\lambda\left(I_1'+I_3\lambda\right)^2 & -b^2\varepsilon^2\lambda^2 I_1' I_3\left(I_1'+I_3\lambda\right) & 0 \end{bmatrix} \tag{6.53}$$

where

$$D_4 = \left[\left(I_1' + I_3\lambda\right)^2 + \left(b\varepsilon\lambda\right)^2\right]\left[\left(I_1' + I_3\lambda\right)^2 + \left(b\varepsilon\lambda I_1' I_3\right)^2\right] \tag{6.54}$$

The partial derivatives of the implicit scalar function, $g(u,b)$ are calculated using Eqs. 6.12– 6.16. After verifying $g = g_u = g_{uu} = g_\alpha = 0$, the following expressions are produced for the remaining partial derivatives

$$g_{\alpha u} = \frac{-2b\varepsilon^2 I_3^2\lambda^3}{I_1' + I_3\lambda} \tag{6.55}$$

$$g_{uuu} = \frac{-3b^2\varepsilon^3 I_3^2\lambda^4\left[-4\varepsilon' I_1'\left(I_1' + I_3\lambda\right)^2 + b^2\varepsilon\left[\left(3I_1' + 2I_3\lambda\right)^2 + 9I_1'^2\lambda\right]\right]}{I_1'\left(I_1' + I_3\lambda\right)^2} \tag{6.56}$$

The partial derivative $g_{\alpha u} > 0$ for any value of b for $h_a < 1$ ($\lambda < 0$), but $g_{\alpha u} < 0$ for $h_a > 1$. However, for $h_a > 1$ there is no pitchfork bifurcation point. The condition $h_a > 1$ always satisfies Eq. 4.9, and the nominal spin equilibria do not bifurcate. The degenerate pitchfork is defined by the condition, $g_{uuu} = 0$. Therefore, the value of b for the degenerate pitchfork is determined by

$$b_{dp}^2 = \frac{4\varepsilon' I_1'\left(I_1' + I_3\lambda\right)^2}{\varepsilon\left[\left(3I_1' + 2I_3\lambda\right)^2 + I_1'^2\lambda\right]} \tag{6.57}$$

Using Eq. 4.9, the critical spring stiffness is

$$k_{dp} = \frac{-4\varepsilon\varepsilon'\lambda^3\left(I_1' + I_3\lambda\right)}{I_1'\left[I_1'^2\lambda + \left(3I_1' + 2I_3\lambda\right)^2\right]} \tag{6.58}$$

This leads to a more general design guideline for avoiding the jump phenomena, for $h_a \neq 0$. For $k > k_{dp}$, the pitchfork is supercritical. For $h_a = 0$, the expression reduces to Eq. 6.44.

Combining the nominal-spin bifurcation point information with two-parameter continuation provides a means to generate parameter charts for a variety of angular momenta. Not all values of h_a correspond to a bifurcation of the $h_1 = +1$ nominal spin. As discussed in Sec. 6.2 and above, Eq. 4.9 provides an existence condition for pitchfork bifurcations along the $h_1 = +1$ axis:

$$1 - I_1'/I_3 < h_a < 1 \tag{6.59}$$

For oblate and near-oblate ($I_1' > I_3$) gyrostats, a pitchfork bifurcation is possible for $h_a < 0$, but only to this limit. Numerical studies demonstrate that degenerate pitchforks cease to exist near the lower limit of Eq. 6.59. Therefore, we select a range of h_a values and examine how rotor momentum affects the nominal-spin bifurcation branches and the degenerate pitchfork transition.

For a range of $h_a \in (-0.05, 0.2)$, the nominal bifurcation branches and degenerate pitchfork points are plotted in Fig. 6.5. Recalling that points in parameter space above each line represent stable nominal spins, we conclude that increasing rotor momentum creates a larger region of stable nominal spins. Since greater rotor momentum should more strongly stabilize the nominal spin

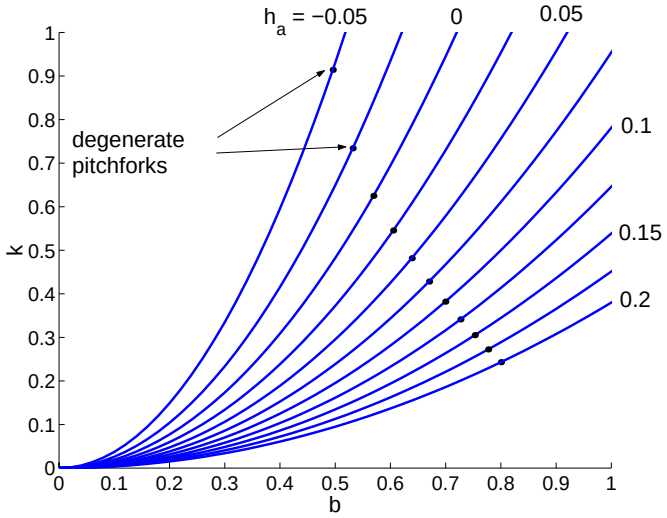

Figure 6.5: Nominal-spin bifurcation branches in the k–b parameter plane

of like sense (positive), this result agrees with intuition. What we also see in Fig. 6.5 is that for increasing rotor momentum, the degenerate pitchfork point is affected. For a given damper position, the transition to a supercritical pitchfork occurs for a softer spring stiffness.

We look more closely at the bifurcation branches, including the turning points in the $\hat{\mathbf{b}}_1$–$\hat{\mathbf{b}}_3$ plane, using two-parameter continuation. We use numerical continuation to produce h_3–b bifurcation diagrams for $h_a = -0.05$ and different values of k, as shown in Fig. 6.6. The corresponding parameter chart in k–b space is Figure 6.7.

Due to the symmetry of the bifurcation diagrams, we only describe the equilibria for $h_3 > 0$. Figure 6.6(a), for $k = 0.9$, includes a separate, continuous Type 4 branch of equilibria, with a single turning point in the nearly degenerate pitchfork. For $k = 0.76$, Figure 6.6(c) shows that the separate Type 4 branch includes two turning points that mark the ends of a stable Type 4 branch, whereas the pitchfork has a single turning point. Between Figs. 6.6(a) and 6.6(c), there is a critical value of k where a singular point first appears in the separate Type 4 branch as an inflection point. This critical value is $k = 0.791$, and the inflection point corresponds to a discontinuity in the k–b parameter chart (Fig. 6.6). This point is called a cusp, or hysteresis point. The region of parameter space near the cusp may have 0, 1 or 2 singular points, not including the nominal-spin bifurcation. Figure 6.6 illustrates the evolution of these turning points for a range of k. The transcritical bifurcation, discussed in Ch. 5, occurs for $k = 0.7524$. The range of possible equilibria is concisely and completely described in k–b parameter space by Fig. 6.7.

The cusp in the k–b parameter space only occurs for $h_a < 0$. For $h_a > 0$, the k–b parameter chart resembles the $h_a = 0$ case. Figure 6.8 is an example, illustrating how the branches flatten out in parameter space, as also seen in Fig. 6.5.

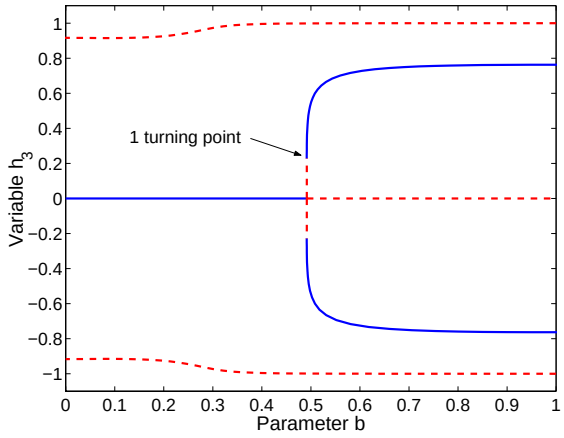

(a) $k = 0.9$

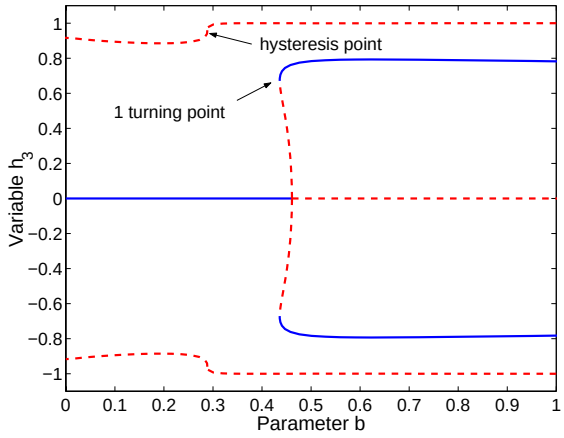

(b) $k = 0.791$

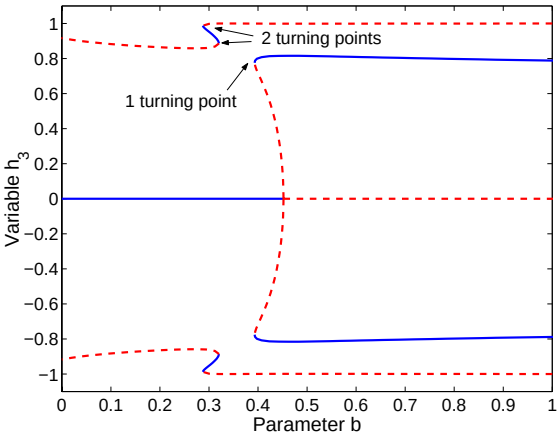

(c) $k = 0.76$

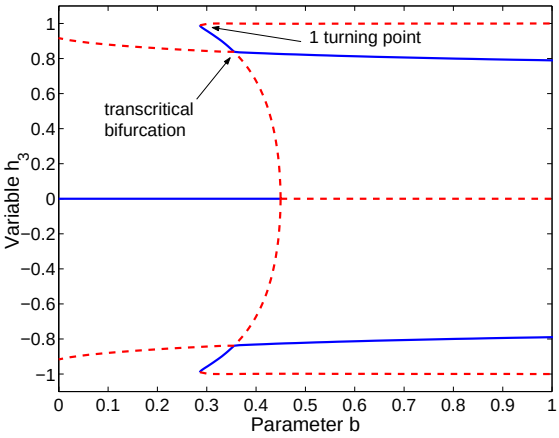

(d) $k = 0.7524$

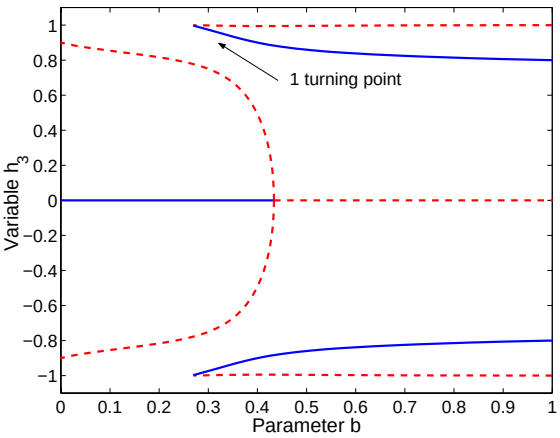

(e) $k = 0.7$

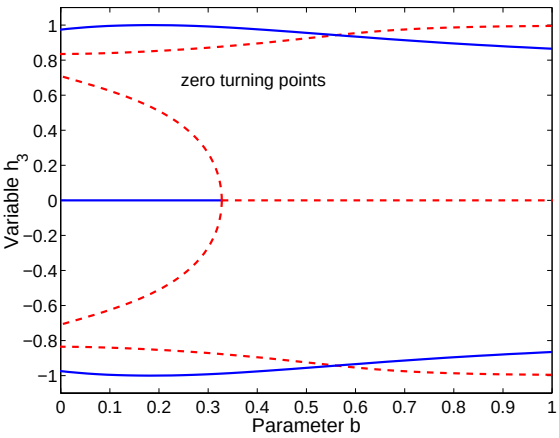

(f) $k = 0.4$

Figure 6.6: Bifurcation diagrams, h_3 *vs.* b, illustrating the evolution of equilibria and singular points as k decreases for $h_a = -0.05$

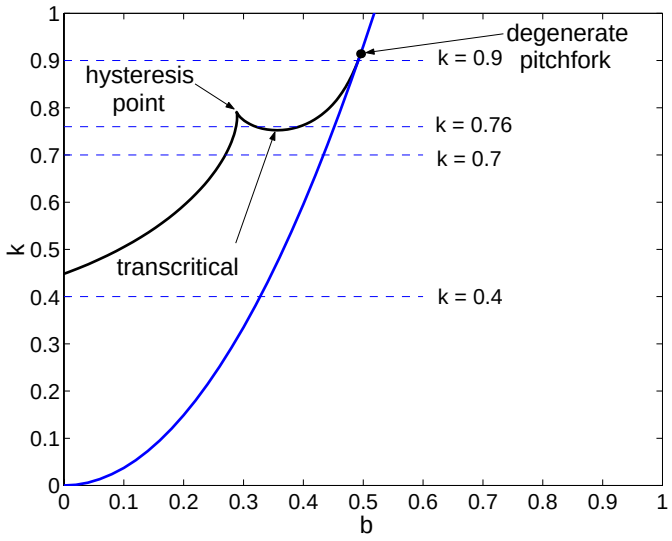

Figure 6.7: Bifurcations in the k–b parameter plane; $h_a = -0.05$

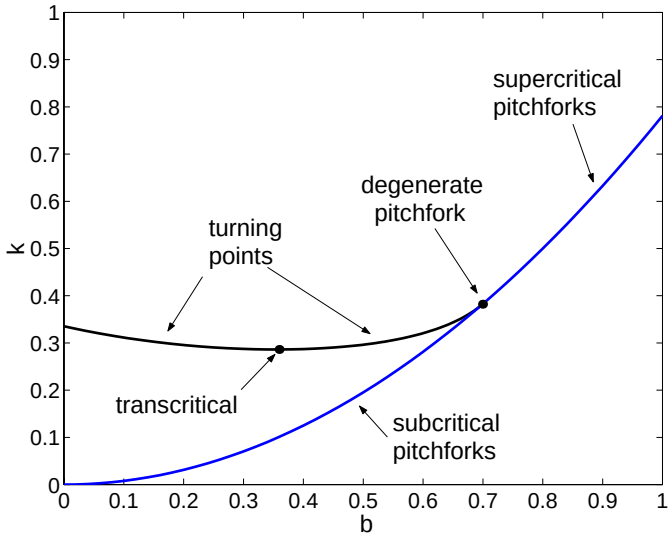

Figure 6.8: Bifurcations in the k–b parameter plane; $h_a = 0.1$

6.3.2 Equilibria in the k–h_a Parameter Plane, for Fixed b

We focus on the k–h_a parameter plane and identify the equilibria in the $\hat{\mathbf{b}}_1$–$\hat{\mathbf{b}}_3$ plane. The degenerate pitchfork, occurring in h_3–b bifurcation diagrams, is also found in h_3–h_a bifurcation diagrams. These degenerate points are related to the existence of stable Type 4 branches of equilibria, and are therefore of practical importance.

For an oblate gyrostat, there can be stable Type 4 branches of equilibria (Fig. 5.28). Numerically, we can determine regions in parameter space where these stable branches occur, and where they are absent. The existence of certain stable branches is important because they may affect the jump phenomenon for changing rotor momentum. The stable Type 4 branches also exist for the prolate or intermediate-axis gyrostats, provided $I_3 > I_2$. This section considers only oblate gyrostats, but similar numerical studies are possible for the other cases.

Jump phenomena are also evident in the h_a–bifurcations of Ch. 5. Figure 5.28 shows a pitchfork bifurcation of the nominal-spin branch of equilibria, for $h_1 = \pm 1$. We focus in this section on the $h_1 = +1$ bifurcation point, but there is an equivalent set of results for the $h_1 = -1$ case. The nominal branch bifurcation point is supercritical, with stable nominal spins for h_a greater than the bifurcation value. A credible design point would be to operate on this stable nominal branch, but if for some reason rotor momentum were lost, the system would be perturbed to another stable equilibrium condition. This is a big jump: using simulation we show that the unstable nominal spin is attracted to a Type 4 equilibrium, with $x \neq 0$, as shown in Fig. 6.9.

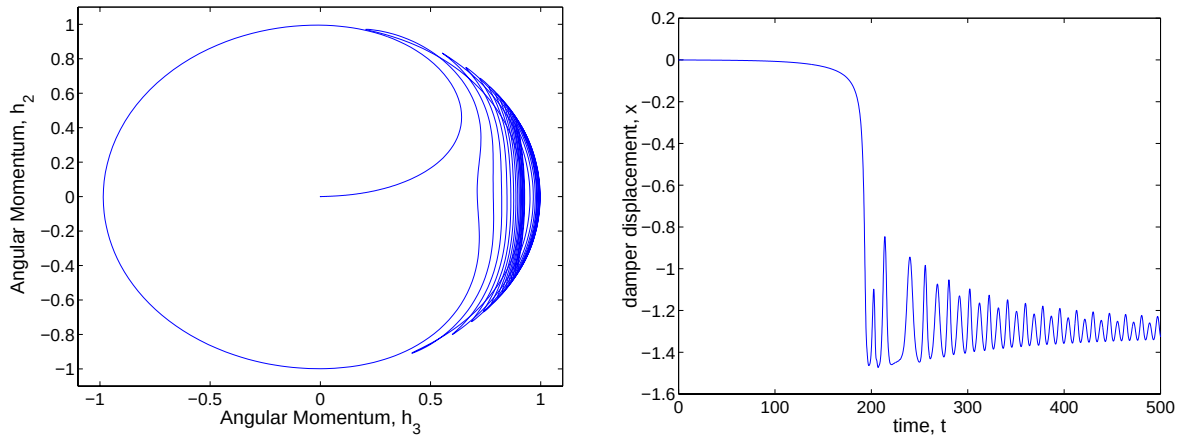

(a) h_2 *vs.* h_3 (b) x *vs.* time

Figure 6.9: Simulation of jump phenomena from a nominal spin. For h_a slightly lower than the nominal-spin bifurcation value, the system jumps to a Type 4 equilibrium state.

Figures 5.28– 5.31 show how the stable Type 4 branches of equilibria consist of branches between two turning points, and these branches ultimately converge as k increases. We use two parameter continuation to trace these turning points in parameter space and establish the hysteresis point

where they converge. However, we show that these two turning points do not always converge in a hysteresis point, but may converge on the nominal bifurcation point, creating a degenerate pitchfork.

Two-parameter continuation is used to trace the first and second turning points of the branches emanating from the nominal bifurcation point (for $h_1 = +1$). The system parameters are

Table 6.1: System parameters for oblate gyrostat equilibria, two-parameter continuation

Inertia Properties	Damper Parameters
$I_1 = 0.40$	$\varepsilon = 0.10$
$I_2 = 0.28$	$c = 0.10$
$I_3 = 0.32$	
$I_s = 0.04$	

We first consider the bifurcation branches of the turning points for $b = 0$ and $b = 0.33$ (Fig. 6.10). Both cases generate a cusp in parameter space. This point defines the point in parameter space where the stable Type 4 branch disappears. For $k > k_{cusp}$, Type 1 equilibria are the only possible stable spins. As with earlier examples of cusps in parameter space, there can be 0, 1, or 2 pairs of turning points depending on the region of parameter space.

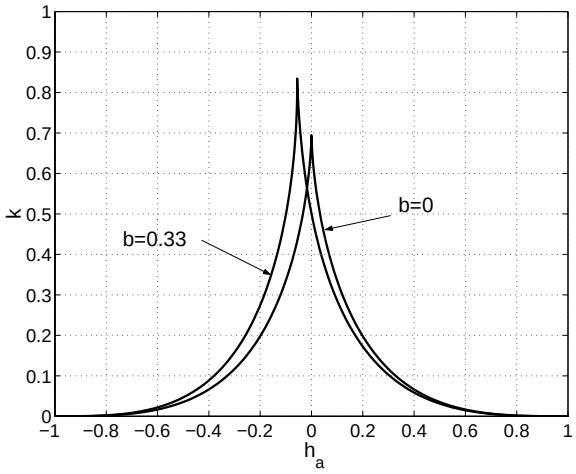

Figure 6.10: Bifurcation branches in the k–h_a parameter plane: $b = 0$ and $b = 0.33$

Certainly, the absence of stable Type 4 branches means if rotor momentum is lost, an $h_1 = +1$ spin will become an $h_1 = -1$ spin. However, this jump may also occur for a small, stable Type 4 branch. If the stable Type 4 branch only occurs for h_a greater than the bifurcation point, the jump will behave as if there were no stable Type 4 branches. To find this transition in parameter space,

we plot the turning point branches along with the locus of nominal bifurcation points in Fig. 6.11. The key point is where the two branches of singular points cross. For k greater than this point, stable Type 4 branches exist, but only for h_a greater than the nominal bifurcation point. For k less than this jump transition point, a nominal equilibrium perturbed to a lower rotor momentum will jump to the corresponding Type 4 equilibrium point. For this example, the two bifurcation branches cross at $k = 0.6194$, which is used to generate Fig. 6.12.

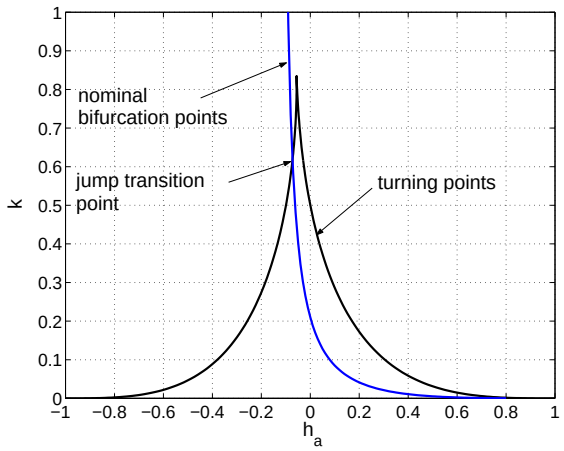

Figure 6.11: Bifurcations in the k–h_a parameter plane; $b = 0.33$

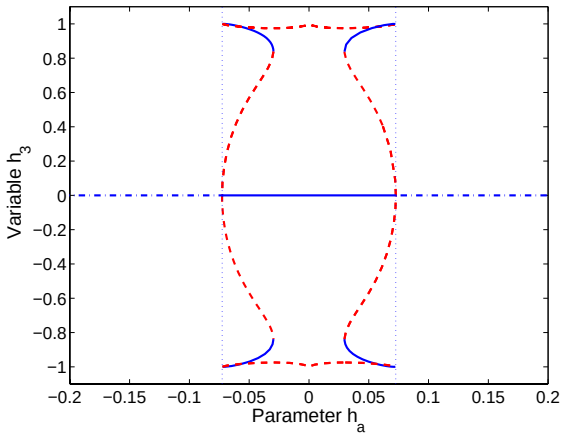

Figure 6.12: Bifurcation diagram: h_3 *vs.* h_a for $b = 0.33$, $k = 0.6194$

As b increases further, there is no longer a cusp, but the turning points ultimately merge with the nominal bifurcation branch, resulting in a degenerate pitchfork. These degenerate points are the same in parameter space as those defined in Sec. 6.3.1. The degenerate pitchfork is identified by Eq. 6.57, and yields a critical value for $\pm b$ for a given value of λ. Due to the symmetry of the problem, the $-b$ case is not separately discussed. For the k–h_a perspective in parameter space, a given value of b yields two distinct values of h_a. For a given value of b, Eq. 6.57 produces real values of h_a when

$$b^2 > \frac{16\varepsilon'(I_1' - I_3)}{\varepsilon(I_1' + 24I_3)} \tag{6.60}$$

For the parameters of the preceding example, the critical value of damper location is $b = 0.4788$. For b below this threshold, a cusp appears in the parameter chart as the two turning points converge for increasing k. For b above this threshold there are two distinct degenerate pitchfork bifurcation points that mark the points in parameter space where the turning points converge with the nominal bifurcation branch. Figure 6.13 shows the bifurcation branches for both turning points of the stable Type 4 branch. Instead of converging, they move toward and combine with the branch of nominal bifurcation points. The k values of the two degenerate points are denoted k_{dg1} and k_{dg2}.

Figures 6.14– 6.15 show the bifurcation diagrams including the pitchforks before and after the degenerate points. The first (lower) turning point converges with the nominal bifurcation point first. For $k_{dg1} < k < k_{dg2}$, the pitchfork branches are stable, precluding any jump phenomena.

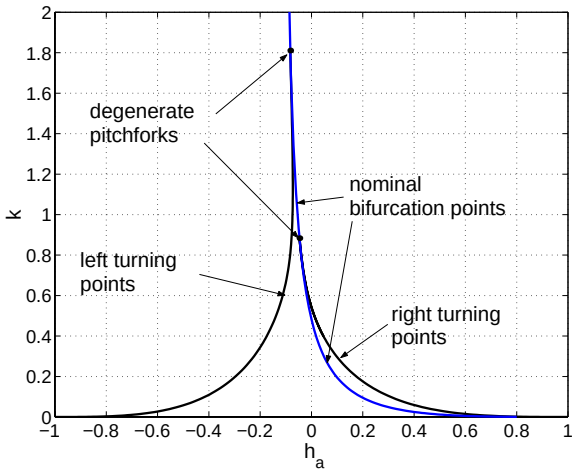

Figure 6.13: Bifurcations in the k–h_a parameter plane: $b = 0.5$

The second turning point becomes degenerate for a higher value of spring stiffness, $k = k_{dg2}$. Increasing k further results in entirely unstable Type 4 equilibria, and therefore the nominal spin is the only stable equilibrium.

6.4 Summary

We used two-parameter continuation and Liapunov-Schmidt reduction to characterize bifurcations in k-b-h_a parameter space. Using two-parameter continuation and the stability criterion for the nominal spin, we produce parameter charts that describe a set of possible singular points in parameter space. We identify subcritical, degenerate, and supercritical pitchfork bifurcations of the nominal-spin equilibrium. We also determine branches of turning points in the $\hat{\mathbf{b}}_1$–$\hat{\mathbf{b}}_3$ plane and their relationship with the nominal-spin equilibria. Special cases are identified, including a transcritical bifurcation and cusps in parameter space. Liapunov-Schmidt reduction generates an analytical relationship between k, b, and h_a that identifies a degenerate pitchfork bifurcation of the nominal spin equilibrium. The degenerate pitchforks are seen in several perspectives, including the h_3–b and h_3–h_a bifurcation diagrams. For larger values of b, two degenerate pitchfork points may occur in the k–h_a parameter space. The degenerate point marks the transition between subcritical and supercritical pitchforks, and provides a design criterion to avoid jump phenomena.

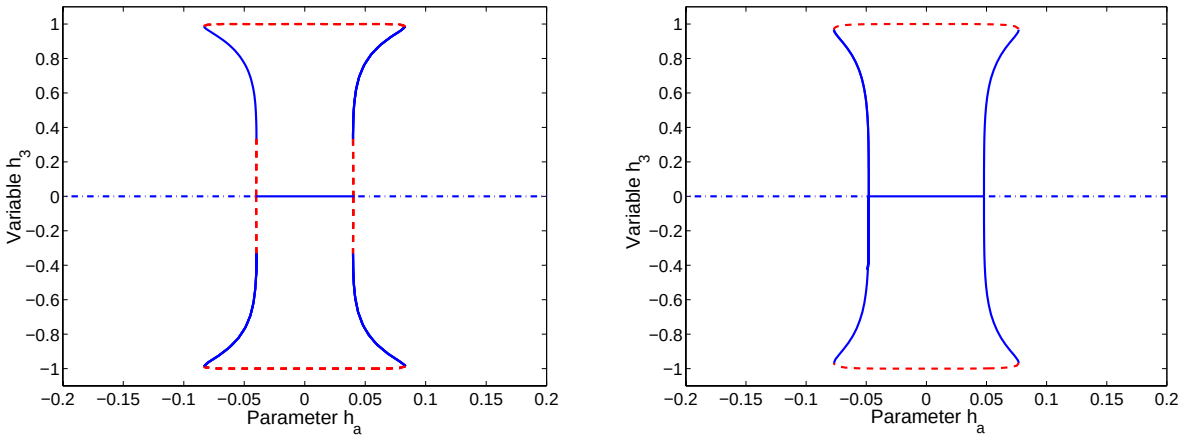

(a) $k = 0.8$ (b) $k = 0.9$

Figure 6.14: Bifurcation diagrams, h_3 *vs.* h_a, near the first degenerate pitchfork for $b = 0.5$. As k increases from $0.8 \rightarrow 0.9$, the turning points on Type 4 branches converge with the nominal-spin bifurcation point, forming degenerate pitchforks. Another set of limit points remains in the Type 4 branches of equilibria.

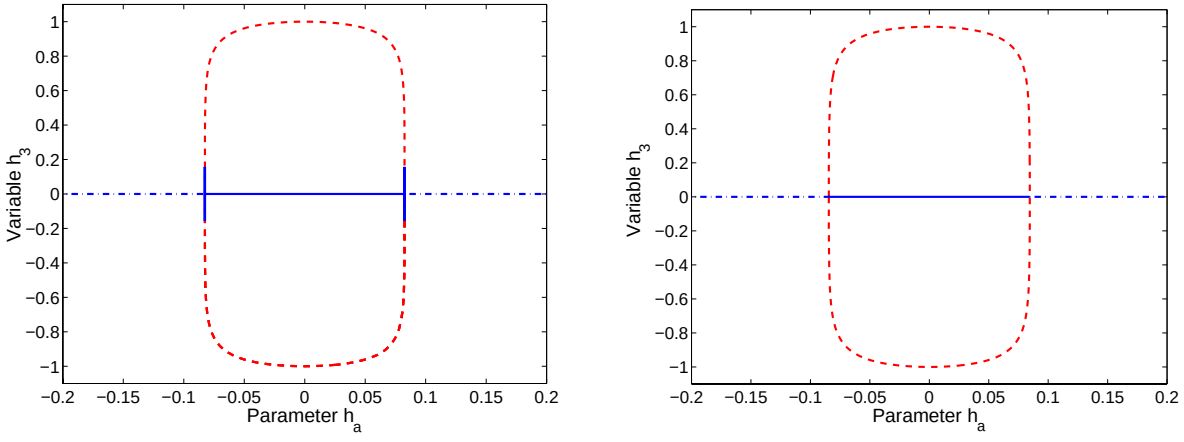

(a) $k = 1.8$ (b) $k = 1.9$

Figure 6.15: Bifurcation diagrams, h_3 *vs.* h_a, near the second degenerate pitchfork for $b = 0.5$. As k increases from $1.8 \rightarrow 1.9$, the final set of turning points on the Type 4 branches converge with the nominal-spin bifurcation point, forming degenerate pitchforks.

Chapter 7

Bifurcations of Perturbed Model

The $\mathcal{B}+\mathcal{R}+\mathcal{P}$ model of a damped gyrostat has precise alignment requirements for the rotor and damper; each are aligned with the $\hat{\mathbf{b}}_1$ axis. Any real dual-spin satellite is likely to have some misalignment of the damper or rotor. In Sec. 5.1 we saw how bifurcations are easily perturbed, and the symmetric bifurcation structures unfold. In this chapter we investigate the effects of small alignment errors for the rotor and damper, and examine the possible unfolding of bifurcations. The loss of these symmetric bifurcations may affect the nominal spin condition, and can change how the system reacts to displacements from the nominal spin.

The standard, unperturbed model is perturbed by adding small angular displacements to the unit vectors $\hat{\mathbf{a}}$ and $\hat{\mathbf{n}}$. Many different combinations of vector perturbations are possible, but we focus on two distinct cases: displacement within the $\hat{\mathbf{b}}_1$–$\hat{\mathbf{b}}_3$ plane (denoted *in-plane*) and perpendicular to the $\hat{\mathbf{b}}_1-\hat{\mathbf{b}}_3$ plane (denoted *out-of-plane*). Introducing the angular displacements as perturbation parameters generates perturbed bifurcation structures from the standard model bifurcations. We start with two standard, unperturbed configurations: an oblate gyrostat and a prolate gyrostat with identical dampers. For each case, we first look at the effects on system equilibria for rotor misalignment, both in-plane and out-of-plane. Then we consider the effects of damper misalignment. The resulting bifurcation structures show how certain symmetries and bifurcations are broken by specific perturbation parameters.

7.1 Perturbed Model

The standard model is repeated in Fig. 7.1, showing the rotor spin vector, $\hat{\mathbf{a}}$, and the damper alignment vector, $\hat{\mathbf{n}}$. These two unit vectors are parallel to the $\hat{\mathbf{b}}_1$ axis. The vector $\hat{\mathbf{n}}$ is within the $\hat{\mathbf{b}}_1$–$\hat{\mathbf{b}}_3$ plane, whereas $\hat{\mathbf{a}}$ may originate outside the $\hat{\mathbf{b}}_1$–$\hat{\mathbf{b}}_3$ plane.

We parameterize the possible rotor and damper alignment errors by defining an angular displacement cone angle and rotation angle, as seen in Fig. 7.2.

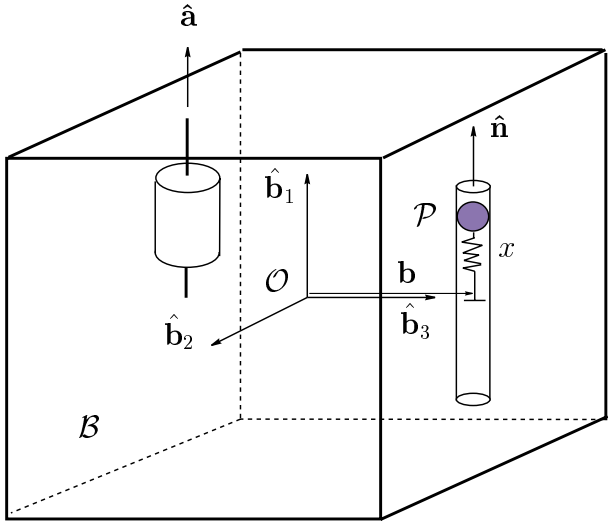

Figure 7.1: Standard model with aligned rotor and damper

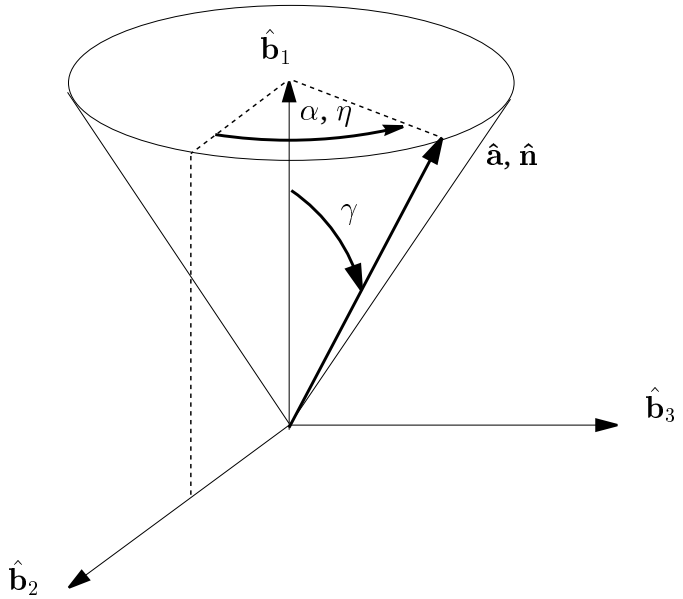

Figure 7.2: Rotor and damper alignment error angles are defined by a cone angle, γ, and a rotation angle: α or η is used to locate $\hat{\mathbf{a}}$ or $\hat{\mathbf{n}}$, respectively

The cone angle, γ, is a small angle displacing the unit vector $\hat{\mathbf{a}}$ or $\hat{\mathbf{n}}$ from the intended direction. The direction of the displacement is defined by α for $\hat{\mathbf{a}}$, and η for $\hat{\mathbf{n}}$. In terms of these parameters, the alignment vectors are

$$\hat{\mathbf{a}} = \cos\gamma_a \hat{\mathbf{b}}_1 + \cos\alpha \sin\gamma_a \hat{\mathbf{b}}_2 + \sin\alpha \sin\gamma_a \hat{\mathbf{b}}_3 \tag{7.1}$$

$$\hat{\mathbf{n}} = \cos\gamma_n \hat{\mathbf{b}}_1 + \cos\eta \sin\gamma_n \hat{\mathbf{b}}_2 + \sin\eta \sin\gamma_n \hat{\mathbf{b}}_3 \tag{7.2}$$

These perturbed vectors are used within Eqs. 3.68–3.70, for specific values of the alignment error angles, to numerically study the effects on equilibria of rotor and damper alignment errors. Table 7.1 defines the parameters used for each case. The larger cone angle is necessary for the out-of-plane case to clearly distinguish the perturbed bifurcations from the standard-model bifurcations.

Table 7.1: Rotor and Damper Alignment Errors

In-Plane Error	Out-of-Plane Error
$\gamma_a = 1^\circ$	$\gamma_a = 0^\circ$
$\gamma_n = 0^\circ$	$\gamma_n = 2^\circ$
$\alpha = 90^\circ$	$\alpha = 0^\circ$
$\eta = 0^\circ$	$\eta = 90^\circ$

7.2 Oblate Gyrostat

The oblate gyrostat is designed to spin about a major axis. We use the same system parameters for each result, only changing the rotor or damper alignment error angle.

Table 7.2: System parameters for oblate gyrostat used to determine perturbed equilibria

Inertia Properties	Damper Parameters
$I_1 = 0.40$	$k = 0.40$
$I_2 = 0.28$	$b = 0.33$
$I_3 = 0.32$	$\varepsilon = 0.10$
$I_s = 0.04$	$c = 0.10$

This combination of system parameters is the same standard model used in Ch. 5 to introduce the different types of equilibria. These parameters are used with the perturbed model to numerically investigate the effects on system equilibria.

7.2.1 Rotor Misalignment for Oblate Gyrostat

We investigate the effects of rotor misalignment by adding a small angular displacement to $\hat{\mathbf{a}}$. Two types of rotor alignment error are considered: in-plane and out-of-plane errors.

In-Plane Error

We apply numerical continuation to the perturbed model for a 1° perturbation of $\hat{\mathbf{a}}$, within the $\hat{\mathbf{b}}_1$–$\hat{\mathbf{b}}_3$ plane. Including this perturbation parameter breaks the structure of several pitchforks. We compare the perturbed bifurcations with the bifurcations of the standard model with the same system parameters from Ch. 5, shown in Figs. 5.4, 5.15, and 5.17. For this first example, the unperturbed bifurcations are repeated and shown with the perturbed bifurcations, as shown in Figs. 7.3–7.5. We denote the bifurcation points by the types of equilibria the bifurcation branches include. For example, the nominal-spin bifurcation is a pitchfork of Type 1 and Type 4 branches of equilibria, denoted a Type 1-4 bifurcation point.

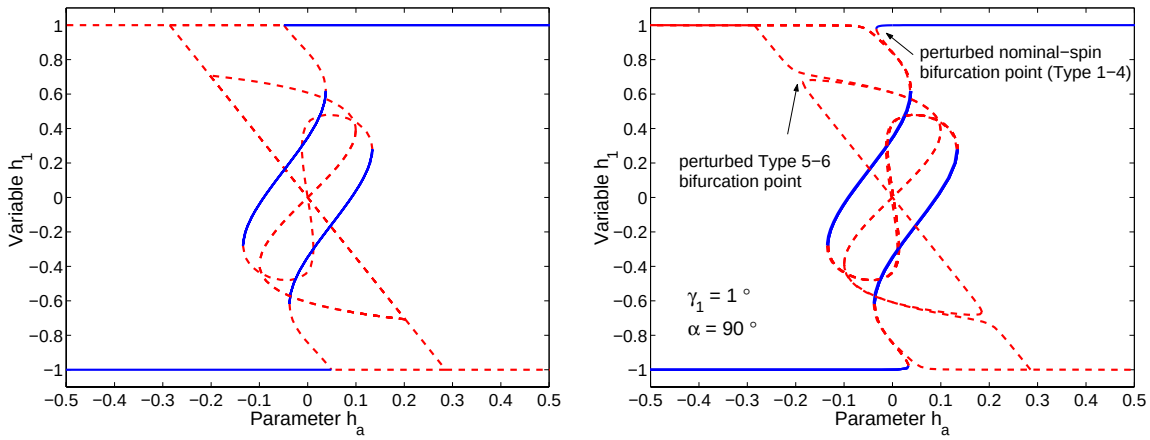

(a) Unperturbed bifurcation

(b) Perturbed bifurcation, with in-plane rotor misalignment

Figure 7.3: Bifurcation diagrams, h_1 *vs.* h_a, for standard and perturbed models of an oblate gyrostat. The model is perturbed by an in-plane rotor alignment error.

Most significantly, the Type 1-4 bifurcation point, defining the stability threshold of the nominal spin, breaks into two separate branches, as seen in Figs. 7.3(b) and 7.4(b). The perturbed structure is typical for perturbed pitchfork bifurcations: the pitchfork unfolds into two separate branches, with one continuous branch without singular points and another branch with a turning point. In fact, the existence of the turning point could be considered typical, and the pitchfork bifurcation a special case for $\gamma = 0$.

The rotor misalignment causes the desired nominal spin to deviate from a pure $\hat{\mathbf{b}}_1$-axis spin. There

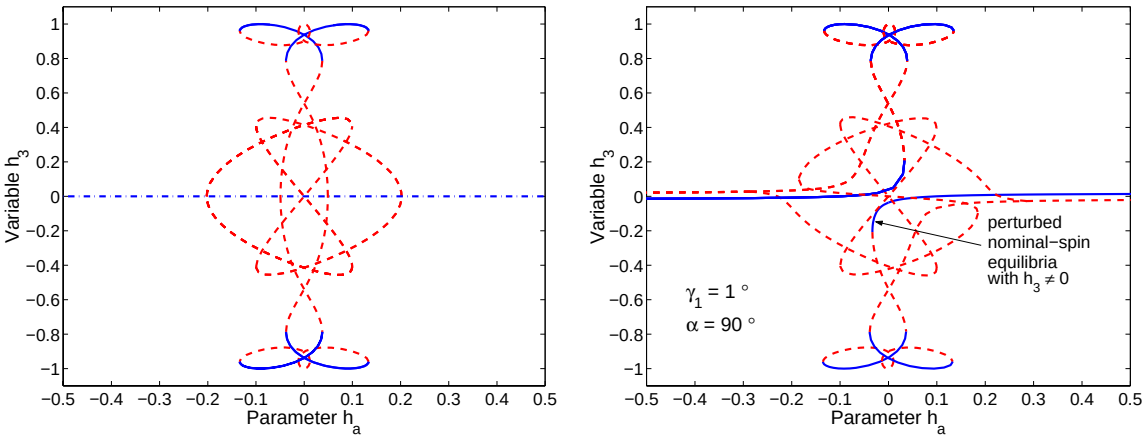

(a) Unperturbed bifurcation

(b) Perturbed bifurcation, with in-plane rotor misalignment

Figure 7.4: Bifurcation diagrams, h_3 *vs.* h_a, for standard and perturbed models of an oblate gyrostat. The model is perturbed by an in-plane rotor alignment error.

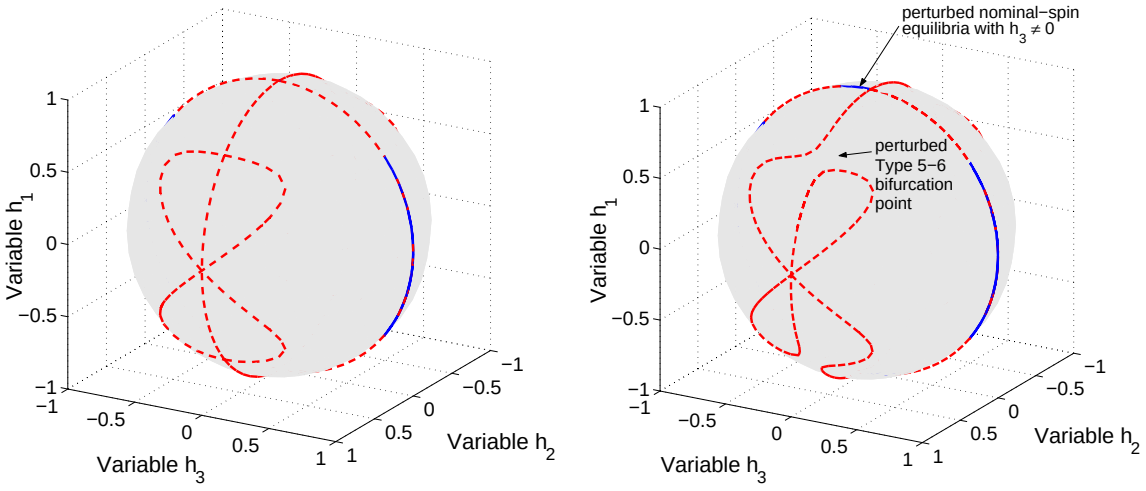

(a) Unperturbed equilibria

(b) Perturbed equilibria, with in-plane rotor misalignment

Figure 7.5: Equilibria on the momentum sphere for standard and perturbed models of an oblate gyrostat. The model is perturbed by an in-plane rotor alignment error.

is a small $\hat{\mathbf{b}}_3$ component of $\mathbf{h}$ which increases as h_a decreases in magnitude toward the stability threshold. We see this non-zero h_3 component of the stable near-nominal branch in Fig. 7.4(b) as well in the momentum sphere, as shown in Fig. 7.5(b).

For the standard model, the nominal spin stability changes at the bifurcation point, but for this perturbed situation the stable branch continues, as h_a decreases in magnitude, further away from the $\hat{\mathbf{b}}_1$-axis until the turning point is reached. For the equilibria on this stable branch, the system is spinning about a slightly different axis than the intended $\hat{\mathbf{b}}_1$ axis due to the rotor misalignment. Not only is there a non-zero h_3 component of angular momentum, but the damper is slightly displaced as well. The desired spin axis precesses around the actual spin axis. The constant nutation angle of this wobble-like motion is greater for h_a near the stability boundary. Therefore, if the rotor momentum were slowly decreased, the satellite would precess around the desired spin axis with an increasingly large nutation angle. If h_a reached the stability boundary at the turning point, the spin would become unstable and the system would experience a significant jump to a different stable equilibrium state.

The $\hat{\mathbf{a}}$-in-plane error also breaks another set of pitchfork bifurcations, those in the $\hat{\mathbf{b}}_1$–$\hat{\mathbf{b}}_2$ plane where Type 5 branches bifurcate into Type 5 and Type 6 branches, denoted the Type 5-6 bifurcation point. The perturbed bifurcation structures are seen on the momentum sphere, Fig. 7.5(b), and in the h_3–h_a bifurcation diagram, Fig. 7.4(b). For the oblate gyrostat, these branches are all unstable.

Moving the $\hat{\mathbf{a}}$ vector within the plane, but in the other direction ($\gamma_1 = -1^\circ$), breaks the pitchforks in the opposite sense. The perturbed pitchfork branch that became a separate branch with a turning point now becomes the continuous branch and *vice versa*.

Appendix F includes a set of bifurcation diagrams for the in-plane rotor misalignment configuration. The diagrams include equilibria on the momentum sphere and bifurcation diagrams for each of the five system states, with h_a as the bifurcation parameter.

Out-of-Plane Error

We use numerical continuation on the perturbed equations for $\alpha = 0^\circ$ and $\gamma_a = 2^\circ$. This perturbs the $\hat{\mathbf{a}}$ vector in the $+\hat{\mathbf{b}}_2$ direction, out of the $\hat{\mathbf{b}}_1$–$\hat{\mathbf{b}}_3$ plane. This rotor alignment error has two primary effects: breaking a set of pitchfork bifurcations and causing Type 4 branches to lie outside of the $\hat{\mathbf{b}}_1$–$\hat{\mathbf{b}}_3$ plane. The broken pitchforks are the set that marks the bifurcation of Type 1 branches into Type 5 branches of equilibria, branching into the $\hat{\mathbf{b}}_1$–$\hat{\mathbf{b}}_2$ plane. These Type 1-5 pitchforks break in the typical fashion: one continuous branch and one separate branch with a turning point. These broken branches are best seen in the h_1–h_a and h_2–h_a bifurcation diagrams (Figs. 7.6–7.7) and displayed on the momentum sphere (Fig. 7.8).

As with in-plane rotor errors, the nominal equilibrium state is not exactly a pure $\hat{\mathbf{b}}_1$-axis spin. Instead, there is a small $\hat{\mathbf{b}}_2$ component, as seen in Figs. 7.7–7.8. For the out-of-plane case, the stability of the nominal spin changes with the unperturbed Type 1-4 bifurcation point (see Fig. 7.6), so the magnitude on any possible stable precession motion is not as great as for the in-plane error

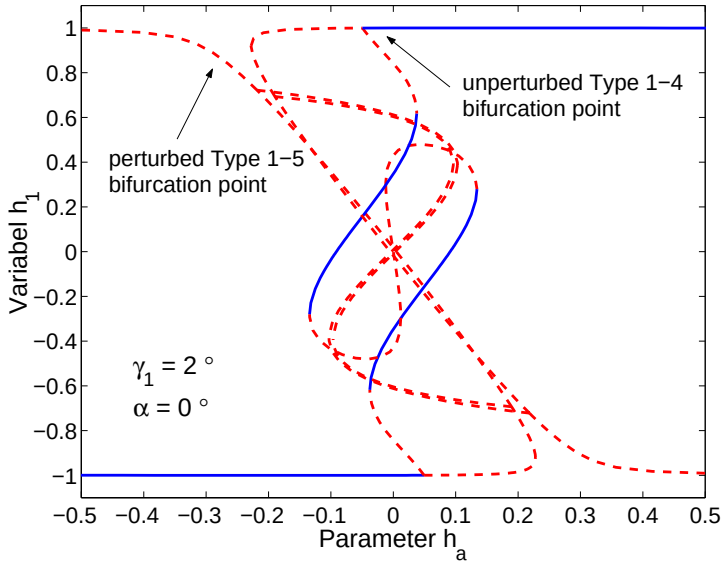

Figure 7.6: Out-of-plane rotor misalignment for an oblate gyrostat, h_1–h_a bifurcations

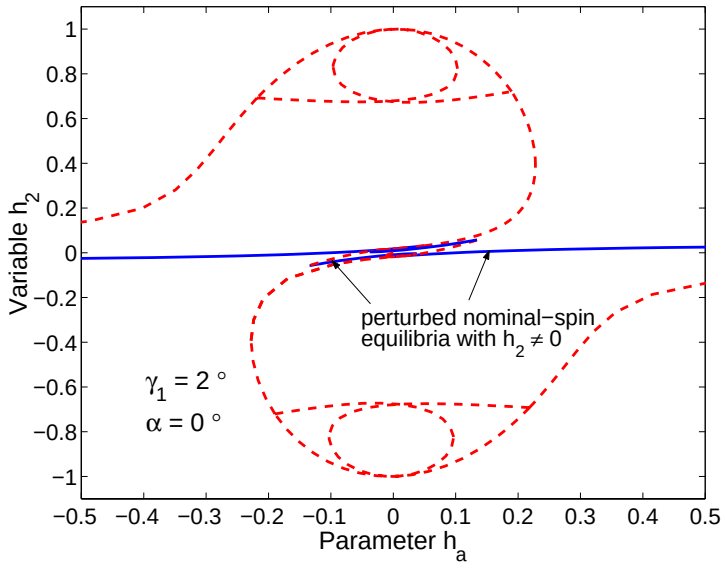

Figure 7.7: Out-of-plane rotor misalignment for an oblate gyrostat, h_2–h_a bifurcations

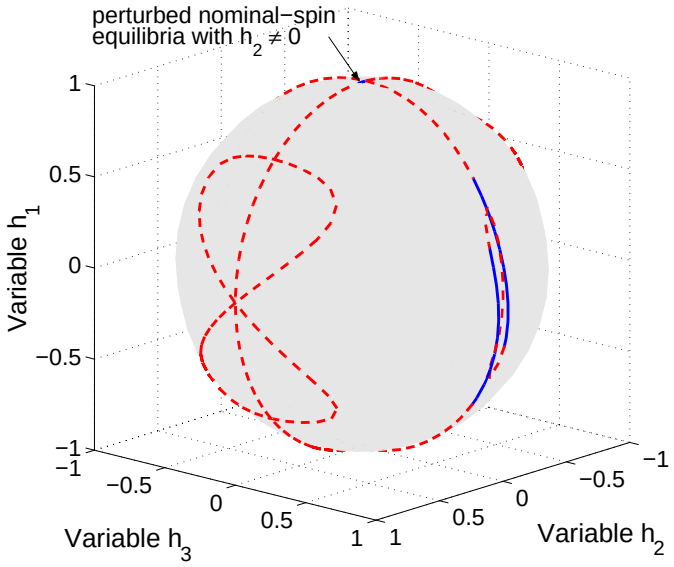

Figure 7.8: Out-of-plane rotor misalignment for an oblate gyrostat, bifurcations on the momentum sphere

case.

The out-of-plane error also affects the Type 4 equilibria. For the standard model these branches all lie within the $\hat{\mathbf{b}}_1$–$\hat{\mathbf{b}}_3$ plane, but for the perturbed model these branches may have non-zero h_2 components, as seen in Fig. 7.8.

Appendix F includes a set of bifurcation diagrams for the out-of-plane rotor misalignment configuration. The diagrams include equilibria on the momentum sphere and bifurcation diagrams for each of the five system states, with h_a as the bifurcation parameter.

7.2.2 Damper Misalignment for Oblate Gyrostat

We investigate the effects of rotor misalignment by adding a small angular displacement to $\hat{\mathbf{n}}$. Two types of damper alignment error are considered: a displacement within the $\hat{\mathbf{b}}_1$–$\hat{\mathbf{b}}_3$ plane and a displacement perpendicular to the $\hat{\mathbf{b}}_1$–$\hat{\mathbf{b}}_3$ plane.

In-Plane Error

We apply numerical continuation to the perturbed model for $\eta = 90\,^\circ$ and $\gamma_n = 1^\circ$. This perturbs the $\hat{\mathbf{n}}$ vector in the $\hat{\mathbf{b}}_3$ direction, within the $\hat{\mathbf{b}}_1$–$\hat{\mathbf{b}}_3$ plane.

The effects of in-plane damper alignment error are similar to those for rotor alignment in-plane

errors. The same two types of pitchforks are broken: the nominal-spin bifurcation point and the Type 5-6 bifurcation point. The nominal pitchfork is broken in the same fashion as the in-plane rotor case. The Type 5-6 pitchfork breaks in the opposite sense as the in-plane rotor case: the continuous branch is now the separate branch with a turning point and *vice versa*. Both these pitchforks break in the opposite sense for $\gamma_n = -1\,^\circ$. These results are shown in Figs. 7.9–7.11.

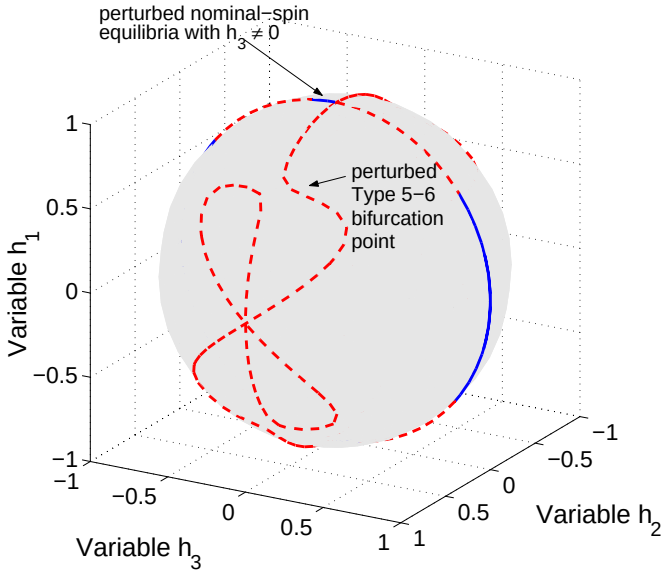

Figure 7.9: In-plane damper misalignment for an oblate gyrostat, bifurcations on the momentum sphere

Appendix F includes a set of bifurcation diagrams for the in-plane damper misalignment configuration. The diagrams include equilibria on the momentum sphere and bifurcation diagrams for each of the five system states, with h_a as the bifurcation parameter.

Out-of-Plane Error

We apply numerical continuation to the perturbed model for $\eta = 0\,^\circ$ and $\gamma_n = 2\,^\circ$, causing the $\hat{\mathbf{n}}$ vector to tilt in the $+\hat{\mathbf{b}}_2$ direction. This damper alignment error does not break any pitchfork bifurcations, but it does disturb the symmetry of the standard model branches of equilibria.

We display the perturbed equilibria on the momentum sphere, shown in Fig. 7.12. At first glance, the equilibria appear to be similar to the rotor out-of-plane case, but there are important differences. First, all pitchforks remain intact, whereas the Type 1-5 pitchfork is broken in the rotor out-of-plane case. With this pitchfork intact, the nominal spin remains a pure $\hat{\mathbf{b}}_1$-axis spin (see Fig. 7.13).

The Type 4 branches are perturbed from the $\hat{\mathbf{b}}_1$–$\hat{\mathbf{b}}_3$ plane, as they are for the rotor out-of-plane case. Type 6 equilibrium branches are not symmetric with respect to $\pm h_a$ (see Fig. 7.14). The Type 6

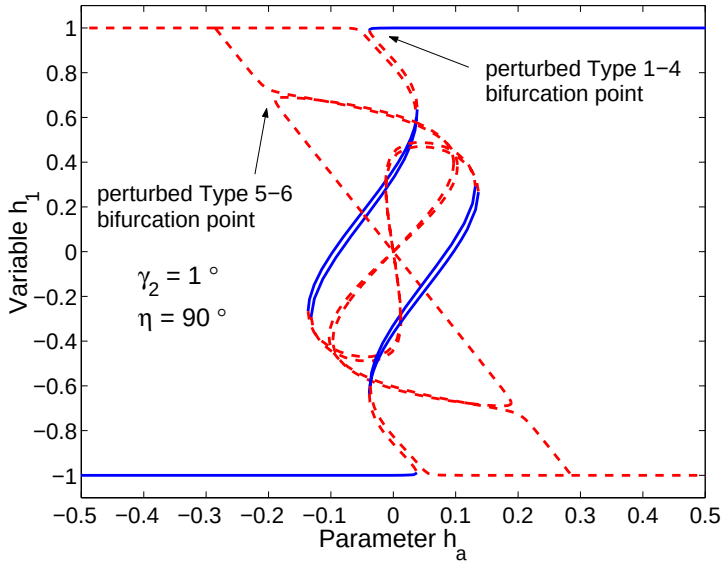

Figure 7.10: In-plane damper misalignment for an oblate gyrostat, h_1–h_a bifurcations

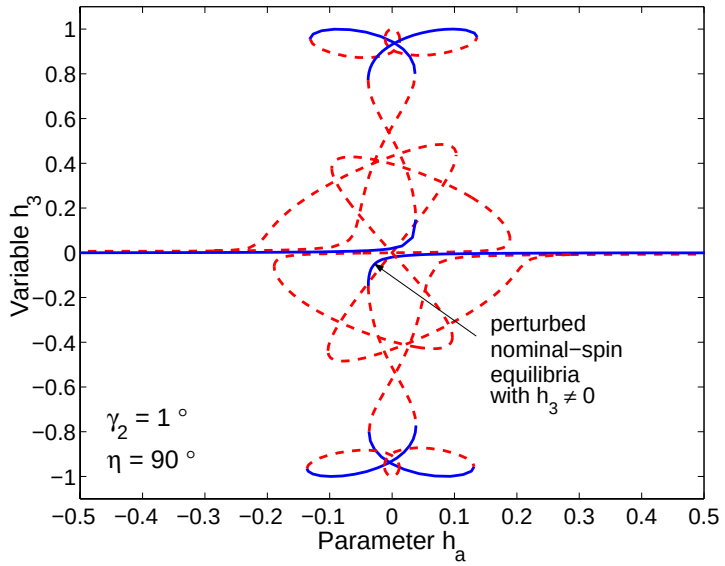

Figure 7.11: In-plane damper misalignment for an oblate gyrostat, h_3–h_a bifurcations

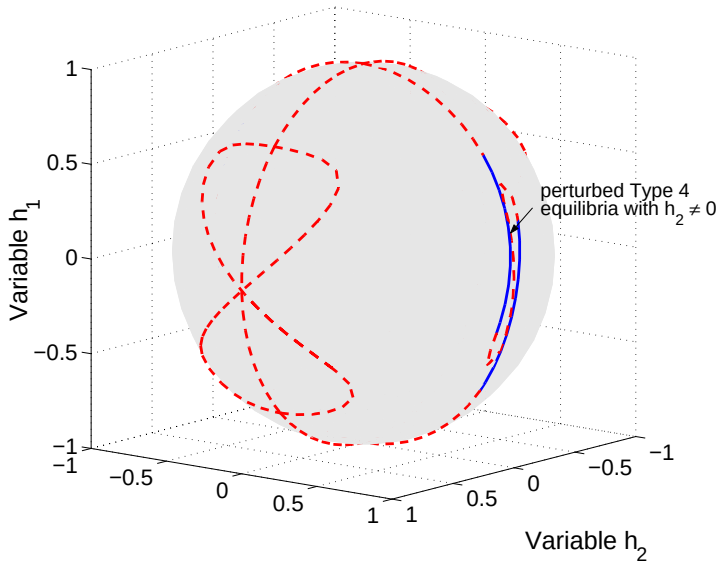

Figure 7.12: Out-of-plane damper misalignment for an oblate gyrostat, bifurcations on the momentum sphere

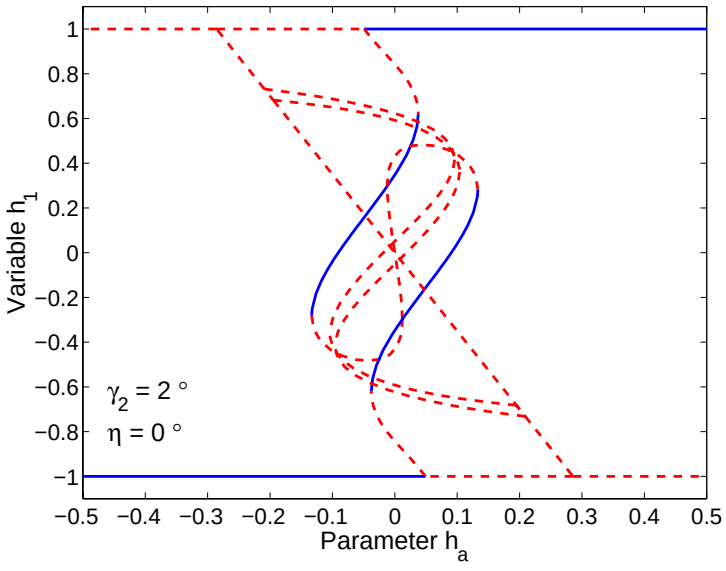

Figure 7.13: Out-of-plane damper misalignment for an oblate gyrostat, h_1–h_a bifurcations

branches are distorted much more than for the rotor out-of-plane case, even when accounting for the larger γ value.

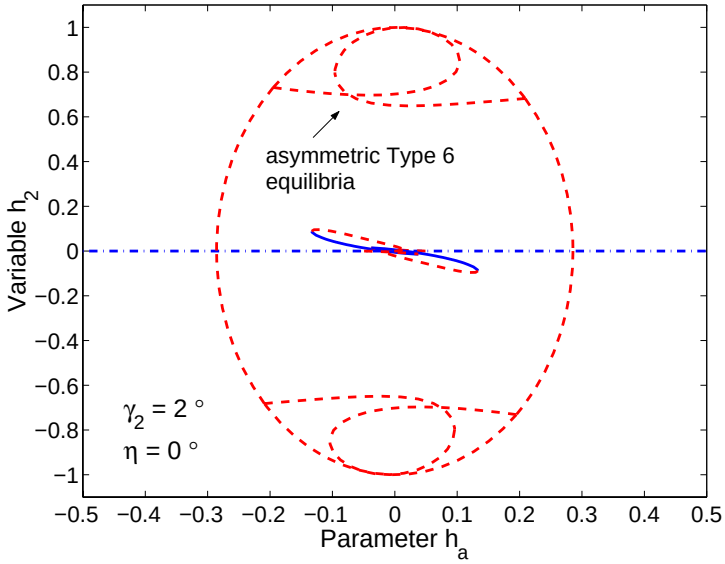

Figure 7.14: Out-of-plane damper misalignment for an oblate gyrostat, h_2–h_a bifurcations

Appendix F includes a set of bifurcation diagrams for the out-of-plane damper misalignment configuration. The diagrams include equilibria on the momentum sphere and bifurcation diagrams for each of the five system states, with h_a as the bifurcation parameter.

7.3 Prolate Gyrostat

The prolate gyrostat is designed to spin about a minor axis. The system parameters for the prolate gyrostat are defined in Table 7.3. We use the same system parameters for each result, only changing the rotor or damper alignment error angle. This combination of inertia properties and parameters

Table 7.3: System parameters for prolate gyrostat used to determine perturbed equilibria

Inertia Properties	Damper Parameters
$I_1 = 0.28$	$k = 0.40$
$I_2 = 0.40$	$b = 0.33$
$I_3 = 0.32$	$\varepsilon = 0.10$
$I_s = 0.04$	$c = 0.10$

is used for the standard model in Ch. 5. These parameters are used with the perturbed model to numerically investigate the effects on system equilibria.

7.3.1 Rotor Misalignment for Prolate Gyrostat

We investigate the effects of rotor misalignment by adding a small angular displacement to $\hat{\mathbf{a}}$. Two types of rotor alignment error are considered: a displacement within the $\hat{\mathbf{b}}_1$–$\hat{\mathbf{b}}_3$ plane and a displacement perpendicular to the $\hat{\mathbf{b}}_1$–$\hat{\mathbf{b}}_3$ plane.

In-Plane Error

We apply numerical continuation to the prolate gyrostat for $\gamma_a = 1^\circ$ and $\alpha = 90^\circ$, tilting the $\hat{\mathbf{a}}$ vector in the $+\hat{\mathbf{b}}_3$ direction. This rotor alignment error breaks the same types of pitchforks as in

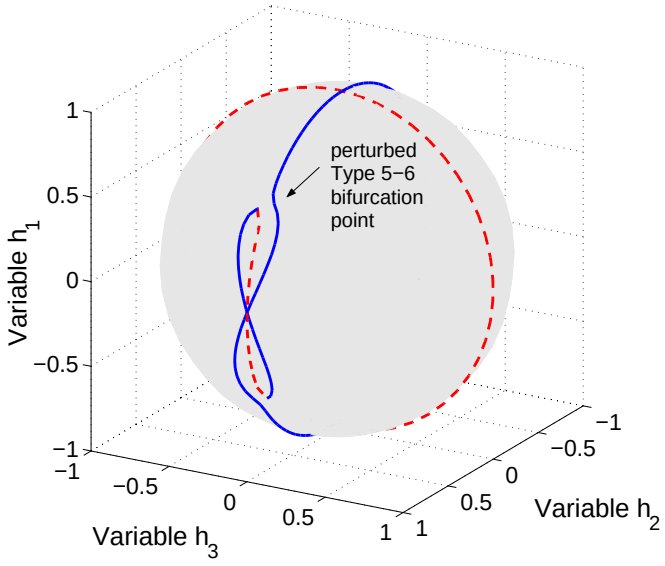

Figure 7.15: In-plane rotor misalignment for a prolate gyrostat, bifurcations on the momentum sphere

the oblate model: the Type 5-6 and Type 1-4 pitchforks. However, the prolate case has different stability properties than the oblate gyrostat. These differences change how the rotor alignment errors affect the system dynamics.

Figure 7.16 shows the broken bifurcation point along the nominal spin axis. For the prolate, rotor in-plane error case, with $I_2 > I_3$, the nominal spin stability changes at the Type 1-5 pitchfork, branching into the $\hat{\mathbf{b}}_1$–$\hat{\mathbf{b}}_2$ plane (see Fig. 7.15). This result is a change from the oblate gyrostat,

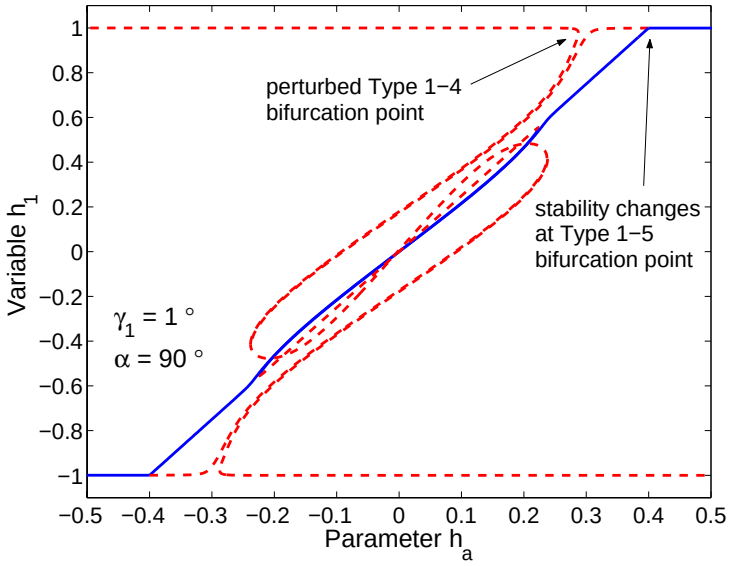

Figure 7.16: In-plane rotor misalignment for a prolate gyrostat, h_1–h_a bifurcations

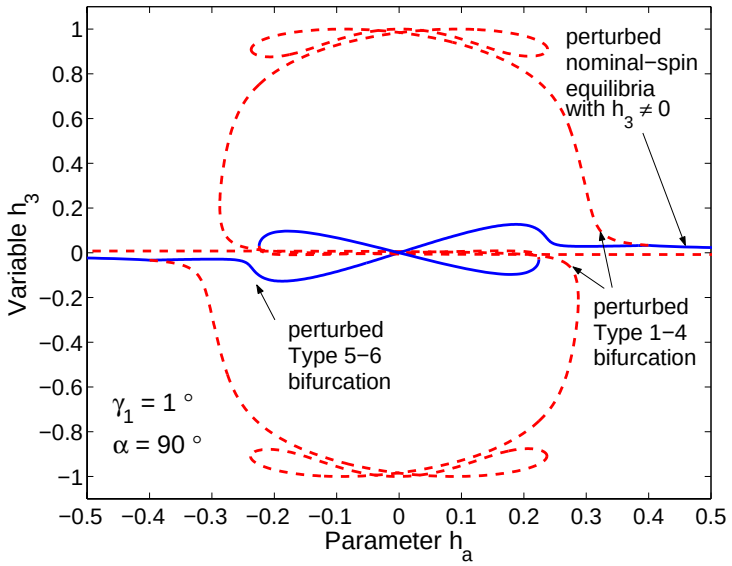

Figure 7.17: In-plane rotor misalignment for a prolate gyrostat, h_3–h_a bifurcations

where the stability changes at the Type 1-4 pitchfork, branching into the $\hat{\mathbf{b}}_1$–$\hat{\mathbf{b}}_3$ plane. The stability threshold for the nominal-axis spin is still defined, at least approximately, for the perturbed model, by the stability conditions defined in Eqs. 4.8–4.9. The stability conditions identify the Type 1-5 bifurcation point for the prolate case, whereas they mark the Type 1-4 bifurcation point for the oblate case.

The nominal spin has a small $\hat{\mathbf{b}}_3$ component of angular momentum, as shown in Fig. 7.17. This deviation of $\mathbf{h}$ from $\hat{\mathbf{b}}_1$, at equilibrium, produces a slight precession motion about the intended spin axis. For slowly decreasing rotor momentum, there is no jump to a separate stable branch. Instead, the stable Type 5 and Type 6 branches provide a path along the momentum sphere for a possible smooth transition to a pure $\hat{\mathbf{b}}_2$-axis spin (see Fig. 7.15). Alternatively, the in-plane rotor error does not preclude a smooth transition from a Type 2B, pure $\hat{\mathbf{b}}_2$-axis spin, to a stable nominal spin (Type 1) for slowly increasing h_a. Slowly changing h_a can simulate maneuvers using a small rotor torque to change h_a and system attitude. In Ch. 8, we discuss a simple spin-up maneuver in more detail and simulate the spin-up maneuver for small rotor torques.

Appendix G includes a set of bifurcation diagrams for the in-plane rotor misalignment, prolate gyrostat configuration. The diagrams include equilibria on the momentum sphere and bifurcation diagrams for each of the five system states, with h_a as the bifurcation parameter.

Out-of-Plane Error

We apply numerical continuation to the perturbed model for a prolate gyrostat with $\gamma_a = 2^\circ$ and $\alpha = 0^\circ$, tilting the $\hat{\mathbf{a}}$ vector in the $+\hat{\mathbf{b}}_2$ direction. As with the oblate gyrostat case, the Type 1-5 pitchfork unfolds (see Figs. 7.19–7.20) and Type 4 equilibria do remain in the $\hat{\mathbf{b}}_1$–$\hat{\mathbf{b}}_3$ plane (see Fig. 7.18). The near-nominal spin has a non-zero $\hat{\mathbf{b}}_3$ component of angular momentum, causing precession of the intended spin axis. With the broken pitchfork, the precession of the intended spin axis has a larger nutation angle than the oblate gyrostat with the same in-plane rotor error. There are continuous stable branches of equilibria from the nominal spin state to a major-axis spin equilibrium.

Appendix G includes a set of bifurcation diagrams for the out-of-plane rotor misalignment, prolate gyrostat configuration. The diagrams include equilibria on the momentum sphere and bifurcation diagrams for each of the five system states, with h_a as the bifurcation parameter.

7.3.2 Damper Misalignment for Prolate Gyrostat

We investigate the effects of rotor misalignment by adding a small angular displacement to $\hat{\mathbf{n}}$. Two types of damper alignment error are considered: a displacement within the $\hat{\mathbf{b}}_1$–$\hat{\mathbf{b}}_3$ plane and a displacement perpendicular to the $\hat{\mathbf{b}}_1$–$\hat{\mathbf{b}}_3$ plane.

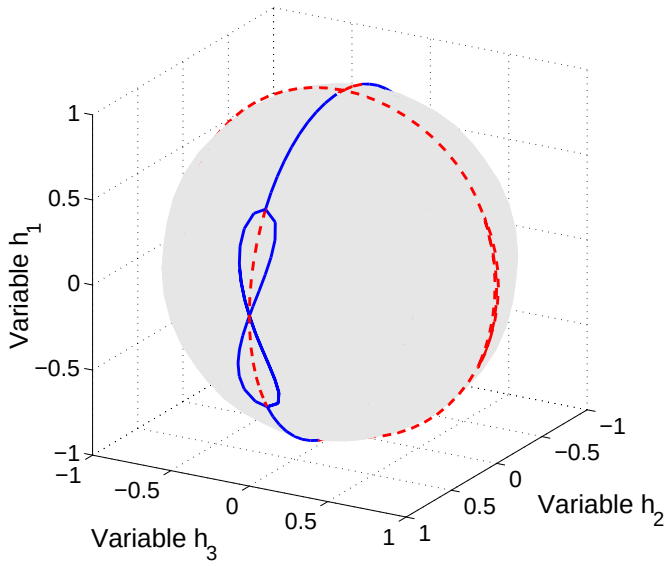

Figure 7.18: Out-of-plane rotor misalignment for a prolate gyrostat, bifurcations on the momentum sphere

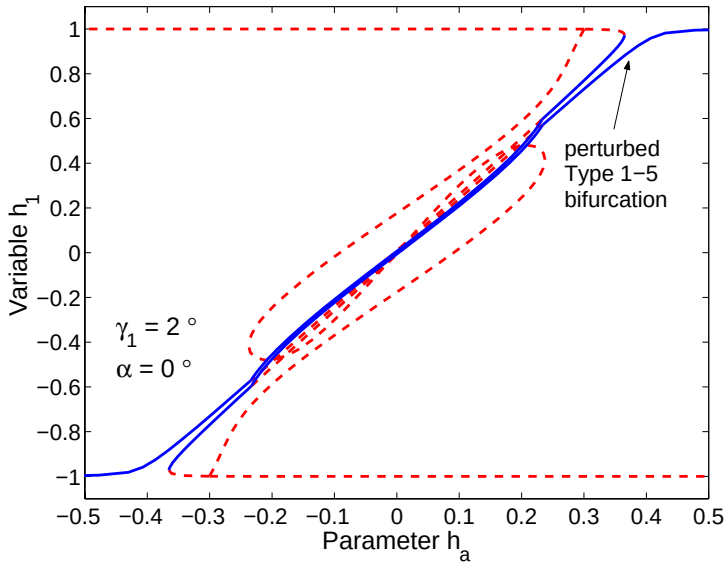

Figure 7.19: Out-of-plane rotor misalignment for a prolate gyrostat, h_1–h_a bifurcations

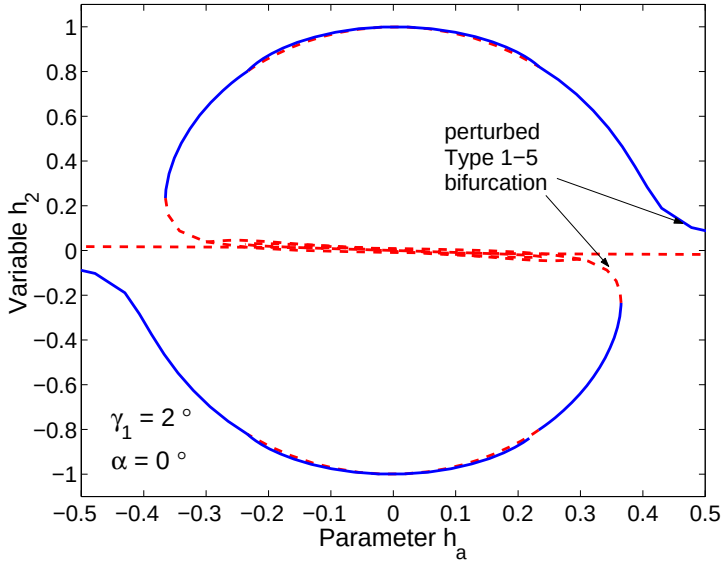

Figure 7.20: Out-of-plane rotor misalignment for a prolate gyrostat, h_2–h_a bifurcations

In-Plane Error

We apply numerical continuation to the perturbed model for $\eta = 90\,^\circ$ and $\gamma_n = 1^\circ$. This perturbs the $\hat{\mathbf{n}}$ vector in the $\hat{\mathbf{b}}_3$ direction.

For the prolate gyrostat, the effects of in-plane damper alignment error are similar to those for rotor alignment in-plane errors. The same two types of pitchforks are broken: the nominal-spin (Type 1-4) bifurcation point and the Type 5-6 bifurcation point. The nominal pitchfork is broken in the same fashion as the in-plane rotor case. The Type 5-6 pitchfork breaks in the opposite sense as the in-plane rotor case: the continuous branch is now the separate branch with a turning point and vice versa. Both these pitchforks break in the opposite sense for $\gamma_n = -1\,^\circ$. These results are shown in Figs. 7.21–7.23.

Comparing the prolate gyrostat to the oblate case, the perturbed bifurcation structures for in-plane damper errors have the same stability changes as the in-plane rotor errors. A smooth transition from a flat spin to the nominal spin is possible for increasing angular momentum.

Appendix G includes a set of bifurcation diagrams for the in-plane damper misalignment, prolate gyrostat configuration. The diagrams include equilibria on the momentum sphere and bifurcation diagrams for each of the five system states, with h_a as the bifurcation parameter.

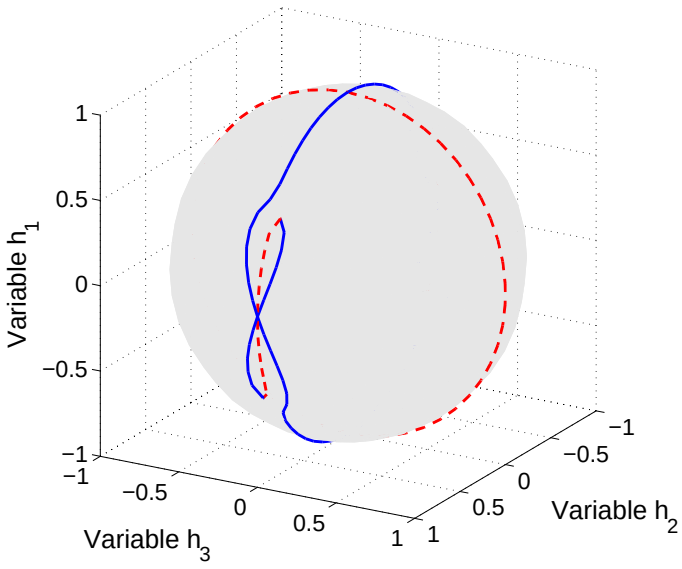

Figure 7.21: In-plane damper misalignment for a prolate gyrostat, bifurcations on the momentum sphere

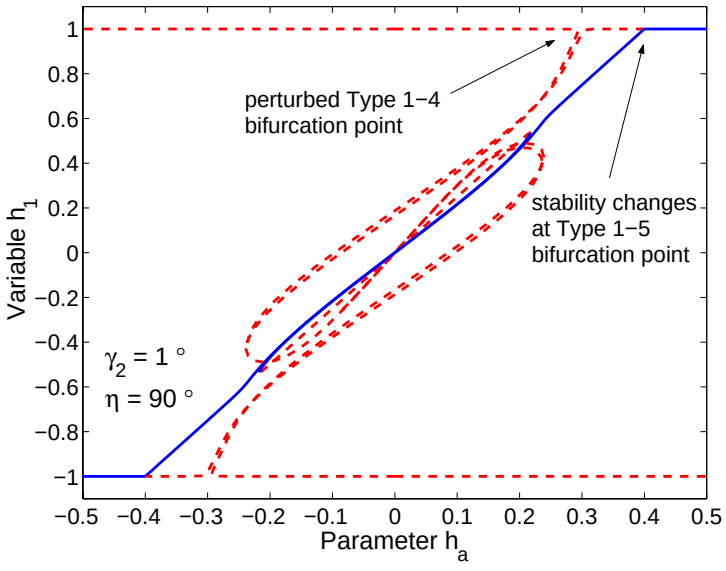

Figure 7.22: In-plane damper misalignment for a prolate gyrostat, h_1–h_a bifurcations

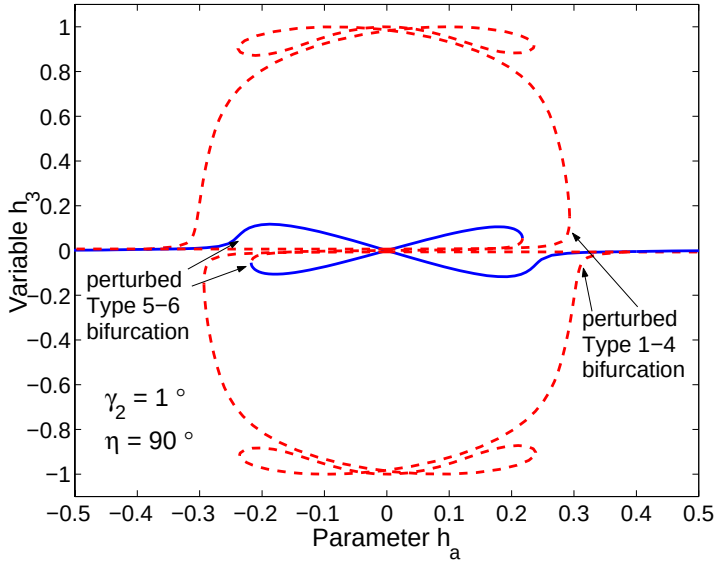

Figure 7.23: In-plane damper misalignment for a prolate gyrostat, h_3–h_a bifurcations

Out-of-Plane Error

For a prolate gyrostat, we apply numerical continuation to the perturbed model for $\eta = 0\,^\circ$ and $\gamma_n = 2\,^\circ$, causing the $\hat{\mathbf{n}}$ vector to tilt in the $+\hat{\mathbf{b}}_2$ direction. As with the oblate case, this damper alignment error does not break any pitchfork bifurcations, but it does disturb the symmetry of the standard model equilibria branches.

We display the perturbed equilibria on the momentum sphere, shown in Fig. 7.24. All pitchforks remain intact, and the nominal spin remains a pure $\hat{\mathbf{b}}_1$-axis spin (see Fig. 7.25).

The Type 4 branches are perturbed from the $\hat{\mathbf{b}}_1$–$\hat{\mathbf{b}}_3$ plane, as they are for the rotor out-of-plane case.

Appendix G includes a set of bifurcation diagrams for the out-of-plane damper misalignment, prolate gyrostat configuration. The diagrams include equilibria on the momentum sphere and bifurcation diagrams for each of the five system states, with h_a as the bifurcation parameter.

7.4 Summary

We applied numerical continuation to determine the effects of rotor or damper alignment errors on the global equilibria of oblate and prolate gyrostats. In general, perturbing the rotor axis in the $\hat{\mathbf{b}}_1$–$\hat{\mathbf{b}}_3$ plane breaks two types of pitchfork bifurcations: the Type 1-4 and Type 5-6 pitchforks. Perturbing the rotor axis out of the $\hat{\mathbf{b}}_1$–$\hat{\mathbf{b}}_3$ plane breaks the Type 1-5 pitchfork bifurcations and

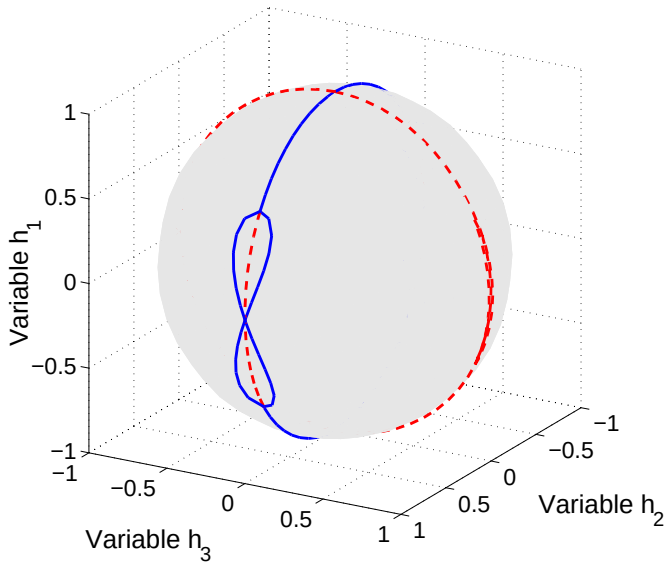

Figure 7.24: Out-of-plane damper misalignment for a prolate gyrostat, bifurcations on the momentum sphere

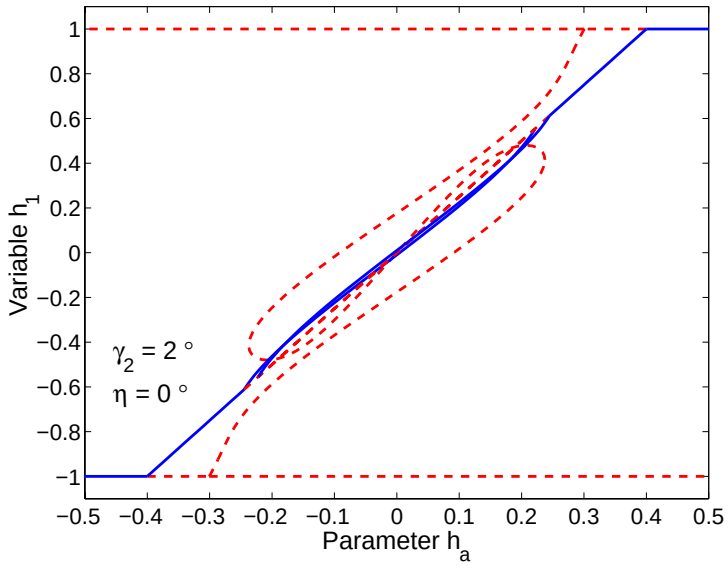

Figure 7.25: Out-of-plane damper misalignment for a prolate gyrostat, h_1–h_a bifurcations

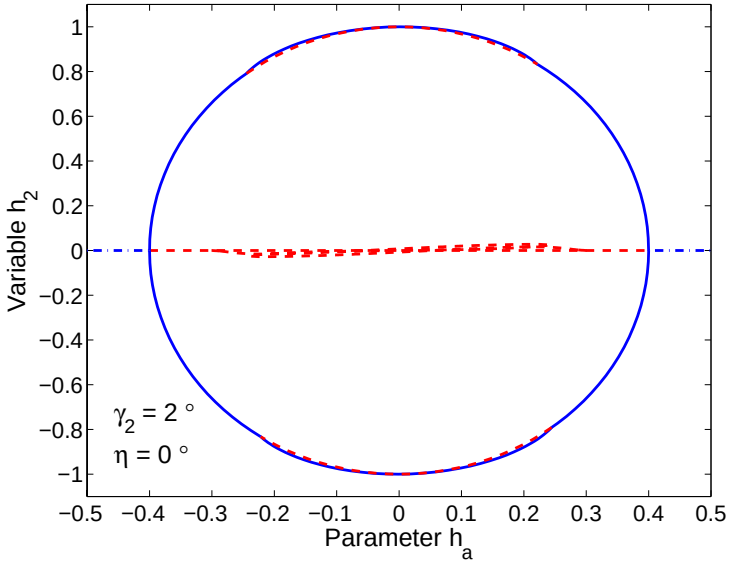

Figure 7.26: Out-of-plane damper misalignment for a prolate gyrostat, h_2–h_a bifurcations

perturbs Type 4 branches out of the $\hat{\mathbf{b}}_1$–$\hat{\mathbf{b}}_3$ plane. In-plane damper errors have similar effects to in-plane rotor alignment errors. Perturbing the damper out of plane does not break pitchforks, but does distort symmetries of the unperturbed equilibria. These alignment errors may cause precession of the intended, nominal spin-axis around the true principal axis.

The oblate gyrostat, for $I_2 < I_3$, has stable equilibria exclusively near the $\hat{\mathbf{b}}_1$–$\hat{\mathbf{b}}_3$ plane. If perturbed from the near-nominal equilibrium state, the only alternate stable branches are near a flat spin condition about the $\hat{\mathbf{b}}_3$ axis. The prolate gyrostat, for $I_2 > I_3$, has stable near-nominal equilibria only if the rotor provides sufficient gyroscopic stabilization. There is continuous path of stable equilibria between the nominal spin and flat spin near the $\hat{\mathbf{b}}_2$ axis.

Chapter 8

Practical Applications

In this chapter we apply the bifurcation results from previous chapters to realistic dual-spin satellite configurations and simple rotor spin-up maneuvers. We use typical inertial properties, damper location, and damping coefficient values for a dual-spin satellite, obtained from the literature. Dampers are often tuned by matching the natural frequency of the spring-mass-damper to the satellite precession frequency about the nominal-spin axis. We use a tuning algorithm to select the spring stiffness value, k. Many dual-spin satellites are approximately axisymmetric, such as TACSAT I, but we use numerical continuation to show how slight inertia asymmetries affect equilibria. Finally, the equilibria and bifurcation diagrams for varying h_a provide a useful perspective of rotor spin-up dynamics.

8.1 Dual-Spin Examples

In Ch. 5, we are concerned with global equilibria in a general sense, considering the set of possible equilibria for an extensive range of parameter combinations. In this section, we examine a configuration that emulates real dual-spin satellites. Satellite designers have successfully used the dual-spin concept for communication satellites, first demonstrated with TACSAT 1. Like TACSAT I, many dual-spin satellites are prolate gyrostats with a relatively large rotor aligned with the nominal spin axis ($\hat{\mathbf{b}}_1 = \hat{\mathbf{a}}$).[46] An axisymmetric gyrostat, defined as $I_2 = I_3$, is often used to model a dual-spin satellite.[37,45,52] Since any real system is probably not perfectly axisymmetric, we examine the effects of slight asymmetric dual-spin satellites as well as the axisymmetric case. Dual-spin satellite designers often tune the spring-mass-damper to match its natural frequency to the precession frequency of the satellite. A tuned damper is excited by the precession motion it is designed to attenuate, thereby damping out the precession more quickly than untuned dampers. The damper spring stiffness is calculated from a simple tuning condition. Once the parameter set is determined, we use numerical continuation to characterize the equilibria of the dual-spin satellite examples.

8.1.1 Dual-Spin Parameter Set

Likins, Tseng, and Mingori studied the effects of damper nonlinearities in an attempt to explain in-flight precession data for TACSAT 1.[47] We use their satellite inertia properties and damper information to generate the dimensionless parameters defined in Table 8.1. This configuration has a relatively large rotor. The damper mass and damping coefficient are an order of magnitude less than previously considered in Chs. 5– 7.

Table 8.1: System parameters for example dual-spin gyrostat

Inertia Properties	Damper Parameters
$I_1 = 0.20$	$b = 0.33$
$I_2 = 0.40$	$\varepsilon = 0.01$
$I_3 = 0.40$	$c = 0.01$
$I_s = 0.14$	

We choose the desired, nominal spin configuration to have a despun platform, where $\boldsymbol{\omega} = 0$ and all the angular momentum is in the rotor, $h_a = 1$. Most dual-spin satellites have either a despun or slowly spinning platform. Typical dimensional rates, presented by Iorillo, are $\omega^* = 10^{-3}$ rpm and $\omega_s^* = 60$ rpm.[37] Even for a slowly spinning platform, the despun condition is a good approximation of the desired nominal spin.

8.1.2 Damper Tuning

To increase the damping efficiency, we match the damper natural frequency and the frequency of precession about the nominal spin. This classic method of damper tuning is often used by satellite dynamicists,[58,60] although most often for the $\mathcal{B}+\mathcal{P}$ model. Equations 3.68 – 3.70 are linearized about $\mathbf{z} = (1,0,0,0,0)$, keeping h_a arbitrary. The damper dynamics are coupled with the precession motion, but for small ε, the linearized $\dot{\mathbf{h}}$ equations decouple from the damper variables and become

$$\dot{h}_2 = -\frac{(I_1' + \lambda I_3)}{I_1' I_3} h_3 \tag{8.1}$$

$$\dot{h}_3 = \frac{(I_1' + \lambda I_2)}{I_1' I_2} h_2 \tag{8.2}$$

Substituting for h_3 leads to a second-order equation:

$$\ddot{h}_2 + \frac{(I_1' + \lambda I_2)\,(I_1' + \lambda I_3)}{I_1'^2 I_2 I_3} h_2 = 0 \tag{8.3}$$

The natural frequency of this second-order equation is the precession frequency of $\mathbf{h}$ around $\hat{\mathbf{b}}_1$, in the body frame. We define this precession frequency as

$$\omega_b = \left[\frac{(I_1' + \lambda I_2)(I_1' + \lambda I_3)}{I_1'^2 I_2 I_3} \right]^{1/2} \tag{8.4}$$

The spring-mass-damper natural frequency, without damping, is

$$\omega_n = \sqrt{k/\varepsilon} \tag{8.5}$$

Matching the precession and damper frequencies results in the following tuned-damper condition:

$$k_d = \frac{\varepsilon (I_1' + \lambda I_2)(I_1' + \lambda I_3)}{I_1'^2 I_2 I_3} \tag{8.6}$$

For the despun platform $\lambda = 0$, Eq. 8.6 reduces to

$$k_d = \frac{\varepsilon}{I_2 I_3} \tag{8.7}$$

Using this tuning condition, the damper is tuned for the dual-spin satellite example, yielding a spring stiffness, $k_d = 0.0625$. We use this k value to produce equilibria for the dual-spin example.

We simulate the effectiveness of the tuned damper by numerically integrating the equations of motion using both tuned and untuned dampers. We use the system parameters in Table 8.1, except we use a larger damper mass, $\varepsilon = 0.1$. This heavier damper mass is unrealistic compared to actual precession dampers, but the smaller damper mass takes longer to damp the precession motion. We use the larger mass to simplify the simulation results and clearly illustrate the effects of damper tuning. Results for a tuned damper are shown in Fig. 8.1(a), with $k = k_d = 0.625$. The h_3 history illustrates the precession motion while x shows the damper displacement. These two variables appear to be approximately in resonance, with similar frequencies, and the tuned damper effectively damps the precession motion. Results for a untuned damper are shown in Fig. 8.1(b), with $k = 0.8$. In the untuned case, the precession motion is damped, but not as effectively as the tuned damper.

Other parameters influence damper performance, such as damper position, b, and the viscous damping coefficient, c. We choose to use typical values from Ref. 47, but other researchers have considered methods to determine optimal values of damper parameters for related models.[5,58] We proceed with the system parameters of Table 8.1, and a tuned-damper value of k, to examine equilibria for a dual-spin satellite.

8.1.3 Axisymmetric Dual-Spin Example

Axisymmetric dual-spin satellites are common in the literature. As with any real system, slight inertia asymmetries are possible and are examined in Sec. 8.1.4. For the parameter set in Table 8.1,

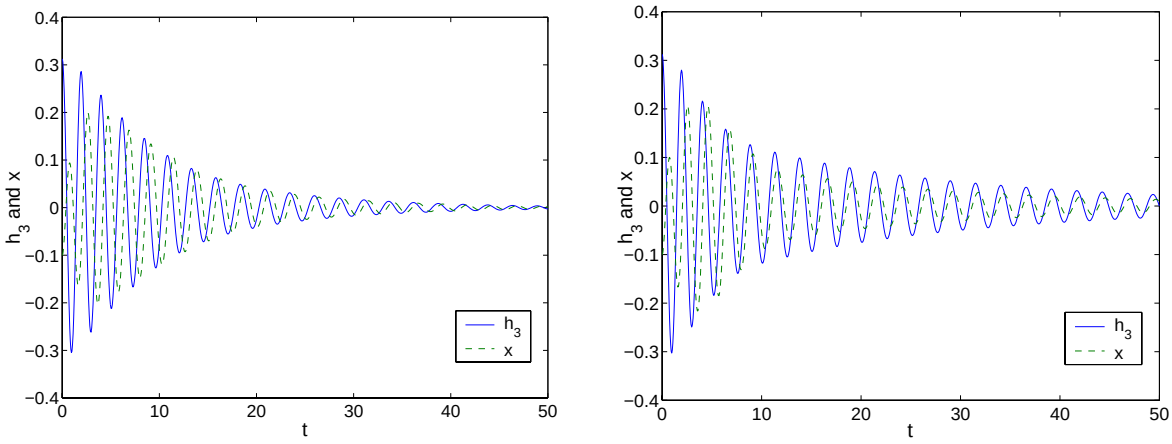

(a) Tuned damper: $k_d = 0.625$

(b) Untuned damper: $k = 0.8$

Figure 8.1: Simulation of precession damping for a tuned and untuned damper

we use numerical continuation to produce branches of equilibria for varying h_a. The damper is tuned for the $h_a = 1$, despun-platform condition. The equilibria are displayed on the momentum sphere and in five state-parameter bifurcation diagrams in Fig. 8.2.

Unlike the axisymmetric gyrostat in Fig. 5.48(a), the equilibria for this axisymmetric dual-spin satellite are on the $\hat{\mathbf{b}}_1$–$\hat{\mathbf{b}}_2$ and $\hat{\mathbf{b}}_1$–$\hat{\mathbf{b}}_3$ planes; no equilibria appear in the $\hat{\mathbf{b}}_2$–$\hat{\mathbf{b}}_3$ plane. There are two separate bifurcation points in the h_1–h_a bifurcation diagram (Fig. 8.2(b)); Type 1 branches bifurcate into Type 4 branches (Type 1-4 bifurcation point) and Type 5 branches (Type 1-5 bifurcation point). These two bifurcation points occur for nearly the same h_a value, and they are almost indistinguishable in Fig. 8.2(b). Within the $\hat{\mathbf{b}}_1$–$\hat{\mathbf{b}}_3$ plane, Type 4 equilibria are stable, whereas the Type 5 equilibria in the $\hat{\mathbf{b}}_1$–$\hat{\mathbf{b}}_2$ plane are unstable. For this example, the Type 4 and Type 5 equilibria are continuous branches without any turning points between bifurcation points (see Figs. 8.2(c) – 8.2(d)). These branches are similar to the Type 4 branches in Fig. 5.31; a tuned-damper value of k yields fewer equilibria than smaller k.

The stability of the simple $\hat{\mathbf{b}}_2$ and $\hat{\mathbf{b}}_3$-axis spin (Type 2A and Type 3 equilibria) is uncertain. For both cases, a linear stability analysis is inconclusive due to purely imaginary eigenvalues. The Liapunov function of Ch 4 is not positive definite for the axisymmetric case, and therefore it provides no stability information. Simulation of system dynamics with Type 2A or Type 3A initial conditions indicates instability. More work is needed to analytically verify the stability of these simple spins. Center manifold theory may provide a method of assessing the stability of motion within these zero-eigenvalue regions of state space.

Type 6 equilibria, which appear in the $\hat{\mathbf{b}}_2$–$\hat{\mathbf{b}}_3$ plane in Fig. 5.48(a), do not exist for this axisymmetric case. Neither simple spin with $x \neq 0$ (Types 2B and 3B) exist for this parameter set. Although not rigorous, numerical continuation results suggest that the existence of the Type 2B equilibrium corresponds to the existence of Type 6 equilibria. We look more closely at the example axisym-

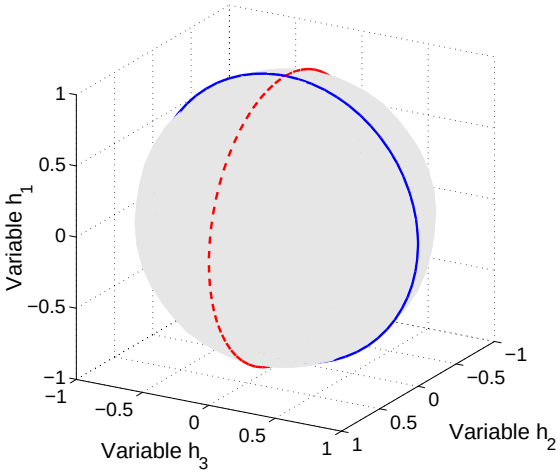

(a) Momentum sphere

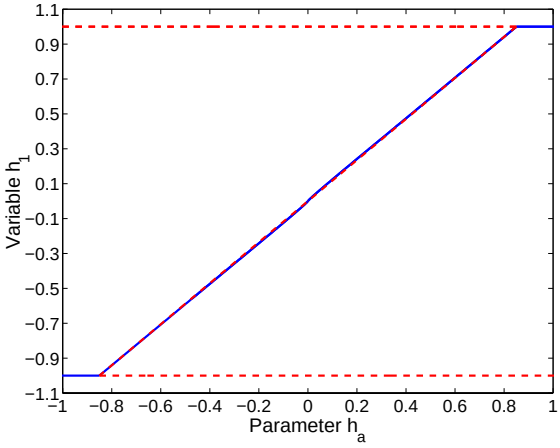

(b) h_1 *vs.* h_a

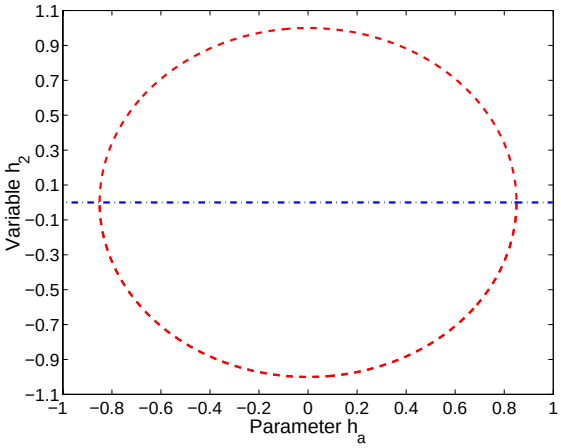

(c) h_2 *vs.* h_a

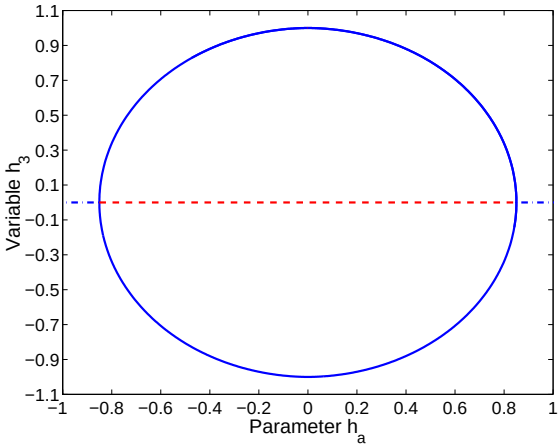

(d) h_3 *vs.* h_a

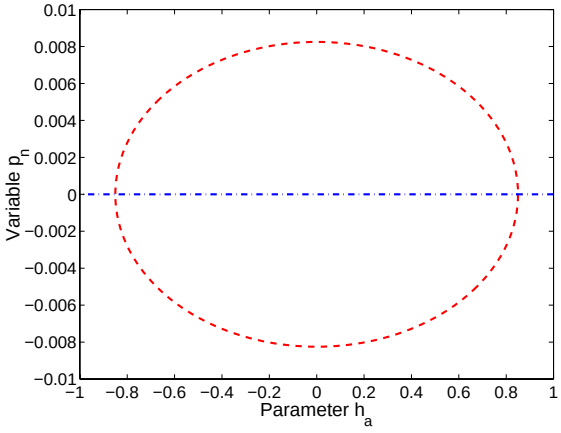

(e) p_n *vs.* h_a

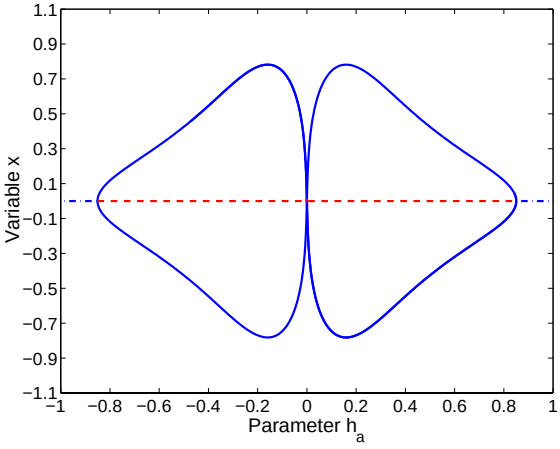

(f) x *vs.* h_a

Figure 8.2: Bifurcation diagrams for axisymmetric dual-spin satellite

metric gyrostat for k values near the Type 2B threshold, defined in Ch. 4 by Eq. 4.29:

$$k_{2B} = \varepsilon\varepsilon'/I_2^2 \tag{8.8}$$

Figure 8.3 shows the equilibria for k just lower and higher than the Type 2B existence threshold.

For $k = 0.06187 < k_{2B}$, the equilibria include the Type 2B equilibrium state and Type 6 branches in the $\hat{\mathbf{b}}_2$–$\hat{\mathbf{b}}_3$ plane, whereas these equilibria do not occur for $k = 0.06188 > k_{2B}$.

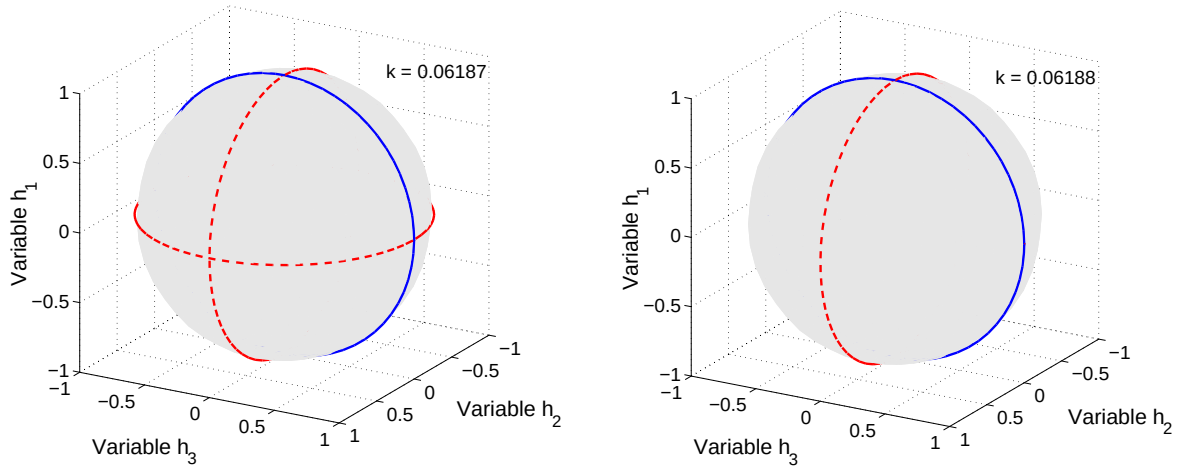

(a) $k < k_{2B}$ (b) $k > k_{2B}$

Figure 8.3: Axisymmetric dual-spin satellite equilibria near Type 2B existence threshold, $k_{2B} = 0.061875$

The Type 2B existence threshold is related to the damper tuning condition of k. We examine the damper tuning condition to explain the relationship with the existence of Type 2B and Type 6 equilibria.

Restating the Type 2B equilibrium existence condition from Eq. 4.29

$$k < \varepsilon\varepsilon'/I_2^2$$

we note that this condition is similar to the tuned-damper condition for a despun platform, Eq. 8.7. Expanding Eq. 4.29 in terms of ε, we relate the the Type 2B existence condition to the tuned-damper value, k_d, assuming an axisymmetric gyrostat ($I_2 = I_3$):

$$k < \varepsilon/I_2^2 - \varepsilon^2/I_2^2 \tag{8.9}$$
$$k < k_d(1-\varepsilon) \tag{8.10}$$
$$k < \varepsilon' k_d \tag{8.11}$$

Therefore, the classic damper tuning condition produces a k_d value greater than the existence threshold for the Type 2B equilibrium. The Type 2B equilibrium does not exist for $k = k_d$. For

small ε, k_d is also near the existence threshold for Type 2B equilibria for nearly axisymmetric gyrostats ($I_2 \approx I_3$). Because of this result, we find that Type 6 equilibria are not prevalent for nearly axisymmetric dual-spin satellites with tuned dampers.

8.1.4 Near Axisymmetric Dual-Spin Examples

We consider the effects of a slightly asymmetric platform on the equilibria for the example dual-spin satellite. We examine two cases: $I_2 > I_3$ and $I_3 > I_2$. The parameter set remains unchanged except for these two inertia values. The tuned-damper value of k does not change appreciably for these inertia properties. In the first example, we use $\mathbf{I} = (0.20, 0.41, 0.39)$ and in the second example, $\mathbf{I} = (0.20, 0.39, 0.41)$. We apply numerical continuation to the prolate dual-spin satellite, with $I_2 > I_3$, to produce equilibria for varying h_a, shown as Fig. 8.4. For the $I_3 > I_2$ example, the results are shown as Fig. 8.5.

We see in Fig. 8.4 that for $I_2 > I_3$ the stability of Type 4 and Type 5 equilibria changes from the axisymmetric example. The Type 5 equilibria and the $\hat{\mathbf{b}}_2$-axis spin, with $x = 0$ (Type 2A), are stable. The Type 4 equilibria and the $\hat{\mathbf{b}}_3$-axis spin (Type 3) are unstable. As with the axisymmetric case, the Type 2B spin does not exist. The slight increase in I_2, relative to the axisymmetric example, lowers the Type 2B existence threshold to $k < 0.059$ and is lower than the tuned-damper value of $k = 0.0625$.

Figure 8.5 shows that for $I_3 > I_2$, Type 4 equilibria are stable, whereas Type 5 equilibria are unstable. The slight decrease in I_2, relative to the axisymmetric example, raises the Type 2B existence threshold to $k < 0.065$. The tuned-damper value, $k = 0.0625$, allows the Type 2B equilibrium state. This configuration also has relatively small Type 6 equilibrium branches near the Type 2B state, although these off-axis equilibria are unstable.

As discussed in Sec. 5.4, decreasing k affects the Type 6 branches. For lower k values, the Type 6 branches have larger h_3 components. For sufficiently small k, the Type 6 branches intersect the Type 4 branches in the $\hat{\mathbf{b}}_1$–$\hat{\mathbf{b}}_3$ plane, as seen in Fig. 5.41(a). For prolate gyrostats with $I_2 > I_3$, the Type 6 equilibria can be stable. These stable, off-axis equilibria are potential trap states for systems disturbed from their nominal spin. Also, stable Type 6 branches can affect the dynamics of maneuvers that use rotor torques to change the system attitude. In the next section we consider a simple maneuver using small rotor torques, and how stable Type 6 branches of equilibria affect the motion.

8.2 Spin-up Maneuvers

In this section we examine how different system parameter sets affect the path of $\mathbf{h}$ in state space during a rotor spin-up maneuver called a dual-spin turn. A dual-spin turn is often used to deploy a dual-spin satellite from an initial configuration, with locked damper and rotor, to its final, despun

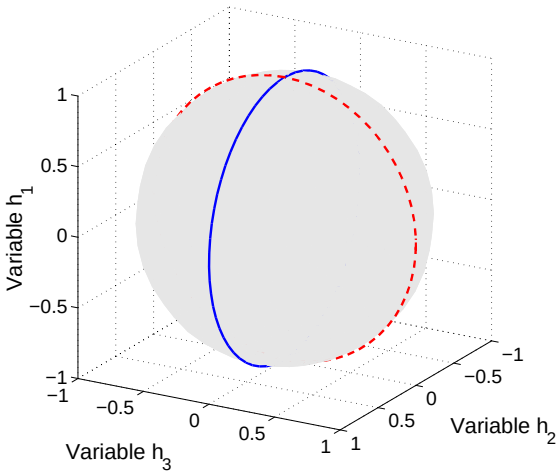

(a) Momentum sphere

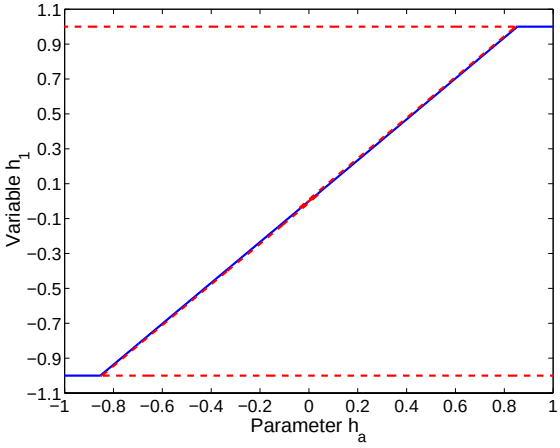

(b) h_1 *vs.* h_a

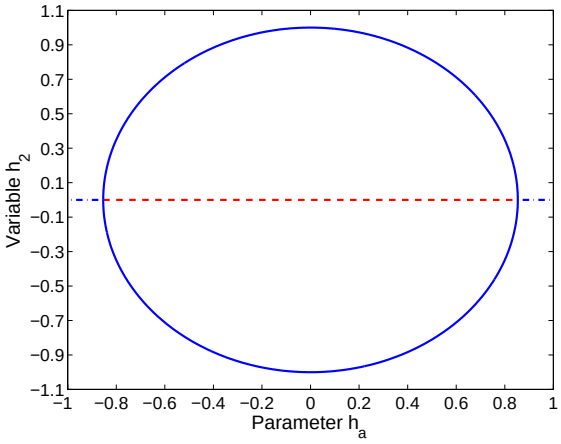

(c) h_2 *vs.* h_a

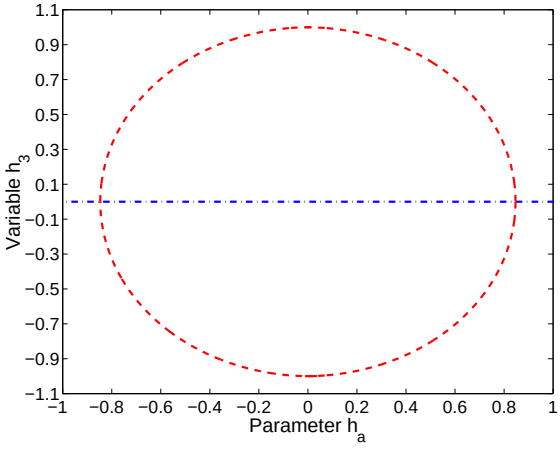

(d) h_3 *vs.* h_a

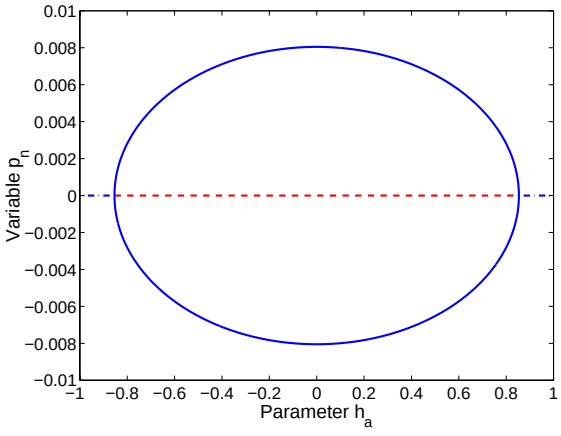

(e) p_n *vs.* h_a

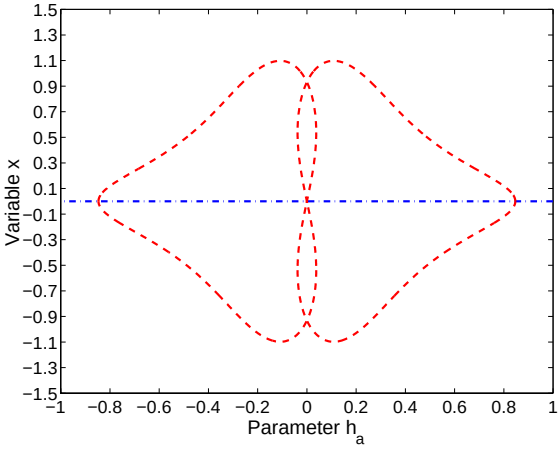

(f) x *vs.* h_a

Figure 8.4: Bifurcation diagrams for near-axisymmetric dual-spin satellite, $I_2 > I_3$

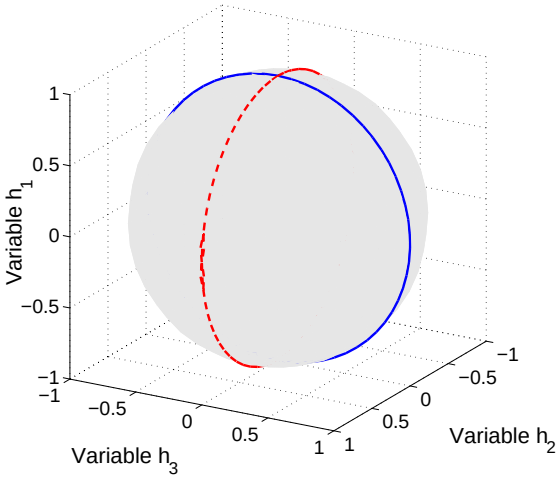

(a) Momentum sphere

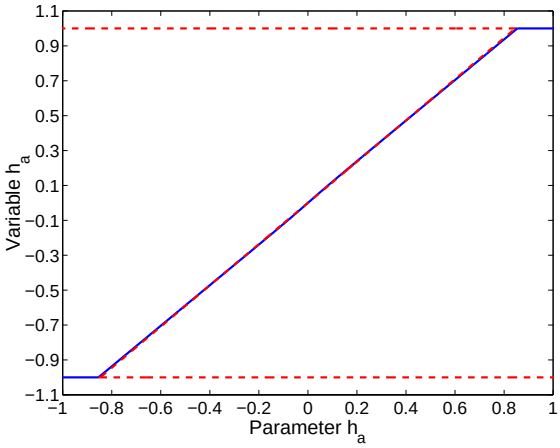

(b) h_1 *vs.* h_a

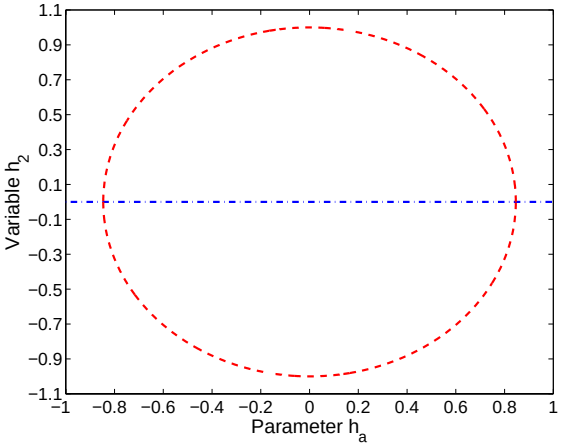

(c) h_2 *vs.* h_a

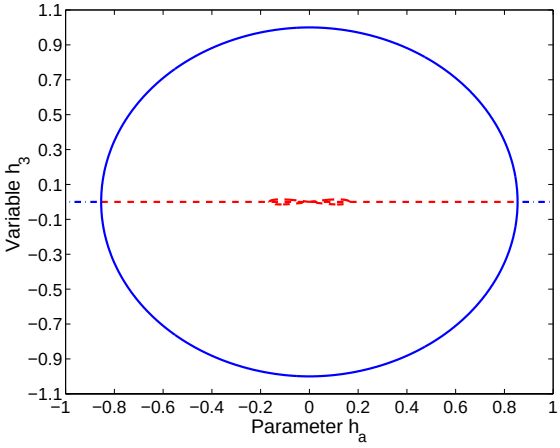

(d) h_3 *vs.* h_a

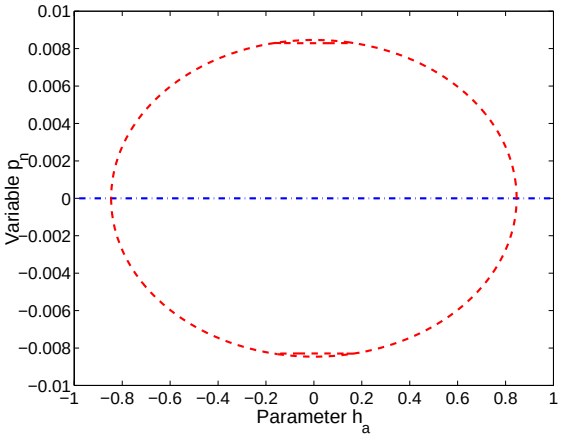

(e) p_n *vs.* h_a

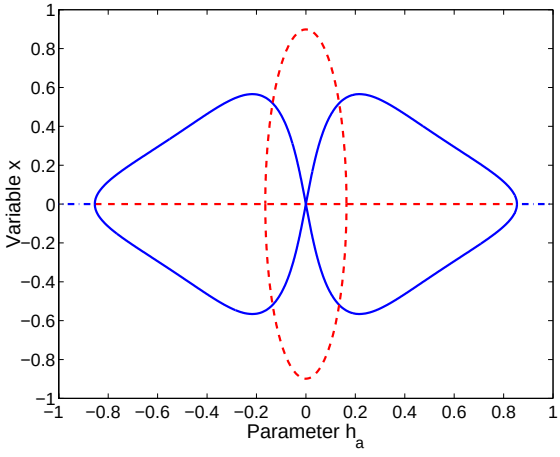

(f) x *vs.* h_a

Figure 8.5: Bifurcation diagrams for near-axisymmetric dual-spin satellite, $I_3 > I_2$

platform, configuration. Because the typical dual-spin satellite is prolate, its initial configuration is a major-axis spin. The dual-spin turn involves applying a small rotor torque until the rotor is in its final, $h_a = 1$, state. The satellite spin-axis transitions from the major-axis to the nominal (minor), $\hat{\mathbf{b}}_1$-axis. The bifurcation diagrams for varying h_a provide a unique perspective on the dynamics of the dual-spin turn. For spin-up maneuvers with sufficiently small g_a, the system state approximately follows branches of stable equilibria for increasing h_a. We simulate the dual-spin turn dynamics for the two nearly-axisymmetric dual-satellites of the previous section. Depending on the parameter set, the path of the $\mathbf{h}$ vector in state-space may vary significantly.

A practical problem with the spin-up maneuvers is that the final configuration may be a trap state instead of the intended state. Several studies have examined the problem of trap states and how to escape from these states. Scher and Farrenkopf suggested a periodic torquing of the rotor to escape from the minimum energy trap state for dual-spin satellites.[59] Hall showed that periodic torquing is relatively ineffective in the presence of significant damping, and proposed a method using a nearly constant rotor torque that is guaranteed to lead to escape.[31] Escape from minimum-energy trap states is an important operational issue for dual-spin satellites, but we focus on a despun-platform final state, with $h_1 = h_a = 1$. This nominal-spin state is the only stable equilibrium for $h_a = 1$ and trap states are not a problem.

The steps in the dual-spin turn are: 1) unlock the damper and let the system reach equilibrium; 2) apply a small, constant g_a until $h_a = 1$; and 3) allow the damper to dissipate any residual coning motion. We first consider the asymmetric dual-spin satellite with $I_3 > I_2$, shown in Fig 8.6, with a tuned damper. Because the equilibrium branches are relatively simple for this configuration, $\mathbf{h}$ transitions along the $\hat{\mathbf{b}}_1$–$\hat{\mathbf{b}}_3$ plane for a dual-spin turn from the $\hat{\mathbf{b}}_3$-axis spin to the $\hat{\mathbf{b}}_1$-axis spin, approximately following the stable Type 4 branch. Figure 8.6(a) shows the path of $\mathbf{h}$ on the momentum sphere and the damper displacement time history.

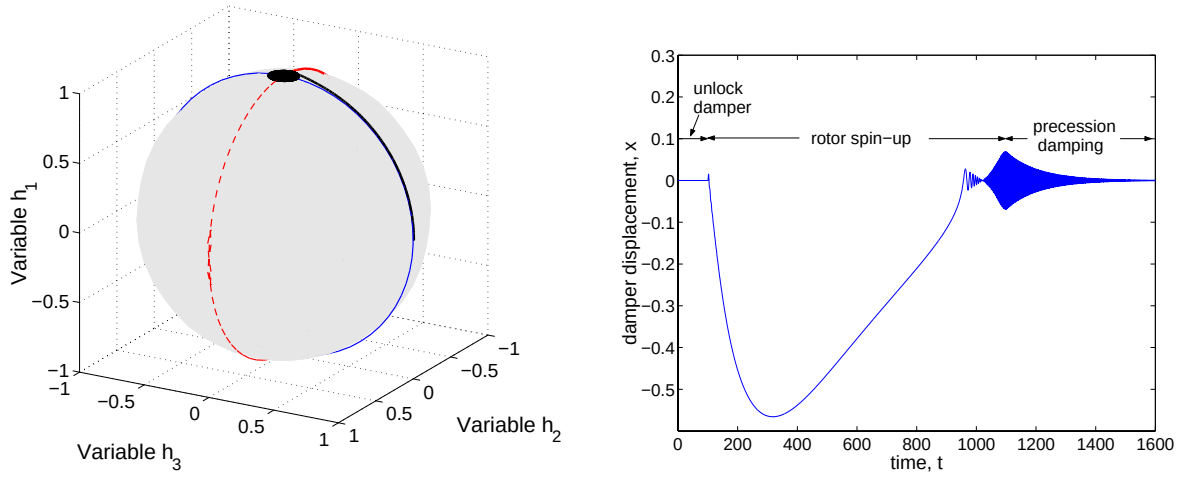

(a) Path of $\mathbf{h}$ on the momentum sphere

(b) Damper displacement during dual-spin turn

Figure 8.6: Dynamics of dual-spin turn for near-axisymmetric, prolate dual-spin satellite, $I_3 > I_2$

We use $g_a = 0.001$, requiring 1000 dimensionless time units (TU) to spin-up the rotor. The stable $\hat{\mathbf{b}}_3$-axis spin has $x = 0$, so the 100 TU allowed for the damper to stabilize is much longer than required. As $h_a \to 1$, the system experiences a coning motion around the nominal spin axis. After the rotor torque ends, and $h_a = 1$, the damper dissipates the precession as the system approaches the nominal spin asymptotically.

We simulate the dynamics of a dual-spin turn for the $I_2 > I_3$ configuration of Fig. 8.4. The system transitions from a $\hat{\mathbf{b}}_2$-axis spin to a $\hat{\mathbf{b}}_1$-axis spin, approximately following the stable Type 5 equilibrium branch. Figure 8.7 illustrates the dual-spin dynamics on the momentum sphere and the damper displacement history. The results are similar to the $I_3 > I_2$ configuration: the $\mathbf{h}$ vector transitions in a direct fashion to near the nominal spin, precesses slightly, and is damped to the desired nominal spin state. All Type 5 equilibria have $x = 0$, so the damper remains largely undisplaced until the precession begins.

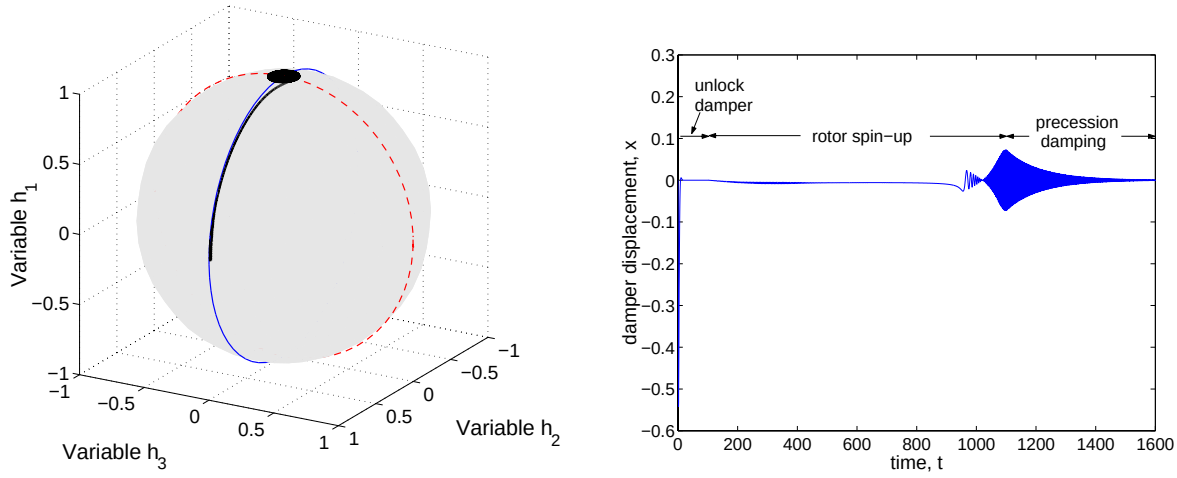

(a) Path of $\mathbf{h}$ on the momentum sphere

(b) Damper displacement during dual-spin turn

Figure 8.7: Dynamics of dual-spin turn for near-axisymmetric, prolate dual-spin satellite, $I_2 > I_3$

In the previous two examples, the equilibria did not include stable Type 6 (off-axis) equilibria, due to the tuned-damper value of k. As discussed in Sec. 5.4, decreasing k results in more pronounced and potentially complex Type 6 equilibria. For systems with $k < k_{tune}$, the dual-spin turn dynamics are not as simple as for systems with tuned dampers.

We repeat the simulation of the $I_2 > I_3$ configuration, but for $k = 0.04$. Figure 8.8 shows the dynamics on the momentum sphere and the damper displacement history. As with earlier simulations, the rotor torque is small: $g_a = 0.001$. The lower value of k changes the stability properties of the major-axis spin: Type 2B ($x \neq 0$) is stable whereas Type 2A ($x = 0$) is unstable. The unlocked damper stabilizes at a non-zero value of x. This large damper displacement may not be physically feasible for real damper designs, but we do not restrict x in the simulation. The system oscillates slightly as $\mathbf{h}$ approximately follows the stable Type 6, then Type 5 branches of equilibria. As with

previous examples, the system experiences coning motion as $\mathbf{h}$ approaches $\hat{\mathbf{b}}_1$. The indirect transition of the spin axis from major-axis to minor-axis is clearly explained by the momentum sphere representation of the bifurcation results for varying h_a.

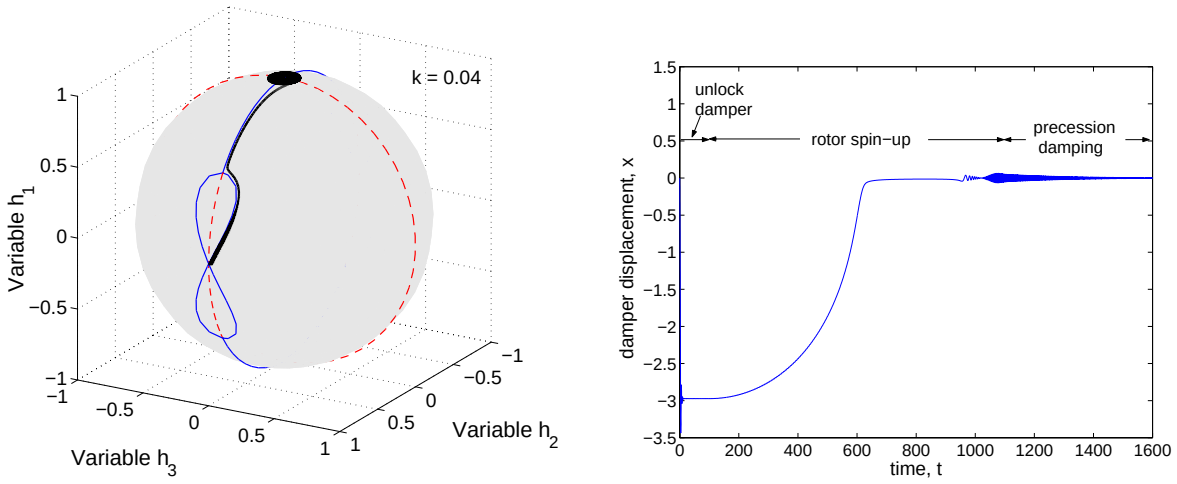

(a) Path of $\mathbf{h}$ on the momentum sphere

(b) Damper displacement during dual-spin turn

Figure 8.8: Dynamics of dual-spin turn for, prolate dual-spin satellite ($I_2 > I_3$) with $k < k_{tune}$

Section 5.4 shows that for sufficiently small k, the Type 6 equilibria intersect the Type 4 equilibria at bifurcation points. For these low values of k, the spin-up dynamics are significantly affected. We examine the same $I_2 > I_3$ configuration, but for $k = 0.005$. Figure 8.9 shows the spin-up dynamics displayed on the momentum sphere for this configuration using two different rotor torques. In Fig. 8.9(a), we use $g_a = 0.001$. For this rotor torque, $\mathbf{h}$ transitions in the direction of the stable Type 6 branch, then the stable Type 4 branch. The system oscillates more than examples with larger k, and $\mathbf{h}$ only roughly follows the Type 6 branch. The abrupt change at the bifurcation point produces more oscillation, but $\mathbf{h}$ proceeds roughly along the Type 4 branch toward the nominal spin. However, the Type 4 branch is not entirely stable; there is a bifurcation point, with Type 6 equilibria forming a ring aroung the $\hat{\mathbf{b}}_1$ axis. The stability change at the bifurcation point produces a jump phenomenon, and $\mathbf{h}$ jumps toward a stable Type 5 branch before beginning precession followed by damping to the nominal spin. Smaller rotor torques allow $\mathbf{h}$ to more closely follow the stable branches, but also lengthen the spin-up time. In Fig. 8.9(b) we use $g_a = 0.0001$, which reduces the system oscillation and allows $\mathbf{h}$ to more closely follow stable branches of equilibria. However, the spin-up maneuver requires 10,000 TU.

8.3 Summary

Equilibrium motions of dual-spin satellites are affected by varying system parameters, but for typical parameter values the set of equilibria is relatively simple. Whereas a perfectly axisymmetric

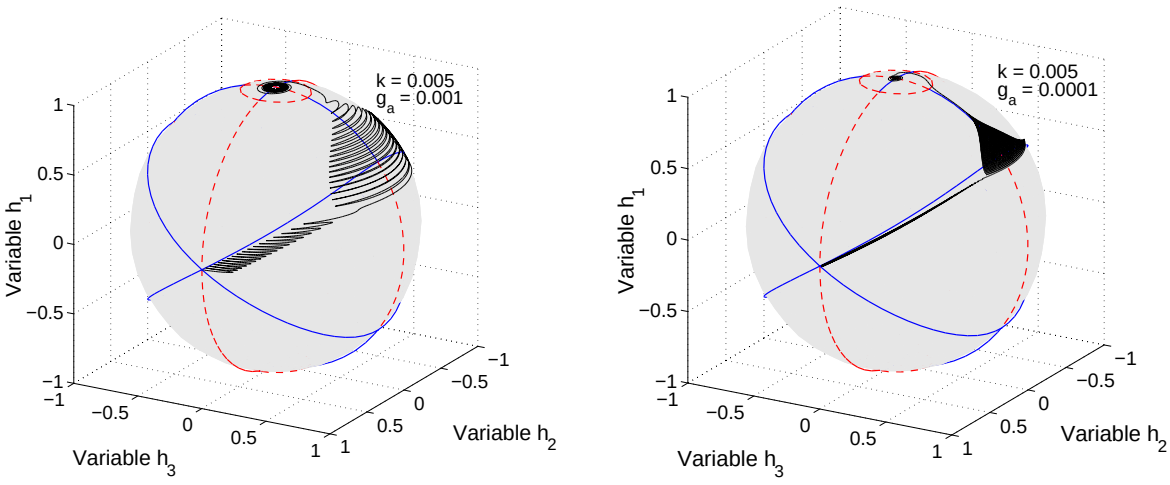

(a) Path of $\mathbf{h}$ on the momentum sphere

(b) Damper displacement during dual-spin turn

Figure 8.9: Dynamics of dual-spin turn for, prolate dual-spin satellite ($I_2 > I_3$) with $k < k_{tune}$

gyrostat has fewer branches of equilibria than asymmetric configurations, slight inertia asymmetries produce addition possible equilibria. For tuned dampers, the spring stiffness is sufficiently large to produce continuous branches of equilibria that primarily lie in principal planes. The bifurcation results for varying rotor momentum provides a unique perspective on the dynamics of rotor spin-up. For a tuned damper, the dual-spin turn transitions directly along principal planes toward the nominal spin equilibrium. The spin-up dynamics are more complex if the spring stiffness is less than the tuned-damper value.

Chapter 9

Conclusions and Recommendations

The gyrostat with spring-mass-damper is a useful model for studying the motion of spinning satellites with a rotor, especially dual-spin satellites. Rotor momentum is effective in stabilizing prolate gyrostats, even in the presence of energy dissipation. Though most research has focused on the nominal-axis spin, other equilibria exist that can have important consequences. Multiple stable equilibria may yield trap states for systems perturbed from the nominal spin or affect the dynamics of attitude maneuvers.

The equations of motion are determined from a Newton-Euler approach, resulting in equations in terms of angular momentum and damper variables: $\mathbf{z} = (h_1, h_2, h_3, p_n, x)$. Analytic solutions and stability conditions are derived for the equilibrium equations for simple spins, but numerical techniques are required for determining general equilibria and their stability. Linear stability analysis is successful in assessing stability in most cases, but a nonlinear, Liapunov stability technique is required for certain regions of state-parameter space.

Numerical continuation is an effective method of numerically determining equilibria. However, for a system with conserved angular momentum, success depends on reducing the system and eliminating the persistent zero eigenvalue in the system Jacobian. A spherical-coordinate transformation yields an appropriate reduction, but a singularity in the transformation of the system state to spherical coordinates requires at least two separate transformations to adequately explore the entire state space. An alternative reduction is possible within the $\hat{\mathbf{b}}_1$–$\hat{\mathbf{b}}_3$ plane, where the equilibrium solutions are augmented with conserved angular momentum to provide effective equations in a three-dimensional state space, $\mathbf{z}_r = (h_1, h_3, x)$. With an adequate set of reduced equations, numerical continuation produces equilibria and bifurcations for varying system parameters.

Bifurcation diagrams for $h_a = 0$, using the damper location as the bifurcation parameter, are identical to those for a rigid body with a spring-mass-damper. Small values of h_a perturb these bifurcations and unfold certain pitchfork bifurcations. Using h_a as the bifurcation parameter, we identify multiple equilibria throughout the state space. Multiple equilibria exist in the $\hat{\mathbf{b}}_1$–$\hat{\mathbf{b}}_3$ plane for varying b or h_a. Equilibria also exist in the $\hat{\mathbf{b}}_1$–$\hat{\mathbf{b}}_2$ plane. For axisymmetric gyrostats, equilibria

exist throughout the $\hat{\mathbf{b}}_2$–$\hat{\mathbf{b}}_3$ plane. Also, branches of equilibria may occur that do not lie in any of the pseudo-principal planes of the body axes. The stability of these equilibria depends on the system inertia properties, damper parameters, and rotor momentum. Increasing spring stiffness, k, changes the structure of the system equilibria. Similar effects are found for decreasing damper location, b, or changing system inertia properties.

For changing b or h_a, the nominal-spin equilibria bifurcate into branches of equilibria in either the $\hat{\mathbf{b}}_1$–$\hat{\mathbf{b}}_2$ plane or $\hat{\mathbf{b}}_1$–$\hat{\mathbf{b}}_3$ plane. This bifurcation point is defined analytically in terms of damper parameters, inertia properties, and rotor momentum. For certain combinations of the system parameters, a jump phenomenon may occur. The Liapunov-Schmidt reduction technique produces an analytic condition for determining if the jump phenomenon is possible and therefore provides a design criterion for avoiding the jump phenomenon. Two-parameter continuation and the stability criterion for the nominal spin produces parameter charts that describe possible singular points in parameter space, including turning points and their relationship with the nominal-spin equilibria. This parameter space representation concisely characterizes possible equilibria near the nominal spin and divides the parameter space into regions of stable and unstable nominal-spin configurations.

The gyrostat with damper is an idealized model with considerable symmetry. The rotor and damper axes are aligned with the nominal spin axis. However, for slight alignment errors of either the rotor or damper, certain bifurcations of the standard, unperturbed, model unfold. The perturbed branches of equilibria may produce precession of the intended spin axis around the actual spin axis. As real systems are always subject to imperfections, these perturbed bifurcation results show how actual satellites may behave for slight rotor or alignment errors.

The global equilibria for the damped gyrostat provide new insights into several practical aspects of dual-spin satellites. Satellites with typical values for inertia properties and damper parameters have relatively simple global equilibria. Damper parameters are often selected to match the undamped spring-mass natural frequency to the satellite precession frequency to more efficiently attenuate precession. A classic damper-tuning condition is analytically related to the existence of out-of-plane equilibria, and we find that these equilibria do not exist for tuned dampers. Simple satellite maneuvers that use small rotor torques are examined with respect to stable, global equilibria. The maneuver dynamics are combined with equilibria on the momentum sphere, producing a unique perspective of these maneuvers in state space. Changing damper parameters has a significant effect on the dynamics of simple rotor spin-up maneuvers.

Further analysis of the system equilibria is possible for different bifurcation parameters. Varying spring stiffness, or inertia properties and the bifurcation parameter will generate different bifurcation diagrams that may better characterize certain bifurcations.

Additional research may investigate active control techniques for stabilizing a pure $\hat{\mathbf{b}}_2$-axis spin by exploiting the stable submanifold. This equilibrium state has zero rotor momentum, so the model is equivalent to a rigid body with a circumferential damper. The global branches of stable equilibria may provide useful insights into controlled attitude maneuvers, as they do for uncontrolled spin-up maneuvers.

One possible extension to this work is to consider a similar gyrostat with damper model, but placed in a gravitational field and subject to the gravity gradient torque. We could no longer simplify the original equations by assuming zero external forces and moments. Attitude variables are required to locate the direction of the external force and torque with respect to the body frame. One possible approach is to use an orbiting reference frame that rotates once per orbit. Equilibria relative to this rotating reference frame may require the gravity gradient torque to precess the satellite at the orbital angular rate.

Appendix A

Proof that $I_2' > 0$

In the stability analysis of the damped gyrostat, we encounter a recurring, dimensionless term, denoted I_2', defined as

$$I_2' = \varepsilon' I_2 - \varepsilon b^2 \tag{A.1}$$

The linear stability analysis requires that I_2' be positive for a stable $\hat{\mathbf{b}}_1$ axis spin. Here we show that I_2' is always positive.

We start by examining a system consisting of a rigid body $\mathcal{B}$, with a separate point mass, $\mathcal{P}$, representing the damper mass (see Fig. A.1). The system mass center is point $\mathcal{O}$ and principal axes are defined by the $\mathcal{F}_b$ coordinate system axes. The mass center and principal axes of $\mathcal{B}$ are point $\mathcal{O}'$ and the coordinate axes of frame $\mathcal{F}_b'$. The distance between $\mathcal{O}$ and $\mathcal{O}'$ is defined as d^*. Particle $\mathcal{P}$ has mass m_p^* and is a distance b^* from $\mathcal{O}$. Note that dimensional quantities are distinguished with an asterisk, whereas dimensionless quantities are without the asterisk.

By the parallel axis theorem, the moment of inertia of $\mathcal{B}$ about the $\hat{\mathbf{b}}_2$ axis is

$$I_{2_b}^* = I_{2_b}'^* + m^* d^{*2} \tag{A.2}$$

where $I_{2_b}'^*$ is the moment of inertia of $\mathcal{B}$ about $\hat{\mathbf{b}}_2{}'$ and m^* is the mass of $\mathcal{B}$. Since $\mathcal{O}$ is the system mass center, $m^* d^* = m_p^* b^*$. Therefore,

$$I_{2_b}^* = I_{2_b}'^* + \left(m_p^* b^*\right)^2 / m^* \tag{A.3}$$

The moment of inertia of the system, $\mathcal{B} + \mathcal{P}$, about $\hat{\mathbf{b}}_2$ is also easily determined from the parallel axis theorem and Eq. A.3 ,

$$I_2^* = I_{2_b}^* + m_p^* b^{*2} = I_{2_b}'^* + \left(\frac{m_p^{*2} + m_p^* m^*}{m^*}\right) b^{*2} \tag{A.4}$$

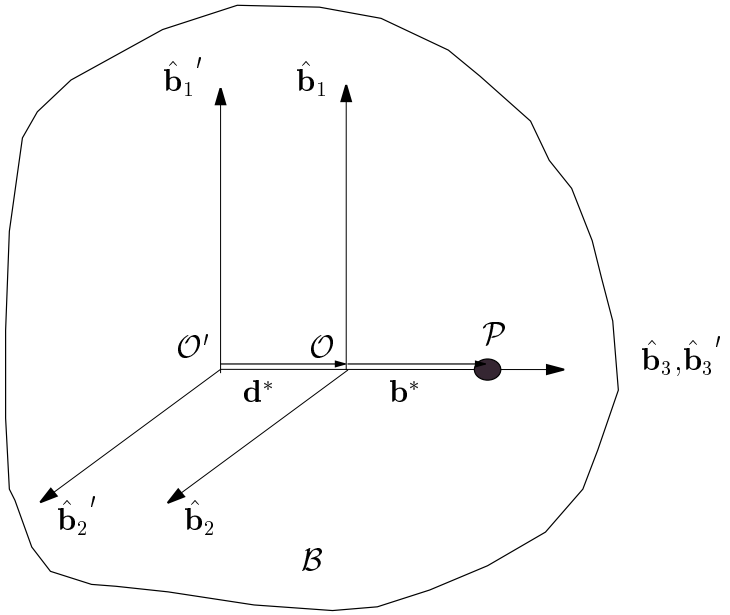

Figure A.1: Rigid body with a point mass

Non-dimensionalizing the moment of inertia, as in Ch. 3, and realizing that

$$\varepsilon' = \frac{m^*}{m^* + m_p^*}$$

leads to

$$I_2 = I_{2_b} + \varepsilon b^2/\varepsilon'$$

or after rearranging,

$$\varepsilon' I_2 - \varepsilon b^2 = \varepsilon' I_{2_b} = I_2' \tag{A.5}$$

It is clear that the term, $I_2' = \varepsilon' I_{2_b}$, and is therefore always positive. Notice also that as the damper mass approaches zero and $\varepsilon' \to 1$, then $I_2' \to I_{2_b}$.

Appendix B

Bifurcation Diagrams for Equilibria in the $\hat{\mathbf{b}}_1$–$\hat{\mathbf{b}}_3$ Plane

This appendix includes bifurcation diagrams in the reduced state space, $\mathbf{z}_r = (h1, h3, x)$, corresponding to equilibria in the $\hat{\mathbf{b}}_1$–$\hat{\mathbf{b}}_3$ plane. Damper position, b, and rotor momentum, h_a, are used in different cases as the bifurcation parameter. These equilibria are discussed for selected bifurcation diagrams in Sec. 5.3. This Appendix displays equilibria on the momentum sphere and three state-parameter bifurcation diagrams, providing a more complete description of the equilibria. All the bifurcation diagrams in this appendix use the system parameters defined in Table 5.1. Spring stiffness (k), damper location (b), and rotor momentum (h_a) are specified in each section.

B.1 Rigid Body With Damper ($\mathcal{B}+\mathcal{P}$) Equilibria ($h_a = 0$): Varying b

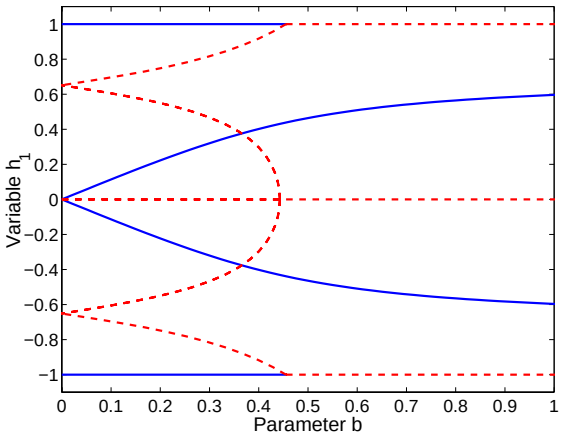

(a) h_1 *vs.* b

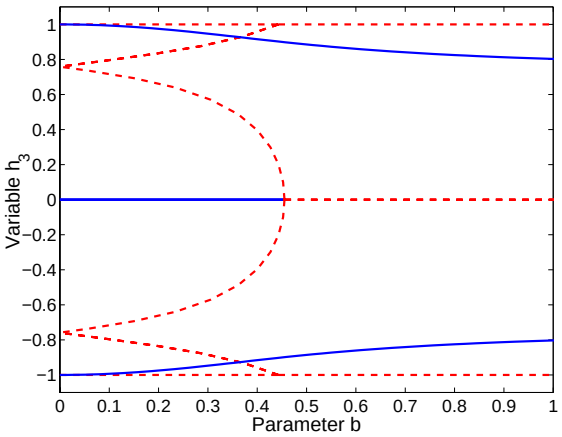

(b) h_3 *vs.* b

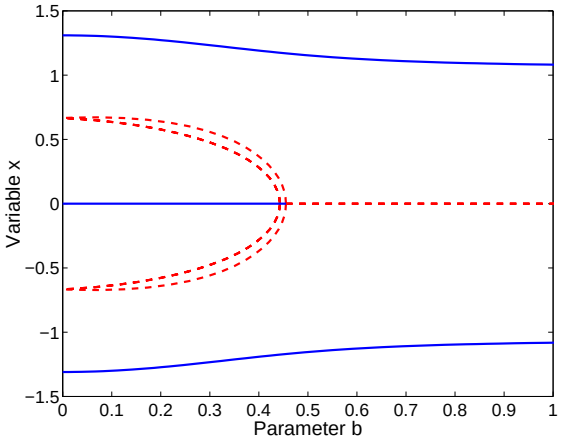

(c) x *vs.* b

Figure B.1: Damper position bifurcations for $\mathcal{B}+\mathcal{P}$ with $k = 0.4$. This combination produces a subcritical pitchfork bifurcation, with the bifurcation point occurring at the nominal spin. A separate type of pitchfork occurs along the Type 3 equilibrium branch.

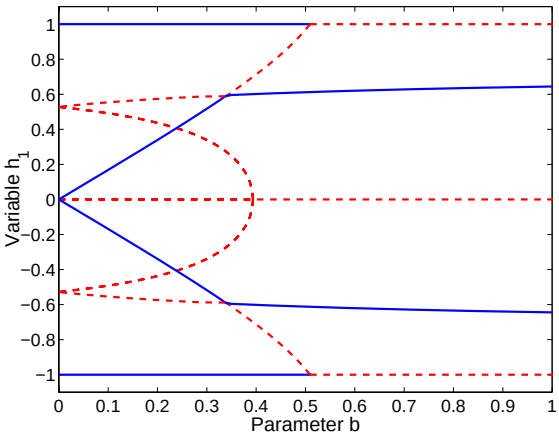

(a) h_1 *vs.* b

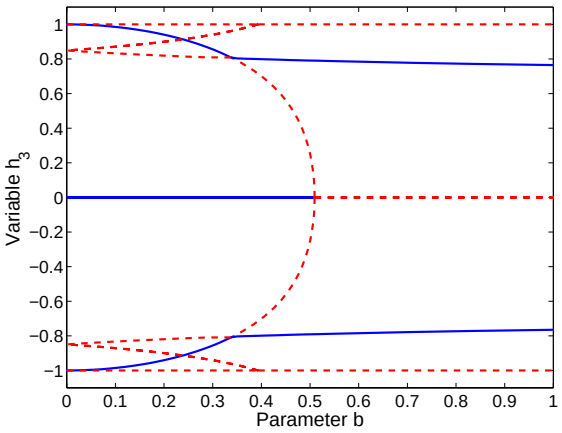

(b) h_3 *vs.* b

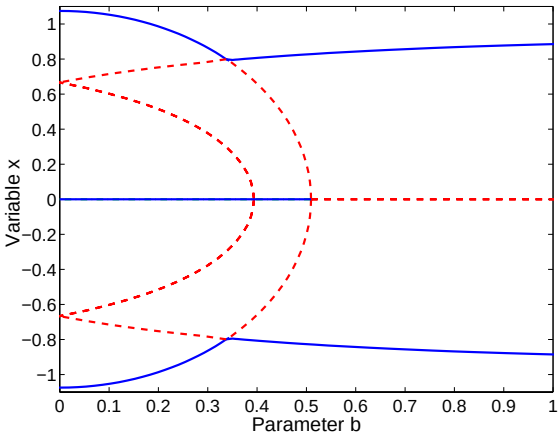

(c) x *vs.* b

Figure B.2: Damper position bifurcations for $\mathcal{B} + \mathcal{P}$ with $k = 0.50075$. This combination produces a transcritical bifurcation in the Type 4 equilibrium branches. The nominal-spin pitchfork bifurcation is subcritical.

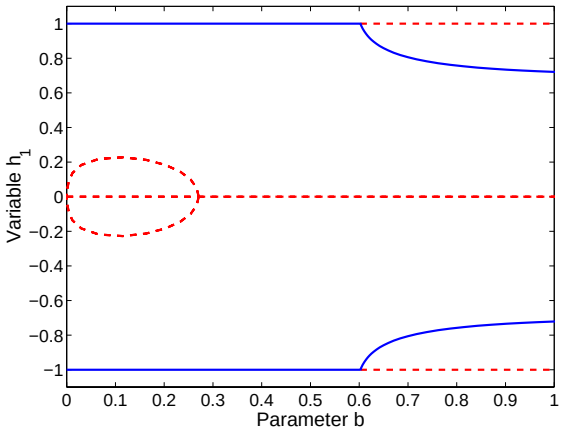

(a) h_1 *vs.* b

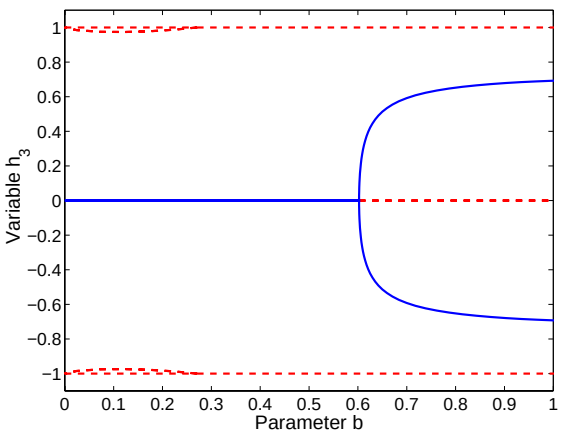

(b) h_3 *vs.* b

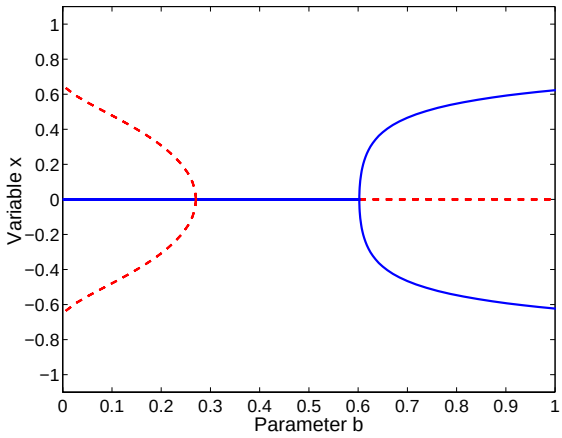

(c) x *vs.* b

Figure B.3: Damper position bifurcations for $\mathcal{B} + \mathcal{P}$ with $k = 0.7$. This combination produces a supercritical pitchfork along the nominal-spin branch of equilibria.

B.2 Gyrostat with Damper ($\mathcal{B}+\mathcal{R}+\mathcal{P}$) Equilibria for Different Spring Stiffness, k: Varying h_a

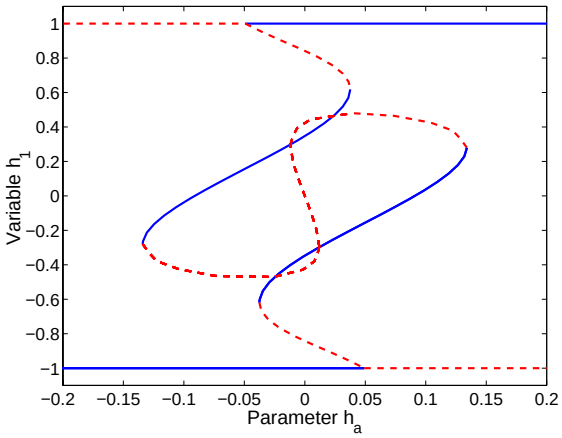

(a) h_1 *vs.* h_a

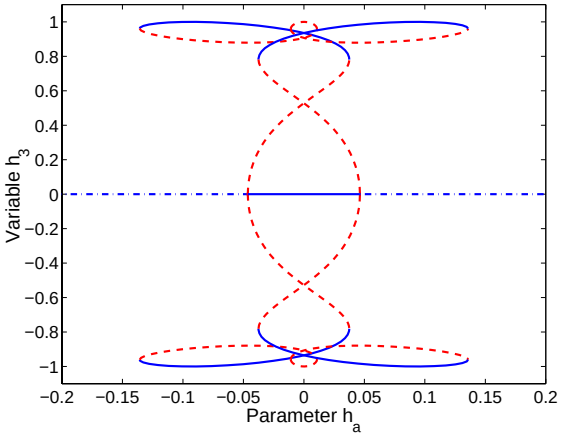

(b) h_3 *vs.* h_a

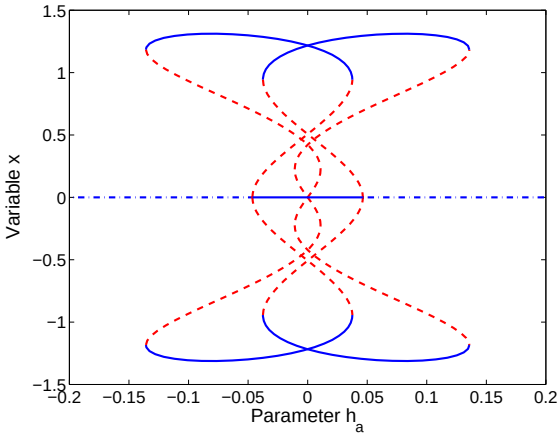

(c) x *vs.* h_a

Figure B.4: Rotor momentum bifurcations for $\mathcal{B}+\mathcal{R}+\mathcal{P}$ with $b=0.33$ and $k=0.4$.

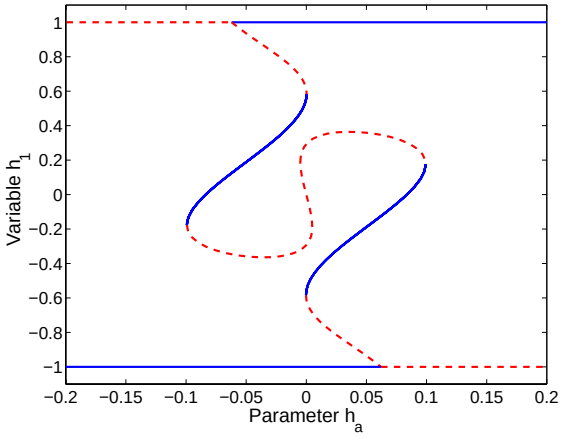

(a) h_1 *vs.* h_a

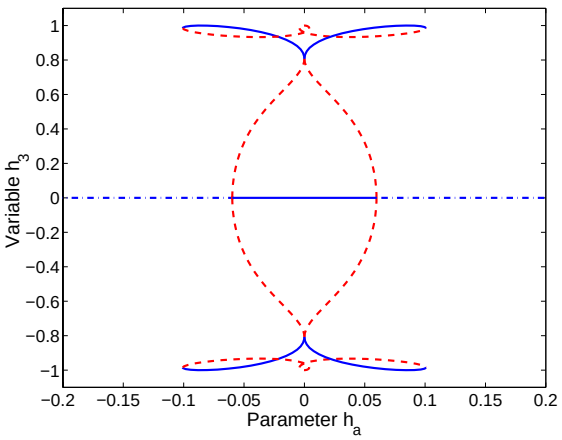

(b) h_3 *vs.* h_a

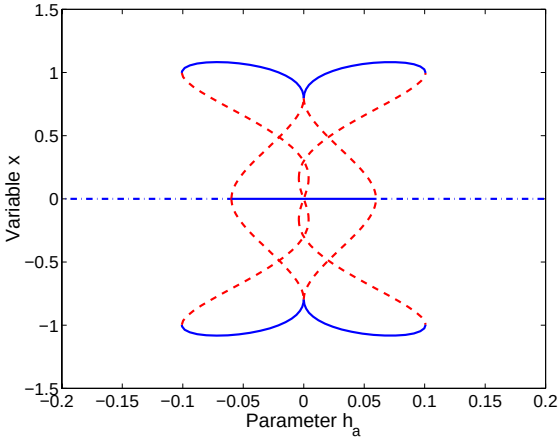

(c) x *vs.* h_a

Figure B.5: Rotor momentum bifurcations for $\mathcal{B} + \mathcal{R} + \mathcal{P}$ with $b = 0.33$ and $k = 0.50075$.

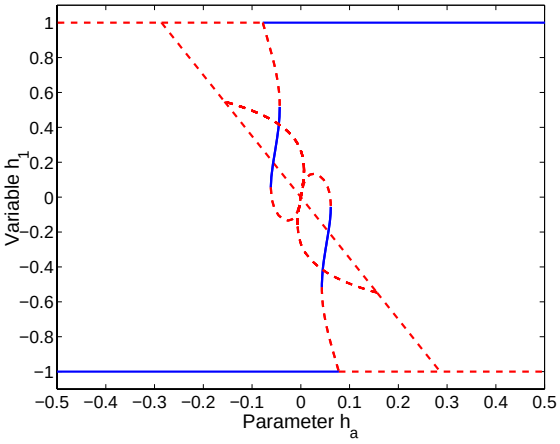

(a) h_1 *vs.* h_a

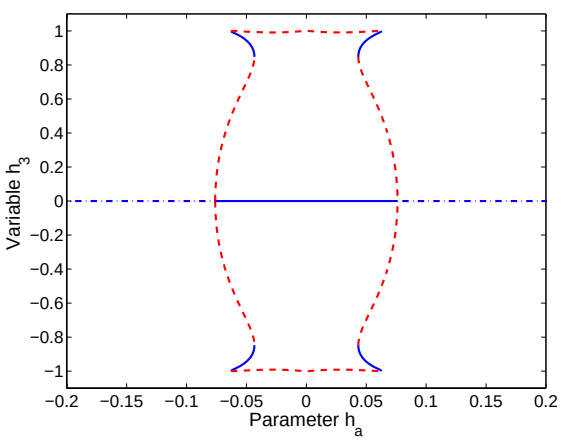

(b) h_3 *vs.* h_a

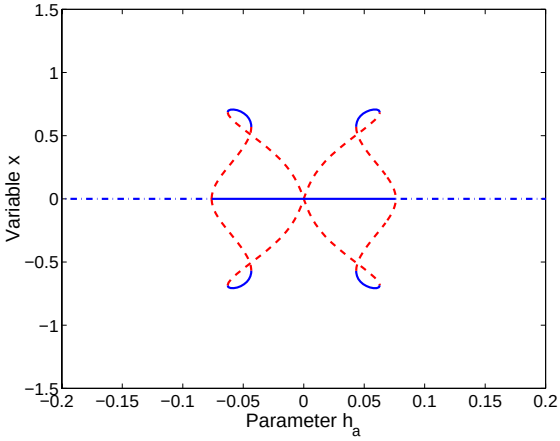

(c) x *vs.* h_a

Figure B.6: Rotor momentum bifurcations for $\mathcal{B} + \mathcal{R} + \mathcal{P}$ with $b = 0.33$ and $k = 0.7$.

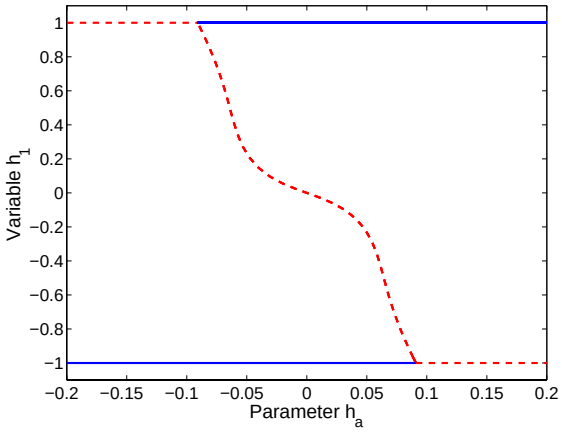

(a) h_1 *vs.* h_a

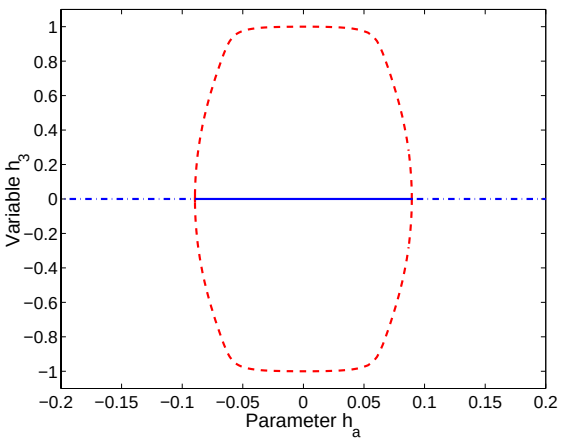

(b) h_3 *vs.* h_a

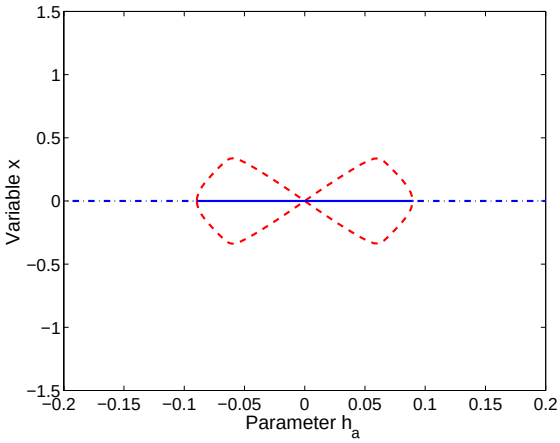

(c) x *vs.* h_a

Figure B.7: Rotor momentum bifurcations for $\mathcal{B} + \mathcal{R} + \mathcal{P}$ with $b = 0.33$ and $k = 1.0$.

B.3 Gyrostat with Damper ($\mathcal{B}+\mathcal{R}+\mathcal{P}$) Equilibria for Different Damper Location, b: Varying h_a

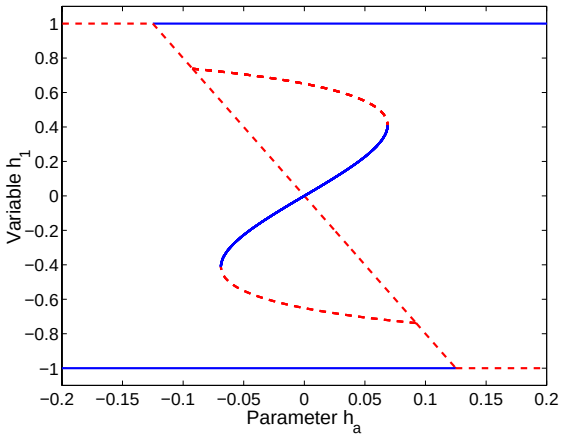

(a) h_1 *vs.* h_a

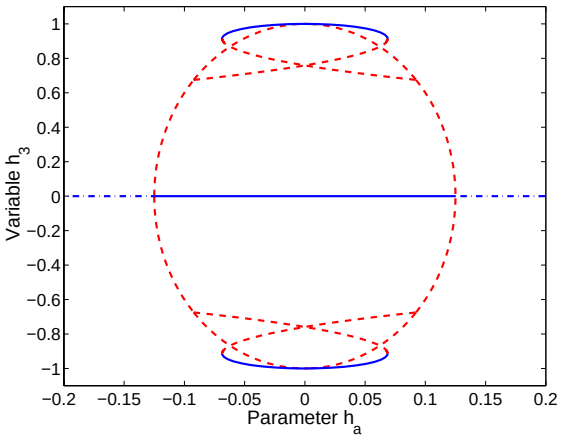

(b) h_3 *vs.* h_a

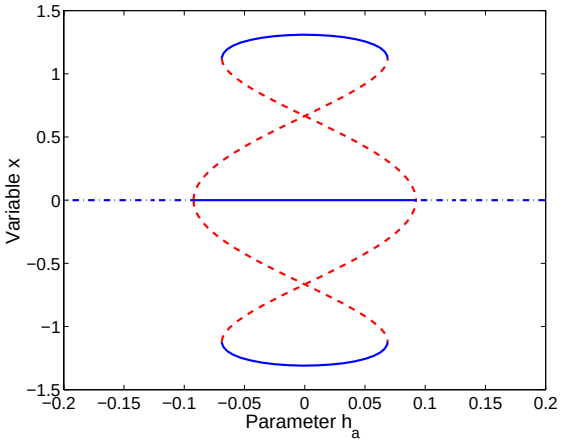

(c) x *vs.* h_a

Figure B.8: Rotor momentum bifurcations for $\mathcal{B}+\mathcal{R}+\mathcal{P}$ with $b=0$ and $k=0.4$.

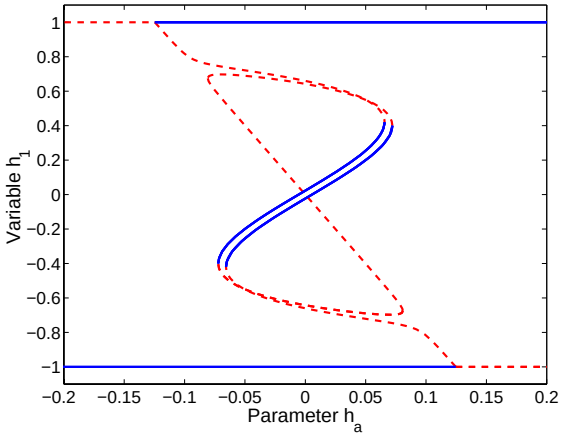

(a) h_1 *vs.* h_a

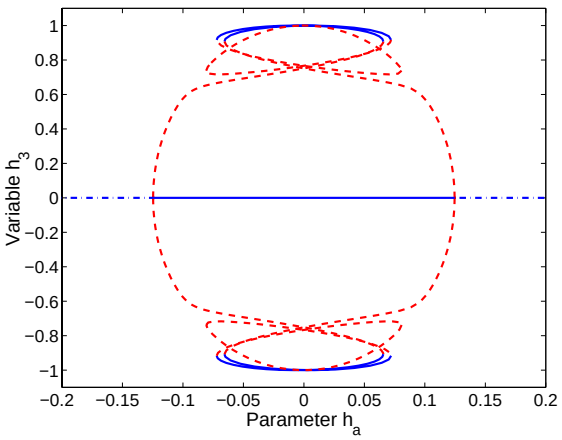

(b) h_3 *vs.* h_a

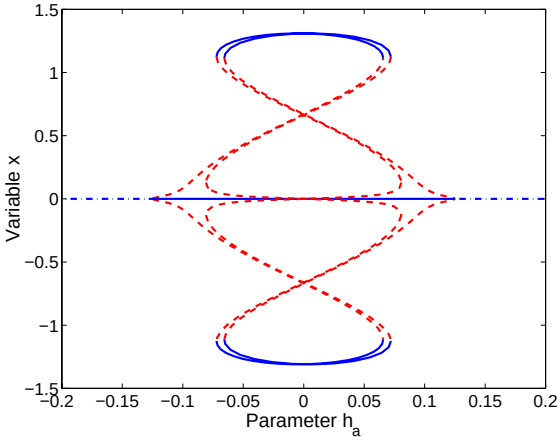

(c) x *vs.* h_a

Figure B.9: Rotor momentum bifurcations for $\mathcal{B} + \mathcal{R} + \mathcal{P}$ with $b = 0.02$ and $k = 0.4$.

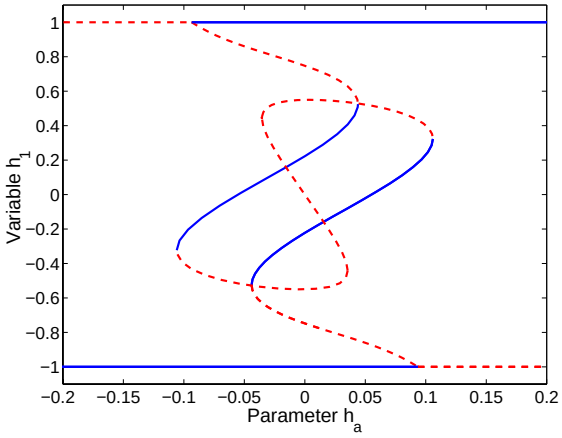

(a) h_1 *vs.* h_a

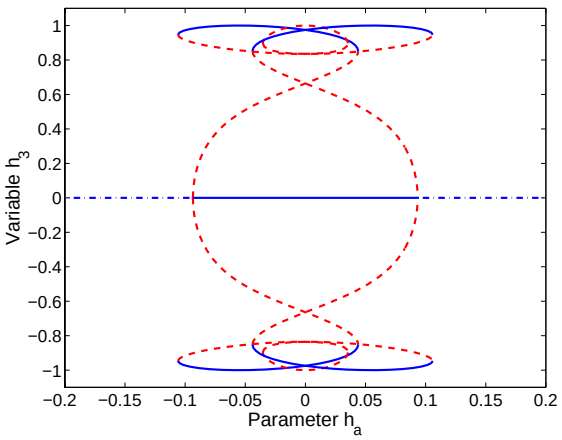

(b) h_3 *vs.* h_a

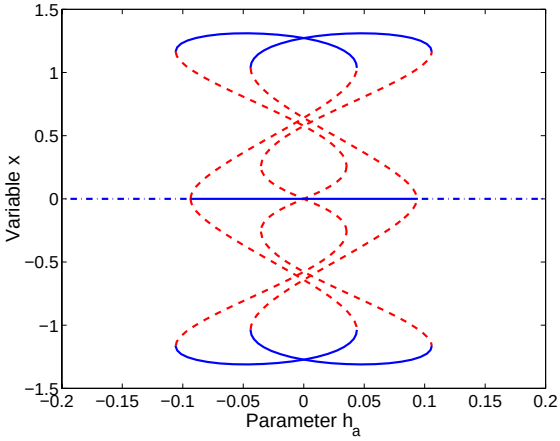

(c) x *vs.* h_a

Figure B.10: Rotor momentum bifurcations for $\mathcal{B} + \mathcal{R} + \mathcal{P}$ with $b = 0.2$ and $k = 0.4$.

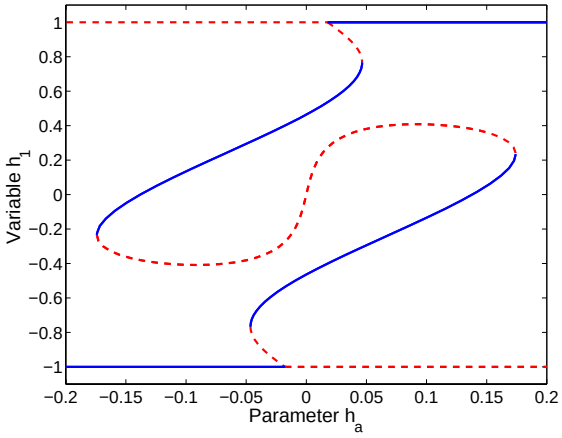

(a) h_1 *vs.* h_a

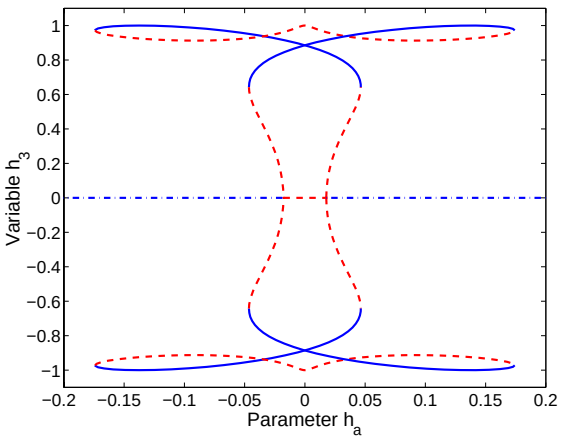

(b) h_3 *vs.* h_a

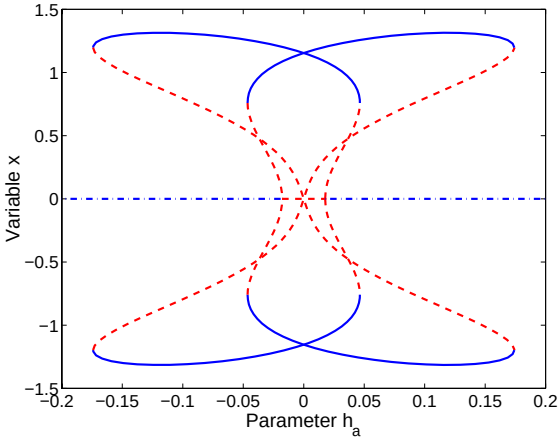

(c) x *vs.* h_a

Figure B.11: Rotor momentum bifurcations for $\mathcal{B} + \mathcal{R} + \mathcal{P}$ with $b = 0.5$ and $k = 0.4$.

B.4 Gyrostat with Damper ($\mathcal{B}+\mathcal{R}+\mathcal{P}$) Equilibria for Different Rotor Momentum, h_a: Varying b

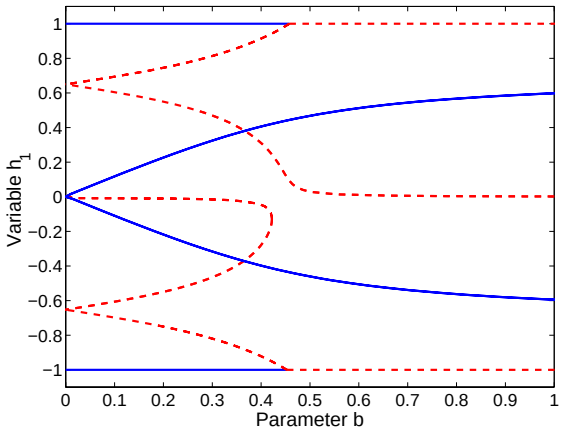

(a) h_1 *vs.* b

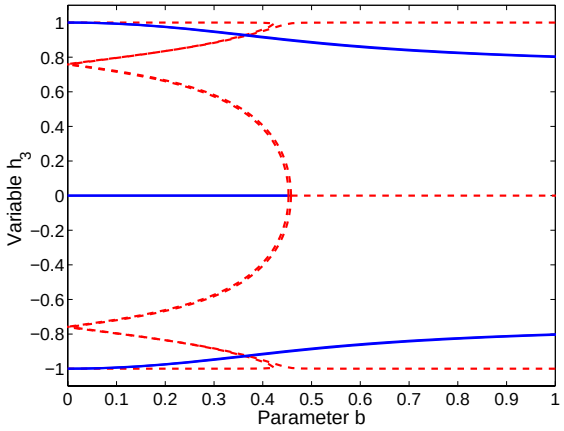

(b) h_3 *vs.* b

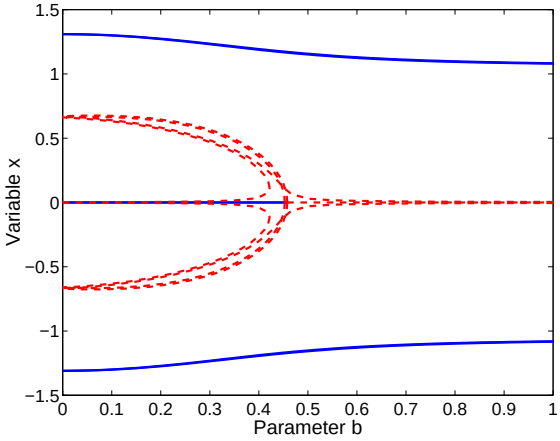

(c) x *vs.* b

Figure B.12: Damper position bifurcations for $\mathcal{B}+\mathcal{R}+\mathcal{P}$ with $h_a = 0.001$ and $k = 0.4$. This represents a very small perturbation from the $h_a = 0$ case. This perturbation breaks the Type 3 branch pitchfork into two separate branches.

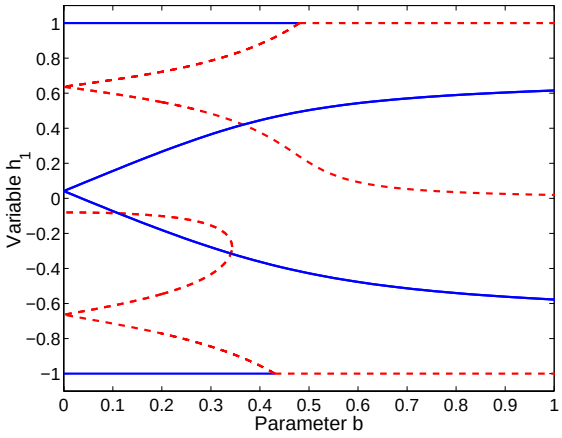

(a) h_1 *vs.* b

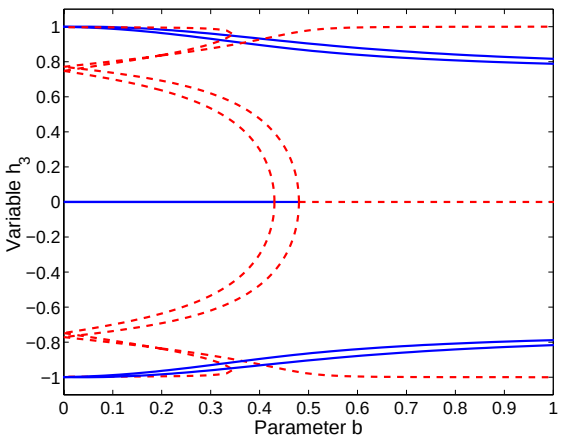

(b) h_3 *vs.* b

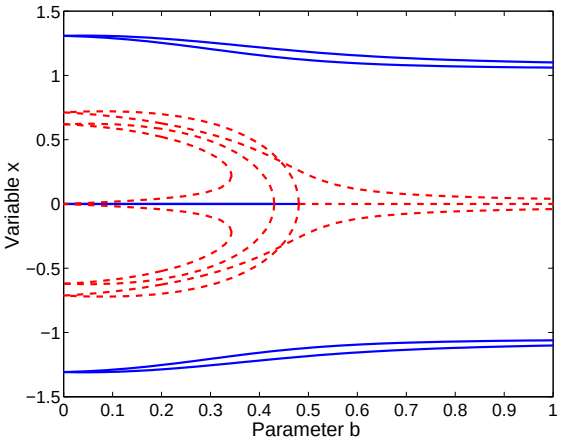

(c) x *vs.* b

Figure B.13: Damper position bifurcations for $\mathcal{B}+\mathcal{R}+\mathcal{P}$ with $h_a = 0.01$ and $k = 0.4$. This represents a small perturbation from the $h_a = 0$ case. Non-zero h_a changes the nominal pitchfork bifurcation points for $h_1 = \pm 1$. For $h_a = 0$, these two bifurcation points occurred for the same b value.

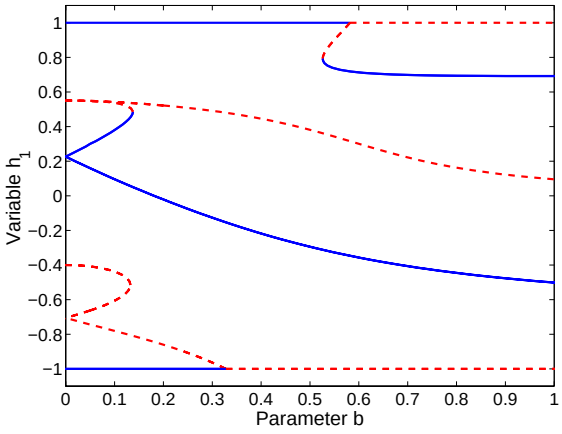

(a) h_1 *vs.* b

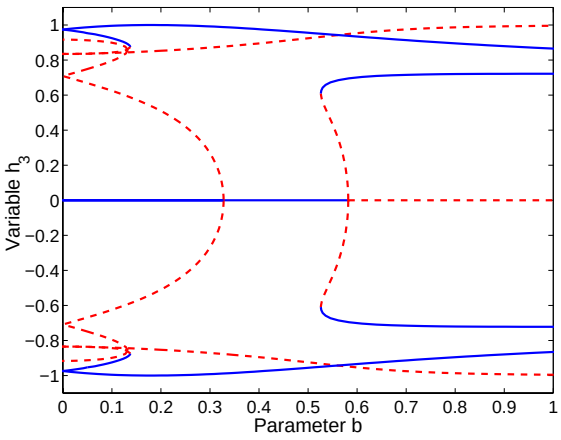

(b) h_3 *vs.* b

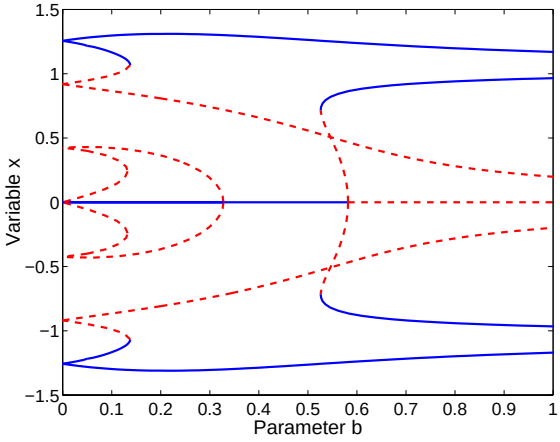

(c) x *vs.* b

Figure B.14: Damper position bifurcations for $\mathcal{B}+\mathcal{R}+\mathcal{P}$ with $h_a = 0.05$ and $k = 0.4$. This represents a medium-size perturbation from the $h_a = 0$ case.

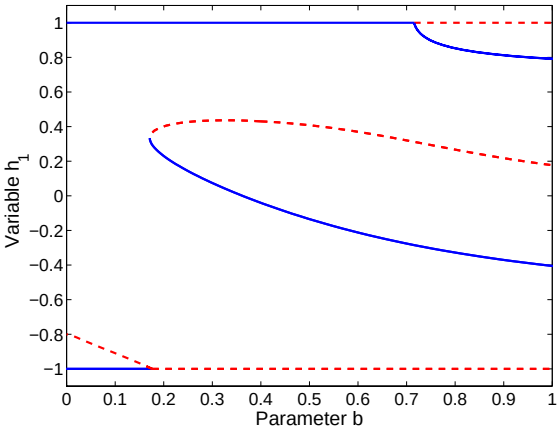

(a) h_1 *vs.* b

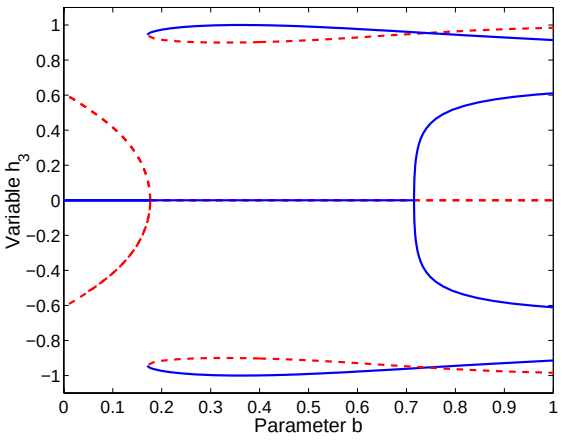

(b) h_3 *vs.* b

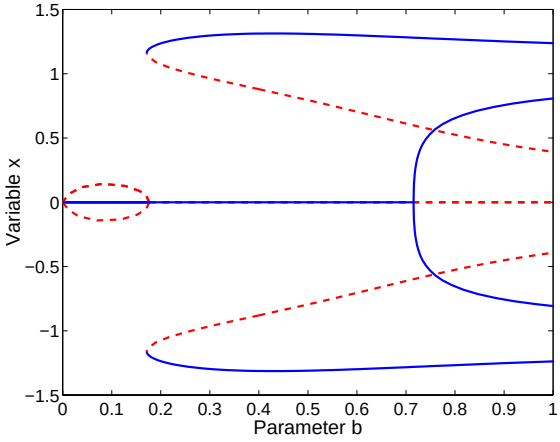

(c) x *vs.* b

Figure B.15: Damper position bifurcations for $\mathcal{B}+\mathcal{R}+\mathcal{P}$ with $h_a = 0.1$ and $k = 0.4$. This represents a large perturbation from the $h_a = 0$ case.

Appendix C

Bifurcation Diagrams For Global Equilibria: Effects of Spring Stiffness

This appendix includes bifurcation diagrams in the full state space, $\mathbf{z} = (h_1, h_2, h_3, p_n, x)$. Rotor momentum, h_a, is the bifurcation parameter for each diagram. Selected bifurcation diagrams are discussed in Sec. 5.4. This Appendix displays the equilibria on the momentum sphere and on five state-parameter bifurcation diagrams, providing a more complete description of the equilibria. All the bifurcation diagrams in this appendix use the system parameters defined in Table C.1.

Table C.1: System parameters for oblate gyrostat equilibria, varying spring stiffness

Inertia Properties	Damper Parameters
$I_1 = 0.40$	$\varepsilon = 0.10$
$I_2 = 0.28$	$c = 0.10$
$I_3 = 0.32$	$b = 0.33$
$I_s = 0.04$	

In this appendix, the spring stiffness, k, is different for each set of bifurcation diagrams. The values of k are selected to demonstrate the qualitative changes possible in the equilibria branch structures. We selected the following values: $k = 0.1, 0.2, 0.4,$ and 0.7.

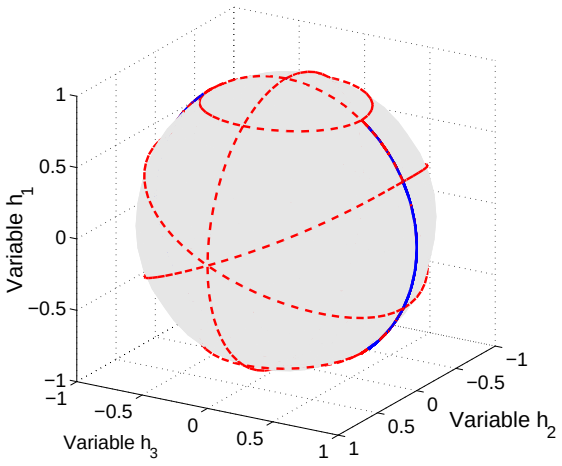

(a) Momentum sphere

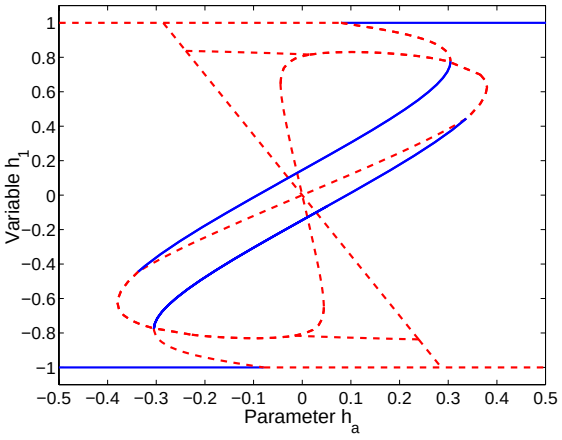

(b) h_1 *vs.* h_a

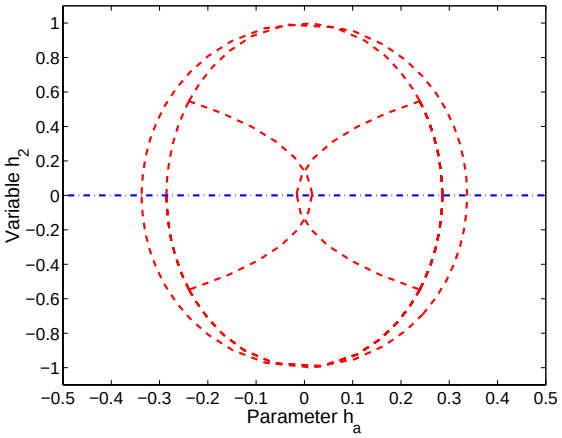

(c) h_2 *vs.* h_a

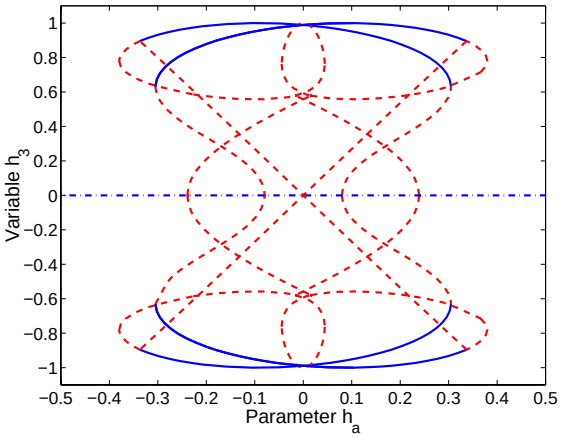

(d) h_3 *vs.* h_a

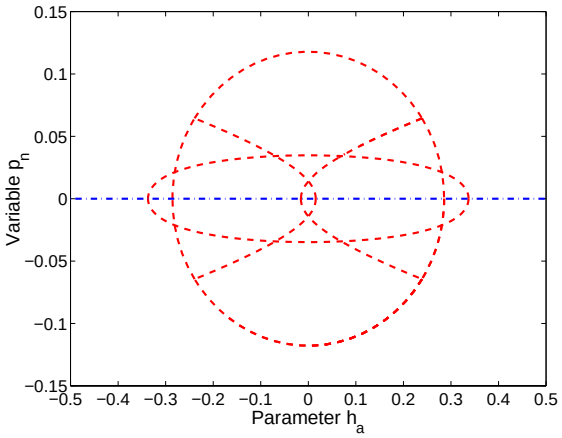

(e) p_n *vs.* h_a

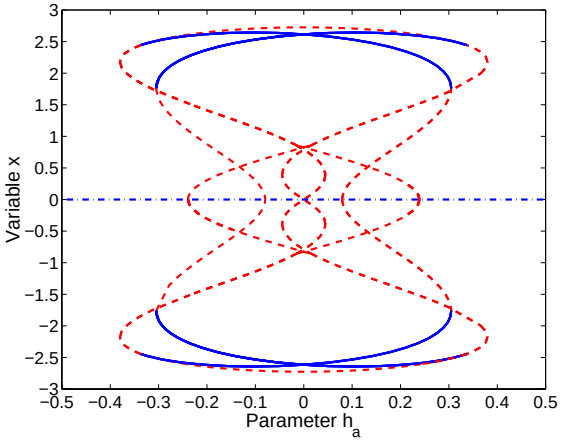

(f) x *vs.* h_a

Figure C.1: Rotor momentum bifurcation diagrams: $b = 0.33$ and $k = 0.1$

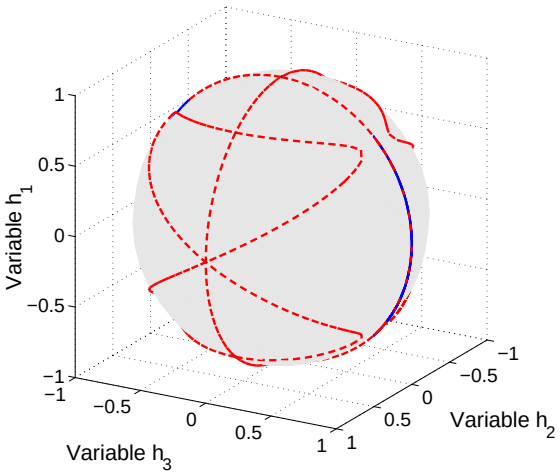

(a) Momentum sphere

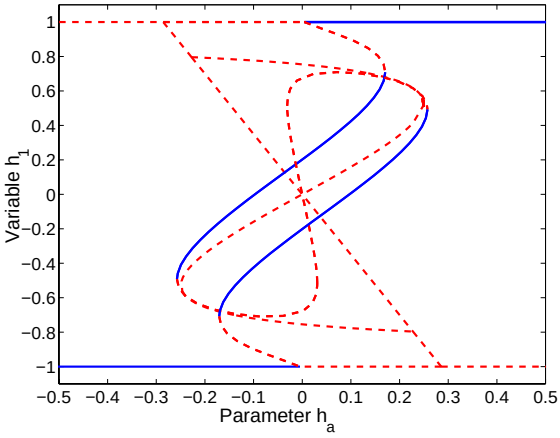

(b) h_1 *vs.* h_a

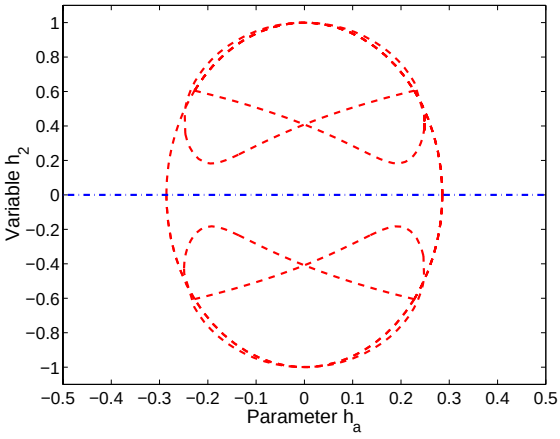

(c) h_2 *vs.* h_a

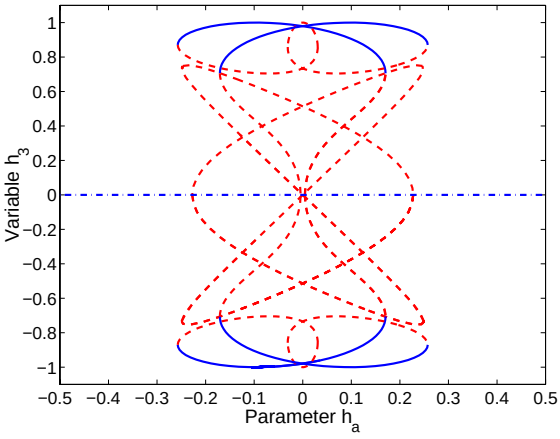

(d) h_3 *vs.* h_a

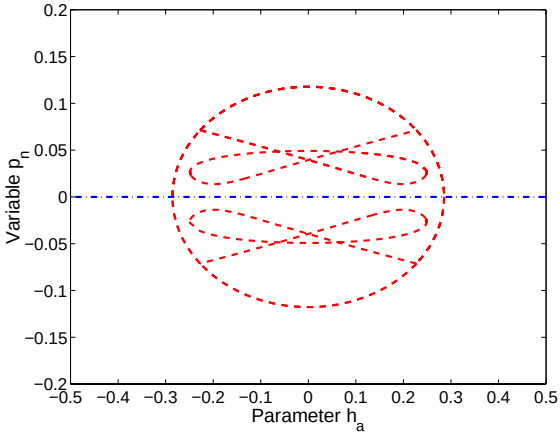

(e) p_n *vs.* h_a

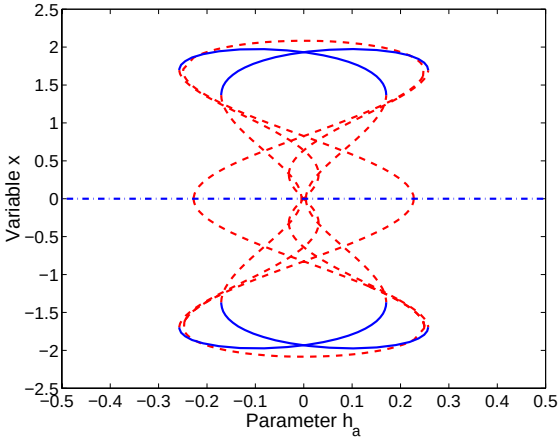

(f) x *vs.* h_a

Figure C.2: Rotor momentum bifurcation diagrams: $b = 0.33$ and $k = 0.2$

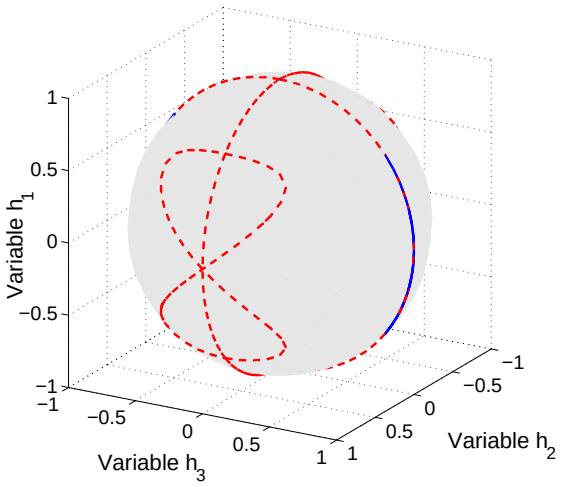

(a) Momentum sphere

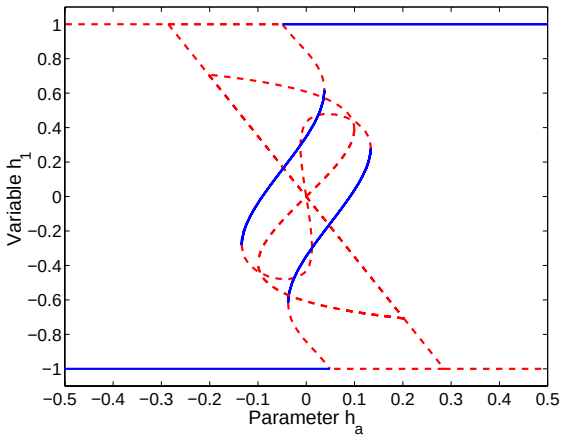

(b) h_1 *vs.* h_a

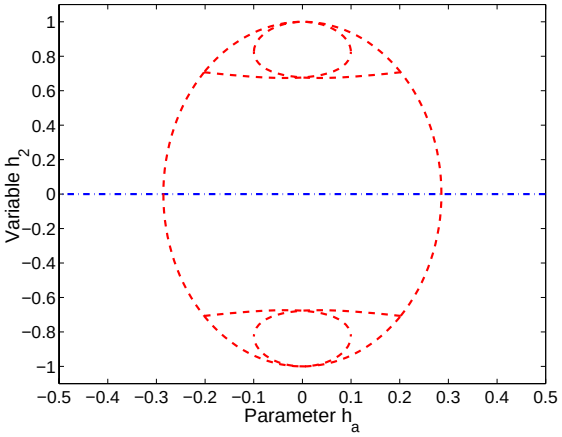

(c) h_2 *vs.* h_a

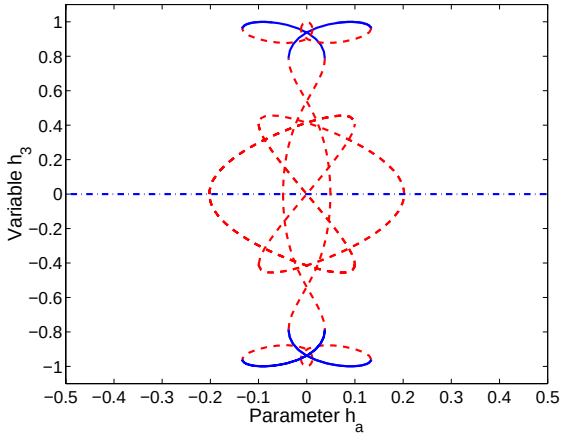

(d) h_3 *vs.* h_a

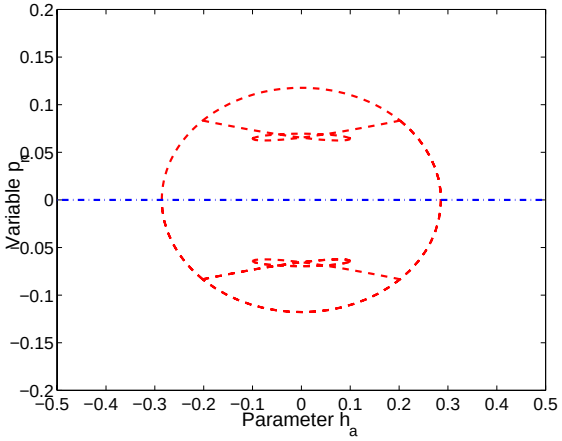

(e) p_n *vs.* h_a

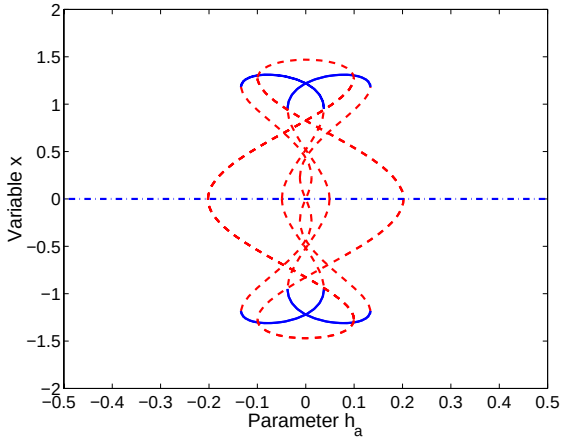

(f) x *vs.* h_a

Figure C.3: Rotor momentum bifurcation diagrams: $b = 0.33$ and $k = 0.4$

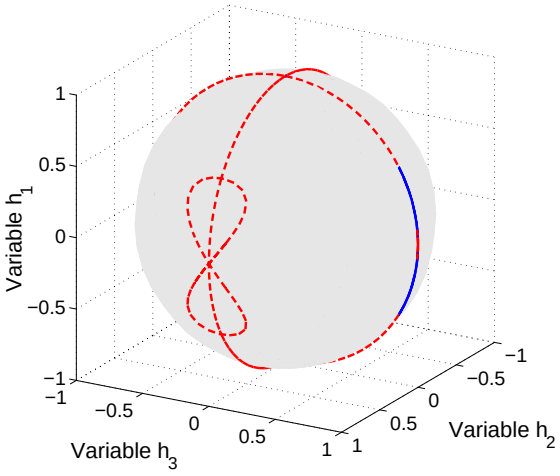

(a) Momentum sphere

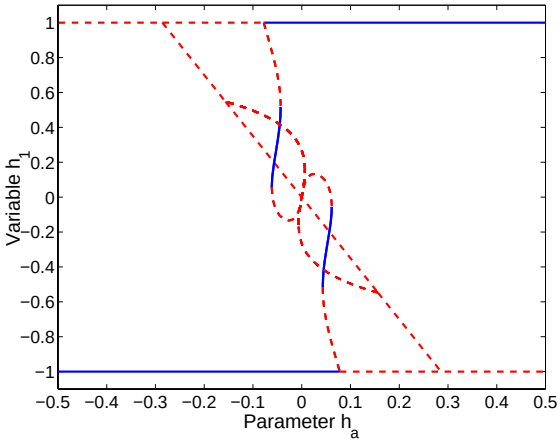

(b) h_1 *vs.* h_a

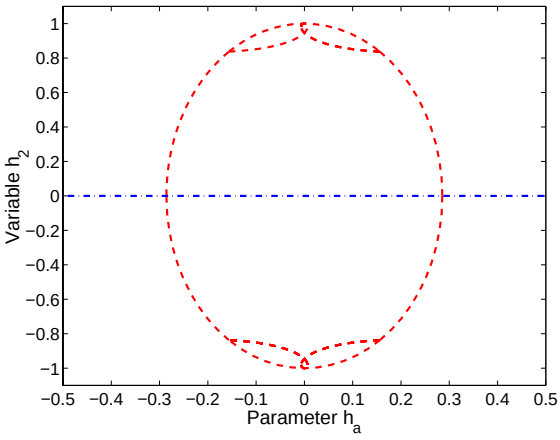

(c) h_2 *vs.* h_a

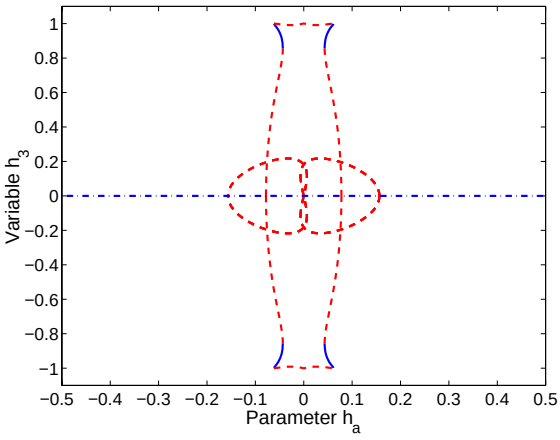

(d) h_3 *vs.* h_a

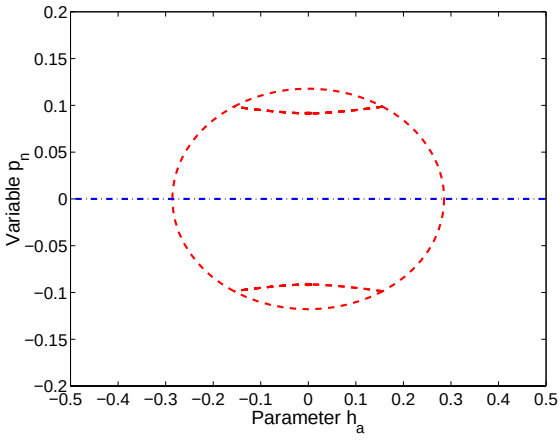

(e) p_n *vs.* h_a

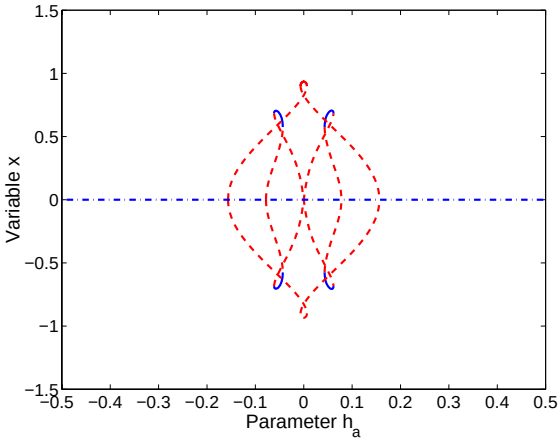

(f) x *vs.* h_a

Figure C.4: Rotor momentum bifurcation diagrams: $b = 0.33$ and $k = 0.7$

Appendix D

Bifurcation Diagrams For Global Equilibria: Effects of Damper Location

This appendix includes bifurcation diagrams in the full state space, $\mathbf{z} = (h_1, h_2, h_3, p_n, x)$. Rotor momentum, h_a, is the bifurcation parameter for each diagram. Selected bifurcation diagrams are discussed in Sec. 5.4. This Appendix displays the equilibria on the momentum sphere and on five state-parameter bifurcation diagrams, providing a more complete description of the equilibria. All the bifurcation diagrams in this appendix use the system parameters defined in Table D.1.

The equilibria are displayed on the momentum sphere and on five state-parameter bifurcation diagrams. All the bifurcation diagrams in this appendix use the following system parameters:

Table D.1: System parameters for oblate gyrostat equilibria, varying damper location

Inertia Properties	Damper Parameters
$I_1 = 0.40$	$\varepsilon = 0.10$
$I_2 = 0.28$	$c = 0.10$
$I_3 = 0.32$	$k = 0.40$
$I_s = 0.04$	

In this appendix, the damper location, b, is different for each set of bifurcation diagrams. The values of b are selected to demonstrate the qualitative changes possible in the equilibria branch structures. We selected the following values: $b = 0, 0.02, 0.2, 0.2,$ and 0.5. The first, $b = 0$, is a special organizing case. For the damper just slightly displaced from the body frame origin ($b = 0.02$), the $b = 0$ equilibria branches are perturbed into new branch structures. Qualitative changes continue for increasingly large b.

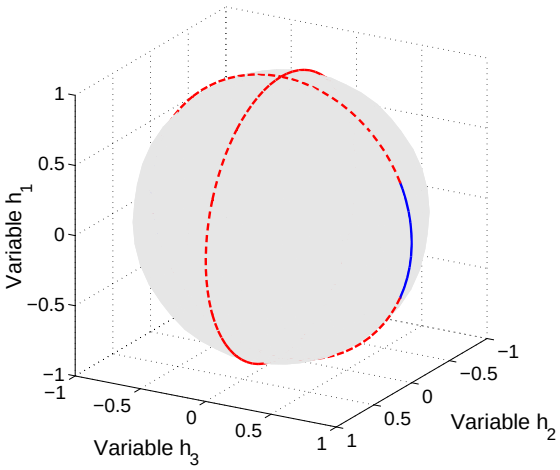

(a) Momentum sphere

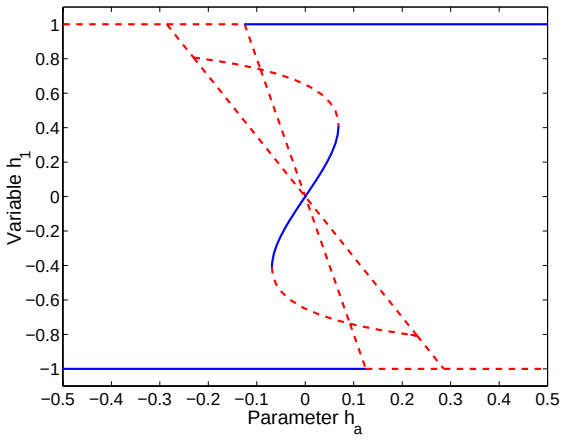

(b) h_1 *vs.* h_a

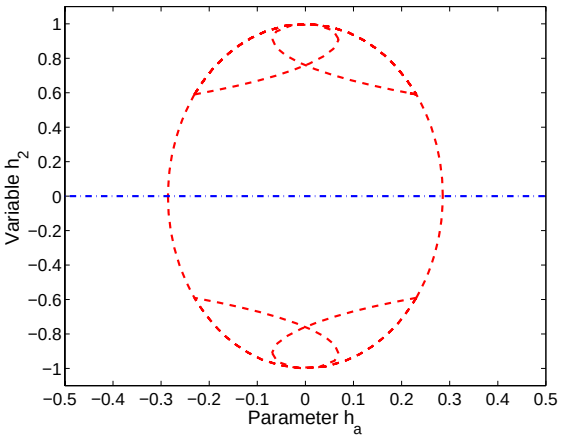

(c) h_2 *vs.* h_a

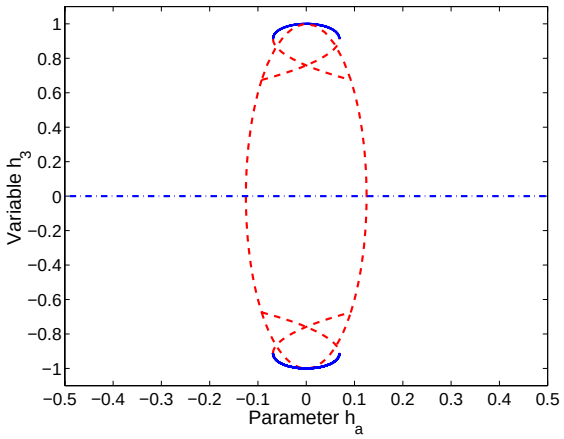

(d) h_3 *vs.* h_a

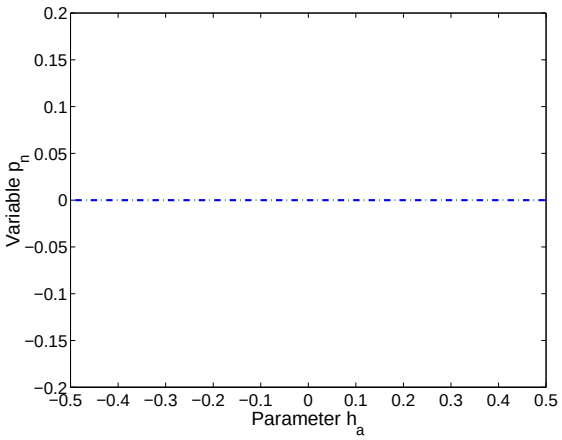

(e) p_n *vs.* h_a

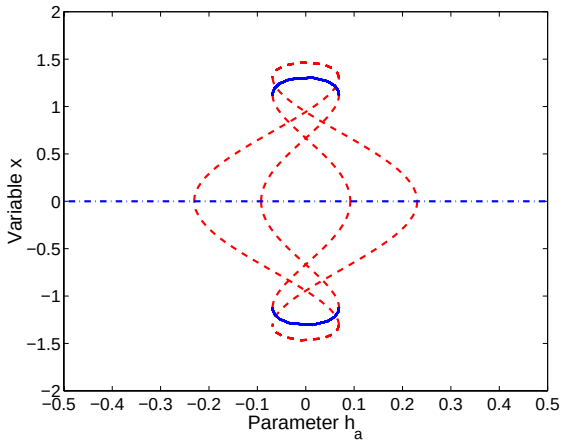

(f) x *vs.* h_a

Figure D.1: Rotor momentum bifurcation diagrams: $b = 0$ and $k = 0.4$

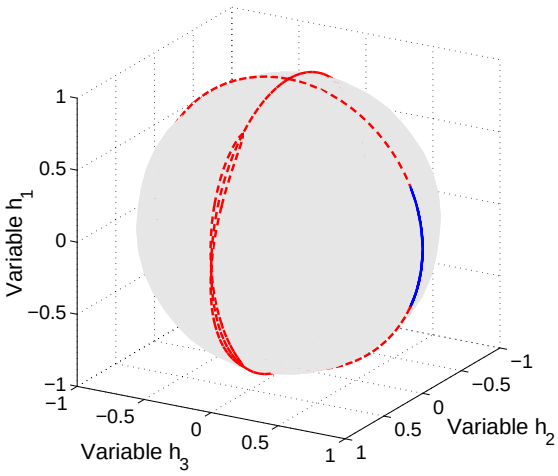

(a) Momentum sphere

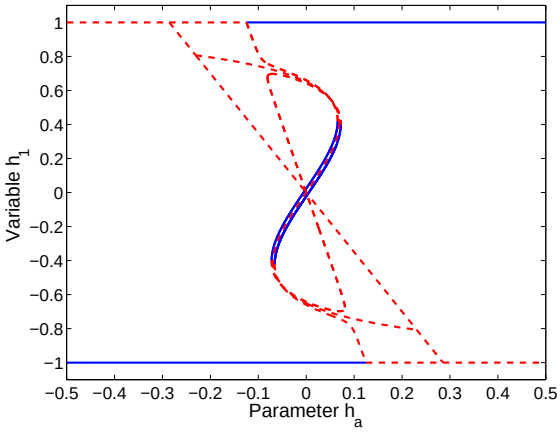

(b) h_1 *vs.* h_a

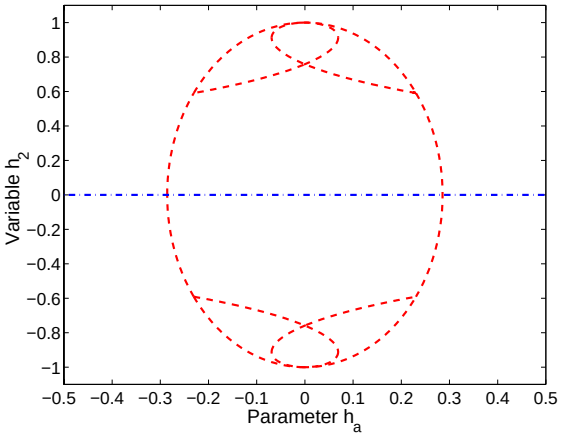

(c) h_2 *vs.* h_a

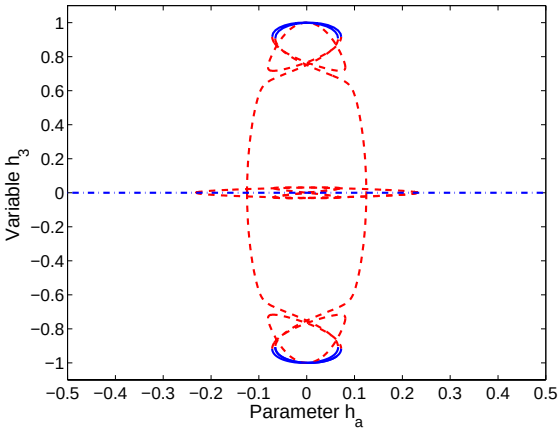

(d) h_3 *vs.* h_a

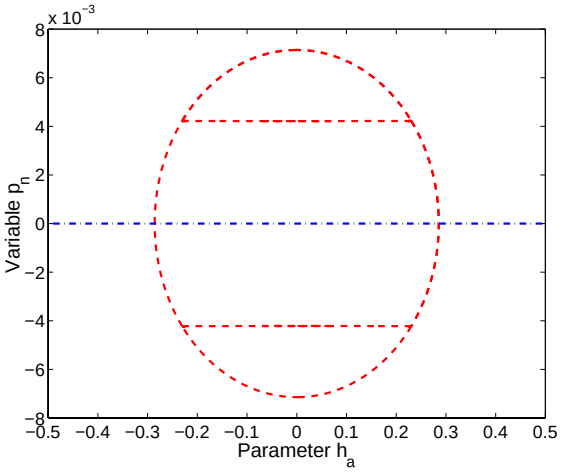

(e) p_n *vs.* h_a

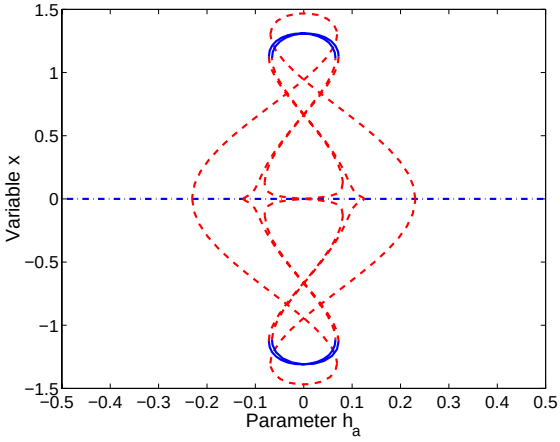

(f) x *vs.* h_a

Figure D.2: Rotor momentum bifurcation diagrams: $b = 0.02$ and $k = 0.4$

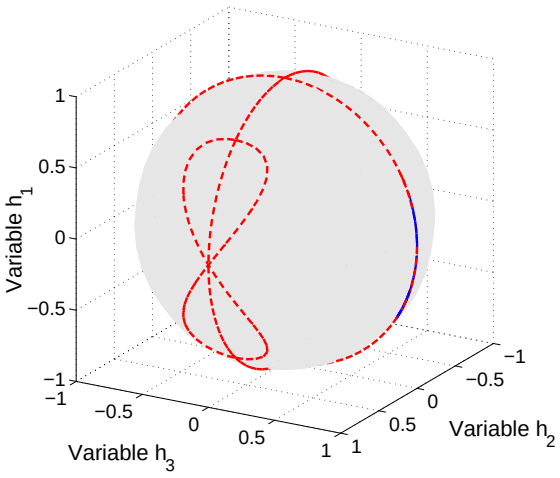

(a) Momentum sphere

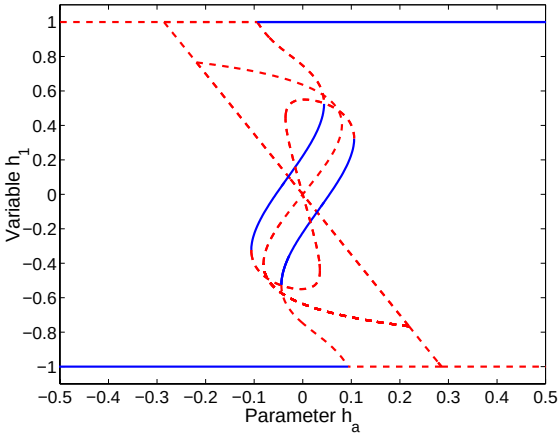

(b) h_1 *vs.* h_a

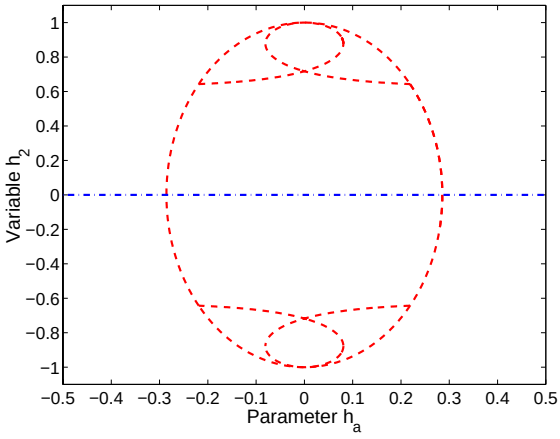

(c) h_2 *vs.* h_a

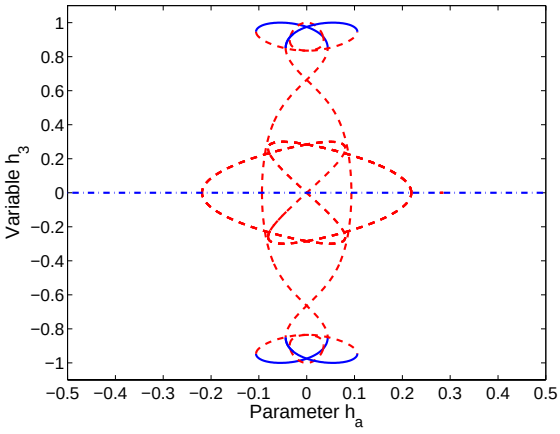

(d) h_3 *vs.* h_a

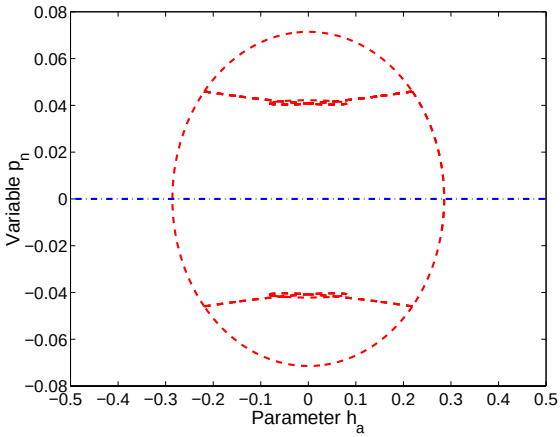

(e) p_n *vs.* h_a

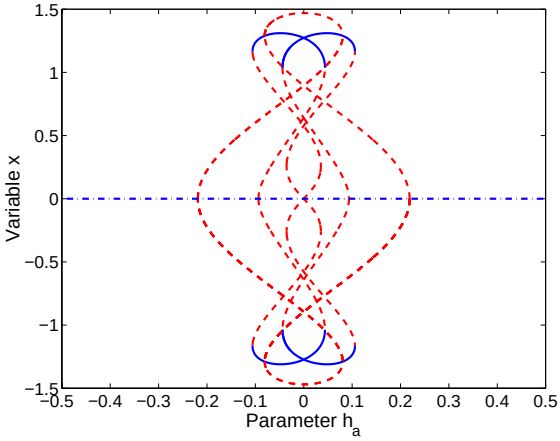

(f) x *vs.* h_a

Figure D.3: Rotor momentum bifurcation diagrams: $b = 0.2$ and $k = 0.4$

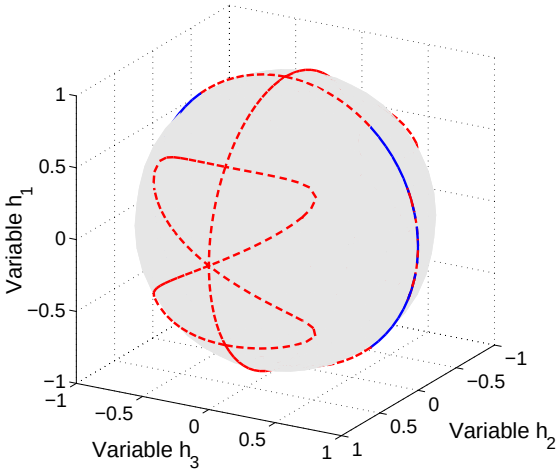

(a) Momentum sphere

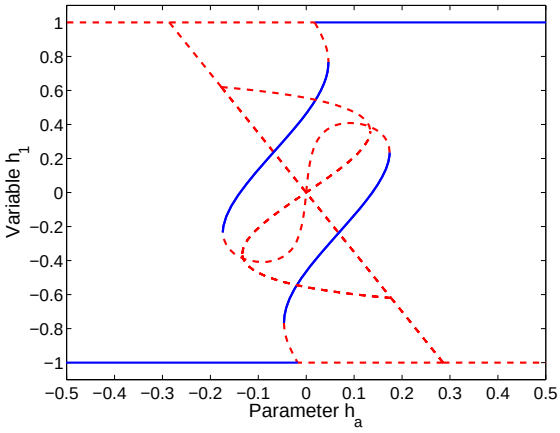

(b) h_1 *vs.* h_a

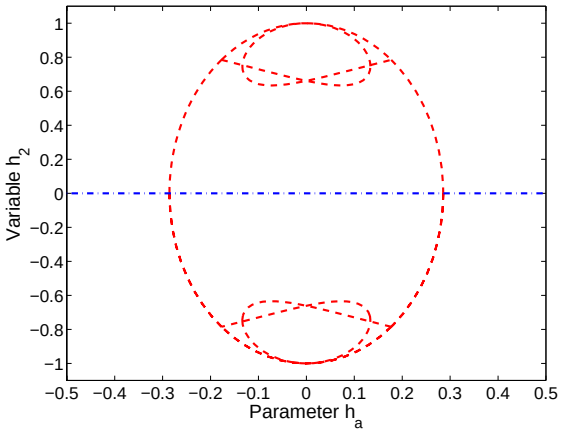

(c) h_2 *vs.* h_a

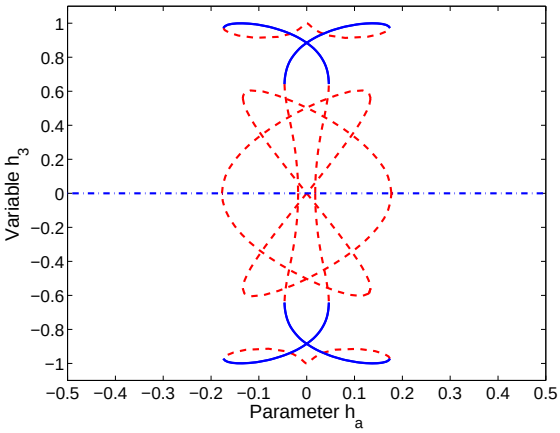

(d) h_3 *vs.* h_a

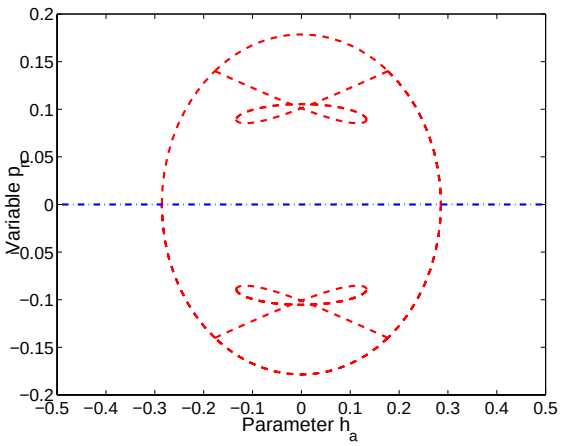

(e) p_n *vs.* h_a

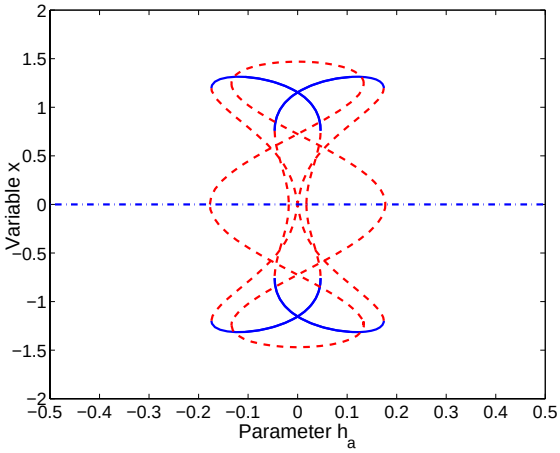

(f) x *vs.* h_a

Figure D.4: Rotor momentum bifurcation diagrams: $b = 0.5$ and $k = 0.4$

Appendix E

Bifurcation Diagrams For Global Equilibria: Different Inertia Properties

This appendix includes bifurcation diagrams in the full state space, $\mathbf{z} = (h_1, h_2, h_3, p_n, x)$. Rotor momentum, h_a, is the bifurcation parameter for each diagram. Selected bifurcation diagrams are discussed in Sec. 5.5. This Appendix displays the equilibria on the momentum sphere and on five state-parameter bifurcation diagrams, providing a more complete description of the equilibria.

Bifurcation diagram sets are included for different permutations of major, minor, and intermediate axes. Since the stability analysis in Ch. 4 shows that $I_1' = I_1 - I_s$ is the important inertia parameter for nominal spin stability, we use numerical examples where I_1 and also I_1' are the major, minor, or intermediate axis as specified.

E.1 Oblate Gyrostats: Major Nominal Spin-Axis

There are two possible types of oblate gyrostats, for either I_2 or I_3 as the least moment of inertia. Bifurcations for $I_1 > I_1' > I_3 > I_2$ are presented in Ch. 5 and are not repeated. For reference, see the bifurcations in Sec 5.2.3.

Bifurcations for $I_1 > I_1' > I_2 > I_3$ are produced using the system parameters defined in Table 5.6:

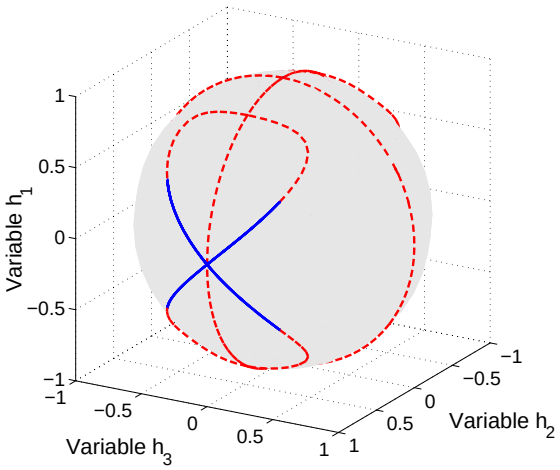

(a) Momentum sphere

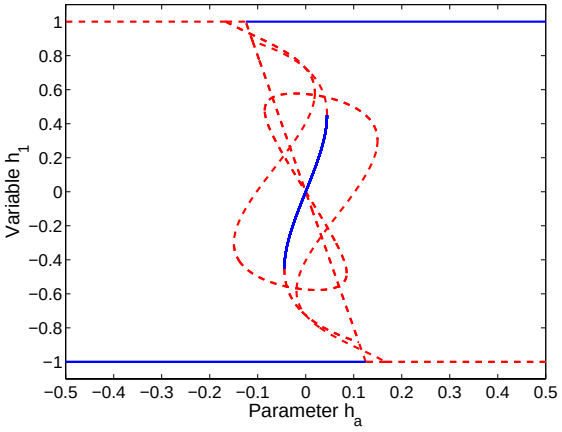

(b) h_1 *vs.* h_a

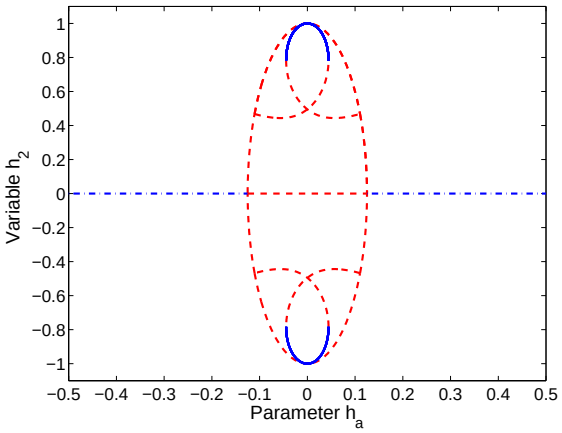

(c) h_2 *vs.* h_a

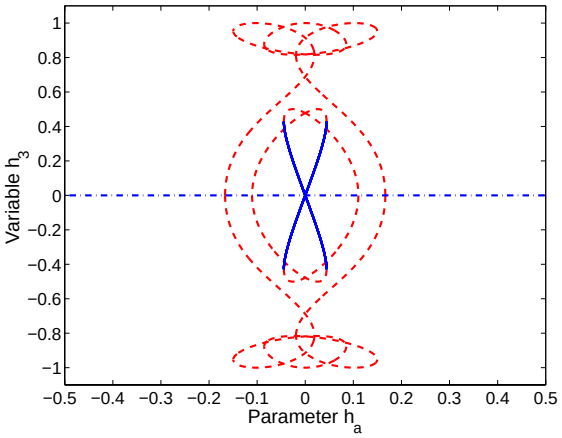

(d) h_3 *vs.* h_a

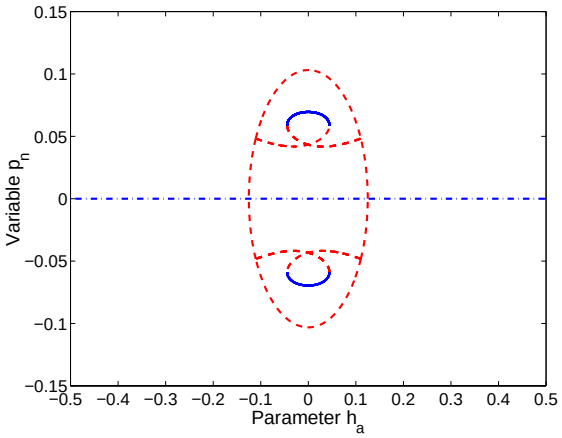

(e) p_n *vs.* h_a

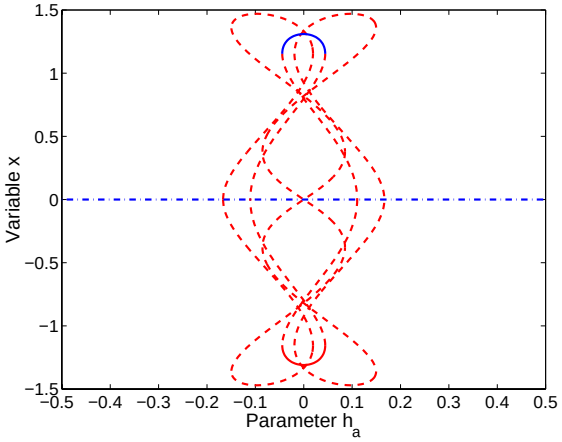

(f) x *vs.* h_a

Figure E.1: Rotor momentum bifurcation diagrams for oblate gyrostats: $I_1 > I_1' > I_2 > I_3$

E.2 Prolate Gyrostats: Minor Nominal Spin-Axis

A range of inertia properties is possible for minor-axis gyrostats. The Table E.1 illustrates the selected points of inertia properties used in this section. The remaining parameters are defined in Table 5.6.

Table E.1: Range of Inertia Properties for a Prolate Gyrostat

I_1	I_2	I_3
0.28	0.40	0.32
0.28	0.37	0.35
0.28	0.36	0.36
0.28	0.35	0.37
0.28	0.32	0.40

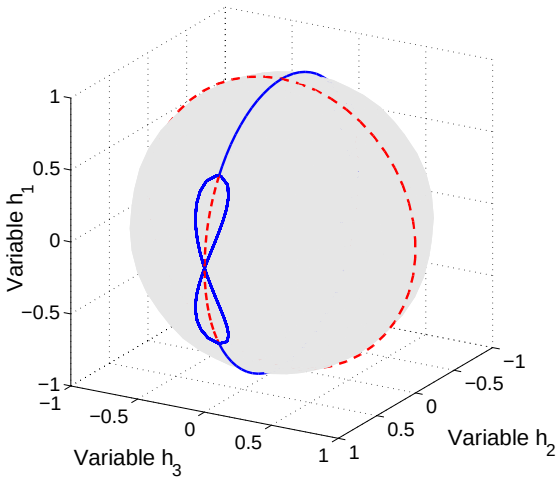

(a) Momentum sphere

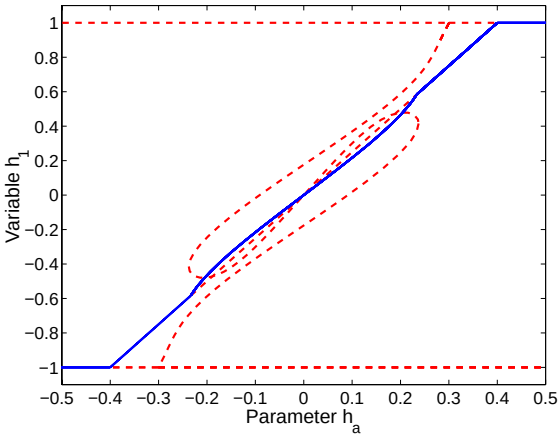

(b) h_1 *vs.* h_a

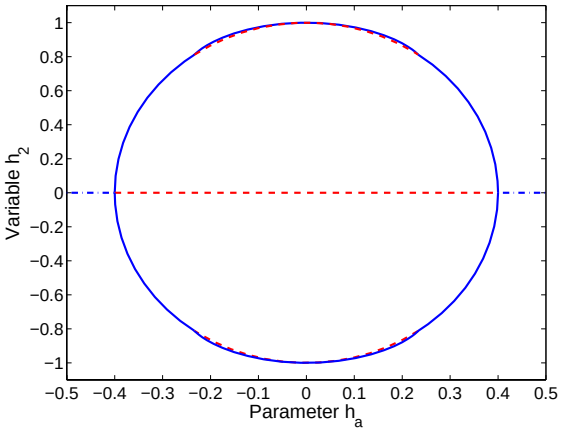

(c) h_2 *vs.* h_a

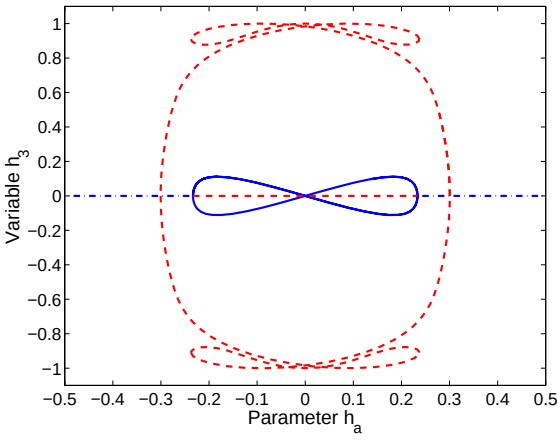

(d) h_3 *vs.* h_a

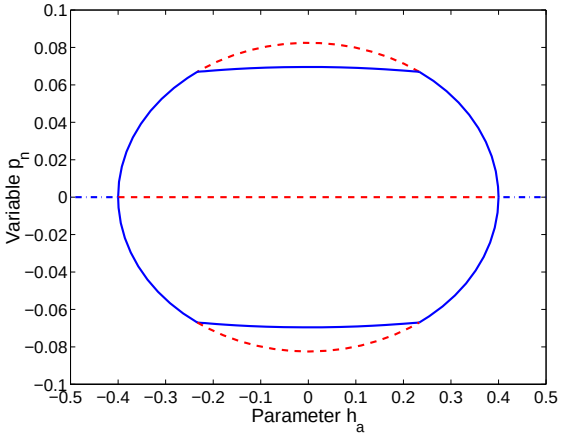

(e) p_n *vs.* h_a

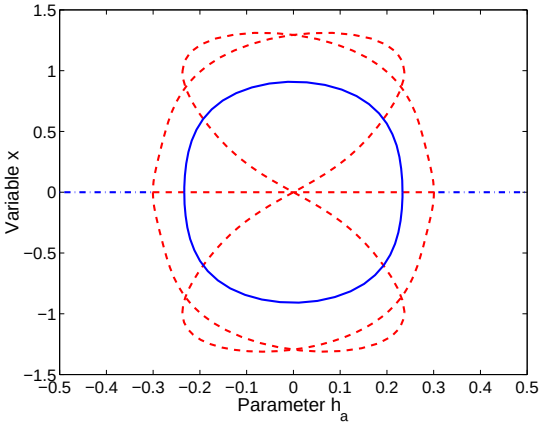

(f) x *vs.* h_a

Figure E.2: Rotor momentum bifurcation diagrams for prolate gyrostats: $I_1 = 0.28$, $I_2 = 0.4$, and $I_3 = 0.32$

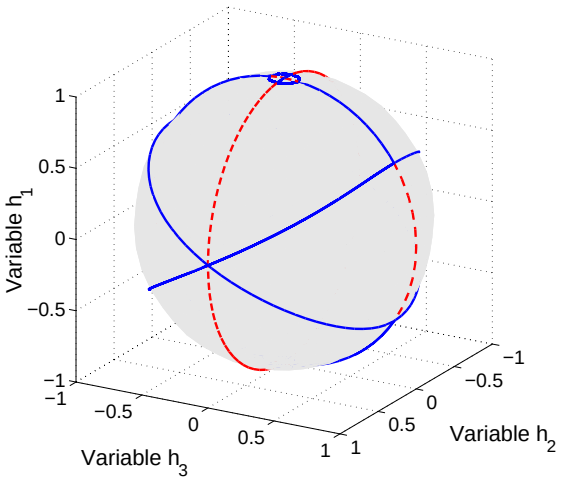

(a) Momentum sphere

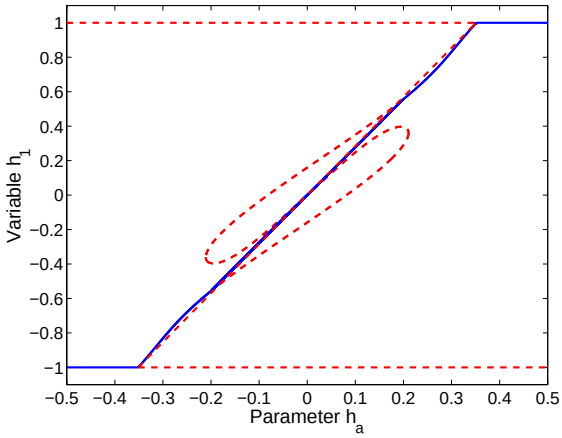

(b) h_1 *vs.* h_a

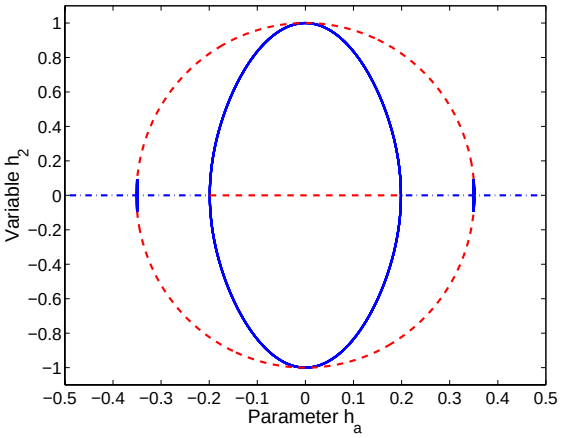

(c) h_2 *vs.* h_a

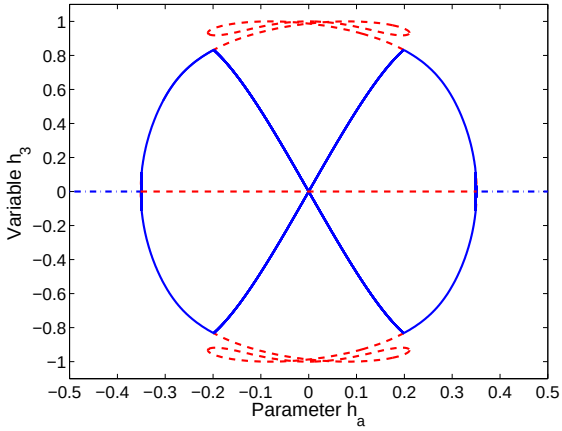

(d) h_3 *vs.* h_a

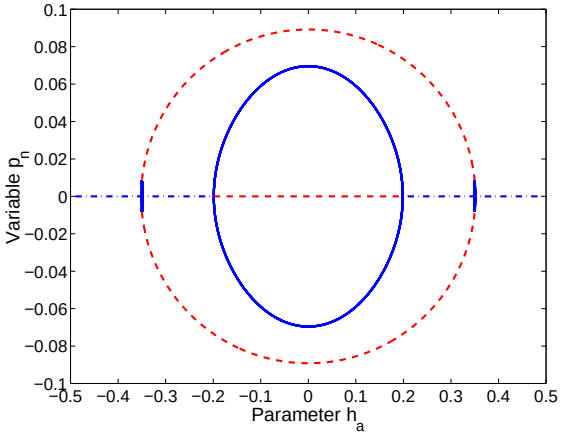

(e) p_n *vs.* h_a

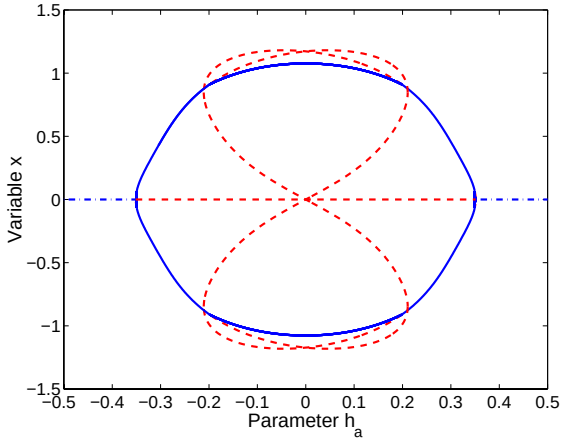

(f) x *vs.* h_a

Figure E.3: Rotor momentum bifurcation diagrams for prolate gyrostats: $I_1 = 0.28$, $I_2 = 0.37$, and $I_3 = 0.35$

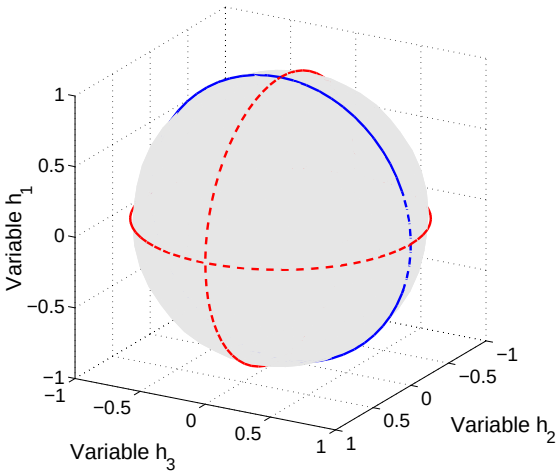

(a) Momentum sphere

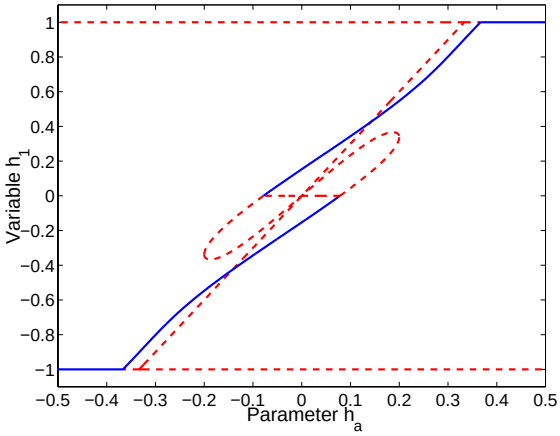

(b) h_1 *vs.* h_a

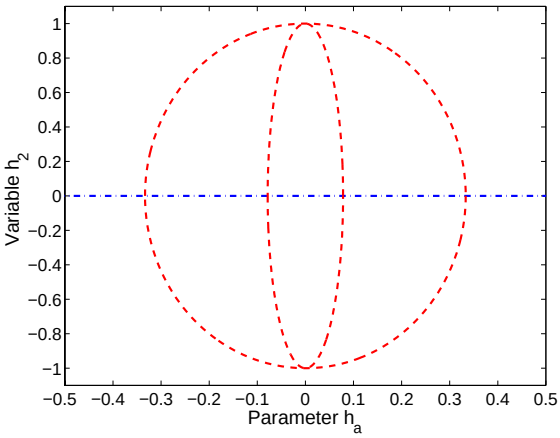

(c) h_2 *vs.* h_a

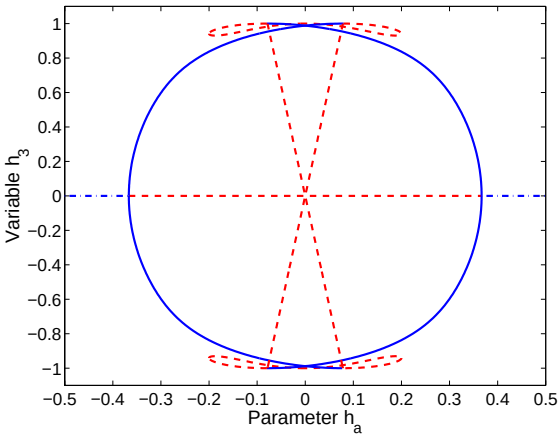

(d) h_3 *vs.* h_a

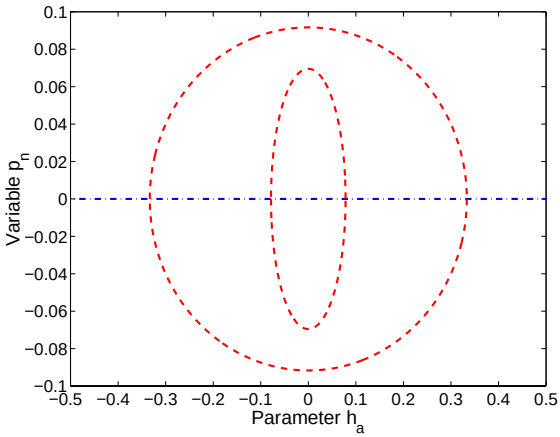

(e) p_n *vs.* h_a

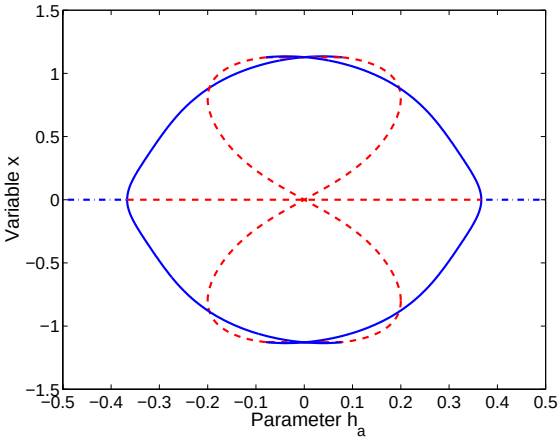

(f) x *vs.* h_a

Figure E.4: Rotor momentum bifurcation diagrams for prolate gyrostats: $I_1 = 0.28$, $I_2 = 0.36$, and $I_3 = 0.36$

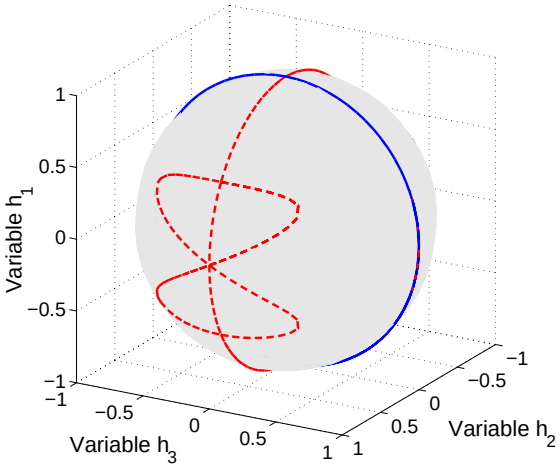

(a) Momentum sphere

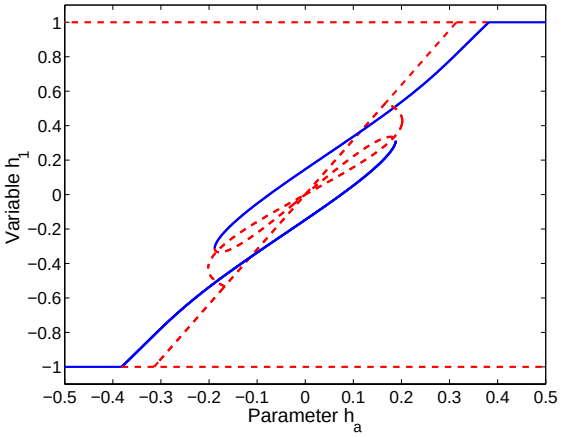

(b) h_1 *vs.* h_a

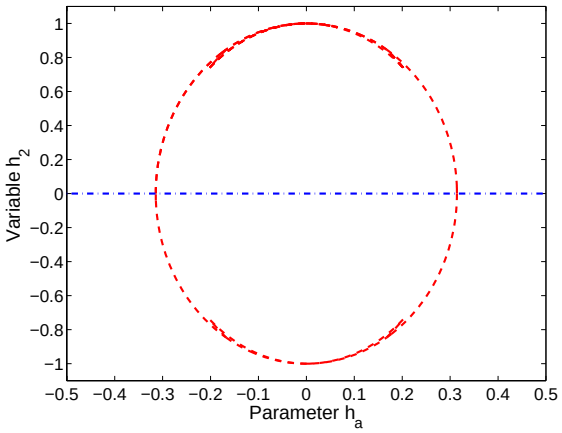

(c) h_2 *vs.* h_a

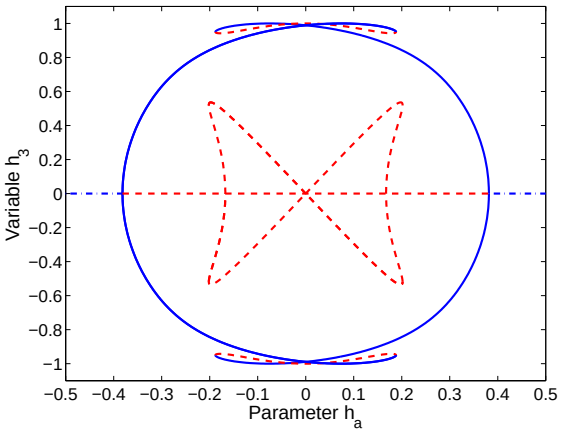

(d) h_3 *vs.* h_a

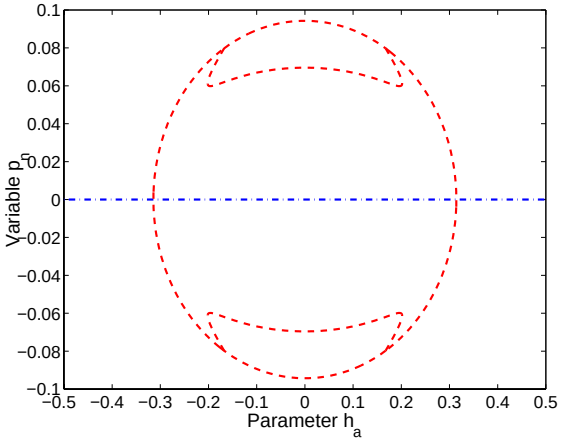

(e) p_n *vs.* h_a

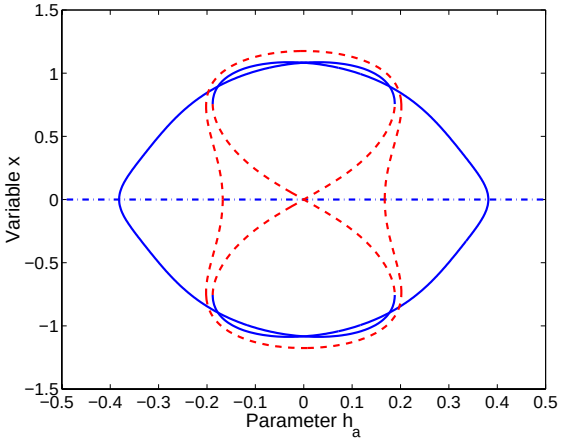

(f) x *vs.* h_a

Figure E.5: Rotor momentum bifurcation diagrams for prolate gyrostats: $I_1 = 0.28$, $I_2 = 0.35$, and $I_3 = 0.37$

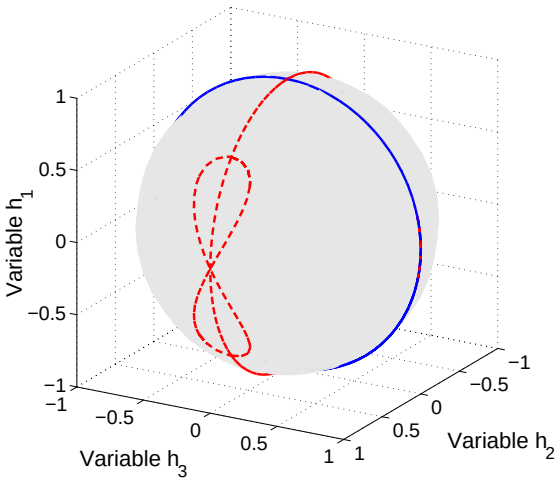

(a) Momentum sphere

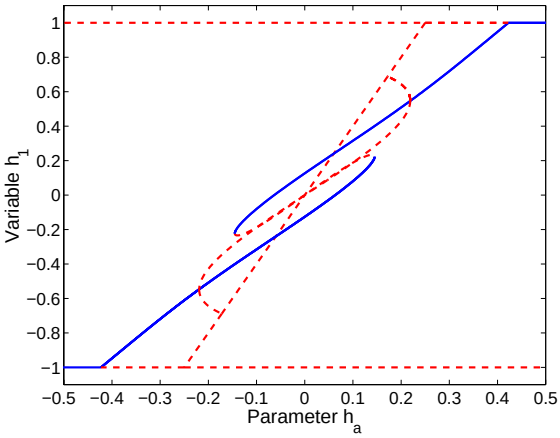

(b) h_1 *vs.* h_a

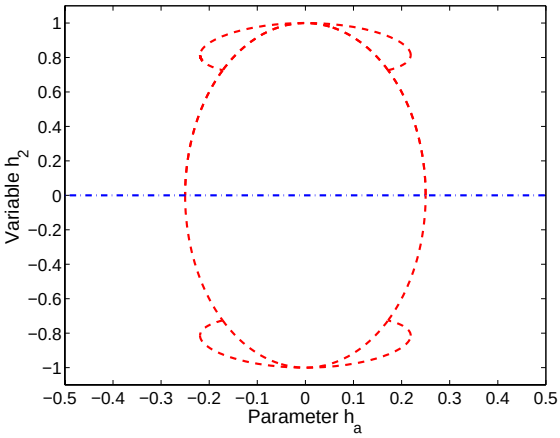

(c) h_2 *vs.* h_a

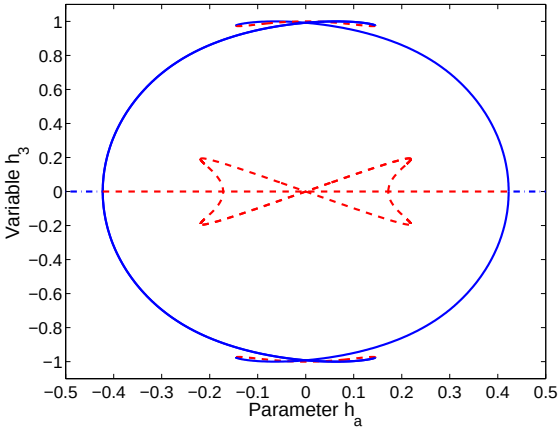

(d) h_3 *vs.* h_a

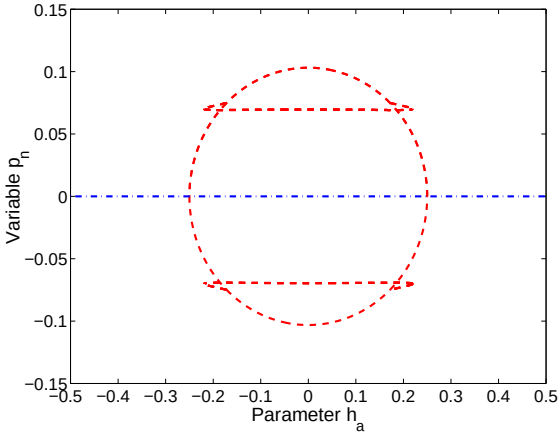

(e) p_n *vs.* h_a

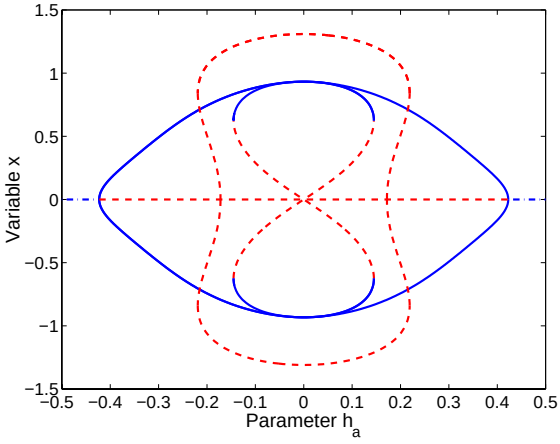

(f) x *vs.* h_a

Figure E.6: Rotor momentum bifurcation diagrams for prolate gyrostats: $I_1 = 0.28$, $I_2 = 0.32$, and $I_3 = 0.4$

E.3 Intermediate Nominal Spin-Axis

E.3.1 Bifurcations for the $I_3 > I_1 > I_1' > I_2$ case

The equilibria are displayed on the momentum sphere and on five state-parameter bifurcation diagrams, using the system parameters defined in Table 5.7

E.3.2 Bifurcations for the $I_2 > I_1 > I_1' > I_3$ case

The equilibria are displayed on the momentum sphere and on five state-parameter bifurcation diagrams, using the system parameters defined in Table 5.9.

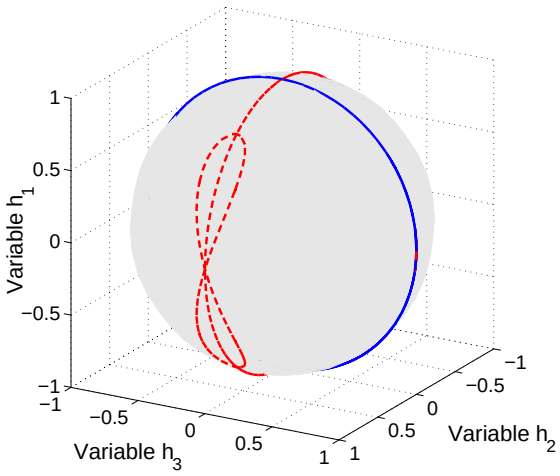

(a) Momentum sphere

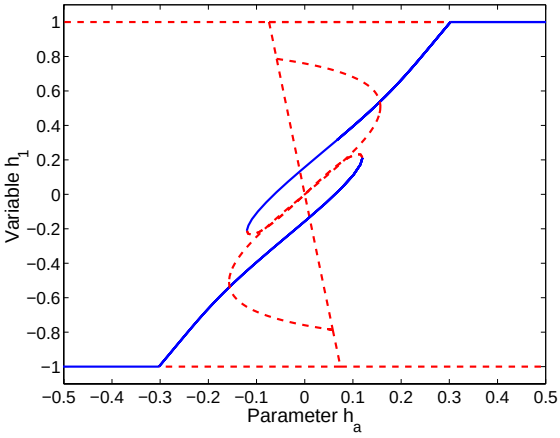

(b) h_1 *vs.* h_a

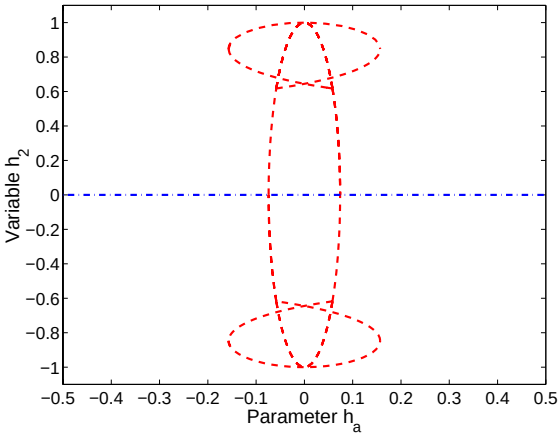

(c) h_2 *vs.* h_a

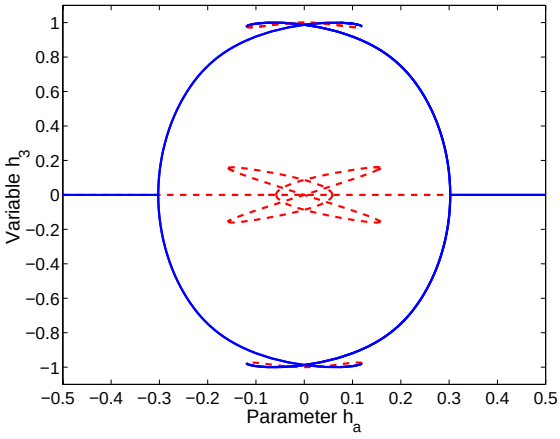

(d) h_3 *vs.* h_a

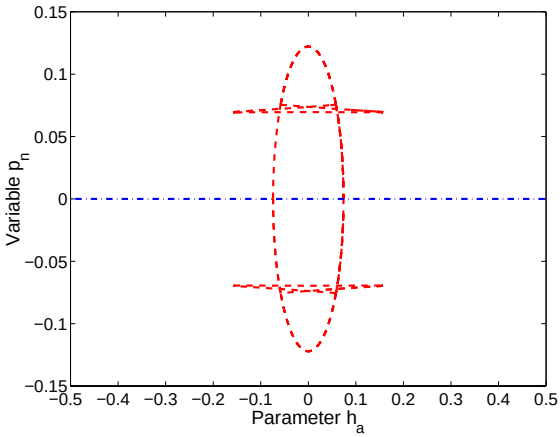

(e) p_n *vs.* h_a

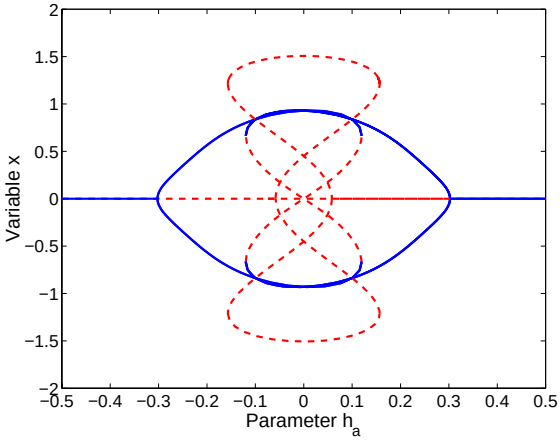

(f) x *vs.* h_a

Figure E.7: Rotor momentum bifurcation diagrams for intermediate-axis gyrostats: $I_3 > I_1 > I_1' > I_2$

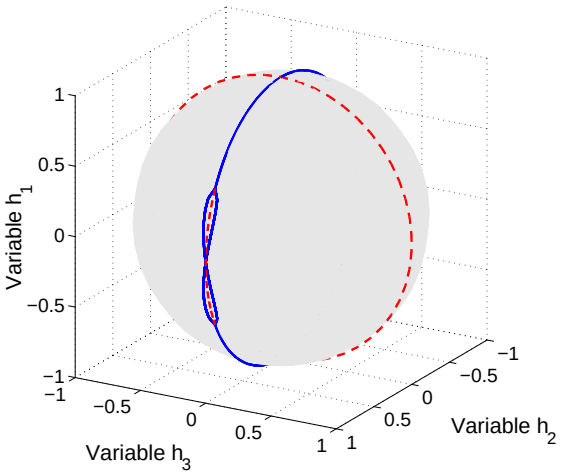

(a) Momentum sphere

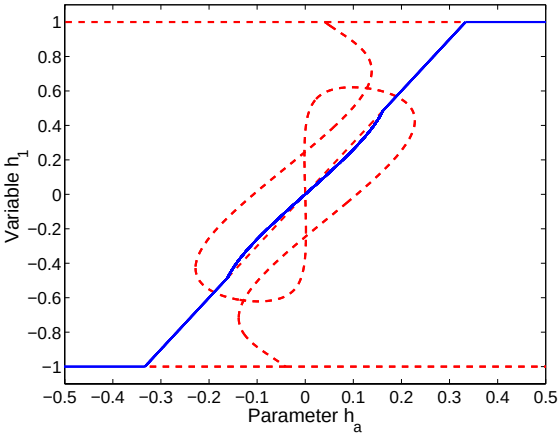

(b) h_1 *vs.* h_a

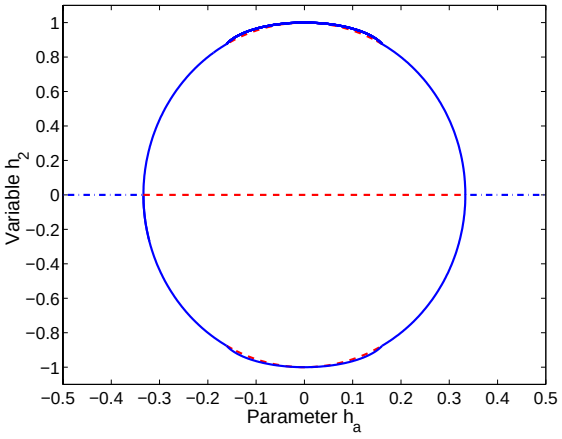

(c) h_2 *vs.* h_a

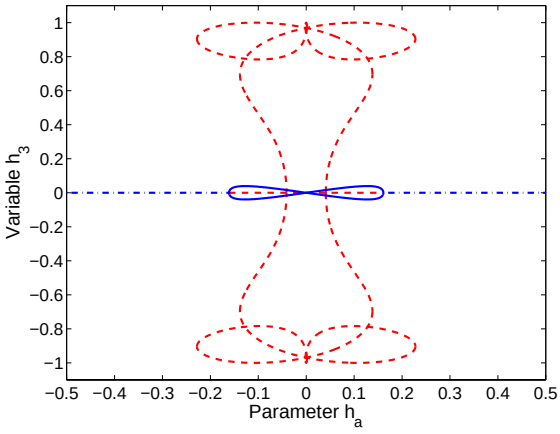

(d) h_3 *vs.* h_a

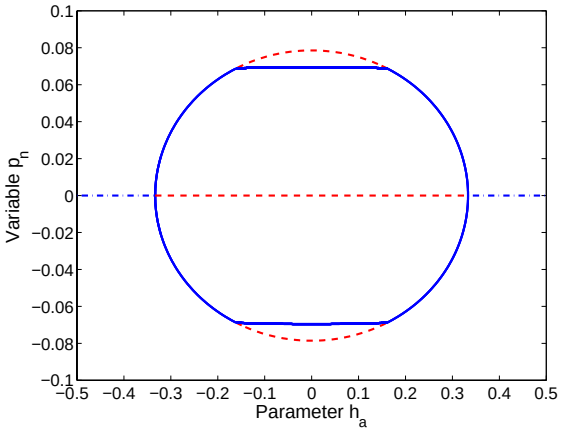

(e) p_n *vs.* h_a

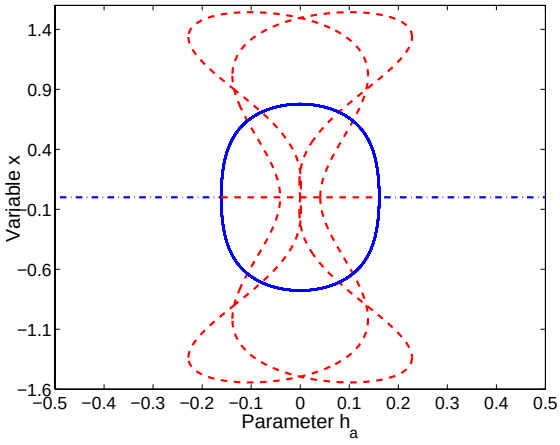

(f) x *vs.* h_a

Figure E.8: Rotor momentum bifurcation diagrams for intermediate-axis gyrostats: $I_2 > I_1 > I_1' > I_3$

Appendix F

Bifurcation Diagrams For Perturbed Model–Oblate Gyrostat

The standard model is perturbed by adding alignment errors to the model for the rotor alignment vector, $\hat{\mathbf{a}}$, and the damper alignment vector, $\hat{\mathbf{n}}$. Separate cases are presented for displacements of these vectors within the $\hat{\mathbf{b}}_1$–$\hat{\mathbf{b}}_3$ plane (in-plane) and perpendicular to the $\hat{\mathbf{b}}_1$–$\hat{\mathbf{b}}_3$ plane (out-of-plane). The in-plane errors are perturbed by 1° in the $+\hat{\mathbf{b}}_3$ direction. The out-of-plane errors are perturbed by 2° in the $+\hat{\mathbf{b}}_2$ direction. The larger displacement is necessary to clearly show the effects of the out-of-plane errors. We apply numerical continuation and produce branches of equilibria for varying rotor momentum. Selected bifurcation diagrams are discussed in Sec. 7.2. This Appendix displays the equilibria on the momentum sphere and on five state-parameter bifurcation diagrams, providing a more complete description of the equilibria. The bifurcation diagrams use the system parameters defined in Table 7.2.

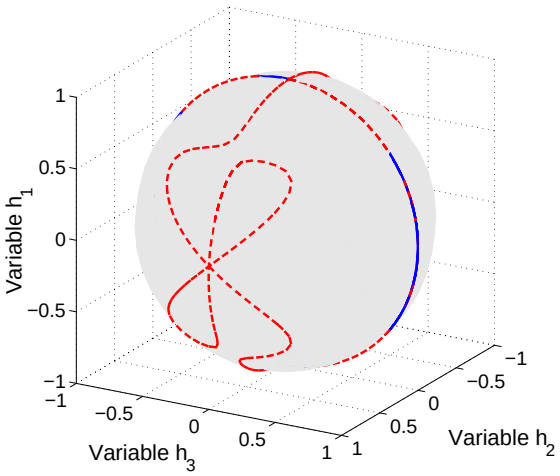

(a) Momentum sphere

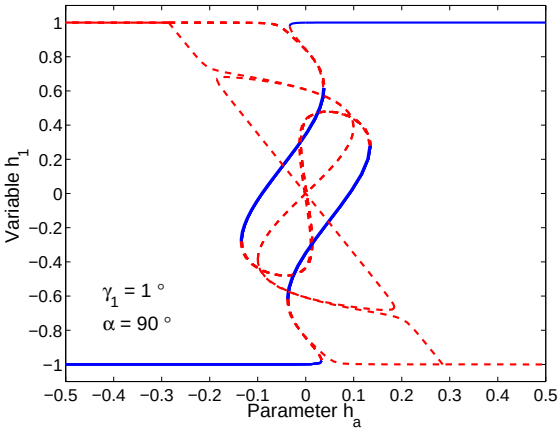

(b) h_1 *vs.* h_a

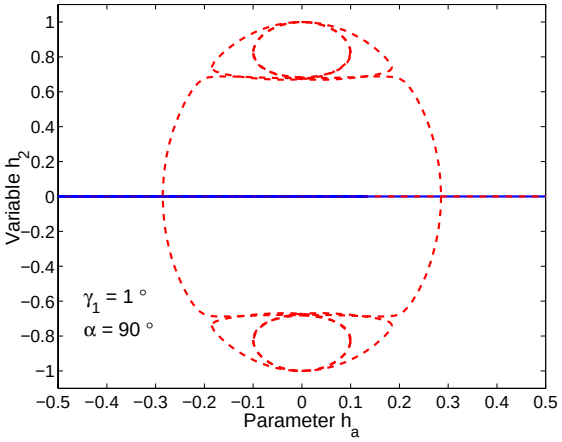

(c) h_2 *vs.* h_a

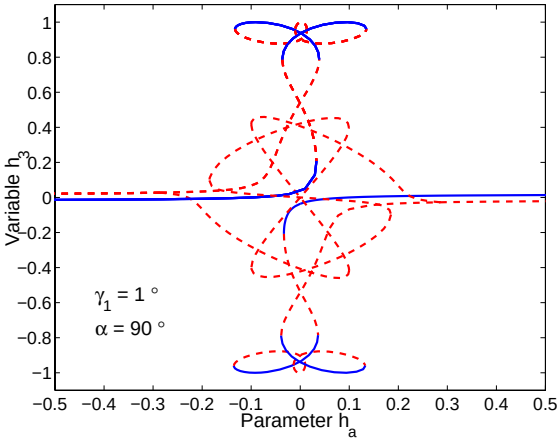

(d) h_3 *vs.* h_a

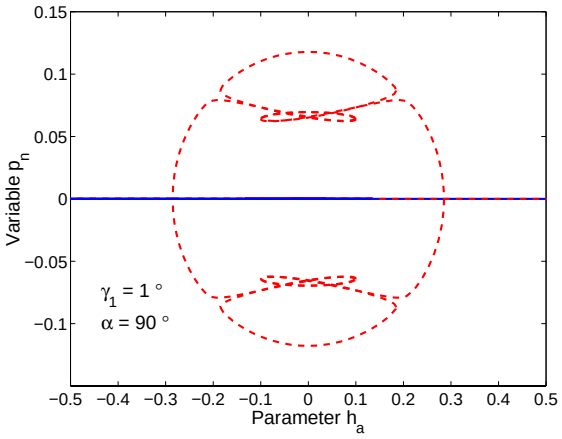

(e) p_n *vs.* h_a

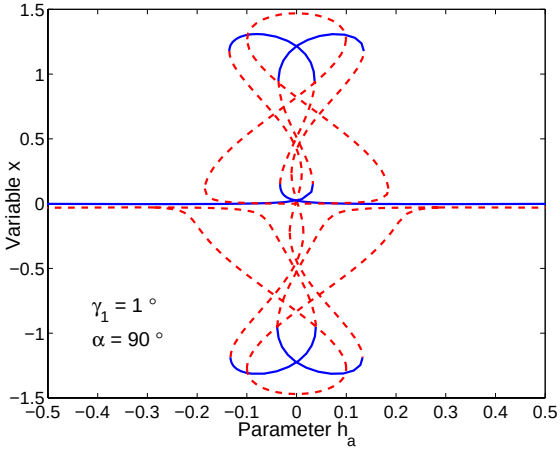

(f) x *vs.* h_a

Figure F.1: Rotor momentum bifurcation diagrams for oblate gyrostat with 1° in-plane rotor misalignment

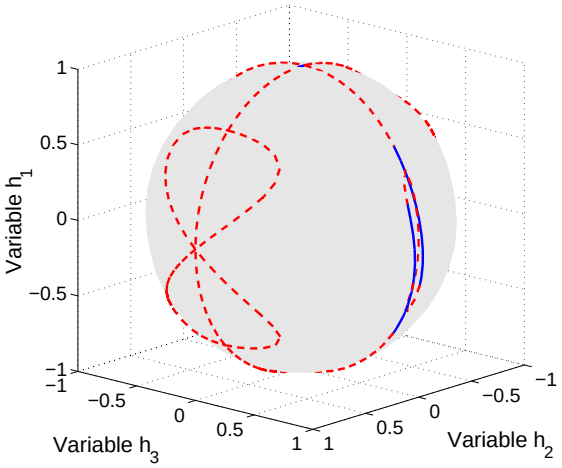

(a) Momentum sphere

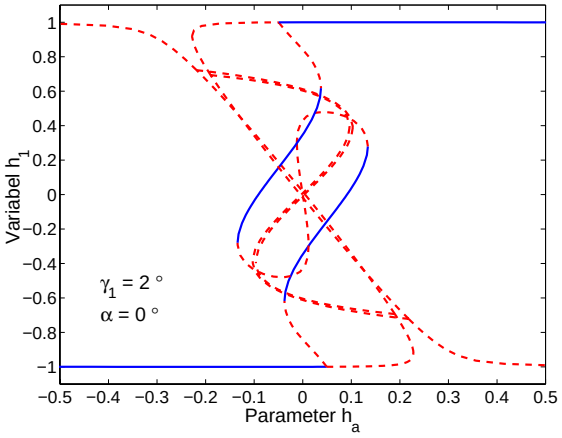

(b) h_1 *vs.* h_a

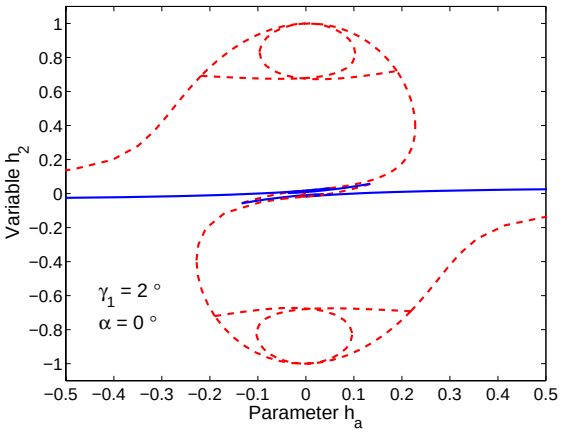

(c) h_2 *vs.* h_a

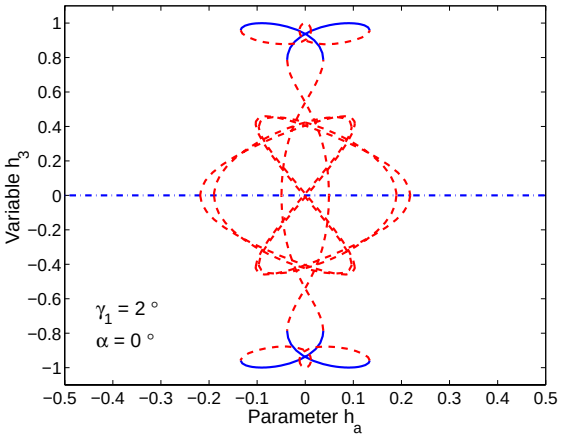

(d) h_3 *vs.* h_a

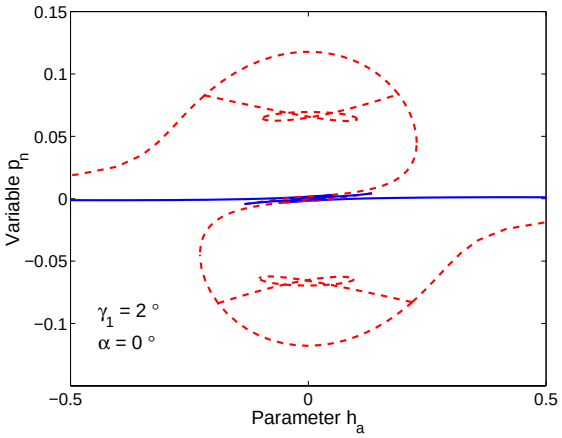

(e) p_n *vs.* h_a

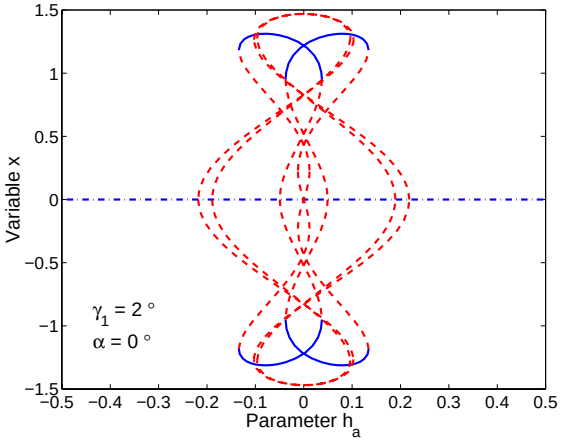

(f) x *vs.* h_a

Figure F.2: Rotor momentum bifurcation diagrams for oblate gyrostat with $2\,^\circ$ out-of-plane rotor misalignment

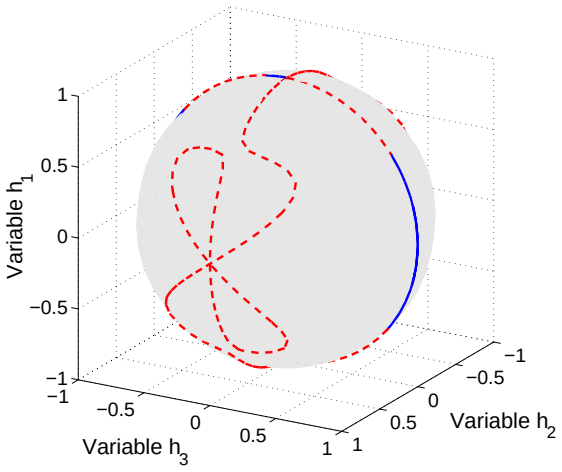

(a) Momentum sphere

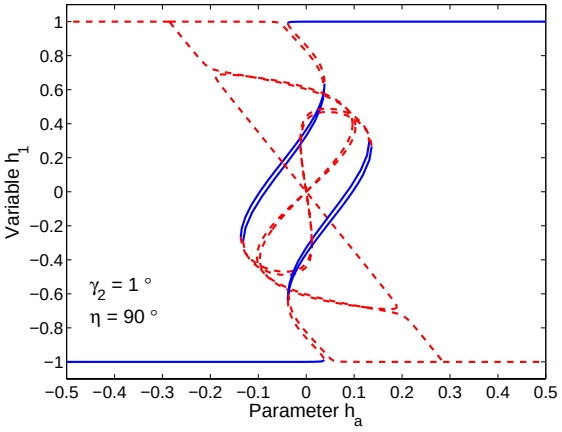

(b) h_1 *vs.* h_a

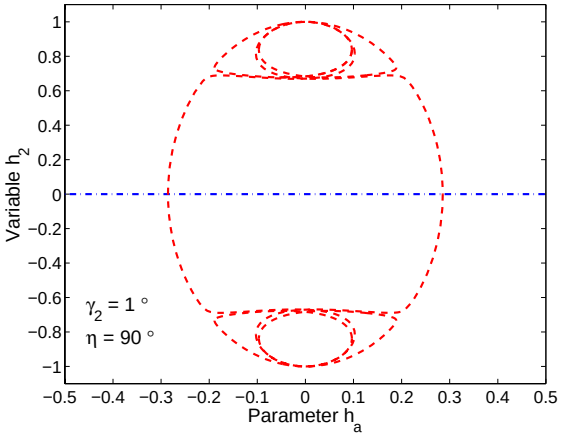

(c) h_2 *vs.* h_a

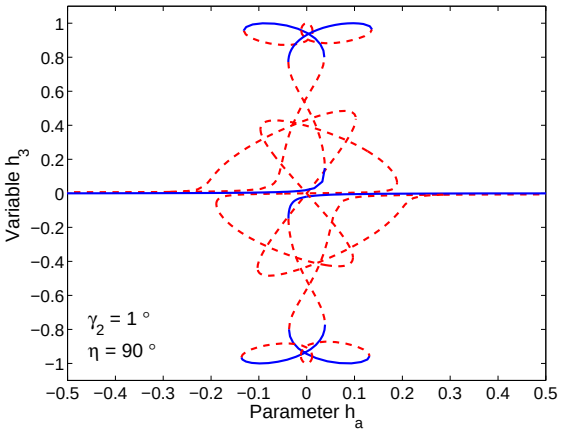

(d) h_3 *vs.* h_a

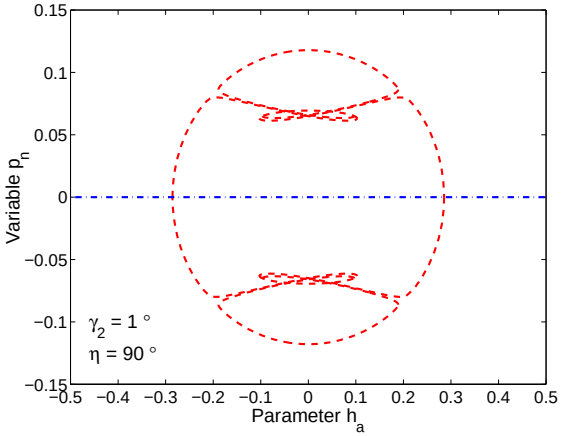

(e) p_n *vs.* h_a

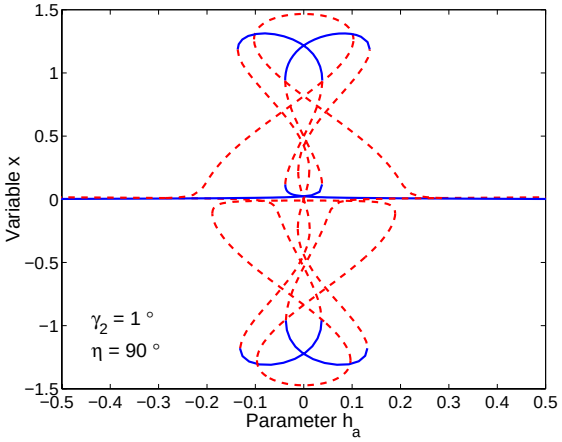

(f) x *vs.* h_a

Figure F.3: Rotor momentum bifurcation diagrams for oblate gyrostat with 1° in-plane damper misalignment

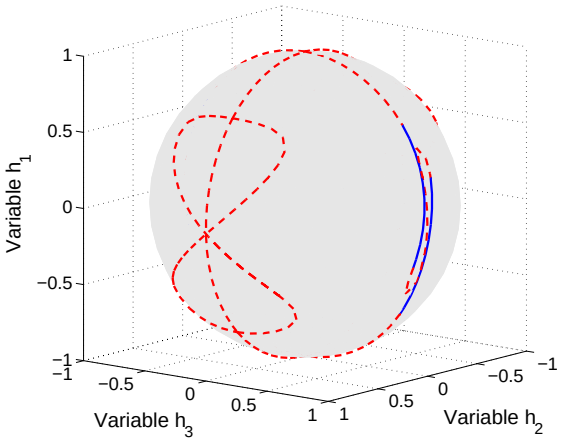

(a) Momentum sphere

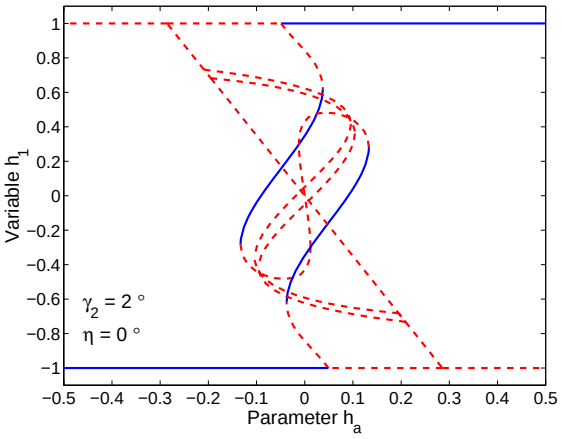

(b) h_1 *vs.* h_a

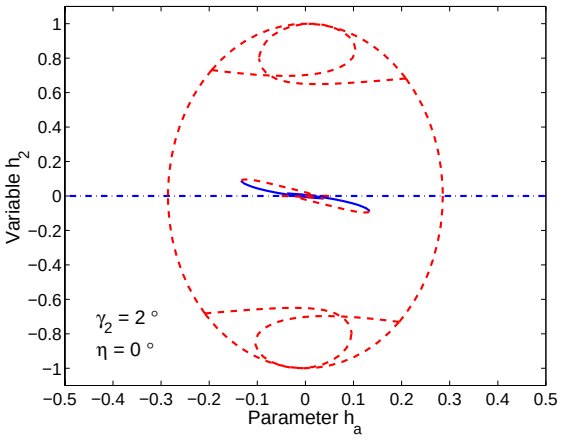

(c) h_2 *vs.* h_a

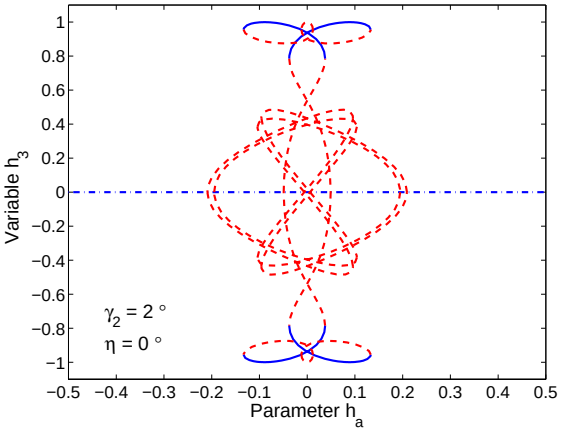

(d) h_3 *vs.* h_a

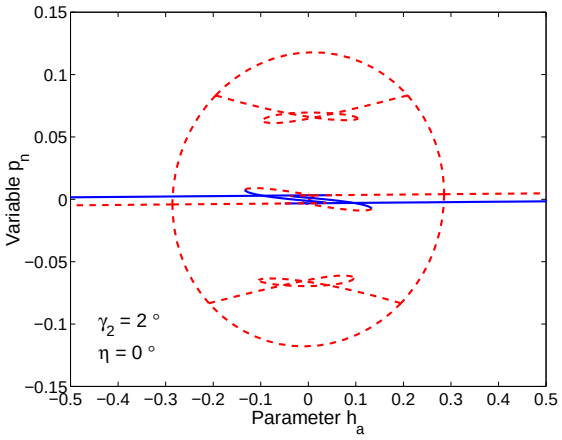

(e) p_n *vs.* h_a

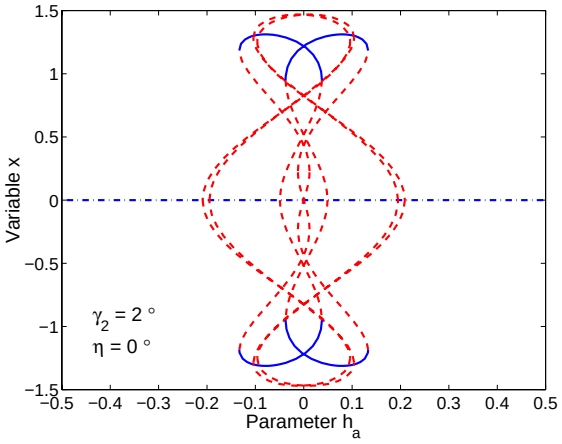

(f) x *vs.* h_a

Figure F.4: Rotor momentum bifurcation diagrams for oblate gyrostat with $2\,^\circ$ out-of-plane damper misalignment

Appendix G

Bifurcation Diagrams For Perturbed Model–Prolate Gyrostat

The standard model is perturbed by adding alignment errors to the model for the rotor alignment vector, $\hat{\mathbf{a}}$, and the damper alignment vector, $\hat{\mathbf{n}}$. Separate cases are presented for displacements of these vectors within the $\hat{\mathbf{b}}_1$–$\hat{\mathbf{b}}_3$ plane (in-plane) and perpendicular to the $\hat{\mathbf{b}}_1$–$\hat{\mathbf{b}}_3$ plane (out-of-plane). The in-plane errors are perturbed by 1° in the $+\hat{\mathbf{b}}_3$ direction. The out-of-plane errors are pertubed by 2° in the $+\hat{\mathbf{b}}_2$ direction. The larger displacement is necessary to clearly show the effects of the out-of-plane errors. We apply numerical continuation and produce branches of equilibria for varying rotor momentum. Selected bifurcation diagrams are discussed in Sec. 7.3. This Appendix displays the equilibria on the momentum sphere and on five state-parameter bifurcation diagrams, providing a more complete description of the equilibria. The bifurcation diagrams use the system parameters from Table 7.3.

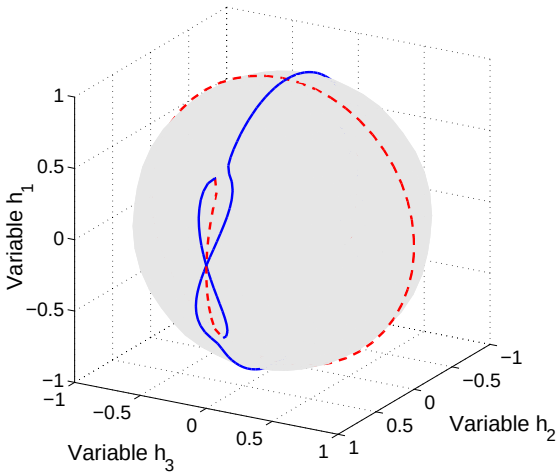

(a) Momentum sphere

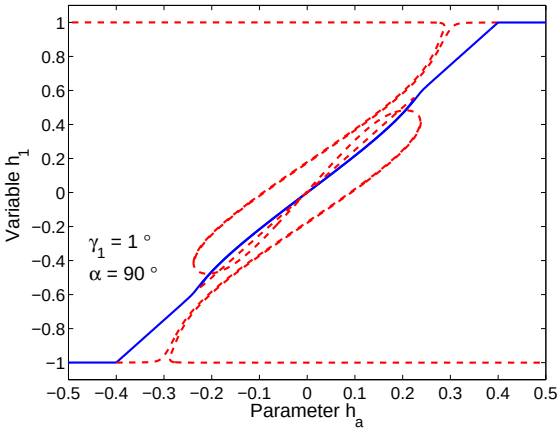

(b) h_1 *vs.* h_a

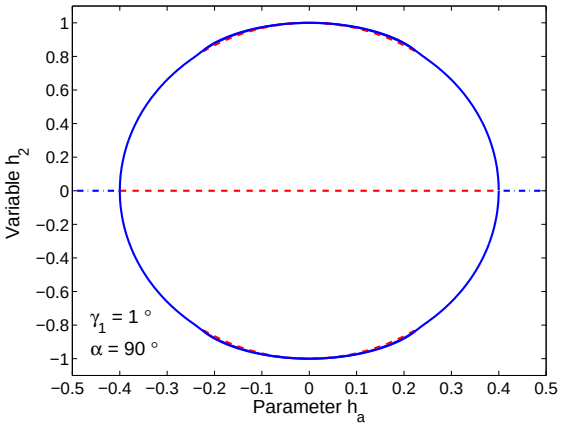

(c) h_2 *vs.* h_a

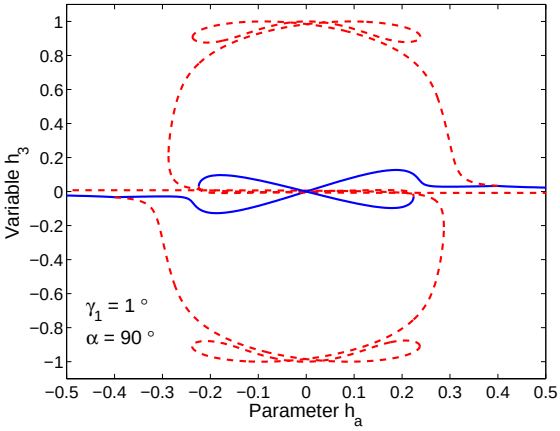

(d) h_3 *vs.* h_a

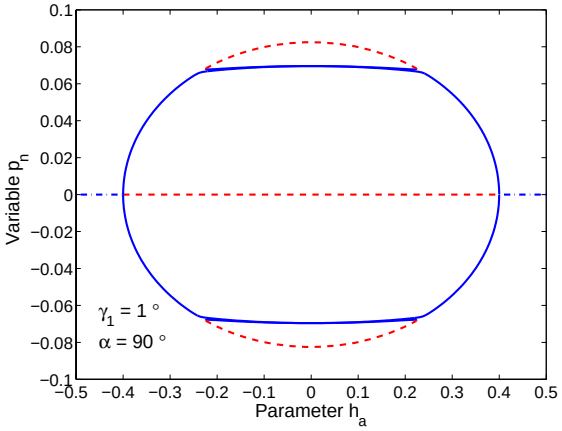

(e) p_n *vs.* h_a

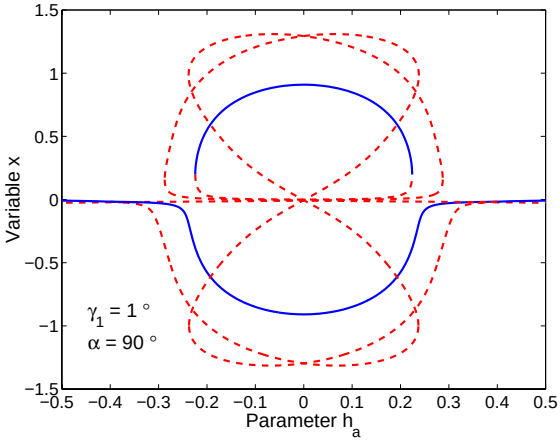

(f) x *vs.* h_a

Figure G.1: Rotor momentum bifurcation diagrams for prolate gyrostat with 1° in-plane rotor misalignment

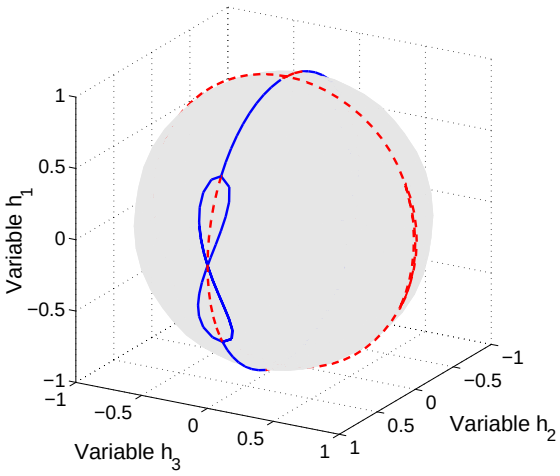

(a) Momentum sphere

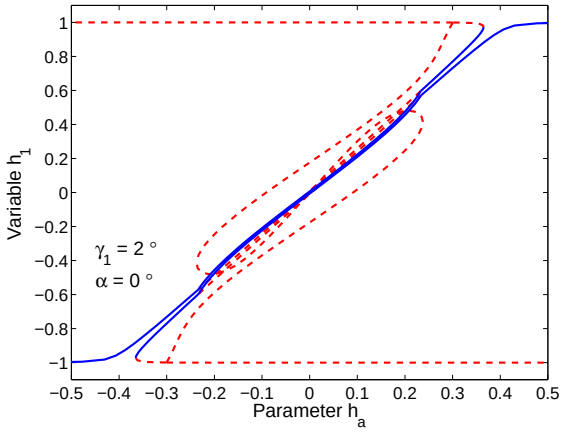

(b) h_1 *vs.* h_a

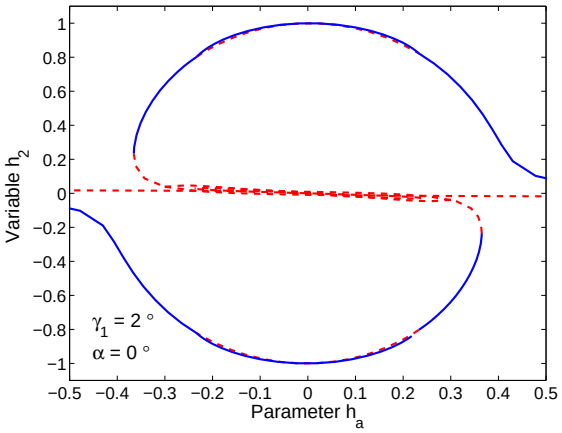

(c) h_2 *vs.* h_a

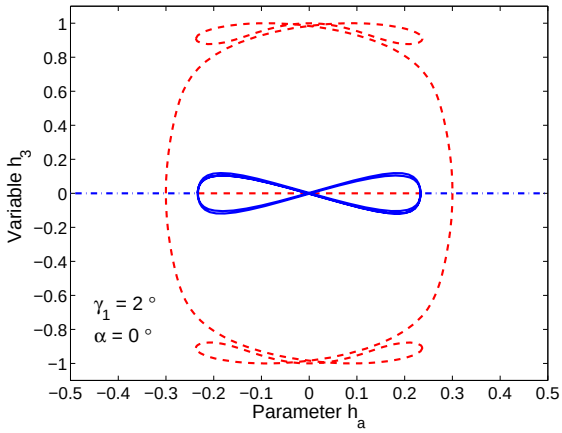

(d) h_3 *vs.* h_a

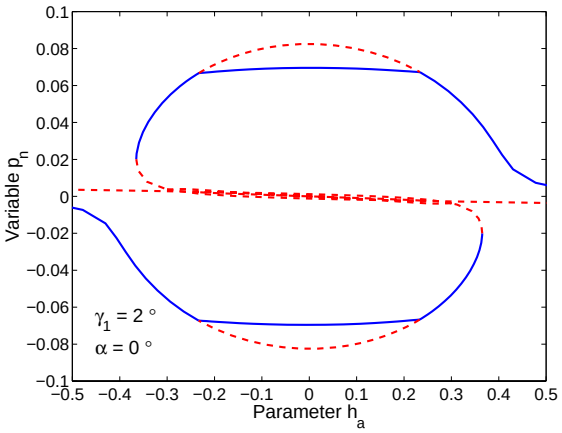

(e) p_n *vs.* h_a

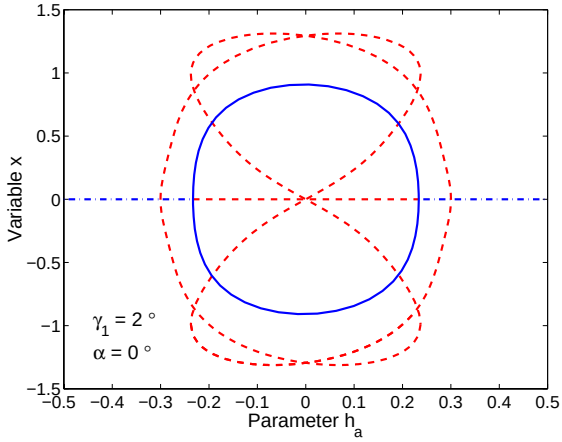

(f) x *vs.* h_a

Figure G.2: Rotor momentum bifurcation diagrams for prolate gyrostat with $2\,^\circ$ out-of-plane rotor misalignment

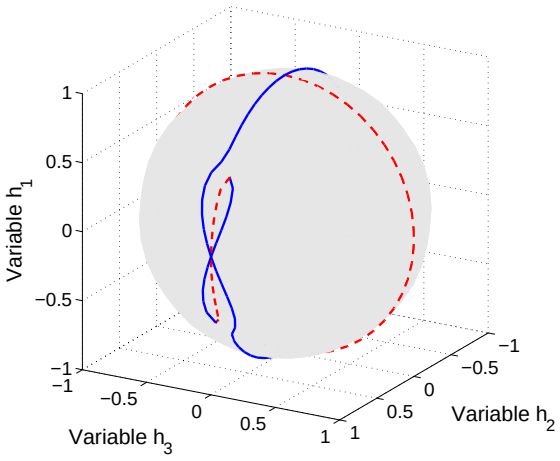

(a) Momentum sphere

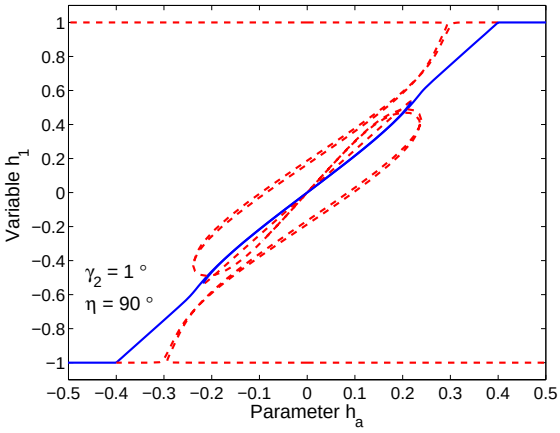

(b) h_1 *vs.* h_a

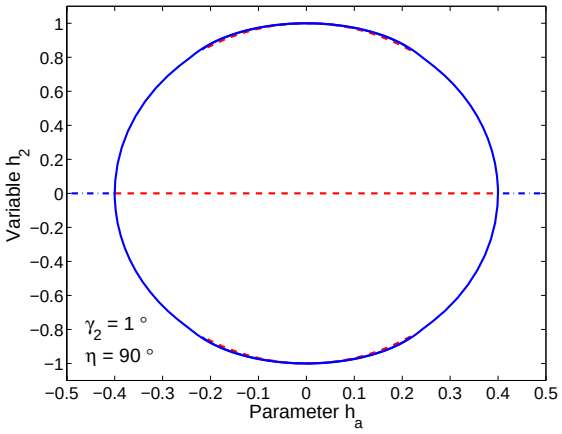

(c) h_2 *vs.* h_a

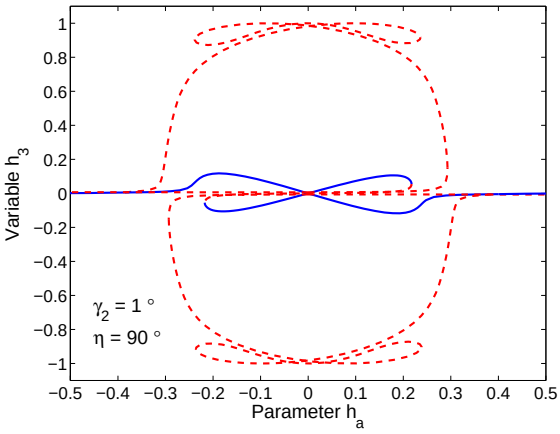

(d) h_3 *vs.* h_a

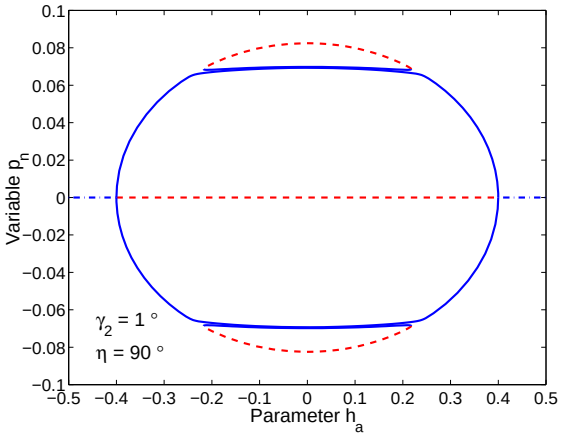

(e) p_n *vs.* h_a

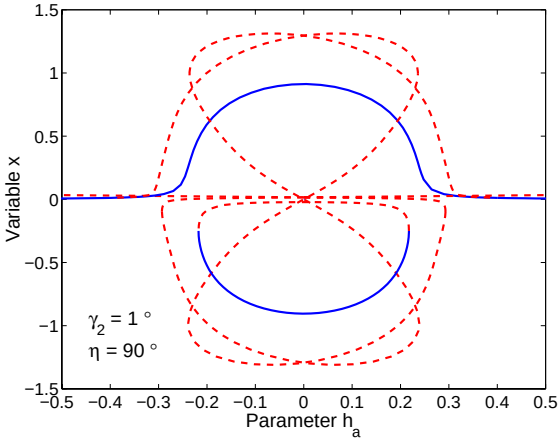

(f) x *vs.* h_a

Figure G.3: Rotor momentum bifurcation diagrams for prolate gyrostat with 1° in-plane damper misalignment

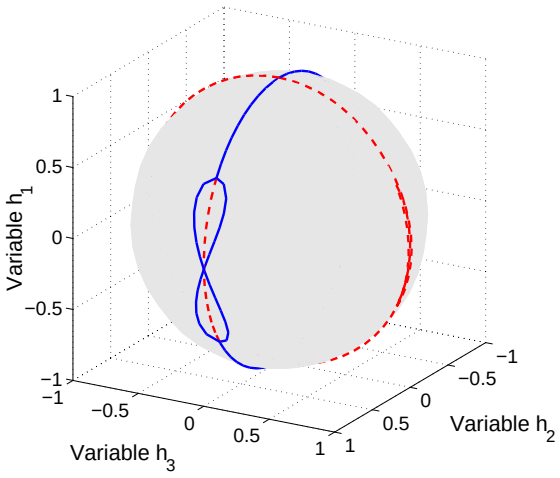

(a) Momentum sphere

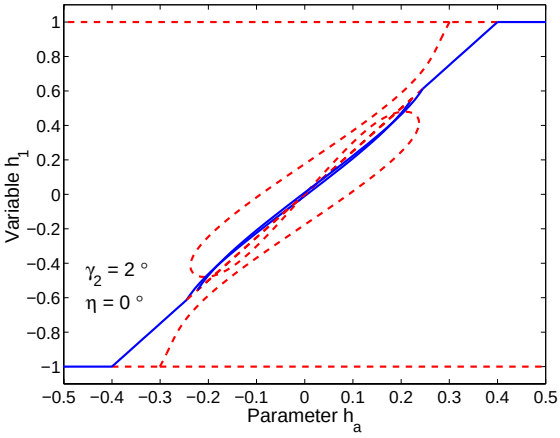

(b) h_1 *vs.* h_a

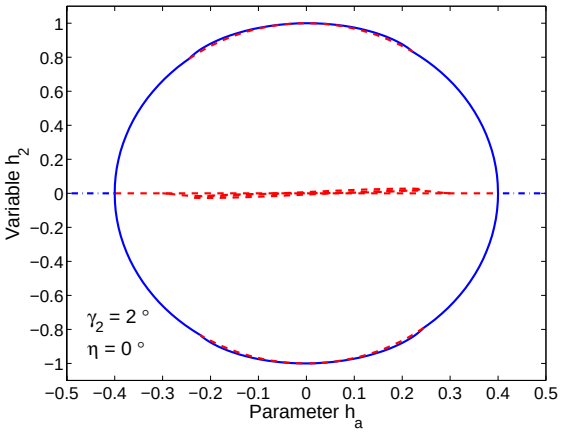

(c) h_2 *vs.* h_a

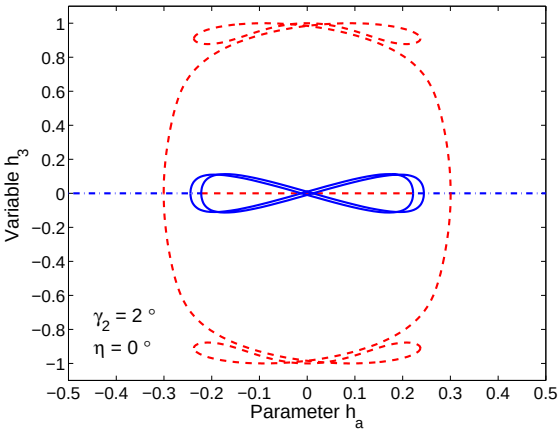

(d) h_3 *vs.* h_a

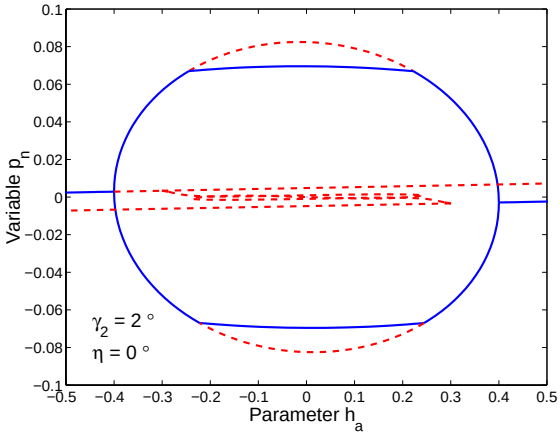

(e) p_n *vs.* h_a

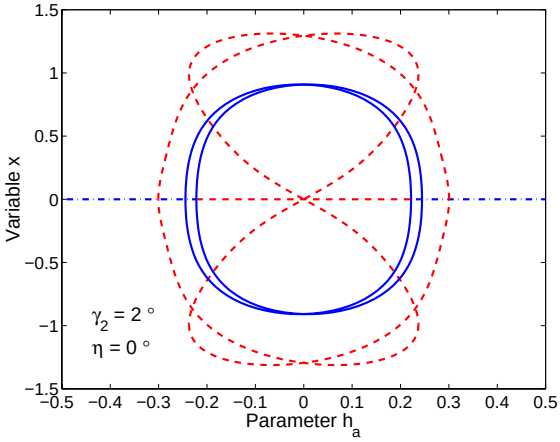

(f) x *vs.* h_a

Figure G.4: Rotor momentum bifurcation diagrams for prolate gyrostat with 2° out-of-plane damper misalignment

Vita

Ralph Sandfry was raised in Columbia, Missouri, and graduated from David H. Hickman High School in 1984. He accepted an Air Force ROTC scholarship to attend the University of Kansas where he earned a B.S. in Aerospace Engineering in 1989 and was commissioned as a 2nd Lieutenant in the United States Air Force.

On his best day, Ralph married the former Marilyn Gregory and two days later they began the long drive from Kansas to their first Air Force assignment in Los Angeles. Somehow between five moves and four universities, this remarkable woman completed her undergraduate education, earned a law degree, and blessed Ralph with two beautiful children, Kate (born in 1993) and Matthew (born in 1996).

Ralph began his Air Force career by serving in the Global Positioning System Joint Program Office at Los Angeles AFB, California. He served as a Systems Analyst and Payload Integration Engineer until fate called (actually the Air Force personnel center), and he accepted an offer to attend graduate school at the Air Force Institute of Technology (AFIT), Wright-Patterson AFB, Ohio. He completed a M.S. in Systems Engineering in 1992 as a distinguished graduate. He next traveled to Hill AFB, Utah and became the Lead Systems Engineer for the AGM-65 Maverick Missile Program Office. In 1995, he was selected as an Instructor of Astronautics at the US Air Force Academy. In addition to teaching, he served as Director of Research and Executive Officer for the Department of Astronautics. In 1998, the Air Force selected Ralph for the AFIT Civilian Institution program, and he chose to attend Virginia Tech to pursue a doctorate degree in Aerospace Engineering. After graduation, Ralph will return to the world of Air Force space systems and eventually resume teaching at the US Air Force Academy.

Bibliography

[1] Air Force Systems Command and Aerospace Corporation, *Proceedings of the Symposium on Attitude Stabilization and Control of Dual-Spin Spacecraft*, El Segundo, CA, 1967 Air Force Report No. SAMSO-TR-68-191, Aerospace Report No. TR-0158(3307-01)-16. (Also available as NTIS ADA 670 154.).

[2] Alfriend, K. T., "Partially Filled Viscous Ring Nutation Damper," *Journal of Spacecraft and Rockets*, Vol. 11, No. 7, 1974, pp. 456–462.

[3] Alfriend, K. T. and Hubert, C. H., "Stability of a Dual-Spin Satellite With Two Dampers," *Journal of Spacecraft and Rockets*, Vol. 11, No. 7, 1974, pp. 469–474.

[4] Alper, J. R., "Analysis of Pendulum Damper for Satellite Wobble Damping," *Journal of Spacecraft and Rockets*, Vol. 2, No. 1, 1965, pp. 50–54.

[5] Amieux, J. C. and Dureigne, M., "Analytical Design of Optimal Nutation Dampers," *Journal of Spacecraft and Rockets*, Vol. 9, No. 12, 1972, pp. 934–935.

[6] Bainum, P. M., Fuechsel, P. G., and Fedor, J. V., "Stability of a Dual-Spin Spacecraft With a Flexible Momentum Wheel," *Journal of Spacecraft and Rockets*, Vol. 9, No. 9, 1972, pp. 640–646.

[7] Bainum, P. M., Fuechsel, P. G., and Mackison, D. L., "Motion and Stability of a Dual-Spin Satellite With Nutation Damping," *Journal of Spacecraft and Rockets*, Vol. 7, No. 6, 1970, pp. 690–696.

[8] Beck, J. A., *Relative Equilibria of a Rigid Satellite in a Central Gravitational Field*, PhD thesis, Air Force Institute of Technology, 1997.

[9] Bhuta, P. G. and Koval, L. R., "Decay Rates of a Passive Precession Damper and Bounds," *Journal of Spacecraft and Rockets*, Vol. 3, No. 3, 1966, pp. 335–338.

[10] Bhuta, P. G. and Koval, L. R., "A Viscous Ring Damper for a Freely Precessing Satellite," *International Journal of Mechanical Sciences*, Vol. 8, 1966, pp. 383–395.

[11] Bracewell, R. N. and Garriott, O. K., "Rotation of Artificial Earth Satellites," *Nature*, Vol. 182, No. 4638, 1958, pp. 760–762.

[12] Carrier, G. F. and Miles, J. W., "On the Annular Damper for a Freely Precessing Gyroscope," *Journal of Applied Mechanics*, Vol. 27, 1960, pp. 237–240.

[13] Cartwright, W. F., Massingill, E. C., and Trueblood, R. D., "Circular Constraint Nutation Damper," *AIAA Journal*, Vol. 1, No. 6, 1963, pp. 1375–1380.

[14] Chang, C. O., Chou, C. S., and Tsai, M. L., "On the Viscoelastic Beam Damper for a Freely Precessing Gyroscope," *Journal of Sound and Vibration*, Vol. 153, No. 2, 1992, pp. 259–289.

[15] Chang, C. O., Liu, L. Z., and Alfriend, K. T., "Dynamics and Stability of a Freely Precessing Spacecraft Containing a Nutation Damper," *Journal of Guidance, Control, and Dynamics*, Vol. 19, No. 2, 1996, pp. 297–305.

[16] Chinnery, A. E., Numerical Analysis of a Rigid Body with an Attached Spring-Mass-Damper. Master's thesis, Air Force Inst. of Technology, Wright-Patterson AFB, Ohio, Dec 1994.

[17] Chinnery, A. E. and Hall, C. D., "Motion of a Rigid Body with an Attached Spring-Mass Damper," *Journal of Guidance, Control, and Dynamics*, Vol. 18, No. 6, 1995, pp. 1404–1409.

[18] Cloutier, G. J., "Stable Rotation States of Dual-Spin Spacecraft," *Journal of Spacecraft and Rockets*, Vol. 5, No. 4, 1968, pp. 490–492.

[19] Cloutier, G. J., "Nutation Damper Instability on Spin-Stabilized Spacecraft," *AIAA Journal*, Vol. 7, No. 11, 1969, pp. 2110–2115.

[20] Cochran, J. E. and Shu, P. H., "Effects of Energy Addition and Dissipation on Dual-Spin Spacecraft Attitude Motion," *Journal of Guidance, Control, and Dynamics*, Vol. 6, No. 5, 1983, pp. 368–373.

[21] Cochran, J. E., Jr. and Thompson, J. A., "Nutation Dampers vs Precession Dampers for Asymmetric Spacecraft," *Journal of Guidance and Control*, Vol. 3, No. 1, 1980, pp. 22–28.

[22] Doedel, E. J., Champneys, A. R., Fairgrieve, T. F., Kuznetsov, Y. A., Sandstede, B., and Wang, X., *AUTO 97: Continuation and Bifurcation Software for Ordinary Differential Equations*, Concordia University, Montreal, Canada, 1998.

[23] Fang, B. T., "Energy Considerations for Attitude Stability of Dual-Spin Spacecraft," *Journal of Spacecraft and Rockets*, Vol. 5, No. 10, 1968, pp. 1241–1243.

[24] Flatley, T. W., Equilibrium States for a Class of Dual-Spin Spacecraft. Technical Report R-362, NASA, Mar 1971.

[25] Gill, P. E., Murray, W., and Wright, M. H., *Practical Optimization*, Academic Press, London, 1981.

[26] Golubitsky, M. and Schaeffer, D. G., *Singularities and Groups in Bifurcation Theory, Volume I*, Springer-Verlag, New York, 1985.

[27] Gray, G. L., Kammer, D. C., Dobson, I., and Miller, A. J., "Heteroclinic Bifurcations in Rigid Bodies Containing Internally Moving Parts and a Viscous Damper," *SIAM Journal of Applied Mechanics*, Vol. 66, pp. 720–728.

[28] Guckenheimer, J. and Holmes, P., *Nonlinear Oscillations, Dynamical Systems, and Bifurcations of Vector Fields*, Springer-Verlag, New York, 1983.

[29] Hall, C. D., "Spinup Dynamics of Gyrostats," *Journal of Guidance, Control, and Dynamics*, Vol. 18, No. 5, 1995, pp. 1177–1183.

[30] Hall, C. D., "Momentum Transfer Dynamics of a Gyrostat with a Discrete Damper," *Journal of Guidance, Control, and Dynamics*, Vol. 20, No. 6, 1997, pp. 1072–1075.

[31] Hall, C. D., "Escape From Gyrostat Trap States," *Journal of Guidance, Control, and Dynamics*, Vol. 21, No. 3, 1998, pp. 421–426.

[32] Haseltine, W. R., "Passive Damping of Wobbling Satellites: General Stability Theory and Example," *Journal of the Aerospace Sciences*, Vol. 29, No. 5, 1962, pp. 543–549.

[33] Hubert, C., "Spacecraft Attitude Acquisition from an Arbitrary Spinning or Tumbling State," *Journal of Guidance and Control*, Vol. 4, No. 2, 1981, pp. 164–170.

[34] Hughes, P. C., *Spacecraft Attitude Dynamics*, John Wiley and Sons, New York, 1986.

[35] Huston, R. L., "Gyroscopic Stabilization of Space Vehicles," *AIAA Journal*, Vol. 1, No. 7, 1963, pp. 1694–1696.

[36] Iorillo, A. J., "Nutation Damping Dynamics of Axisymmetric Rotor Stabilized Satellites," In *ASME Annual Winter Meeting*, Chicago, 1965.

[37] Iorillo, A. J., "Hughes Gyrostat System," In *Proceedings of the Symposium on Attitude Stabilization and Control of Dual-Spin Spacecraft*, El Segundo, CA, 1967. Air Force Systems Command and Aerospace Corporation.

[38] Johnson, D. A., "Attitude Stability of Multibody Symmetrical Satellites with Mechanical Dampers," *Journal of Spacecraft and Rockets*, Vol. 11, No. 9, 1974, pp. 645–649.

[39] Kane, T. and Levinson, D., "Energy-Sink Analysis of Systems Containing Driven Rotors," *Journal of Guidance and Control*, Vol. 3, No. 3, 1980, pp. 234–238.

[40] Katucki, R. J. and Moyer, R. G., Systems Analysis and Design of a Class of Gravity Gradient Satellites Utilizing Viscous Coupling Between Earth's magnetic and Gravity Fields. Technical Report SP-107, NASA, 1966.

[41] Khalil, H. K., *Nonlinear Systems*, Macmillan, New York, 1992.

[42] Landon, V. D. and Stewart, B., "Nutational Stability of an Axisymmetric Body Containing a Rotor," *Journal of Spacecraft and Rockets*, Vol. 1, No. 6, 1964, pp. 682–684.

[43] Laskin, R. A., Sirlin, S., , and Likins, P. W., "Stability of a Dual-Spin Spacecraft with Spherical Dampers," In *AAS/AIAA Astrodynamics Specialist Conference*, Lake Placid, NY, August 1983.

[44] Levi, M.,"Morse Theory for a Model Space Structure," *Dynamics and Control of Multibody Systems, Contemporary Mathematics*, Vol. 97, American Mathematical Society, Providence, RI, 1989, pp. 209–216.

[45] Likins, P. W., "Attitude Stability Criteria for Dual Spin Spacecraft," *Journal of Spacecraft and Rockets*, Vol. 4, No. 12, 1967, pp. 1638–1643.

[46] Likins, P. W., "Spacecraft Attitude Dynamics and Control — A Personal Perspective on Early Developments," *Journal of Guidance, Control, and Dynamics*, Vol. 9, No. 2, 1986, pp. 129–134.

[47] Likins, P. W., Tseng, G.-T., and Mingori, D. L., "Stable Limit Cycles due to Nonlinear Damping in Dual-Spin Spacecraft," *Journal of Spacecraft and Rockets*, Vol. 8, No. 6, 1971, pp. 568–574.

[48] Liu, Y. Z. and Rimrott, F. P. J., "Global Motion of a Dissipative Asymmetric Gyrostat," *Archive of Applied Mechanics*, Vol. 62, No. 5, 1992, pp. 329–337.

[49] Liu, Y. Z. and Rimrott, F. P. J., "Global Motion of a Torquefree Flexible Multi-spin Satellite," *Transactions of the Canadian Society for Mechanical Engineering*, Vol. 17, No. 1, 1993, pp. 17–27.

[50] Meehan, P. A. and Asokanthan, S. F., "Chaotic motion in a Spinning Spacecraft with Circumferential Nutational Damper," *Nonlinear Dynamics*, Vol. 12, 1996, pp. 69–87.

[51] Miles, J. W., "On the Annular Damper for a Freely Precessing Gyroscope-II," *Journal of Applied Mechanics*, Vol. 30, 1963, pp. 189–192.

[52] Mingori, D. L., "Effects of Energy Dissipation on the Attitude Stability of Dual-Spin Satellites," *AIAA Journal*, Vol. 7, No. 1, 1969, pp. 20–27.

[53] Mingori, D. L., Tseng, G.-T., and Likins, P. W., "Constant and Variable Amplitude Limit Cycles in Dual-Spin Spacecraft," *Journal of Spacecraft and Rockets*, Vol. 9, No. 11, 1972, pp. 825–830.

[54] Nise, N. S., *Control Systems Engineering*, Addison-Wesley, Menlo Park, CA, 1995.

[55] Or, A. C., "Chaotic Motions of a Dual-Spin Body," *Journal of Applied Mechanics*, Vol. 65, 1998, pp. 150–156.

[56] Ross, I. M., "Nutational Stability and Core Energy of a Quasirigid Gyrostat," *Journal of Guidance, Control, and Dynamics*, Vol. 16, No. 4, 1993, pp. 641–647.

[57] Ross, I. M., "Formulation of Stability Conditions for Systems Containing Driven Rotors," *Journal of Guidance, Control, and Dynamics*, Vol. 19, No. 2, 1996, pp. 305–308.

[58] Sarychev, V. A. and Sazonov, V. V., "Spin-Stabilized Satellites," *Journal of the Astronautical Sciences*, Vol. 24, No. 4, 1976, pp. 291–310.

[59] Scher, M. P. and Farrenkopf, R. L., "Dynamic Trap States of Dual-Spin Spacecraft," *AIAA Journal*, Vol. 12, No. 12, 1974, pp. 1721–1724.

[60] Schneider, C. C. Jr and Likins, P. W., "Nutation Dampers vs Precession Dampers for Asymmetric Spinning Spacecraft," *Journal of Spacecraft and Rockets*, Vol. 10, No. 3, 1973, pp. 218–222.

[61] Sen, A. K., "Stability of a Dual-Spin Satellite with a Four-Mass Nutation Damper," *AIAA Journal*, Vol. 8, No. 4, 1970, pp. 822–823.

[62] Seydel, R., *Practical Bifurcation and Stability Analysis*, Springer-Verlag, New York, 2nd edition, 1994.

[63] Slotine, J.-J. E. and Li, W., *Applied Nonlinear Control*, Prentice Hall, Englewood Cliffs, NJ, 1991.

[64] Spencer, T. M., "Energy-Sink Analysis for Asymmetric Dual-Spin Spacecraft," *Journal of Spacecraft and Rockets*, Vol. 11, No. 7, 1974, pp. 463–468.

[65] Strang, G., *Linear Algebra and its Applications*, Harcourt Brace Jovanovich, San Diego, 3rd edition, 1988.

[66] Thomson, W. T. and Reiter, G. S., "Motion of an Asymmetric Spinning Body with Internal Dissipation," *AIAA Journal*, Vol. 1, No. 6, 1963, pp. 1429–1430.

[67] Vigneron, F. R., "Stability of a Dual-Spin Satellite with Two Dampers," *Journal of Spacecraft and Rockets*, Vol. 8, No. 4, 1971, pp. 386–389.

[68] Winfree, P. W. and Jr., J. E. C., "Nonlinear Attitude Motion of a Dual-Spin Spacecraft Containing Spherical Dampers," *Journal of Guidance, Control, and Dynamics*, Vol. 9, No. 6, 1986, pp. 681–690.